The Legacy of the First Galaxies: Exploring Ancient Stars in the Milky Way

by

Kaley Brauer

Sc.B., Brown University (2017)

Submitted to the Department of Physics
in partial fulfillment of the requirements for the degree of

Doctor of Philosophy in Physics
at the
MASSACHUSETTS INSTITUTE OF TECHNOLOGY
June 2023

Author .....
Department of Physics
May 17, 2023

Certified by .....
Anna Frebel
Professor of Physics
Thesis Supervisor

Accepted by .....
Lindley Winslow
Associate Department Head of Physics

The Legacy of the First Galaxies: Exploring Ancient Stars in the Milky Way

by

Kaley Brauer

Submitted to the Department of Physics
on May 17, 2023, in partial fulfillment of the
requirements for the degree of
Doctor of Philosophy in Physics

Abstract

In the first several hundred million years after the Big Bang, the first stars and galaxies transformed the Universe. These ancient systems launched the creation of every galaxy we see today, including the Milky Way. Ever since, for the last 13 billion years, the Milky Way has grown through galaxy mergers. Several of these mergers were with other similarly-sized galaxies and possibly a hundred of these mergers were with small dwarf galaxies. The smallest dwarf galaxies accreted by the Milky Way, the ultra-faint dwarfs (UFDs), are relics of the first galaxies in the Universe and provide important insight into early galaxy formation and chemical enrichment. Currently, though, accreted UFDs are poorly understood and we lack ways to identify stars that accreted from UFDs. By utilizing a simulation suite of 35 Milky Way-mass galaxies forming, I find that chemical tagging with r-process elements and clustering in kinematic phase space can help us identify stars that accreted together from these dwarf galaxies. Kinematic clustering only identifies recently accreted UFDs ($z \lesssim 0.5$), so we recommend chemical tagging as the more robust method to identify these stars. I also present an analytic model of collapsar enrichment that can self-consistently explain the observed scatter in r-process chemical elements of old stars. I am expanding on these studies with highly-resolved hydrodynamic simulations of the earliest dwarf galaxies, the *Aeos* simulations. The methodology and initial results for these simulations are also presented.

Thesis Supervisor: Anna Frebel
Title: Professor of Physics

Acknowledgments

I first want to acknowledge my advisor, Anna Frebel, and bonus advisor, Alexander Ji, without whom this thesis would not exist. Anna is endlessly supportive and insightful, and I am so thankful for her keen sense of interesting science directions and always connecting me to vital resources and collaborators. Alex is wonderfully talented and generous with his time, ideas, and advice. I am forever grateful for his guidance and friendship and I hope I can be an Alex Ji to future students.

I also want to acknowledge all the wonderful collaborators I have worked with throughout my PhD. To Jenn, Greg, John, Mordecai, Alex, Anna: thank you for sharing the struggles as we developed the *Aeos* simulations. Without your endless slack help, example code, analysis, and commiseration, we would not have the beautiful simulations we have today. To Hillary: thank you for working with me throughout the depths of the pandemic and helping produce cluster plot after cluster plot. I am so excited to see all the wonderful things you'll do at UChicago with Alex. To Brian: thank you for all of your insight on Caterpillar analysis, hospitality at Michigan, and always enjoyable conversations at JINA. To the Weekly Goals crew, Alex, Katy, Sal, Ivanna, Ani, Sanjana, Hillary, Allen, Jandrie, Mimi, and more: thank you for keeping me sane and at least moderately productive during the pandemic, and thank you for giving me the data for my April Fools paper (easily my most-read paper). I have been lucky to work with all of you and many more not mentioned. People are by far my favorite part of science.

I owe a huge debt of gratitude to my fellow MIT astrograds for helping me firmly keep the life in work-life balance. To the AstroPals, Michael, Ben, David, Chris, Stephanie, Sylvia, Halston, Alex D: thank you for the years of laughter, painting, dancing, crafting, puzzling, rooftop bar-ing, boating, fancy dinner-ing, skiing, themed partying, cooking, baking, scheming, occasional science, and more. To Mason: thank you for the cat pictures. To Nick D: thank you for the wonderful lunches. To Lisa, Danielle, Ani, Champ, Collin, Alex Y, Cian, Meredith, Laurel, Megan, Devin, Haochen, Dominika, Kaitlyn, Calvin, Rahul, Geoffrey, Swadha, Ellie, and so many

others: thank you for making MKI a fantastic place to work. You all make me grateful I came to MIT.

I also have to acknowledge the support of my friends from outside MIT astrophysics. To Andrew: thank you for your incredible friendship. It has been a joy growing alongside you for the last ten years. To Hunter: thank you for the seal watching, jet ski tubing, and the gloomiest of dream teams. To Sarah: thank you for both the joy and the commiseration – we did it. To Ryan and Claire: thank you so much for your friendship from elementary school to now. To Sydney: thank you for the gauntlet outings, tulips, and always wonderful conversations. To Kyle: thank you for the games out of anything, road trips, and great friendship. To Thomas and Ellie: thank you for the paints, putts, and scavenger hunts. To the '24 Indian Ocean, Haruka, Dogan, Nadine, Taylor, Nico, Ingrid, Kieran, Richa, George, Cyndi, Mary, Valerie, Cris, Jenny, Clara, Abe, McCoy, Henk, Hannah, Alyssa, Leighton, Katherine, and more: thank you for including me as an honorary Indie, the incredible conversations & hangouts, and the first standing ovation I've seen at a thesis defense. Also thank you to many other non-astro MIT grad students I have had the joy to spend time with throughout the years. I am lucky to know you all.

To all of the MIT community members who have supported me throughout the years, thank you as well. Thank you Cathy, Sydney, Thea, Debbie, and Nayanika for your incredible work organizing and running this department and division. Thank you Phyllis for always chatting whenever I was working late. And thank you Rob for running this institute and supporting my crazy ideas.

I would not be where I am today without the love and support of my family. Mom, Dad, and Ryan, thank you for encouraging me and supporting me in everything I have ever done. I am so proud to be a Brauer.

Lastly, thank you Tim for your endless love and support. Your belief in me makes hard things seem easy.

Contents

List of Figures

The flipbook images in the corner of each page are based on a galaxy collision visualization from the Advanced Visualization Laboratory at the National Center for Supercomputing Applications, a collaboration with NASA and Drs. Brant Robertson and Lars Hernquist

List of Tables

Chapter 1

Introduction

1.1 Galactic Archaeology: Studying the History of our Galaxy

The goal of galactic archaeology is to study the history of our home galaxy, the Milky Way. Like traditional archaeologists who study the history of humanity by finding and analyzing ancient artifacts, galactic archaeologists study the history of the Milky Way by observing and analyzing ancient stars and stellar systems. Galactic archaeologists aim to contextualize our galaxy's past, present, and future in the Universe.

1.1.1 Galaxy Formation

The standard cosmological model, called "ΛCDM" or "Big Bang cosmology", is the simplest model in general agreement with observations of the Universe. The "Λ" represents the cosmological constant of dark energy and "CDM" stands for "Cold Dark Matter". Together, dark energy and dark matter compose the majority of the Universe, while "baryonic matter", e.g. normal matter like ourselves, composes less than 5%. This model has been incredibly successful at explaining the large-scale structure of galaxies, abundances of chemical elements, the cosmic microwave background, and more.

According to ΛCDM, the first galaxies formed 200-300 million years after the

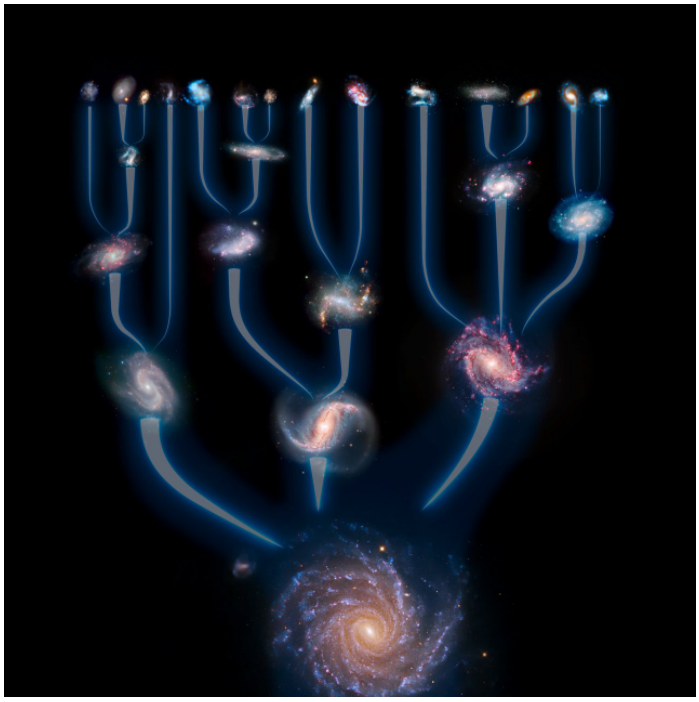

Figure 1-1: Large galaxies grow over time through mergers with many smaller dwarf galaxies. The formation history of a galaxy can be summarized through a "merger tree" such as the one depicted here. The merger history of the Milky Way is a major unsolved problem in galactic archaeology. Source: ESO/L. Calçada

Big Bang. During initial galaxy formation, baryonic matter was too hot to form gravitationally-bound objects, so dark matter was necessary to form large structures. Halos of dark matter arose from tiny initial density perturbations that grew under the effect of gravity until they collapsed. Galaxies then grew hierarchically, merging with other galaxies to grow larger over cosmic time. This hierarchical growth continues today, over 13 billion years since the first galaxies formed [White and Rees, 1978, Davis et al., 1985].

To understand the formation history of a galaxy, we thus must understand its merger history. Characterizing the galaxy mergers (how many galaxies of different masses, what times the mergers occurred, and more) experienced by the Milky Way is a major goal of galactic archaeology. The merger history of a galaxy can be visualized as a "merger tree" as shown in Figure 1-1.

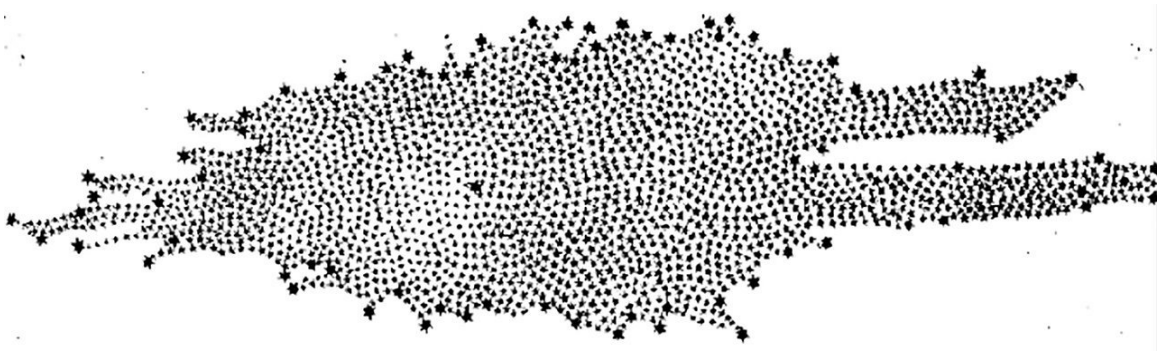

a) One of the first known maps of the Milky Way, a drawing from astronomer William Herschel in 1785. Source: [Herschel, 1785]

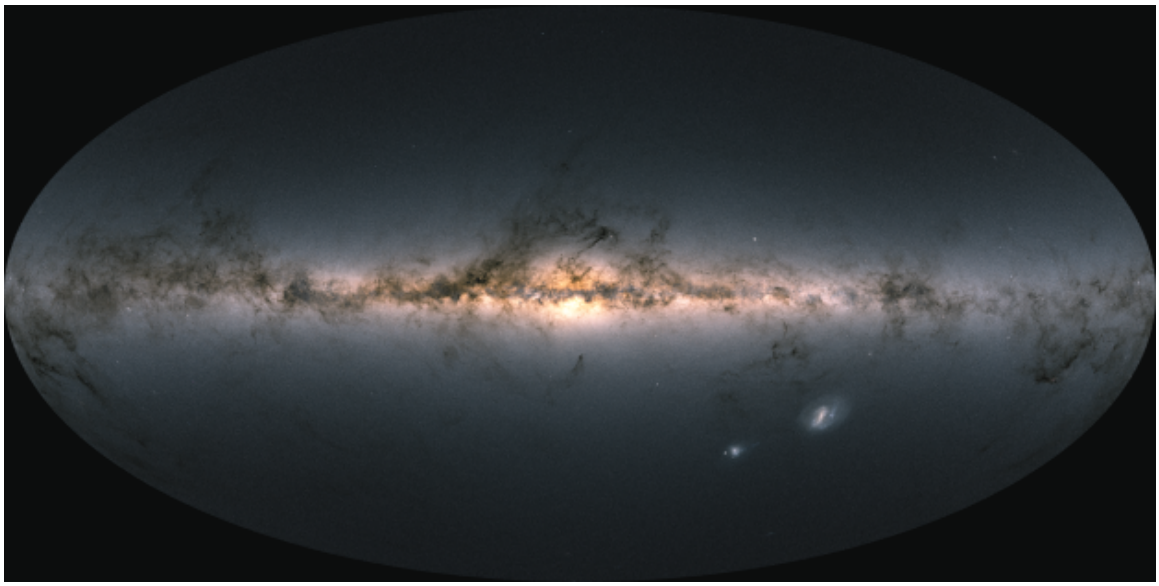

b) The most complete map of the Milky Way to-date, a 2020 star map from the European Space Agency's Gaia mission. Source: ESA/Gaia/DPAC

Figure 1-2: Our image of the Milky Way has been revolutionized by the Gaia mission. Gaia is a space observatory which has observed over a billion stars, roughly 1% of the total number of stars in the Galaxy.

1.1.2 The Milky Way

The Milky Way is a large galaxy with a mass of about a trillion solar masses [Fragione and Loeb, 2017] that formed from dozens of mergers over cosmic time. Recently, astronomers have made incredible advances in mapping the Milky Way. The European Space Agency's Gaia mission has observed 1.8 billion stars over the last several years, forming the most complete map of our Galaxy to-date (see Figure 1-2b). This is an extreme leap from the days of astronomers drawing the locations of stars and

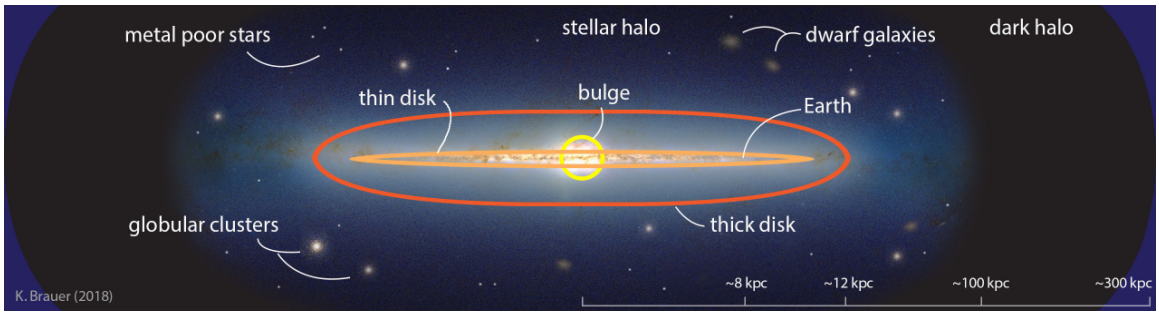

Figure 1-3: Diagram of the Milky Way from an external point of view. This diagram looks into the plane of the Galaxy, so the spiral arms are not visible. The outskirts of the Galaxy (the "stellar halo") contain many accreted stars left over from merger events.

mapping the Milky Way by hand (see Figure 1-2a), allowing us to identify subtle structures left over from merger events in the past. For example, the identification of the Gaia Sausage or Gaia-Enceladus structure (so-named because of its sausage-like shape in velocity space) is a significant recent finding indicating that the Milky Way experienced a major galaxy merger about 8-11 billion years ago [Belokurov et al., 2018, Helmi et al., 2018]. Stellar kinematic data from the Gaia mission has also lead to a better understanding of several other major mergers (e.g., Sequoia, Myeong et al. 2019; Kraken, Kruijssen et al. 2019, 2020, Forbes 2020; and more, Naidu et al. 2020).

A schematic of the Milky Way can be seen in Figure 1-3. The majority of stars are located in the plane of the Galaxy, in the disks and the bulge. The Sun is located in the thin disk about 8 kpc from the center. The disk is where star formation occurs, so the *in situ* stars that formed in the Milky Way are mostly found in these areas. On the other hand, the accreted stars – the stars that formed in other galaxies which merged into the Milky Way – can be found all over the Galaxy. When dwarf galaxies merge with the Milky Way, they are stripped apart and their stars are scattered throughout the Galaxy. In particular, the stellar halo, the extended outskirts of the Galaxy, is home to old metal-poor stars which largely accreted from now-destroyed dwarf galaxies [Bell et al., 2008, Bullock and Johnston, 2005]. The stars in the stellar halo thus form a fossil record of the many galaxy mergers throughout the Milky Way's formation history.

When we observe stars in the Milky Way today, we can obtain two primary cat-

egories of stellar data: stellar kinematics (e.g., through parallax measurements like Gaia) and stellar chemical abundances (e.g., through spectral analysis). Astronomers have collected kinematic data on over a billion Milky Way stars and chemical abundances on thousands to millions of Milky Way stars (depending on which chemical elements). Obtaining detailed chemical abundances is difficult because it requires high-resolution spectra and careful analysis, but the chemical abundances of a star are important because they reveal information about the star's origins. This is because chemical composition of any unevolved star we observe has been roughly constant until now, so observations of the present-day composition in a 13 billion year old star are actually measurements of the chemical composition of their birth gas cloud 13 billion years ago [Freeman and Bland-Hawthorn, 2002]. In this way, chemical abundances of old stars are windows into the early Universe and an important tool in galactic archaeology.

1.2 The Origins of Chemical Elements

In the Big Bang, only hydrogen (H), helium (He), and trace amounts of lithium (Li) were created. All other chemical elements (called "metals" in astronomy) had to be synthesized through other processes. The basic nucleosynthetic processes are described in Burbidge et al. [1957]. Elements up to iron (Fe) are synthesized in the cores of massive stars and expelled into the Universe when the star dies in a core-collapse supernova. Lower mass stars can only synthesize elements up to carbon and oxygen before they become white dwarfs after having exhausted their nuclear fuel. White dwarfs can then accrete material until they explode in a Type Ia supernova, producing iron-peak elements (elements around Fe). The lightest elements (Li, Be, B) are created when a high energy cosmic ray collides with heavier nuclei in the interstellar medium, fragmenting them into lighter nuclei.

When elements lighter than iron (Fe) fuse, the process *produces* energy because the fusion creates a nucleus that is lighter than the two initial nuclei combined. Producing elements heavier than iron would require excess energy, however. All heavier elements

thus must be made through "neutron-capture" processes [e.g., Sneden et al., 2008]. In neutron-capture processes, nuclei are bombarded with free neutrons, producing heavier nuclei that decay to stability through beta decay. There are two primary neutron-capture processes: the slow neutron capture process (s-process) and the rapid neutron capture process (r-process). The s-process occurs when densities of neutrons are low ($n \lesssim 10^8$ cm^{-3}), primarily in asymptotic giant branch (AGB) stars [Busso et al., 1999]. The r-process occurs when densities of neutrons are sufficiently high ($n \sim 10^{24}$ cm^{-3}) that multiple neutron captures occur before a beta decay. Following observations of the neutron star merger GW170817 in 2017 [Abbott et al., 2017a,b], neutron star mergers have been confirmed as an astrophysical site of the r-process. A periodic table summarizing the astrophysical origins of every chemical element in shown is Figure 1-4.

The amount of "metals" in the Universe increases with time. The Universe begins essentially metal-free, and then stars and stellar remnants synthesize metals over time. “Metallicity” is thus often treated as a rough proxy for time; metal-poor stars are generally older than metal-rich stars. Fe is the typical reference element used to quantify a star’s metallicity because it is both relatively easy to measure and produced in nearly all supernovae. By convention, chemical abundance ratios are typically defined in relation to the Sun: $[\mathrm{A/B}] \equiv \log_{10}(N_X/N_Y)_* - \log_{10}(N_X/N_Y)_\odot$ for elements A and B, where N_A represents the abundance of A. Therefore, a star with $[\mathrm{Fe/H}] = -2$ has 1/100th the metallicity of the Sun and is likely billions of years older.

1.2.1 Rapid Neutron Capture Process (r-Process)

As one of the two main neutron capture processes, the r-process produces around half of the isotopes of the heaviest elements in the periodic table. Gold, platinum, and silver are all formed primarily by the r-process. Because the r-process requires extremely neutron-dense, high-energy environments, however, it can only occur in specific astrophysical sites. There has been debate over which astrophysical sites produce r-process material since the 1950s. Thanks to the detection of an optical

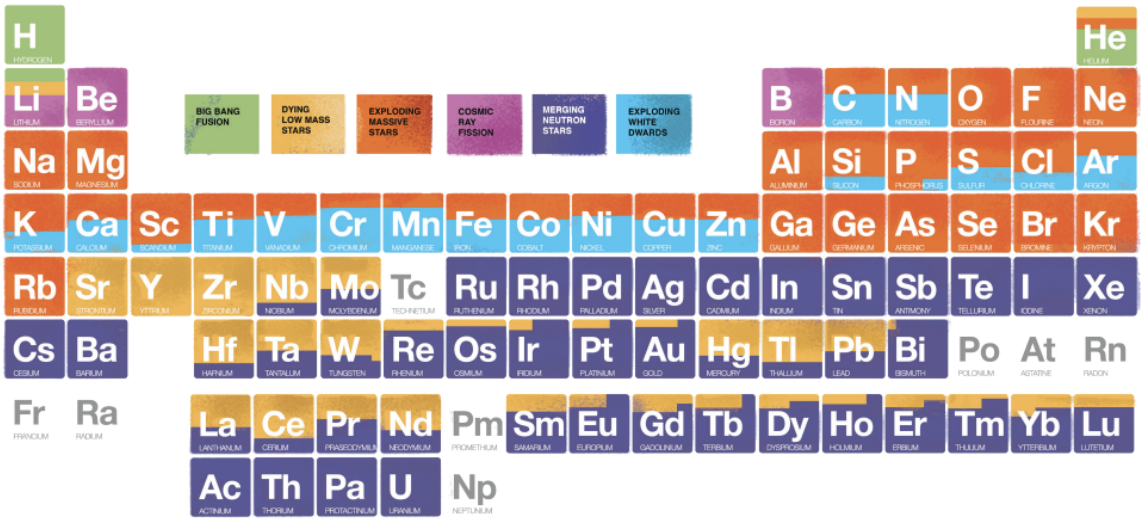

Figure 1-4: This periodic table is color coded to indicate humanity's best guess as to the nuclear origin of all known elements. Source: NASA/CXC/K. Divona; Reference: SDSS blog, J. Johnson

transient associated with the neutron star merger GW170817, one confirmed astrophysical site is neutron star mergers [Abbott et al., 2017a,b]. When two neutron stars collide, neutron-rich ejecta is blown out into space, hosting the production of radioactive heavy nuclei whose decay is visible through a "kilonova" associated with the merger [e.g., Drout et al., 2017, Pian et al., 2017]. Neutron star mergers are thus one source of the r-process, but it is unclear if other significant sources exist.

In particular, neutron star mergers may be unable to explain observations of r-process material in metal-poor stars. Neutron star binaries take time to form and coalesce, and it is unclear if this occurs sufficiently quickly to enrich the gas which forms metal-poor ([Fe/H] $\lesssim -2.5$) stars [e.g., Argast et al., 2004, Skúladóttir et al., 2019, Cescutti et al., 2015, Wehmeyer et al., 2015, Haynes and Kobayashi, 2019]. Furthermore, when a neutron stars form during supernova explosions, they receive natal kicks that could send them flying out of small, early galaxies [Bramante and Linden, 2016, Beniamini et al., 2016, Bonetti et al., 2019]. Collapsing massive stars ("collapsars") could be an alternative source of r-process material, but this remains observationally unconfirmed. The astrophysical sites of the r-process remain a source of debate, especially in early, small galaxies. Chapter 3 investigates this problem in

more detail.

1.3 Relics of the First Galaxies: Ultra-Faint Dwarf Galaxies

The smallest, earliest galaxies only formed stars from redshift $z \sim 20$ until $z \sim 6$ when they were quenched by reionization [Brown et al., 2014]. Because of this, they are primitive systems that are frozen in time with ancient stars from 13 billion years ago. Over time, many of these small galaxies merged to help form the galaxies we observe today, including the Milky Way [Frebel, 2010]. Stars from these tiny galaxies ("ultra-faint dwarfs", $L < 10^5 L_\odot$) thus are relics from the era of the first stars and galaxies, preserving clean signatures of early chemical enrichment. They are also vital ingredients in our own formation history. The stars from these accreted ultra-faint dwarf galaxies (UFDs) are found largely in the extended outskirts of our galaxy, the stellar halo [Bell et al., 2008]. The stars in the stellar halo thus reveal information about the assembly history of the galaxy. However, we currently lack ways to reliably identify which stars originated in which dwarf galaxies. This is particularly difficult for ultra-faint dwarfs, the smallest dwarf galaxies, because even though they represent $> 90\%$ of all accreted galaxies in the Milky Way, they contributed fewer than 1% of the total number of stars [e.g., Brauer et al., 2022]. They only contribute significantly at stellar metallicities [Fe/H] $\lesssim -2.5$ (see Figure 1-5). These poorly-understood building blocks of the stellar halo are important examples of some of the first galaxies in the Universe, but we are unable to identify their remnants. Chapters 2 and 4 tackle this problem, investigating both chemical tagging and kinematic clustering as methods to identify stars from ultra-faint dwarfs.

Surviving ultra-faint dwarf galaxies can also be found orbiting the Milky Way today. In the past 15 years, dozens of UFDs have been discovered in the Local Group [e.g., Bechtol et al., 2015]. High-resolution spectroscopy has provided chemical abundances of over 15 of these dwarfs, with dozens to come in the next decade.

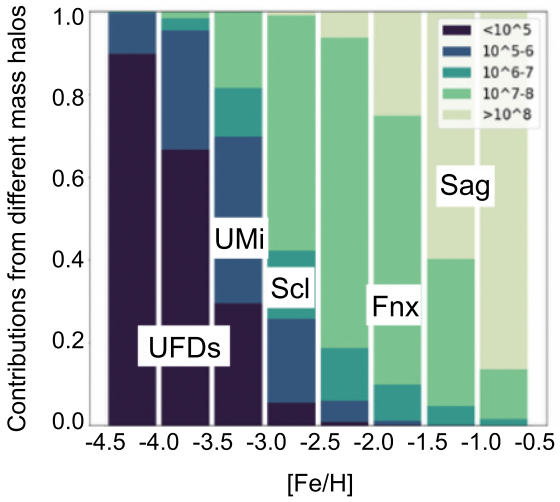

Figure 1-5: Contribution by galaxy mass to a Milky Way-mass stellar halo at different [Fe/H]. This plot shows results for an example simulated accreted stellar halo of a Milky Way-mass galaxy (see Chapter 3). High [Fe/H] is dominated by a few massive satellites (Sagittarius- and Fornax-mass accreted galaxies) and low [Fe/H] is dominated by many smaller satellites (Sculptor-, Ursa Minor-, and UFD-mass accreted galaxies). UFDs do not contribute significantly until [Fe/H] $\lesssim -2.5$.

Simultaneously, chemical abundances of millions of stars in the Milky Way stellar halo are being obtained through wide-field spectroscopic programs such as GALAH (De Silva et al. 2015), H3 (Conroy et al. 2019), APOGEE (Majewski et al. 2017), RAVE (Steinmetz et al. 2006), SEGUE (Yanny et al. 2009), and LAMOST (Cui et al. 2012), with more to come from WEAVE (Dalton et al. 2014), DESI (Allende Prieto et al. 2020), 4MOST (de Jong et al. 2019), SDSS-V (Kollmeier et al. 2017), and the Rubin Observatory (Ivezić et al. 2019).

The problem is that observations of stars in dwarf galaxies and our stellar halo are outpacing theoretical models. We have a wealth of data, but we cannot leverage the full detail within it. Observations show scatter around the mean trends of chemical abundances in dwarf stellar populations [e.g., Ji et al., 2020]. Current state-of-the-art chemical evolution models can explain mean trends in the data, but are incapable of modeling the scatter and full distribution because they assume instantaneous formation of clusters of stars with homogeneous mixing of yields [e.g., Côté and Ritter, 2018]. New, more detailed models are necessary to fully utilize the data to explore

complex galaxy formation processes including source-dependent metal mixing, hierarchical galaxy merging, bursty star formation, and variations across different galaxies. This is especially vital for stars from small, high-redshift galaxies because even JWST cannot directly observe these faint objects [Boylan-Kolchin et al., 2016], meaning our only path forward is to take full advantage of the dwarf stellar populations around us. Chapter 5 describes a novel cosmological simulation of early galaxy formation that will allow star-by-star comparison with the UFD populations in and around the Milky Way.

1.4 Overview of Thesis

The goal of this thesis is to study the evolution of the first galaxies, their contributions to the Milky Way, and the origins of heavy chemical elements. The remaining chapters comprise several published papers, the methodology for a new cosmological simulation, and a conclusion. All of the work in this thesis is theoretical and computational, mostly using cosmological simulations. The theoretical results are put into context with observational data.

Chapter 2 reproduces the paper *The Origin of r-process Enhanced Metal-Poor Halo Stars in Now-Destroyed Ultra-Faint Dwarf Galaxies* [Brauer et al., 2019]. In this paper, I investigate the possibility of using observations of r-process chemical elements in old stars as a method of identifying accreted stars that originated in ultra-faint dwarf galaxies. Using the *Caterpillar* simulation suite – a dark-matter-only suite of 35 Milky Way-mass galaxies forming in a cosmological setting [Griffen et al., 2016] – and analytical prescriptions for baryonic matter, I simulate producing r-process stars exclusively in accreted ultra-faint dwarfs. I then compare the fraction of simulated stars with r-process enhancement to the fraction of real stars in the Milky Way stellar halo with r-process enhancement to determine whether metal-poor r-process stars may have largely originated in accreted ultra-faint dwarfs.

Chapter 3 reproduces the paper *Collapsar r-process Yields Can Reproduce [Eu/Fe] Abundance Scatter in Metal-Poor Stars* [Brauer et al., 2021]. In this paper, I study

whether collapsars could be the primary astrophysical site of r-process material in the early Universe. Neutron star mergers are a confirmed site of the r-process [Drout et al., 2017, Abbott et al., 2017a], but it is unclear if they are able to produce the material observed in metal-poor stars. Collapsars are a possible alternative. We produce an analytic model to study whether collapsars can reproduce observed r-process abundance scatter in old stars.

Chapter 4 reproduces the paper *Possibilities and Limitations of Kinematically Identifying Stars from Accreted Ultra-Faint Dwarf Galaxies* [Brauer et al., 2022]. In this paper, I quantify the success of different clustering algorithms at kinematically identifying remnants of ultra-faint dwarfs in the stellar halos of Milky Way-mass galaxies. Identifying clusters of stars in kinematic phase space has been a useful method of studying recent high-mass galaxy mergers, but tiny ultra-faint dwarf galaxies have significantly weaker kinematic signatures. Using a suite of 32 Milky Way-mass galaxies, I run 10,000 clustering tests with different algorithms, radial cuts, hyperparameter choices, and more. I quantify the possibilities and limitations of this method with regards to ultra-faint dwarfs.

Chapter 5 describes ongoing work to produce, for the first time, a high-resolution cosmological simulation of galaxy formation with individual star particles, individual stellar feedback with detailed stellar yields, and adaptive grids to capture detailed metal mixing in the interstellar medium from the first stars. The simulation is called *Aeos*, and its value is its detailed tracing of 13 chemical elements associated with different nucleosynthetic channels in individual star particles. Using a modified version of Enzo adaptive mesh refinement simulation code [Bryan et al., 2014], the simulation has currently been run to redshift $z = 14.5$ with 124 star-forming halos and over 140,000 star particles. I present the methodology, initial results, and planned next steps.

Chapter 6 concludes and summarizes all results.

Chapter 2

The Origin of r-Process Enhanced Metal-Poor Halo Stars In Now-Destroyed Ultra-Faint Dwarf Galaxies

This chapter is based on work previously published in *The Astrophysical Journal* (Brauer et. al 2019).

2.1 Introduction

In the favored cosmological paradigm, galaxies grow hierarchically over time [White and Rees, 1978, Davis et al., 1985]. Dark matter halos (and the galaxies inside them) merge together to form larger and larger galaxies, resulting in a final galaxy comprising both stars that formed *in situ* and stars that formed in the now-destroyed progenitor galaxies. The *in situ* stars are found primarily in the disk and bulge of the galaxy, where star formation is ongoing. The accreted stars are found primarily in the extended outskirts of the galaxy: the stellar halo [Bell et al., 2008]. The stars in a galaxy's stellar halo thus preserve information about the now-destroyed building blocks of that galaxy [Bullock and Johnston, 2005].

The stellar halo can include a significant number of *in situ* stars as well, though [Monachesi et al., 2018]. Furthermore, even among the stars that are believed to have been accreted, the properties of the galaxies in which they formed are largely a mystery. To decode the information stored in stellar halo stars, we must identify the stars that were accreted and determine the types of galaxies from which they accreted. One way to do this is by looking for stars with kinematic signatures of accretion [Johnston et al., 1996, Johnston, 1998, Helmi et al., 1999, Venn et al., 2004]. Many galaxy mergers occurred early in the history of the galaxy, however, and by the time we observe the stellar halo, many of these kinematic signatures can be difficult to observe.

Selecting stars with specific chemical signatures provides another way forward. The Milky Way's accreted stellar halo is composed of long-ago destroyed galaxies covering a wide range of stellar masses. Those disrupted galaxies formed their stars at different rates, imprinting different chemical signatures on their most metal-poor stars [e.g., Kirby et al., 2011a, Lee, 2014, Ishimaru et al., 2015]. In particular, early r-process (rapid neutron-capture process) nucleosynthesis events in small dwarf galaxies would imprint a clean r-process signature on the subsequently formed stars in those galaxies.

The r-process is responsible for producing around half of the abundances of the heaviest elements in the periodic table [Burbidge et al., 1957, Cameron, 1957]. For more information, see the recent review papers by Frebel [2018], Thielemann et al. [2017], and Arcones et al. [2017]. Recently, it has become apparent that the majority of r-process material in the universe is likely synthesized in neutron star mergers (NSMs) [Hotokezaka et al., 2015, Ji et al., 2016b, Abbott et al., 2017a,b]. Because neutron star mergers appear to have a long coalescence timescale ($\gtrsim$100 Myr) and the metallicity of a stellar system increases with each new stellar generation, NSM events should only result in metal-poor stars with an r-process signature if those stars formed in dwarf galaxies with low star formation efficiencies (i.e., galaxies that form new generations of stars slowly relative to larger galaxies like the Milky Way or LMC) [Ishimaru et al., 2015, Ojima et al., 2018]. This is supported by observations of the

surviving ultra-faint dwarf galaxy Reticulum II. The metal-poor stars in Reticulum II formed from gas that was enriched by a prolific r-process event, believed to be a neutron star merger [Ji et al., 2016b].

In this paper, we investigate the possibility that metal-poor stellar halo stars with strong r-process signatures originated primarily in now-destroyed ultra-faint dwarf galaxies (UFDs) similar to Reticulum II. If this is true, the r-process stars we observe today could play a key role in understanding how the smallest building blocks of the Milky Way contribute to the Galaxy's formation.

This work is a first attempt to investigate this origin scenario of metal-poor r-process halo stars. We use cosmological models based on hierarchical galaxy formation simulations of Milky-Way-mass galaxies. This is described in Section 2.2, wherein we discuss our simulations and compare them to observed stellar halos (i.e., those of MW, M31, and GHOSTS galaxies). Star formation and chemical enrichment in low-mass galaxies is a field still under development (e.g., it is still difficult for semi-analytic models to reproduce even the mass-metallicity relation, Lu et al. 2017). We thus use empirical relations and parameterized models. In Section 2.3, we describe our simple, empirically motivated treatment of r-process enrichment of early low-mass UFDs. Our results and a detailed discussion of the limitations of our model are found in Section 3.4. Our conclusions are summarized in Section 3.6.

2.2 Simulations

We analyze 31 dark-matter-only cosmological simulations of Milky Way-mass halos from the *Caterpillar Project* [Griffen et al., 2016]. The zoom-in simulations in this suite have an effective resolution of $16{,}384^3$ particles of mass 3×10^4 $M_\odot$ in and around the galaxies of interest, resolving halos down to total mass $\sim10^6$ $M_\odot$. The temporal resolution is 5 Myrs/snapshot from z = 31 to z = 6 and 50 Myrs to $z = 0$. The simulated halos in the suite span an unbiased range of accretion histories. For our analysis, we selected the simulated halos that were most Milky-Way-like, removing the halos that experienced late major mergers.

We briefly summarize details of how the simulations were developed [for a more extensive explanation, see Griffen et al., 2016]. The halos in the zoom-in simulations were selected from a larger, lower resolution parent simulation in which structure evolved in a periodic box of comoving length 100 h^{-1} Mpc with $1{,}024^3$ particles of mass 1.22×10^7 $M_\odot$. The cosmological parameters were adopted from Planck 2013 ΛCDM cosmology: $\Omega_m = 0.32$, $\Omega_\Lambda = 0.68$, $\Omega_b = 0.05$, $\sigma_8 = 0.83$, $n_s = 0.96$, and H = 100 h km s^{-1} Mpc^{-1} = 67.11 km s^{-1} Mpc^{-1} [Planck Collaboration et al., 2014]. Initial conditions were constructed using `MUSIC` [Hahn and Abel, 2011]. In the zoom-in simulations, care was taken to ensure that only the high-resolution volume of the Milky Way at $z > 10$ is studied and that no halos are contaminated with low-resolution particles. Dark matter subhalos were identified using a modified version of `ROCKSTAR` [Behroozi et al., 2013b, Griffen et al., 2016] and mergers trees were constructed by `CONSISTENT-TREES` [Behroozi et al., 2013c]. The halos were assigned a virial mass M_{vir} and radius R_{vir} using the evolution of the virial relation from Bryan and Norman [1998]. For our cosmology, this corresponds to an overdensity of $\Delta_{crit} = 104$ at $z = 0$.

To define the "main branch" and "destroyed subhalos" of a final $z = 0$ halo (called the "host halo"), we trace back the progenitors of the host halo at each simulation time step. At a given time step, the most massive progenitor of the host halo is a member of the "main branch" and all other direct progenitors that merge into main branch halos are the "destroyed subhalos". A subhalo is considered destroyed when it is no longer found by the halo finder.

2.2.1 Assigning Stellar Mass and Metallicity to Subhalos

Since the *Caterpillar* halos only include a dark matter component, we incorporate luminous material through empirical relations, following Deason et al. [2016]. For the results shown in this paper, we use the $M_{star} - M_{peak}$ relation derived by Garrison-Kimmel et al. [2017a] to estimate the stellar mass in each destroyed subhalo. M_{peak} is defined as the peak virial mass from a subhalo's history. We also test the $M_{star} - M_{peak}$ relations derived by Garrison-Kimmel et al. [2014], Brook et al. [2014], Moster et al.

[2013], and Behroozi et al. [2013a] [see Dooley et al., 2017]. The effects of the different relations are discussed in Section 2.4.4.

We also use empirical relations to estimate the metallicity of the stellar mass in the destroyed subhalos. We adopt a mass-metallicity ($M_{star} - \langle[\mathrm{Fe/H}]\rangle$)[1] relation based on the $z = 0$ relation determined by Kirby et al. [2013b] for dwarf galaxies:

$$\langle[\mathrm{Fe/H}]\rangle = (-1.69 \pm 0.04) + (0.30 \pm 0.02) \log\left(\frac{M_{star}}{10^6 M_\odot}\right) \tag{2.1}$$

This $z = 0$ relation is combined with the redshift evolution found by Ma et al. [2016] from hydrodynamical simulations: $\Delta[\mathrm{Fe/H}] = 0.67[e^{-0.5z} - 1]$. This redshift evolution is consistent with observations [Leethochawalit et al., 2018]. For the destroyed subhalos that are sufficiently massive to form stars after reionization, we use the redshift of their destruction (z_{dest}) as the redshift at which to determine their mean metallicity. Determining their metallicity at other redshifts (e.g., the redshift at which they reach peak mass, z_{peak}, or the redshift at first infall, z_{infall}) does not significantly affect results. For subhalos that form stars before reionization but have their star formation permanently suppressed (e.g., UFDs; for our full definition of UFDs see Section 2.3.1), we use $z = 0$ as the redshift at which to determine their mean metallicity. This is because the UFDs observed today at $z = 0$ also stopped forming stars long ago and thus will appear similar (at least in metallicity) to the UFDs that were destroyed.

After determining the mean metallicity of each subhalo, we assume a Gaussian distribution about the mean with standard deviation of 0.4 dex. This standard deviation aligns with the observed intrinsic scatter for dwarfs at $z = 0$ [Deason et al., 2016]. The metallicity distribution function (MDF) of each individual destroyed subhalo is weighted by the stellar mass of the halo and combined to form the MDF of the accreted portion of the stellar halo. Our resolution supports metallicities down to about $[\mathrm{Fe/H}] \sim -4.5$; below this metallicity, the MDF receives a greater than 1% contribution from unresolved halos.

[1]For elements A and B, $[\mathrm{A/B}] \equiv \log(N_A/N_B) - \log(N_A/N_B)_\odot$, where N_A represents the abundance of A.

Table 2.1: Values For Model Parameters

	Fiducial	Values	Justification
z_{reion}	8	6, 8, 10, 12	From radiation-hydrodynamic simulation[1], $\langle z_{reion} \rangle = 7.8$
M_{SF}	$5 \times 10^7\ M_\odot$	$10^8\ M_\odot$	Atomic cooling threshold[2], corresponds to $T_{vir} \sim 10^4$ K
		$5 \times 10^7\ M_\odot$	Results in ∼120 surviving UFDs[3] when $z_{reion} = 8$
M_{filt}	$2 \times 10^9\ M_\odot$	$6 \times 10^9\ M_\odot$	From hydrodynamical simulations[4], corresponds to $v_{max} \sim 25$ km/s
		$2 \times 10^9\ M_\odot$	From radiation-hydrodynamic simulations of reionization[5]
f_{NSM}	10%	$5 - 15\%$	Percentage of UFDs observed to be r-process enhanced[6]
$M_{UFD,max}$	$10^9\ M_\odot$	varied	Max mass for a halo to be highly enriched after a single r-process event[7]

[1]see Aubert et al. [2018]; [2]see Bromm and Yoshida [2011]; [3]see Section 2.2.2 and Newton et al. [2018];
[4]see Okamoto et al. [2008]; [5]see Ocvirk et al. [2016]; [6]see Section 2.3.2; [7]see Section 2.3.1

These methods of assigning stellar mass and metallicity to the destroyed subhalos are nearly the same methods used by Deason et al. [2016]. The two significant differences are (1) our use of an updated $M_{star} - M_{peak}$ relation that assumes increased scatter about the relation for lower mass halos and (2) our use of $z = 0$ as the redshift at which to determine the metallicity of destroyed UFDs. While they used z_{dest} instead of $z = 0$ for UFD metallicity, they acknowledge that $z = 0$ is likely the appropriate redshift to use. They only did not use $z = 0$ because the metallicity of the UFDs did not affect the bulk properties they were interested in.

2.2.2 Mass Scales for Star Formation

To determine which destroyed subhalos have their star formation permanently suppressed by reionization, which subhalos restart star formation after reionization, and which subhalos never form stars, we adopt cutoffs at different halo mass scales [e.g., Dooley et al., 2017]. These mass scales, M_{SF} and M_{filt}, are summarized in Table 2.1.

We also assume instantaneous reionization. The choice of reionization redshift is most important for the stellar mass of low-mass halos. Using a radiation-hydrodynamics simulation of Milky-Way-like galaxies, Aubert et al. [2018] found that progenitor halos with $M_{vir}(z = 0) < 10^{11}\ M_\odot$ reionized around the globally averaged 50% reionization at $\langle z_{reion} \rangle = 7.8$. We therefore assume $z_{reion} \sim 8$, but investigate several possible reionization redshifts ($z_{reion} = 6, 8, 10, 12$).

M_{SF} is the minimum halo mass needed to form stars. One option for M_{SF} is 10^8

$M_\odot$, corresponding to $T_{vir} \sim 10^4$ K. This is motivated by the atomic cooling threshold a halo must exceed before star formation can be efficiently sustained [Bromm and Yoshida, 2011]. We also investigate a slightly lower choice for M_{SF}. Our choice of M_{SF} significantly changes the number of surviving satellite UFDs at $z = 0$. $M_{SF} = 10^8$ $M_\odot$ results in only ∼40 surviving UFDs. About 40 surviving UFDs around the Milky Way have already been discovered and many more are expected to be found, so this number is low [Dooley et al., 2017]. Graus et al. [2018] also recently found that the threshold for M_{SF} must be lowered to match the observed number of satellites. We therefore adopt $M_{SF} = 5{\times}10^7$ $M_\odot$. This choice results in each simulation having ∼120 surviving UFDs at $z = 0$ (assuming $z_{reion} = 8$), which is roughly the number expected to exist around the Milky Way [Newton et al., 2018]. We also tested $M_{SF} = 7 \times 10^7$ $M_\odot$, but this choice results in each simulation having ∼70 surviving UFDs at $z = 0$, which is too few.

M_{filt} is the filtering mass, the mass below which galaxies are significantly affected by the photoionizing background. A halo must surpass this mass scale to continue star formation after reionization [Gnedin, 2000]. Using hydrodynamical simulations of low mass halos in an ionizing background, Okamoto et al. [2008] found that halos with circular velocities below ∼25 km s^{-1} (corresponding to $M_{filt} \sim 6 \times 10^9$ $M_\odot$) lose a significant amount of their gas due to photoheating. More recent radiation-hydrodynamic simulations of reionization by Ocvirk et al. [2016] find that photoheating suppresses the star formation of halos below $M_{filt} \sim 2 \times 10^9$ $M_\odot$. The filtering mass scale is still uncertain, so we try both of these thresholds.

Of the around 20,000 resolved subhalos that are destroyed into each of our 31 host halos, fewer than 100 subhalos become massive enough to ever form stars. If a subhalo has $M_{vir} < M_{SF}$ at reionization and $M_{peak} < M_{filt}$, it does not form stars prior to reionization and has its star formation permanently suppressed by reionization, meaning it does not ultimately contribute to a stellar halo. Subhalos that form after reionization but remain low mass (never surpassing the mass threshold for star formation; $M_{peak} > M_{SF}$) also do not form stars.

These mass scales only affect low-mass halos. Because the stellar halo is domi-

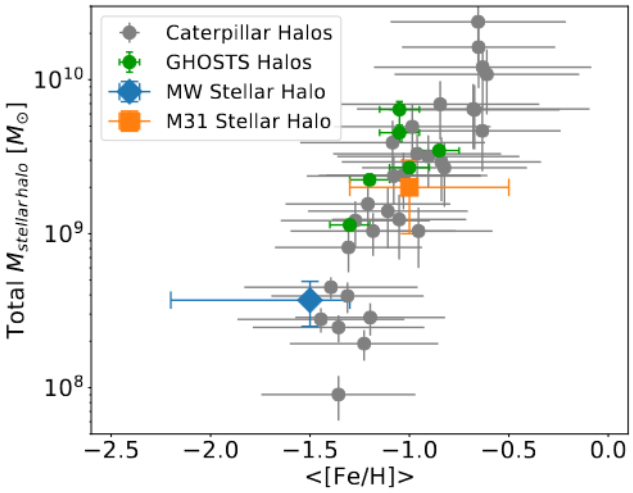

Figure 2-1: The average metallicity and total stellar mass of the *Caterpillar* stellar halos compared to the stellar halos of the Milky Way, M31, and galaxies in the GHOSTS survey. The span of the *Caterpillar* stellar halos well captures the bulk properties of these galaxies and their relative differences.

nated by only a few high-mass destroyed halos, these mass scales do not affect bulk properties of the stellar halo. They are significant for the low-metallicity portion of the stellar halo that we are interested in, however.

2.2.3 Simulated Stellar Halos vs. Observed Stellar Halos

To verify that our stellar mass and metallicity estimations are reasonable, we compare the properties of the simulated stellar halos to those of real, observed stellar halos. Despite the similarities between the *Caterpillar* stellar halos and the observed stellar halos, however, we caution that our simulated stellar halos are formed exclusively from accreted stars while actual stellar halos are not. Some accreted stars inevitably end up in the disk/bulge and some *in situ* disk/bulge stars inevitably end up being thrown into the stellar halo [e.g., Cooper et al., 2015, Gómez et al., 2017]. Thus while we will use the terms “stellar halo" and “accreted stars" somewhat interchangeably, there is a difference. Our simulated stellar halos are approximations of actual stellar halos. We discuss the effects of this approximation in Section 2.4.4.

Figure 2-1 compares the average metallicity and total stellar mass of each of the

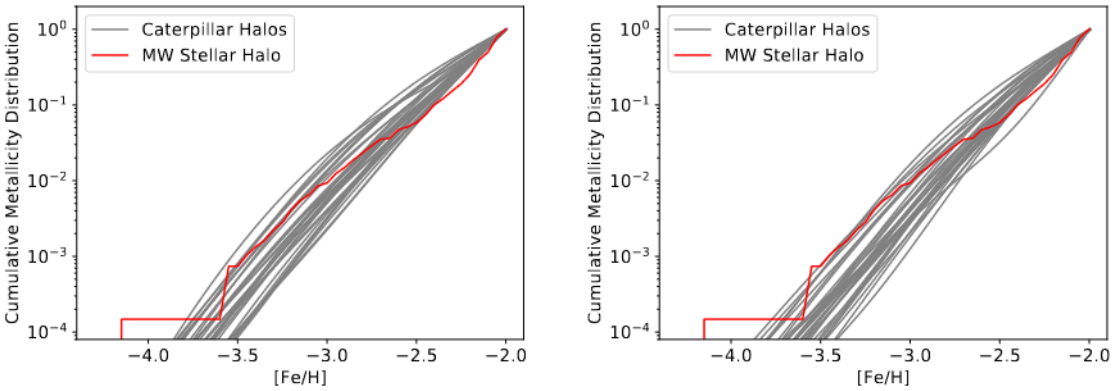

(a) $M_{SF} = 5 \times 10^7\ M_\odot$, $M_{filt} = 2 \times 10^9\ M_\odot$ (b) $M_{SF} = 5 \times 10^7\ M_\odot$, $M_{filt} = 6 \times 10^9\ M_\odot$

Figure 2-2: Cumulative metallicity distribution functions for stellar halo stars with [Fe/H] < -2. The *Caterpillar* halos are compared to the Milky Way stellar halo [Schörck et al., 2009]. Results do not noticeably change for $M_{SF} = 10^8\ M_\odot$. Assumes $z_{reion} = 8$.

Caterpillar stellar halos (composed entirely of *ex situ* stars) to those of observed stellar halos. We compare to galaxies in the GHOSTS survey [NGC253, NGC891, M81, NGC4565, NGC4945, and NGC7814; Monachesi et al., 2016, Harmsen et al., 2017], the Milky Way ($M_{star,halo} \sim 3.7 \pm 1.2 \times 10^8\ M_\odot$, Bell et al. 2008; $\langle$[Fe/H]$\rangle \sim -1.3$ to -2.2, Carollo et al. 2010), and M31 ($M_{star,halo} \sim 2 \pm 1 \times 10^9\ M_\odot$, Williams et al. [2015]; $\langle$[Fe/H]$\rangle \sim -0.5$ to -1.3, Kalirai et al. [2006]). Given the simplicity of the model, the span of the *Caterpillar* stellar halos matches the properties of these observed halos and their relative differences remarkably well. Figure 2-1 is a recreation of Figure 8 from Deason et al. [2016], which also reproduces the relative difference between the Milky Way and M31.

We also compare the cumulative metallicity distribution function of the *Caterpillar* stellar halos to that of the Milky Way. In Figure 2-2 we compare to the cumulative distribution function from Schörck et al. [2009] for metal-poor halo stars with metallicity [Fe/H] < -2. Below [Fe/H] < -3.5, the *Caterpillar* distributions differ significantly from the Milky Way distribution. This is likely because the Gaussians composing the MDFs have a weaker metal-poor tail than the actual distributions in each destroyed subhalo. However, the composite Gaussian MDFs provide a much

better fit than other physically motivated MDFs (e.g., Extra Gas model, power laws), so we keep the Gaussian MDFs for this analysis. We discuss the limitations of these empirical relations and fixed [Fe/H] distributions in Section 2.4.4.

2.3 Treatment of r-Process Enrichment in Early UFDs

We assume that some fraction (see Section 2.3.2) of now-destroyed UFDs experience an early neutron star merger (NSM) or another rare prolific r-process event that enriches the gas from which subsequent stars form. Looking specifically at low-mass UFDs, i.e. dwarf galaxies small enough to form highly r-process enhanced stars after only one r-process event, we consider the stars formed in these galaxies to be r-II stars. r-II stars are stars that are highly enhanced in r-process elements: [Eu/Fe] $> +1$, [Ba/Eu] < 0 [Beers and Christlieb, 2005]. This follows the example set by Reticulum II. We note that the mass range of UFDs is not universally defined, but when creating our definition of UFDs we focus on the low-mass end (see Section 2.3.1) to look specifically at the smallest galaxies that helped form the Milky Way.

In each simulation, we then trace all the galaxies that disrupt into each host galaxy to $z = 0$ and compare the fraction of simulated r-II stars from destroyed UFDs ($f_{r-II,sim}$; see Section 2.3.3) to the observed fraction of r-II stars in the Milky Way's stellar halo ($f_{r-II,obs}$). In this way, we investigate how much of the observed fraction of r-II halo stars may have originated in destroyed ultra-faint dwarfs.

This treatment only considers putative r-II stars that form from gas enriched by a single r-process event in a low-mass destroyed galaxy. Actual r-II halo stars can also form through other pathways, e.g., a higher-mass destroyed galaxy that experiences more than one NSM event could form r-II stars, or r-II stars could form *in situ* through inhomogeneous mixing and later get thrown into the stellar halo [Shen et al., 2015, van de Voort et al., 2015, Naiman et al., 2018]. To specifically investigate the origins of r-II halo stars in low-mass UFDs, though, we do not simulate r-II stars with other origins. We discuss the limitations of this analysis in more depth in Section 2.4.4.

2.3.1 Definition of Ultra-Faint Dwarf

We define an ultra-faint dwarf as a halo that forms stars early in the Universe's history ($M_{vir} > M_{SF}$ before reionization), but has its star formation permanently suppressed by reionization ($M_{peak} < M_{filt}$). This is the "fossil" definition of UFDs [e.g., Bovill and Ricotti, 2011]. We also require that UFDs have a final $M_{star} < 2 \times 10^5\ M_\odot$ (corresponding to $M_{peak} \lesssim 2.8 \times 10^9\ M_\odot$[2]). When identifying now-destroyed UFDs (the smallest building blocks of the galaxy), we consider both UFDs that disrupted directly into the main branch of the host halo and UFDs that disrupted into other dwarf galaxies before merging with the host halo.

Furthermore, we constrain our definition of UFDs to only include halos in which a single prolific r-process event can enrich the gas to produce subsequent r-II stars as defined by high [Eu/Fe]. This excludes "high mass" UFDs because of dilution. We define $M_{UFD,max}$ as the maximum mass a UFD can reach while it is forming stars (before reionization). More massive subhalos would dilute the chemical enrichment products too much to still yield r-II stars after a single NSM event. The calculations to determine $M_{UFD,max}$ are uncertain, however.

For example, in Reticulum II, the prolific r-process event resulted in stars with [Eu/H] ~ -1.3 [Ji et al., 2016b]. This corresponds to $\sim 10^{-4.5}\ M_\odot$ of Eu being injected into $\sim 10^6\ M_\odot$ of gas (possibly an order of magnitude higher or lower; in a $\sim 10^{7-8}\ M_\odot$ halo). Such an event produces r-II stars at [Fe/H] $\lesssim -2.3$. Using proportionality arguments, a halo's mixing mass can be related to its virial mass: $M_{mix} \sim M_{vir}^{1.25}$ [e.g., Ji et al., 2015b]. Increasing the virial mass by an order of magnitude would increase the mixing mass by $10^{1.25}$, producing r-II stars at lower metallicities: around [Fe/H] $\lesssim -2.3 - 1.25 = -3.55$. It is therefore unreasonable to assume all of the stellar mass below [Fe/H] < -2.5 in "high mass" UFDs would be highly r-process enhanced following one NSM event.

We caution that the mixing mass numbers are highly uncertain and based on order-of-magnitude arguments. We thus try several different maximum mass cutoffs: $M_{UFD,max} = 2 \times 10^8$, 5×10^8, 10^9, and $2 \times 10^9\ M_\odot$. Of these, 2×10^8 in particular is

[2]Using the $M_{star} - M_{peak}$ relation derived by Garrison-Kimmel et al. [2017a]

quite low because the minimum mass of a UFD is $M_{SF} \sim 10^8\ M_\odot$, but we include it to encompass the possible parameter values. We use the intermediate choice of $10^9\ M_\odot$ for our fiducial model.

2.3.2 Neutron Star Merger Fraction, f_{NSM}

We empirically determine the fraction of UFDs that experienced r-process enhancement simply by comparing the number of known r-process UFDs to normal UFDs. There are now high-resolution spectroscopic abundances for stars in 15 surviving UFDs: Bootes I [Feltzing et al., 2009, Frebel et al., 2016], Bootes II [Koch and Rich, 2014, Ji et al., 2016d], Canes Venatici II [François et al., 2016], Coma Berenices [Frebel et al., 2010], Grus I [Ji et al., 2018], Hercules [Koch et al., 2013], Horologium I [Nagasawa et al., 2018], Leo IV [Simon et al., 2010], Reticulum II [Ji et al., 2016b], Segue 1 [Frebel et al., 2014], Segue 2 [Roederer and Kirby, 2014], Triangulum II [Venn et al., 2017, Kirby et al., 2017], Tucana II [Ji et al., 2016c], Tucana III [Hansen et al., 2017], and Ursa Major II [Frebel et al., 2010].

Of these, Reticulum II has definitely been enriched by a prolific r-process event, assumed to be a neutron star merger [Ji et al., 2016b]. Tucana III also exhibits r-process enhancement [Hansen et al., 2017], though it is still unclear if this is a tidally disrupted UFD or a globular cluster [Li et al., 2018]. It thus seems that there are $1-2$ UFDs affected by an r-process event out of $14-15$ UFDs, or 7.1% to 13.3%.

For the purposes of this analysis, we therefore assume $5-15\%$ of now-destroyed UFDs experience an early neutron star merger (NSM) or some other rare prolific r-process event. Our default NSM fraction is $f_{NSM} \sim 10\%$. This fraction is agnostic to the actual nature of the r-process event; it directly relates to the fraction of surviving UFDs that have been observed to be r-process enhanced.

2.3.3 r-II Star Fraction, f_{r-II}

The simulated r-II star fraction, $f_{r-II,sim}$, is the amount of low-metallicity, highly r-process enhanced stars that we assume originated in now-destroyed low-mass UFDs

compared to all low-metallicity stars now present in the accreted stellar halo.

$$f_{r-II,sim} = \frac{\text{metal-poor r-II halo stars that formed in UFDs}}{\text{all metal-poor halo stars}} \tag{2.2}$$

We define "metal-poor" as [Fe/H] < -2.5. For the simulated fraction, the numerator and denominator are both in units of stellar mass as opposed to numbers of stars. Our methodology directly estimates the amount of stellar mass in each galaxy, not the number of stars in each galaxy, but this makes little difference for old stellar populations. To determine how much of the stellar mass in a galaxy is metal-poor, we integrate the MDF below [Fe/H] $= -2.5$.

The "as observed" r-II star fraction, $f_{r-II,obs}$, includes all currently known r-II stars in the Milky Way's stellar halo.

$$f_{r-II,obs} = \frac{\text{metal-poor r-II halo stars}}{\text{all metal-poor halo stars}} \tag{2.3}$$

Observed r-II stars are stars which display strong r-process enhancement ([Eu/Fe] > 1 and [Ba/Eu] < 0). For the observed fraction, the numerator and denominator are both in terms of the number of observed stars.

2.4 Results and Discussion

2.4.1 Simulated Fraction of r-II Stars in the Stellar Halo

Using the treatment of r-process enrichment described in the previous section, we calculate the simulated r-II star fraction, $f_{r-II,sim}$, for different z_{reion} and mass thresholds. Figure 2-3 and Table 2.2 show these results.

The simulated r-II fraction is $\sim$1.3% for our fiducial parameter values ($z_{reion} = 8$, $M_{UFD,max} = 10^9\ M_\odot$, $M_{SF} = 5 \times 10^7\ M_\odot$, $M_{filt} = 2 \times 10^9\ M_\odot$, $f_{NSM} = 10\%$). The fraction varies somewhat with all the parameters, as seen in Figure 2-3. It scales linearly with the NSM fraction, f_{NSM}. If we consider $f_{NSM} = 5 - 15\%$ with our fiducial model, the r-II fraction is $\sim 0.7 - 2\%$. If we consider the scatter between the simulations, the r-II fraction is $\sim 1 - 2\%$. Varying all of the parameters to the

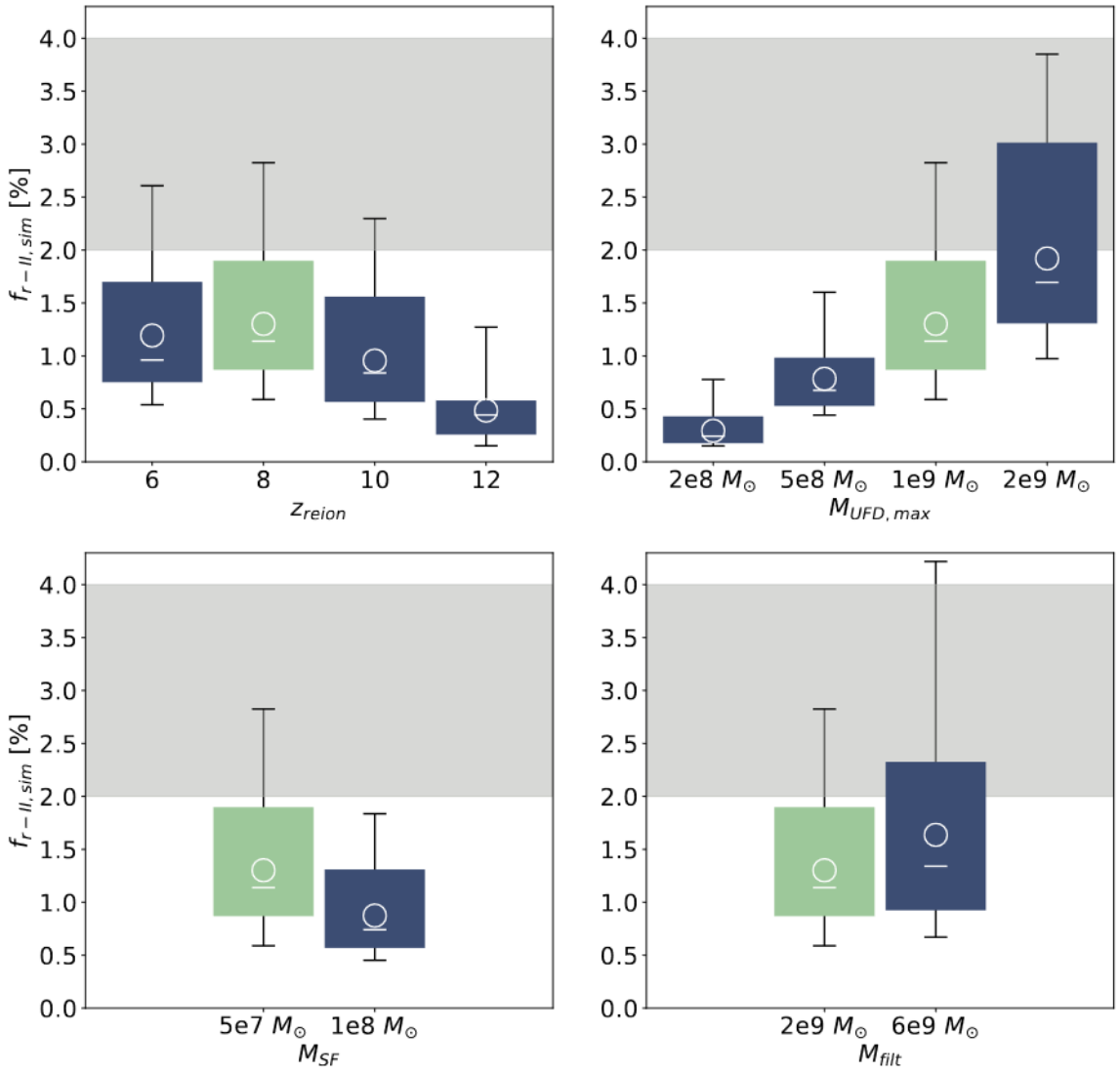

Figure 2-3: The simulated r-II star fraction, $f_{r-II,sim}$, as it varies with different mass thresholds and reionization redshifts. For each set of parameters, the mean $f_{r-II,sim}$ is shown as a white circle and the median is shown as a white line. The colored boxes correspond to 68% scatter between simulations, and the error bars shown the minimum and maximum $f_{r-II,sim}$. Our fiducial model is highlighted in light green, and single-parameter variations on the fiducial model are shown in blue. The currently observed fraction of r-II stars in the Milky Way stellar halo ($f_{r-II,obs} \sim 2-4\%$) is shown in grey. See Section 2.3.3 for definitions of the r-II fractions and Table 2.1 for explanations of the different parameters.

determine the minimum and maximum simulated r-II fraction gives a range of $\sim$0.01$-$4% with the favored value being around $1-2\%$.

For comparison, the observed fraction, $f_{r-II,obs}$ differs a bit from sample to sample

Table 2.2: The simulated r-II star fraction, $f_{r-II,sim}$, for different mass thresholds and reionization redshifts. The reported values are averaged across simulations and the uncertainties correspond to 68% scatter. The fiducial model is bolded. Variations of f_{NSM} are not explicitly shown because $f_{r-II,sim}$ scales linearly with f_{NSM}.

	$M_{SF} = 5 \times 10^7\ M_\odot$ $M_{filt} = 2 \times 10^9\ M_\odot$	$M_{SF} = 5 \times 10^7\ M_\odot$ $M_{filt} = 6 \times 10^9\ M_\odot$	$M_{SF} = 10^8\ M_\odot$ $M_{filt} = 2 \times 10^9\ M_\odot$	$M_{SF} = 10^8\ M_\odot$ $M_{filt} = 6 \times 10^9\ M_\odot$
		$M_{UFD,max} = 2 \times 10^9\ M_\odot$		
$z_{reion} = 6$	$1.7^{+0.9}_{-0.5}$ %	$2.4^{+0.8}_{-0.8}$ %	$1.5^{+0.8}_{-0.7}$ %	$2.1^{+0.8}_{-0.6}$ %
$z_{reion} = 8$	$1.9^{+1.0}_{-0.6}$ %	$2.7^{+0.9}_{-0.8}$ %	$1.5^{+0.9}_{-0.6}$ %	$2.2^{+0.8}_{-0.7}$ %
$z_{reion} = 10$	$1.5^{+0.8}_{-0.5}$ %	$2.3^{+0.7}_{-0.7}$ %	$1.0^{+0.3}_{-0.3}$ %	$1.5^{+0.6}_{-0.4}$ %
$z_{reion} = 12$	$0.9^{+0.4}_{-0.2}$ %	$1.6^{+0.4}_{-0.4}$ %	$0.4^{+0.3}_{-0.2}$ %	$0.8^{+0.2}_{-0.2}$ %
		$M_{UFD,max} = 10^9\ M_\odot$		
$z_{reion} = 6$	$1.2^{+0.5}_{-0.4}$ %	$1.6^{+0.6}_{-0.5}$ %	$0.9^{+0.5}_{-0.3}$ %	$1.4^{+0.5}_{-0.5}$ %
$z_{reion} = 8$	$\mathbf{1.3^{+0.6}_{-0.4}}$ %	$1.6^{+0.7}_{-0.7}$ %	$0.9^{+0.4}_{-0.3}$ %	$1.5^{+0.5}_{-0.4}$ %
$z_{reion} = 10$	$1.0^{+0.6}_{-0.4}$ %	$1.4^{+0.6}_{-0.5}$ %	$0.5^{+0.2}_{-0.1}$ %	$0.9^{+0.4}_{-0.3}$ %
$z_{reion} = 12$	$0.5^{+0.1}_{-0.2}$ %	$0.9^{+0.4}_{-0.3}$ %	$0.2^{+0.1}_{-0.1}$ %	$0.4^{+0.2}_{-0.1}$ %
		$M_{UFD,max} = 5 \times 10^8\ M_\odot$		
$z_{reion} = 6$	$0.7^{+0.2}_{-0.2}$ %	$1.1^{+0.4}_{-0.3}$ %	$0.5^{+0.2}_{-0.2}$ %	$0.9^{+0.4}_{-0.2}$ %
$z_{reion} = 8$	$0.8^{+0.2}_{-0.3}$ %	$1.3^{+0.4}_{-0.4}$ %	$0.5^{+0.2}_{-0.1}$ %	$0.9^{+0.3}_{-0.3}$ %
$z_{reion} = 10$	$0.5^{+0.2}_{-0.2}$ %	$1.0^{+0.3}_{-0.3}$ %	$0.2^{+0.1}_{-0.1}$ %	$0.5^{+0.2}_{-0.1}$ %
$z_{reion} = 12$	$0.2^{+0.1}_{-0.1}$ %	$0.4^{+0.2}_{-0.1}$ %	$0.1^{+0.1}_{-0.1}$ %	$0.2^{+0.1}_{-0.1}$ %
		$M_{UFD,max} = 2 \times 10^8\ M_\odot$		
$z_{reion} = 6$	$0.33^{+0.12}_{-0.10}$ %	$0.47^{+0.25}_{-0.19}$ %	$0.15^{+0.06}_{-0.05}$ %	$0.22^{+0.11}_{-0.07}$ %
$z_{reion} = 8$	$0.29^{+0.14}_{-0.12}$ %	$0.52^{+0.20}_{-0.12}$ %	$0.11^{+0.03}_{-0.03}$ %	$0.24^{+0.10}_{-0.07}$ %
$z_{reion} = 10$	$0.16^{+0.04}_{-0.06}$ %	$0.32^{+0.05}_{-0.05}$ %	$0.05^{+0.02}_{-0.03}$ %	$0.09^{+0.06}_{-0.04}$ %
$z_{reion} = 12$	$0.07^{+0.03}_{-0.03}$ %	$0.13^{+0.04}_{-0.04}$ %	$0.02^{+0.01}_{-0.01}$ %	$0.02^{+0.02}_{-0.01}$ %

(e.g., 3.3%, Jacobson et al. 2015; 2.2%, Roederer et al. 2014c; 2.9%, Barklem et al. 2005). We also note that these fractions depend on the specifically chosen limit [Eu/Fe] > 1 and general sample selections that are not completeness corrected. A recent study from Hansen et al. [2018] found $f_{r-II,obs} \sim 10\%$, but a larger sample has reduced the fraction by about half and data is still being collected (T. Hansen, priv. comm.). This study was also specifically looking for r-process stars and may not be representative of the true r-II fraction. Aggregating the surveys and individual reports in the literature without attempting to account for observational bias gives 3.2% [Abohalima and Frebel, 2017, Hansen et al., 2018]. We note that r-II stars are preferentially likely to be reported in literature over other metal-poor stars, however, so r-II stars are probably overrepresented. Currently, $f_{r-II,obs}$ appears to be $\sim 2-4\%$, but the true fraction is likely lower.

Comparing the simulated $f_{r-II,sim} \sim 1-2\%$ and the observed $f_{r-II,obs} \sim 2-$

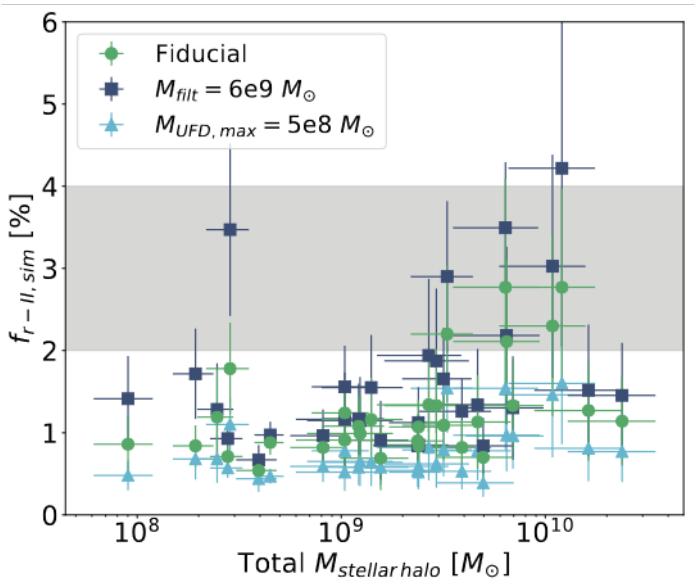

Figure 2-4: The simulated r-II fraction for the individual *Caterpillar* halos as a function of their total accreted stellar mass. Three models are shown as examples: the fiducial model, a variation of M_{filt}, and a variation of $M_{UFD,max}$. As in Figure 2-3, the currently observed fraction of r-II stars in the Milky Way stellar halo is shown in grey. The error bars correspond to uncertainty in the empirical relations. There is a tendency for stellar halos with more accreted stellar mass to have a higher r-II fraction.

4%, around half of the low-metallicity r-II halo stars could have originated in now-destroyed UFDs following a single r-process event. Considering the 68% scatter between simulations and the effects of varying M_{SF} and M_{filt} in the fiducial model, $f_{r-II,sim} \sim 0.6 - 2.3$ can account for $\sim$20 $-$ 80% of the current $f_{r-II,obs}$. Varying $M_{UFD,max}$ from 5×10^8 $M_\odot$ to 2×10^9 $M_\odot$ expands the range to $\sim$20 $-$ 100% of the current "as observed" $f_{r-II,obs}$. Furthermore, because the true $f_{r-II,obs}$ is likely lower, the amount of the true $f_{r-II,obs}$ that $f_{r-II,sim}$ can account for is likely closer to $\sim$80% than 20%. This implies that a significant fraction of the metal-poor r-II halo stars likely originated in now-destroyed UFDs. This is only considering the contribution of "low-mass" UFDs. Including other r-II star creation pathways (e.g., more than one NSM or inhomogeneous mixing in higher-mass UFDs) would increase the fraction. The caveats to this result are discussed in Section 2.4.4. This result is supported by recent kinematic evidence that implies r-II stars were largely accreted. For more on this, see Section 3.6.

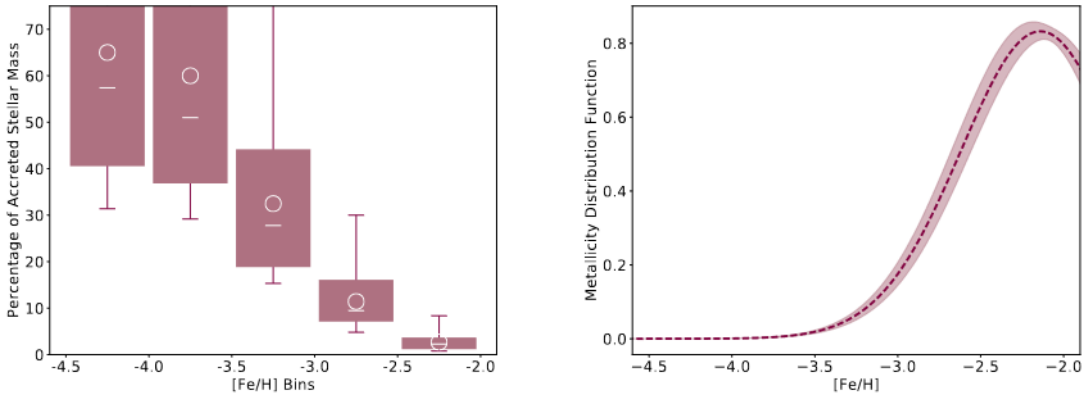

(a) Accreted stellar mass that originated in UFDs

(b) MDF of destroyed UFDs

Figure 2-5: Left: The percentage of accreted stellar mass at different metallicities that originated in now-destroyed UFDs. The mean percentage is shown as a white circle and the median is shown as a white line. The colored boxes correspond to 68% scatter between simulations, and the error bars shown the minimum and maximum percentages across simulations. From [Fe/H] $= -2.5$ to -2, stars from UFDs make up a few percent of the stellar halo. Right: The averaged metallicity distribution function of now-destroyed UFDs. Shaded region shows 68% scatter between simulations. Both plots show results from our fiducial model.

We note that there appears to be a tendency for more massive stellar halos (stellar halos which formed from more massive destroyed galaxies) to have a higher $f_{r-II,sim}$. Figure 2-4 shows this. Because the Milky Way stellar halo is on the lower mass end of the range of *Caterpillar* stellar halos (see Figure 2-1), the simulated r-II fraction is slightly lowered if we only consider the six stellar halos with masses closest to the MW halo: $f_{r-II,sim,MW} \sim 1 - 1.5\%$ for the fiducial model. This apparent trend could also be due to the large scatter, though.

2.4.2 Fraction of Stars from Now-Destroyed UFDs

In Figure 2-5, we plot the total fraction of accreted stellar mass at different metallicities that originated in now-destroyed UFDs, r-process enhanced or not. The figure also shows the metallicity distribution function of all of the now-destroyed UFDs averaged across all simulations.

If we assume an r-process event occurs in approximately 10% of UFDs, approximately 90% of the now-destroyed UFDs produced low neutron-capture stars (stars that exhibit low abundances of neutron-capture elements such as Sr and Ba). Low neutron-capture (low n-cap) could thus be another key signature to identify stars from now-destroyed UFDs. If low n-cap stars at intermediate and low metallicities come primarily from UFDs, the fraction of low n-cap stars in the halo should look roughly like the fractions shown in Figure 2-5a (multiplied by $\sim$0.9).

Figure 2-5b shows that the number of stars from now-destroyed UFDs peaks around [Fe/H] ~ -2. These stars make up only a few percent of the halo stars around this metallicity, though (Figure 2-5a). From [Fe/H] ~ -2.5 to -2, they are about as rare as r-II stars at low metallicities: $f_{low-ncap,sim} \sim 2-3\%$. While rare, finding low n-cap stars in this metallicity range could help us identify stars from now-destroyed UFDs. Based on observations of the Milky Way's satellite galaxies, below [Fe/H] $\lesssim -3$, low n-cap stars are found in both UFDs and more massive satellite galaxies, but from [Fe/H] ~ -2.5 to -2, UFDs appear to be the primary source.

Figure 2-6 shows some of the neutron-capture element abundances ([Sr/Fe] and [Ba/Fe]) of stars in surviving UFDs relative to stars from the more luminous satellite galaxies around the Milky Way, the dwarf spheroidal galaxies (dSph). Halo stars are also shown in gray for comparison. Excluding the surviving UFDs that appear to have experienced an r-process event (Reticulum II and Tucana III), the UFD stars have lower Sr and Ba abundances than the dSph stars, most noticeably above [Fe/H] ~ -3. The UFD Bootes I is highlighted because it displays different behavior from other UFDs: its [Ba/Fe] ratios are higher and increase slightly with [Fe/H]. The other 12 UFDs clearly contain low n-cap stars relative to more luminous galaxies.

In the Roederer et al. [2014c] sample of 313 metal-poor halo stars, the percentage of stars with [Ba/H] < -3.5 from [Fe/H] $= -2.5$ to -2 is 2.8% and the percentage from [Fe/H] $= -3$ to -2.5 is 17.1%, in rough agreement with Figure 2-5a. As always, though, more observations are needed. Upcoming halo star surveys without metallicity bias such as 4MOST and WEAVE [de Jong et al., 2012, Dalton et al., 2012] will expand on observations and allow us to study this question more in depth. For

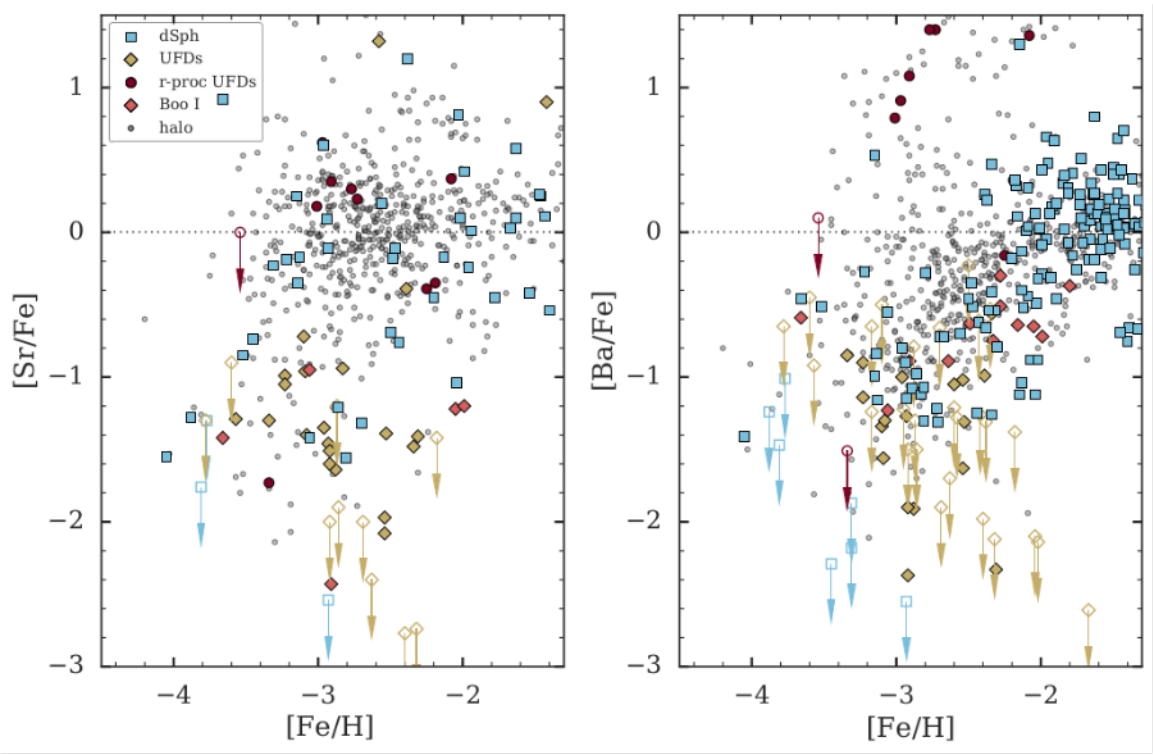

Figure 2-6: Neutron-capture element abundances (Sr and Ba) for stars in surviving UFDs and in surviving dwarf spheroidal galaxies (dSph). The r-process UFDs (Reticulum II and Tucana III) and the UFD Bootes I are highlighted because they exhibit different behavior in their Sr and Ba abundances. Halo stars are shown in grey for comparison. The other 12 UFDs (shown in yellow) exhibit low [Sr/Fe] and [Ba/Fe] compared to the dSph (shown in blue).
References: [Aoki et al., 2007, 2009, Cohen and Huang, 2009, 2010, François et al., 2016, Frebel, 2010, Frebel et al., 2010, 2014, 2016, Fulbright et al., 2004, Geisler et al., 2005, Hansen et al., 2017, 2018, Jablonka et al., 2015, Kirby and Cohen, 2012, Kirby et al., 2017, Shetrone et al., 2001, 2003, Simon et al., 2010, 2015, Skúladóttir et al., 2015, Tafelmeyer et al., 2010, Tsujimoto et al., 2015, 2017, Ural et al., 2015, Chiti et al., 2018, Feltzing et al., 2009, Gilmore et al., 2013, Lai et al., 2011, Ishigaki et al., 2014, Ji et al., 2016b,d, 2018, Roederer and Kirby, 2014, Roederer et al., 2016b, Koch et al., 2008, 2013, Koch and Rich, 2014, Nagasawa et al., 2018, Norris et al., 2010, 2017, Venn et al., 2012, 2017]

now, we merely note that low n-cap signatures are likely another key way to identify stars from now-destroyed UFDs, and we expect them to constitute a few percent of the stellar halo stars with [Fe/H] ~ -2.5 to -2.

2.4.3 Number of Now-Destroyed r-Process Galaxies

From the *Caterpillar* simulations we can estimate the number of UFDs that merged to help form the Milky Way stellar halo. The *Caterpillar* stellar halos are formed from 260 ± 60 UFDs on average. This includes both UFDs that merged directly into the host halo (roughly 1/3 of now-destroyed UFDs) and the UFDs that merged with other galaxies before merging with the host halo (roughly 2/3 of now-destroyed UFDs). Since $\sim$10% of UFDs appear to be r-process-enhanced, this means that $\sim 20 - 30$ r-process UFDs may have contributed directly ($\sim$10) or indirectly ($\sim$20) to our stellar halo.

2.4.4 Limitations

There are potential issues with directly comparing *Caterpillar* stellar halos to the Milky Way stellar halo. As mentioned in Section 2.2.3, we are conflating "accreted stars" with "stellar halo", but actual stellar halos are not exclusively and comprehensively composed of accreted material. In our analysis, we do not consider *in situ* stars. For simplicity's sake, we also do not consider that accreted stars can end up in the disk/bulge [as in, e.g., Gómez et al., 2017]. If a large portion of the metal-poor stellar halo originated *in situ* or a large portion of the accreted material ended up in the disk, it would significantly affect the r-II fraction. The fraction of halo stars that formed *in situ* can be large, and it is unclear how large [Monachesi et al., 2018]. *In situ* halo stars are more metal-rich than accreted stars [Bonaca et al., 2017], however, so metal-poor halo stars — the focus of our analysis — appear to be largely accreted. This is supported by both observations and hydrodynamics simulations [Cooper et al., 2015, Bonaca et al., 2017, El-Badry et al., 2018]. Bonaca et al. [2017] kinematically identified accreted and *in situ* halo stars in the Gaia DR1 + RAVE-on catalog, finding

a bimodality about [Fe/H] $= -1$ with the accreted stars being more metal-poor than the *in situ* stars. Their interpretation is supported by the Latte simulation from the FIRE project. Using more FIRE simulations, El-Badry et al. [2018] found that $\gtrsim$80% of the stellar halo stars below [Fe/H] ~ -2.5 are accreted (see their Figure 7). If none of the *in situ* stars are highly r-process enhanced, this would increase $f_{r-II,obs}$ relative to $f_{r-II,sim}$ by at most a factor of $\sim$1.2. Given the uncertainty around the fractions and the likely overestimation of $f_{r-II,obs}$ due to observational bias, though, this would not change our finding that around half of r-II halo stars formed in now-destroyed UFDs.

We also do not consider the r-II stars that originate *in situ* [as in, e.g., Shen et al., 2015, **?**, Naiman et al., 2018] or in more massive dwarfs. This is because we are specifically interested in how many of the observed r-II stellar halo stars may have originated in the low-mass UFDs. In theory, adding up the r-II fractions that result from each of these different possible r-II star channels should add up to 100% of the observed fraction. Simulating these more complex r-II origins requires more sophisticated modeling than what is in the scope of this paper, however, so this will have to be investigated more in future work. The observed fraction must also be determined more accurately to better determine the overlap of $f_{r-II,sim}$ and $f_{r-II,obs}$. Furthermore, depending on the definition of "ultra-faint dwarf," the r-II fraction from now-destroyed UFDs will be different. By considering only UFDs that can become strongly enriched from a single NSM, we limit ourselves to only the contributions from low-mass UFDs. This is a conservative choice, and if we included the contributions from r-II origin channels in more massive UFDs (e.g., r-II stars can form in more massive halos that experience more than one NSM event or inhomogenous mixing), the r-II fraction from UFDs would increase.

Additionally, we assume that $f_{NSM} \sim 10\%$ of UFDs experience a NSM event (or other prolific r-process event), but this fraction is based on a small number of known UFDs. It may also make sense to determine f_{NSM} in terms of total stellar mass that has been enriched by a prolific r-process event. Reticulum II and Tucana III are on the lower stellar mass end of UFDs, so weighting by stellar mass when determining

f_{NSM} significantly lowers the contribution of now-destroyed UFDs to r-II halo stars. In this case, $f_{NSM} \sim 2-3\%$ and the simulated r-II fraction ($f_{r-II,sim} \sim 0.3\%$) would only account for around $\sim$10% of the observed fraction.

Whether we determine f_{NSM} by the number of UFDs that experience an r-process event or by the amount of stellar mass enriched by an r-process event is dependent on whether the NSM rate is dominated by a retention fraction or a production rate. If the NSM rate is dominated by a retention fraction, it would depend more on the total halo mass than the stellar mass. Because UFDs are in roughly the same halo mass range [Strigari et al., 2008, Jethwa et al., 2018], determining f_{NSM} as we did in Section 2.3.2 should be more appropriate than weighting by stellar mass. On the other hand, if the NSM rate is dominated by a production rate, weighting by stellar mass is likely more appropriate. We note that the current LIGO rate is ten times higher than what is needed to produce all the r-process material in the Milky Way [Ji and Frebel, 2018, Belczynski et al., 2018, Abbott et al., 2017a, Côté et al., 2018a], suggesting that the retention fraction is likely dominant and our determination in Section 2.3.2 is more appropriate. This remains uncertain for now, however. Future LIGO measurements will give clarity to this.

Furthermore, the [Fe/H] distributions have a fixed, simplistic shape. The individual Gaussians representing each destroyed halo have a physically motivated standard deviation and are able to reproduce similar bulk properties to those of observed stellar halos [Deason et al., 2016], but we know they are not the true distributions. For example, the cumulative distribution functions of the *Caterpillar* stellar halos differ from that of the Milky Way stellar halo, particularly at the very lowest metallicities. The Gaussian [Fe/H] distributions used in this analysis are thus a simple choice to produce reasonable stellar halo MDFs, but they are insufficient to completely capture the true distribution of the Milky Way stellar halo and its satellites. We use the Gaussians in this analysis because we are unable to find a physically motivated distribution that better matches observations.

Additionally, our choice of $M_{star} - M_{peak}$ relation affects our results for $f_{r-II,sim}$. Using the Garrison-Kimmel et al. [2017a] relation (GK17) or Garrison-Kimmel et al.

[2014] relation (GK14) produces nearly the same r-II fractions, but using the Moster et al. [2013] relation produces r-II fractions that are roughly half as large. Using the Behroozi et al. [2013a] relation more than doubles the r-II fraction (producing unreasonably high fractions), and using the Brook et al. [2014] relation gives fractions that are roughly one-fourth of those produced by GK17 or GK14. The disagreement between these different relations displays the uncertainty that abundance matching relations have regarding low-mass halos such as UFDs. We focus on the most up-to-date $M_{star} - M_{peak}$ relation, GK17, but the potential issues with using abundance matching relations to assign mass to low-mass halos should be kept in mind.

If future work continues to use empirical relations, the work could potentially be improved by using a [Fe/H] distribution with a more pronounced metal-poor tail. Having used empirical relations here to obtain an initial idea of what is reasonable in our model, however, we believe semi-analytic modeling will provide a better avenue for future investigation into this and similar questions.

Lastly, subhalos passing close to the host galaxy's center should probably be destroyed by the host galaxy's disk, but are not because the *Caterpillar* simulations are dark matter only [Garrison-Kimmel et al., 2017c]. Including surviving subhalos in the stellar halo does not significantly change the r-II fractions, though, so this does not appear to be significant to our results on r-II fractions.

2.5 Conclusions

We investigate the possibility that highly r-process enhanced metal-poor stars (metal-poor r-II stars) largely originated in the smallest, earliest galaxies (early analogs of ultra-faint dwarfs, UFDs) that merged into the Milky Way over the course of its formation history. Our results support this possible connection between r-II stars and the smallest building blocks of our galaxy. We find that around half of r-II stars may have originated in now-destroyed ultra-faint dwarfs that experienced a rare prolific r-process event such as a neutron star merger.

We reach this conclusion by simulating what fraction of low-metallicity stellar halo

stars could have become highly r-process enhanced in now-destroyed UFDs. This fraction is the simulated r-II fraction, $f_{r-II,sim}$. We compare this to the observed r-II fraction, the fraction of low-metallicity stellar halo stars that have been observed to be highly r-process enhanced. Assuming the most likely values for parameters in our model ($z_{reion} \sim 8$, intermediate mass thresholds, $f_{NSM} \sim 10\%$) gives a simulated $f_{r-II,sim} \sim 1-2\%$, accounting for around half of the observed $f_{r-II,obs} \sim 2-4\%$. In cases where we choose the most extreme parameter values, $f_{r-II,sim}$ ranges from $\sim 0.01-4\%$. Considering scatter between simulations and less extreme variation of model parameters, $f_{r-II,sim}$ can account for $\sim 20-80\%$ of $f_{r-II,obs}$. Due to incomplete sampling, though, $f_{r-II,obs}$ likely overrepresents the fraction of r-II halo stars. This means the percentage of $f_{r-II,obs}$ that $f_{r-II,sim}$ can account for is likely closer to $\sim 80\%$ than $\sim 20\%$.

To determine the simulated f_{r-II}, we use high-resolution dark-matter cosmological simulations (the *Caterpillar* suite), empirical relations linking dark matter mass to stellar mass and metallicity, and a simple, empirically motivated r-process treatment. Our r-process treatment assumes that $5-15\%$, or $\sim 10\%$, of early UFDs experience an early prolific r-process event that enriches all of the gas from which their subsequent stars form with r-process elements. The r-process event is most likely a neutron star merger, but the model is agnostic to the specifics of the event. The $\sim 10\%$ fraction comes from the fraction of surviving UFDs that have been observed to be r-process enhanced.

Intriguingly, there is some recent evidence that r-process-enhanced stars may have kinematics associated with accretion. Abundances of high-velocity stars in Gaia DR1 [Herzog-Arbeitman et al., 2018] and Gaia DR2 [Hawkins and Wyse, 2018] have found 2/10 such stars appear to have [Eu/Fe] > 1, a much higher fraction than is found for random metal-poor stars in the halo. The high velocities suggest these stars originate in accreted satellites. Additionally, Roederer et al. [2018] recently studied the kinematics of all known r-process-enhanced stars in Gaia DR2, also finding evidence that these stars appear to have an accretion origin from UFDs or low-luminosity classical dwarf spheroidals. The statistics in these studies are still low, but they support our

hypothesis of an accretion origin for r-process-enhanced stars. The kinematics of r-II Milky Way halo stars are currently being studied in more detail (e.g., Ji et al. in prep).

Stars with low abundances (or no detection) of r-process elements (low neutron-capture stars, or low n-cap stars) could be another way to identify stars that originated in now-destroyed UFDs. If an r-process event occurs in $\sim$10% of UFDs, $\sim$90% of UFDs should produce low n-cap stars. Our model predicts that $\sim$2% of the halo stars with [Fe/H] $= -2.5$ to -2 should be low n-cap stars from UFDs. This is in rough agreement with the sample of metal-poor halo stars from Roederer et al. [2014c], but more data from upcoming halo star surveys such as 4MOST and WEAVE will allow this to be studied more in depth.

There are a number of limitations in this model, including how we determine f_{NSM} and the imperfections of the empirical relations. Future work on predicting the actual number of r-II halo stars or their distribution in the stellar halo will require more detail than we go into here. The results of this initial investigation, however, support a strong connection between metal-poor r-II stars and now-destroyed UFDs. Neutron-capture element abundances of Milky Way halo stars may thus allow us to quantify how much these small, relic galaxies contribute to the formation of our Galaxy.

The software used in this analysis includes `numpy` [van der Walt et al., 2011], `scipy` [Jones et al., 2001], `matplotlib` [Hunter, 2007].

Chapter 3

Collapsar r-Process Yields Can Reproduce [Eu/Fe] Abundance Scatter in Metal-Poor Stars

This chapter is based on work previously published in *The Astrophysical Journal* (Brauer et. al 2021).

3.1 Introduction

Around half of the abundances of the heaviest isotopes in the periodic table, including gold and europium, are produced through the rapid neutron-capture process [r-process, Burbidge et al., 1957, Cameron, 1957]. Since the first discussion of the r-process in the 1950s, there has been debate over which astrophysical sites produce r-process material. Recently, the detection of an optical transient associated with the neutron star merger GW170817 [Abbott et al., 2017a, Coulter et al., 2017] provided strong evidence for r-process production in neutron star mergers [e.g., Drout et al., 2017, Pian et al., 2017]. Neutron star mergers thus appear to be a source of r-process elements, but it is unclear if they are the dominant source in the early universe. One concern stems from observations of r-process abundances in metal-poor ([Fe/H] < -2.5) stars in the Galactic halo.

It is unclear whether the delay time to form and coalesce a binary neutron star system is too long to provide r-process material to near-pristine gas before the formation of metal-poor stars [e.g., Argast et al., 2004, Skúladóttir et al., 2019, Cescutti et al., 2015, Wehmeyer et al., 2015, Haynes and Kobayashi, 2019, Kobayashi et al., 2020]. Possible solutions include processes like inhomogeneous metal mixing or inefficient star formation mitigating the delay time [e.g., Ishimaru et al., 2015, Shen et al., 2015, van de Voort et al., 2015, Ramirez-Ruiz et al., 2015, Ji et al., 2016b, Dvorkin et al., 2020] or common envelope producing a large number of rapidly merging neutron star binaries [e.g., Beniamini et al., 2016, Safarzadeh et al., 2019b, Zevin et al., 2019, Andrews et al., 2020], but concerns have not been eradicated.

Natal kicks received from the supernova explosions that give birth to neutron stars may have also made it unlikely for small, early galaxies to retain neutron star binaries [Bramante and Linden, 2016, Beniamini et al., 2016, Bonetti et al., 2019]. For example, the highly r-process-enriched metal-poor stars in the ultra-faint dwarf galaxy Reticulum II could potentially be explained by a neutron star merger [Ji et al., 2016b], but the natal kick would have to have been very small ($v < v_{esc} \sim 10 - 20$ km s^{-1}) and/or the merger time extremely short to avoid kicking the binary out of the tiny galaxy [Tarumi et al., 2020, Safarzadeh et al., 2019a, Bramante and Linden, 2016]. This is in contrast to larger estimates of $20 - 140$ km s^{-1} based on the offset distribution of short-duration γ-ray bursts from their host galaxies [Fong and Berger, 2013], and $5 - 5450$ km s^{-1} from galactic double neutron star systems [Wong et al., 2010].

In light of these concerns — coupled with the inference that the ejecta from GW170817 was dominated by an accretion disk wind, rather than dynamical tidal tails [e.g. Siegel, 2019] — Siegel et al. [2019] revived the idea that collapsars (the supernova- and γ-ray-burst-triggering collapse of rapidly rotating massive stars) may be an important source of r-process material (see also, e.g., MacFadyen and Woosley 1999, McLaughlin and Surman 2005). In particular, the accretion disks formed in collapsars can have similar conditions to the r-process producing disk of GW170817. Siegel et al. [2019] found that for accretion rates $\gtrsim 10^{-3}$ M$_\odot$ s^{-1}, these disks produce

neutron-rich outflows that synthesize heavy r-process nuclei. They also found that collapsars can yield sufficient r-process material to explain over 80% of the r-process content of the Universe. Although the electron fraction in collapsar disk winds is still debated [Surman et al., 2006, Miller et al., 2019], this is currently one of the most promising ways for core-collapse supernovae (CCSN) to make r-process elements (other than magnetorotationally driven CCSN, e.g., Nishimura et al. 2015, but see Mösta et al. 2018).

The scatter in the abundances of metal-poor stars is a useful probe of different r-process origins. In this paper, we investigate collapsars as a source of the r-process in the early universe by investigating whether they can self-consistently reproduce the scatter of europium (Eu, Z = 63) in the most metal-poor stars. Our results also hold for any prompt r-process site with a power law distribution of effective r-process yields. As our representation was directly inspired by collapsar properties for the purposes of studying r-process collapsars, though, we call the r-process site in our model "collapsars" and discuss alternative interpretations in more detail in Section 3.5.4.

Our model assumes the r-process material in metal-poor stars was formed exclusively in collapsars with stochastic r-process yields. Previous stochastic models primarily assume the r-process is produced in fixed amounts, but comes from multiple different sources and/or mixes into different environments [e.g., Tsujimoto and Shigeyama, 2014, Cescutti et al., 2015, Wehmeyer et al., 2015, Shen et al., 2015]. In contrast, our model assumes the r-process source has an intrinsically stochastic production: each collapsar synthesizes a different amount of r-process material.

In Section 3.2, we outline our stochastic collapsar enrichment model in which we assume each collapsar contributes an r-process yield that is independently drawn from a power law distribution, inspired by models of collapsar jet fits to γ-ray burst data. Our model is constrained using stellar abundance data described in Section 3.3, and the parameter constraints are described in Section 3.4. The implications of these results are discussed in Section 3.5, where we put our results in context with collapsar jet property distributions, different types of core-collapse supernovae, and

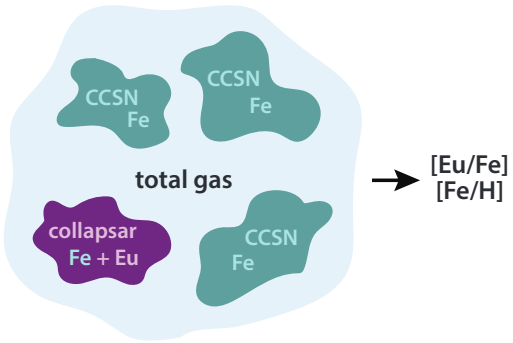

(a) Schematic of our model. Core-collapse supernovae explode into the total gas, yielding iron (Fe), and some fraction of these are collapsars which also yield stochastic amounts of europium (Eu). This produces stars with different [Eu/Fe] and [Fe/H] abundances.

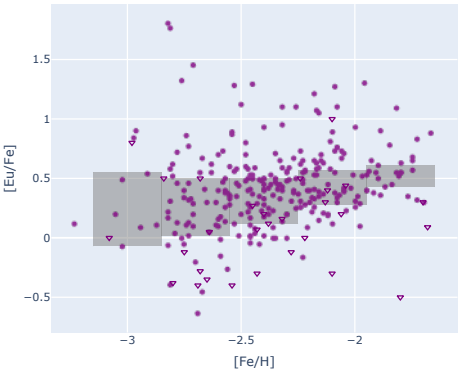

(b) The r-process abundance scatter in the RPA data. The data is shown as dots (Eu detections) and triangles (Eu upper limits). The grey boxes show the estimated $\mathrm{IQR}_{\mathrm{Eu}}$ (the abundance scatter) in several metallicity bins, which decreases with increasing metallicity.

Figure 3-1: Schematic of our theoretical model and scatter plot of the stellar data our models attempts to reproduce. Our model attempts to reproduce the observed Eu scatter at low metallicity by assuming all Eu is produced by collapsars, which are a fraction of all core-collapse supernovae.

different estimates for the amounts of r-process material which may be produced by collapsars. Our conclusions are summarized in Section 3.6.

3.2 Collapsar r-Process Yield Model

The purpose of our model is to determine the distribution of r-process abundances (as measured by [Eu/Fe]) in a fixed metallicity bin (as measured by [Fe/H]). A schematic of the model can be seen in Figure 3-1a. The novel feature of our model is that we explicitly study whether variable r-process yields from a single class of r-process events could produce observed abundance scatter. This is in contrast to previous models [e.g., Cescutti et al., 2015, Ojima et al., 2018, Shen et al., 2015, van de Voort et al., 2015] which generally had a fixed yield per event and produced scatter through different r-process sites and/or different galactic environments.

3.2.1 Defining "Collapsar"

The term "collapsar" typically refers to the collapse of a massive, rapidly-rotating star in which accretion onto a central black hole can produce a beamed jet, commonly evoked as the progenitors of long-duration γ-ray bursts (LGRBs). In the model described below, we more broadly use the term to encompass a population of core-collapse supernovae that produce heavy r-process material with a power-law distribution of yields. This definition is motivated by the traditional collapsar picture in which rapid accretion onto a compact object launches a collimated outflow wherein both the duration and luminosities of LGRBs are well-described by power laws [Petropoulou et al., 2017, Sobacchi et al., 2017]. Connecting jet properties to r-process production is inspired by the possible connection between the accretion phase during which r-process material is produced (due to a sufficiently high accretion rate that neutronizes the disk) and the phase during which the collapsar jet is launched. In particular, Siegel et al. [2019] finds that the production of heavy r-process material requires $\dot{M} \gtrsim 10^{-3}$ $M_\odot$ s^{-1}, closely matched to the accretion rates required for jet production [MacFadyen and Woosley, 1999]. The results described below also hold for any prompt r-process site (e.g., occurring roughly concurrently with CCSN; this could potentially include fast-merging neutron stars) that lead to a power law distribution of heavy r-process material. We discuss other interpretations in Section 3.5.4.

In addition, our model does not require that a jet successfully breaks out of the progenitor star. While the most extreme r-process producing events require large fall-back accretion disks and are likely associated with LGRBs, our model also includes events that eject smaller amounts of r-process material. Such systems may produce weaker outflows/jets and be observed as low-luminosity GRBs [ll-GRBs; e.g., Bromberg et al., 2011, Petropoulou et al., 2017], relativistic supernovae [e.g., Soderberg et al., 2010, Margutti et al., 2014], or broad-lined Type Ic supernovae [Type Ic-BL; e.g., Milisavljevic et al., 2015, Modjaz et al., 2016].

3.2.2 Basic Physical Set-up and Model Parameters

We analytically model the abundance distribution as arising from a burst of core-collapse supernova enrichment, some fraction of which are collapsars that produce non-zero r-process yields. Each core-collapse supernova produces an iron yield and each collapsar also produces an r-process yield that is independently and identically drawn from a power law distribution. We assume the typical star formed in these galaxies forms after the metal yields from all of the supernovae fall into and mix within the hydrogen gas of the system. During this process, some fraction of the metals are permanently lost from the galaxy due to gas outflows.

This model has five free parameters:

1. $N_{\rm SN}$: the number of core-collapse supernovae enriching the gas.

2. $\langle N_r \rangle$: the average number of collapsars (i.e. supernovae that produce non-zero amounts of r-process material).

3. $M_{r,\rm min}$: the minimum mass of r-process material that can be produced by a collapsar.

4. α: the power law exponent for our power law distribution of r-process yield produced per collapsar.

5. $y_{\rm Fe,eff}$: the effective iron yield per supernovae per unit gas mass. $y_{\rm Fe,eff} = y_{\rm Fe} f_{\rm retained}/M_{\rm gas}$, where $y_{\rm Fe}$ is the iron yield per supernova, $f_{\rm retained}$ is the fraction of iron retained in the galaxy and not carried out of the system by gas outflows, and M_{gas} is the total gas mass in the system.

These parameters combine to yield the mean gas metallicity, the the fraction of supernovae that are collapsars (f_r), and the average yield per collapsar ($\langle M_r \rangle$), as described below.

3.2.3 Gas Enrichment

We determine the distribution of europium abundances produced by this model at a given metallicity. The mean metallicity of our stars is found from $M_{\rm Fe}/M_{\rm H} = N_{\rm SN} y_{\rm Fe,eff}$. The mass of iron and hydrogen is converted to [Fe/H] using a mean molecular weight of $\mu_{\rm Fe} = 56$ for Fe, $\log \epsilon_\odot({\rm Fe}) = 7.50$, and $\log \epsilon_\odot({\rm H}) = 12.00$ [Asplund et al., 2009], where we use the stellar spectroscopist notation $[{\rm X/Y}] \equiv \log N_{\rm X}/N_{\rm Y} - \log (N_{\rm X}/N_{\rm Y})_\odot = \log(\frac{M_{\rm X}\mu_{\rm Y}}{M_{\rm Y}\mu_{\rm X}}) - (\log \epsilon_\odot({\rm X}) - \log \epsilon_\odot({\rm Y}))$.

In order to determine the distribution of europium values, we enrich this gas with N_r collapsars, which we draw stochastically from a Poisson distribution with mean $\langle N_r \rangle = f_r N_{\rm SN}$. Each collapsar contributes an r-process yield M_r that is independently drawn from a power law distribution.

$$p(M_r) \propto \left(\frac{M_r}{M_{r,\rm min}} \right)^{-\alpha} \quad M_r \geq M_{r,\rm min} \tag{3.1}$$

The r-process yield for a single explosion, M_r, can be converted to $M_{\rm Eu}$ by using the solar r-process mass fraction of europium compared to all nuclei with mass number A > 70. The mass fraction, $X_{\rm Eu}$, is approximately 10^{-3} (1.75×10^{-3}, Arnould et al. 2007; 9.77×10^{-4}, Sneden et al. 2008). When converting total europium mass to [Eu/Fe], we use a mean molecular weight of $\mu_{\rm Fe} = 152$ for Eu and $\log \epsilon_\odot({\rm Eu}) = 0.52$. We also assume that europium and iron have the same retention fraction, $f_{\rm retained}$, meaning the same fraction of both is lost from the galaxy.

Note that if $\alpha \leq 2$, then the average yield produced per collapsar diverges and our model would also require an upper cutoff to the amount of r-process material that can be produced by a single collapsar, $M_{r,\rm max}$. However, when we compare to observed data in Section 3.4, it will turn out our results imply $\alpha > 2$, in which case the average yield per collapsar is:

$$\langle M_r \rangle = M_{r,\rm min} \frac{\alpha - 1}{\alpha - 2} \tag{3.2}$$

While in principle $y_{\rm Fe}$ is also stochastic, for simplicity we hold it constant. This is fine as long as f_r is small, since variations in the Fe yield will average out.

Operationally, we create a model [Eu/Fe] distribution by considering several thousand instances of supernova enrichment. Each instance is a single data point in our modeled cumulative distribution function. For each instance, we draw an N_r value and then draw M_r for each of the N_r collapsars. The total europium and iron masses retained in the galaxy in each instance are transformed into a [Eu/Fe] measurement. We also add a 0.1 dex Gaussian uncertainty to mimic observational errors.

3.2.4 Constraining Model Parameters: Literature Estimates for Effective Iron Yields

The effective iron yield of core-collapse supernova per unit gas mass cannot be directly constrained from a sample of stellar abundance data. We constrain its value by combining estimates for each component parameter (recall $y_{\mathrm{Fe,eff}} = y_{\mathrm{Fe}} f_{\mathrm{retained}} / M_{\mathrm{gas}}$) from the literature.

The fraction of retained metals is set to $f_{\mathrm{retained}} = 10^{-2\pm0.5}$, assuming that metal-poor stars form early in small galaxies. Observationally, individual faint galaxies have f_{retained} in this range: the Milky Way's moderately faint dSphs (e.g., Ursa Minor) have kept less than 1% of their metals [Kirby et al., 2011b]; while the faint but still star-forming galaxy Leo P has kept about 5% of its metals [McQuinn et al., 2015]. Theoretically, retaining about 1% of metals in small galaxies reproduces the slope and normalization of the mass-metallicity relation [e.g., Dekel and Woo, 2003, Robertson et al., 2005]. The retention fraction is also borne out in hydrodynamic galaxy simulations [e.g., Emerick et al., 2018].

M_{gas} is set by models of how supernovae dilute metals into a mixing mass of gas. For small, early galaxies that form metal-poor stars, the mixing mass is $M_{\mathrm{gas}} \sim 10^6\, M_\odot$ [Ji et al., 2015a]. The strict lower limit on this mass is the mass contained in a single final supernovae remnant, a minimum of around $\sim 10^{4.5}\ M_\odot$ [e.g., Magg et al., 2020, Macias and Ramirez-Ruiz, 2018], with a range of average mixing masses for metal-poor stars of 10^5 to $10^8 M_\odot$ of gas. For systems with higher M_{gas}, more metals are retained, resulting in a higher retention fraction f_{retained} (and vice versa).

To estimate an average iron yield from CCSN, we calculate a weighted average between observations of H-rich CCSN and H-poor CCSN. A detailed discussion can be found in Appendix 3.7, but find that the average yield is $y_{\rm Fe} \approx 0.1 M_{\odot}$, with the uncertainty in $f_{\rm retained}$ and $M_{\rm gas}$ far outweighing that of $y_{\rm Fe}$.

Altogether, $y_{\rm Fe,eff}$ has a wide range of possible values (10^{-10}–10^{-7}), but our fiducial choice is $y_{\rm Fe,eff} = 10^{-9}$. This choice is validated by an independent estimation of the frequency of r-process events in ultra-faint dwarf galaxies in Section 3.4.2. We note, however, that there is tension between the values expected for $y_{\rm Fe,eff}$ in very low mass galaxies based on the theoretical breakdown described in this section and comparisons to several external constraints. For example, the number of supernovae predicted in an ultra-faint dwarf galaxy using the Salpeter initial mass function suggests an effective iron yield closer to $\sim 10^{-7.5}$, and a simulation of extremely metal-poor ([Fe/H] $= -3.42$) stars forming after a single supernova gives an estimated effective iron yield as high as $\sim 10^{-6.5}$ [Chiaki and Wise, 2019]. This is not fully unexpected as $y_{\rm Fe,eff}$ differs in different galaxies and the lowest mass galaxies will have the highest effective yields, but we note that this parameter remains uncertain and may trend higher than its fiducial value.

3.2.5 Constraining Model Parameters: Fitting Stellar Abundance Data

After fixing the effective iron yield, stellar abundances are used to constrain the other model parameters. The stellar abundance data provides us effectively four observable quantities of interest:

1. the mean metallicity of the stars, $\langle$[Fe/H]$\rangle$,
2. the mean r-process abundance, $\langle$[Eu/Fe]$\rangle$,
3. the estimated fraction of stars that formed from gas not enriched by an r-process event, f_0,
4. the observed scatter in r-process abundance between stars, $\mathrm{IQR}_{\rm Eu}$.

Rather than quantifying scatter with standard deviation, σ(Eu), we use the more robust interquartile range, a measure of statistical dispersion equal to the difference between the 75th and 25th percentiles, denoted $\mathrm{IQR_{Eu}}$. Model parameters are then determined as follows:

$\langle N_r \rangle$ and α: The average number of collapsars, $\langle N_r \rangle$, and the exponent of the r-process yield power law distribution, α, are determined by comparing the observed f_0 and r-process scatter, $\mathrm{IQR_{Eu}}$, to those predicted by our models with varying $\langle N_r \rangle$ and α. In a small metallicity bin, the shape of the [Eu/Fe] distribution function is dependent on only these two parameters. The other potentially relevant parameters contribute only to shifting the distribution to higher or lower [Eu/Fe]. By focusing on only the shape of the distribution, we can avoid making assumptions about any additional parameters when determining $\langle N_r \rangle$ and α.

N_{SN} and f_r: The number of SN enriching the gas, N_{SN}, is determined from the mean metallicity of the stars and the effective iron yield using $\langle M_{\mathrm{Fe}}/M_{\mathrm{H}} \rangle = N_{SN} \times y_{\mathrm{Fe,eff}}$. The fraction of supernova that are collapsars, $f_r = \langle N_r \rangle / N_{SN}$, is then found by combining N_{SN} and the average number of collapsars, $\langle N_r \rangle$, from above.

$M_{r,\mathrm{min}}$ and $\langle M_r \rangle$: We first determine the average r-process yield produced per collapsar, $\langle M_r \rangle$, using the relationship: $\langle M_r \rangle \, f_{\mathrm{retained}} X_{\mathrm{Eu}} \approx \langle M_{\mathrm{Eu}} \rangle \, / \, \langle N_r \rangle$. In this equation, $\langle M_{\mathrm{Eu}} \rangle$ is found by considering the mean r-process abundance $\langle$[Eu/Fe]$\rangle$ and mean metallicity $\langle$[Fe/H]$\rangle$ in combination with $M_{\mathrm{H}} \approx M_{\mathrm{gas}}$. The minimum r-process yield is then $M_{r,\mathrm{min}} = \langle M_r \rangle \, \frac{\alpha-2}{\alpha-1}$.

We do not attempt to model higher moments of the [Eu/Fe] distribution beyond the mean and scatter because we expect selection effects in the data to dominate. We also do not attempt to model the shape of the distribution tails for both observational and theoretical reasons. Observationally, the low end of the [Eu/Fe] distribution cannot be well known without a robust selection function. Theoretically, the low and high ends of our distribution are not robust due to our assumption that model stars form after all of the supernova yields have fallen into and mixed with the hydrogen gas. This is because our assumption precludes outlier stars that, for example, could have more or less europium due to inhomogeneous mixing.

Future work will address these concerns through a more detailed treatment of enrichment that incorporates our variable-yield work into a more complete picture that includes scatter due to differences in galaxy formation (e.g., different environments or metal mixing). This will allow for a better determination of whether our assumption of a power law is an appropriate shape for the r-process yield distribution and improved constraints on α and N_r.

3.3 Stellar Abundance Samples

3.3.1 Sample Selection

We use a stellar abundance sample from the R-process Alliance (RPA), a collection of detailed abundances of 601 halo stars [Hansen et al., 2018, Sakari et al., 2018, Ezzeddine et al., 2020b, Holmbeck et al., 2020b]. The RPA stars are bright (V $<$ 13.5), metal-poor ([Fe/H] $\lesssim -2$) red giant stars in the Milky Way stellar halo. They were observed with a focus on obtaining a statistically complete sample of europium abundances. To verify the RPA data, we also consider a sample of 228 metal-poor red giant halo stars from Roederer et al. [2014b] [henceforth R14]. Both of these samples report europium measurements or upper limits for every star.

The R14 sample has [Eu/Fe] abundances that are 0.22 dex lower and [Fe/H] abundances that are 0.19 dex lower from other samples due to using a much cooler effective temperature scale and isochrone-based surface gravities [Roederer et al., 2014a]. We thus shift the reported measurements up by these amounts when plotting in Figure 3-2 and reporting values in Table 3.1.

We restrict most of our analysis to very metal-poor ([Fe/H] < -2.5) stars, and the highest metallicity we consider is [Fe/H] < -1.75 (when analyzing the evolution of the Eu scatter with increasing metallicity in Section 3.4.1). We only consider stars with barium-to-europium abundance ratios that could be produced by the r-process ($-0.9 \lesssim$ [Ba/Eu] $\lesssim -0.4$). [Ba/Eu] higher than ~ -0.4 indicates contamination from the s-process, another nucleosynthetic process which forms europium. The solar

r-process barium-to-europium ratio is [Ba/Eu] ≈ -0.8 [Sneden et al., 2008], and stars with much lower [Ba/Eu] cannot be explained by the r-process pattern. We note that small variations in these purity cuts do not significantly change our results.

Taking into account these restrictions (with [Fe/H] < -2.5), the RPA sample includes 83 stars with Eu measurements and an additional 11 stars with Eu upper limits. The R14 sample includes 36 stars with Eu measurements and 4 with Eu upper limits. The RPA sample (up to [Fe/H] < -1.75) and its $\mathrm{IQR_{Eu}}$ in different metallicity bins can be seen in Figure 3-1b.

3.3.2 Construction of Statistical Distributions

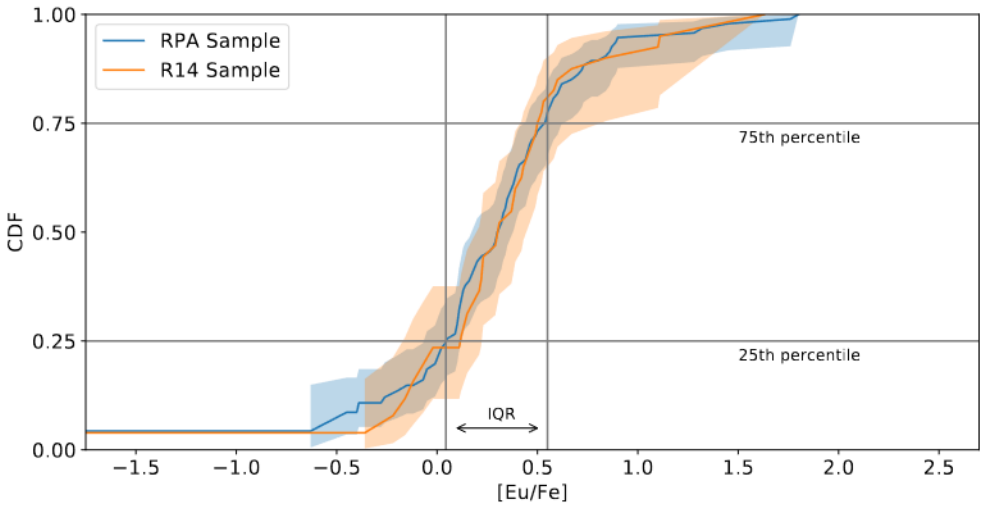

Figure 3-2: Cumulative distribution functions for the RPA and R14 samples. Both CDFs are determined using the Kaplan-Meier estimator, which takes into account detections and upper limits to estimate the true distribution. The shaded regions show 95% confidence on the CDF estimate. Grey lines outline the interquartile range (25%-75%) for the RPA Kaplan-Meier CDF. The CDFs have been extended to the y-axis to show the estimated fraction of stars in each sample that have no r-process elements.

To combine the mixture of measurements and upper limits into a statistical distribution of europium for each sample, we employ survival statistics, a branch of statistics that deals with censored datasets, e.g., upper limits. The most general single variate survival statistic is the Kaplan-Meier estimator (KME), which provides a

Table 3.1: Interquartile ranges and fraction of stars formed from gas with no r-process enrichment for different [Eu/Fe] CDFs from observational stellar samples with [Fe/H] < -2.5. The distributions can be seen in Figure 3-2. $\mathrm{IQR_{Eu}}$ uncertainties are due to both KME confidence levels and uncertain observations. The f_0 values are upper limits as the distribution could continue to lower [Eu/Fe] with lower f_0.

Stellar Abundance Sample	$\mathrm{IQR_{Eu}}$	f_0	$\langle$[Eu/Fe]$\rangle$	$\langle$[Fe/H]$\rangle$
RPA	$0.50^{+0.15}_{-0.10}$	$0.04^{+0.10}_{-0.04}$	$0.3^{+0.1}_{-0.1}$	$-2.7^{+0.1}_{-0.1}$
R14	$0.38^{+0.51}_{-0.14}$	$0.04^{+0.11}_{-0.04}$	$0.2^{+0.2}_{-0.2}$	$-2.9^{+0.1}_{-0.1}$

non-parametric maximum likelihood estimate of a distribution from observed data. The Kaplan-Meier estimator and survival statistics have been used extensively in astronomical literature [e.g. Feigelson and Nelson, 1985, Schmitt, 1985, Wardle and Knapp, 1986, Simcoe et al., 2004]. We use the `KaplanMeierFitter` from the survival analysis python package `lifelines` [Davidson-Pilon et al., 2020]. For this estimate to be valid, two assumptions about the distribution of upper limits must hold. First, the upper limits should be independent of each other, which is true here as the stars are independent. Second, the upper limits should be random – i.e., the probability that a measurement will be censored should not correlate with the measurement value itself. This assumption may not hold because lower [Eu/Fe] values are more likely to be censored. Ideally, we would fully forward model and censor our theoretical results, but that requires many additional assumptions including a completeness function (probability of measuring any value given [Eu/Fe]), an error function (the value we measure for [Eu/Fe] given its true value), and an upper limit function (the probability of setting a [Eu/Fe] upper limit at a specific value given its true value). Fully forward modeling the observational sample is beyond the scope of this paper. We thus use the Kaplan-Meier estimate while keeping in mind that this may not be a perfect estimate.

Figure 3-2 shows the [Eu/Fe] cumulative distribution functions for the RPA and R14 samples. The interquartile range, $\mathrm{IQR_{Eu}}$, differs slightly for the different samples but is consistent within the uncertainty. The mean [Eu/Fe] and [Fe/H] also differ slightly. The zero-limit f_0, the estimated fraction of stars that formed from gas that was not enriched by an r-process event, is the same in both samples. In our model,

f_0 is the fraction of stars with no europium enrichment ([Eu/Fe] = $-\infty$), but we cannot identify if real stars have no r-process enrichment (and stars could receive trace amounts of europium enrichment through other processes despite the [Ba/Eu] cuts we applied to purify our sample). We thus estimate f_0 in the data by taking the lowest CDF value from the observed distribution as estimated by survival statistics. This assumes that the CDF immediately plateaus at lower [Eu/Fe] instead of continuing to decrease. Because the distribution could continue to decrease with lower [Eu/Fe], the observed f_0 values are upper limits. Realistically, the real distribution certainly does not fully plateau even if our f_0 estimate is correct because of the possible other trace sources of europium, but for the purposes of this analysis and because we cannot estimate the CDF to extremely low [Eu/Fe] regardless, we ignore those minor effects. These values are shown in Table 3.1.

3.4 Results

We use the stellar abundance data to constrain the model parameters. The results are summarized in Table 3.2.

Table 3.2: Model parameters determined from observations. The wide ranges of $N_{\rm SN}$, $M_{r,\rm min}$, and $y_{\rm Fe,eff}$ encompass broad uncertainty in the fraction of metals retained in each galaxy and each galaxy's gas mass. To be thorough we include these full ranges. We also validate our fiducial values for $y_{\rm Fe,eff}$, f_r, and $\langle N_r \rangle$ (which also validates $N_{\rm SN}$, $M_{r,\rm min}$, and $\langle M_r \rangle$). For α, the full range of values produce similar distribution shapes. Derived parameter values are shown below the double line.

	Description	Range	Fiducial Value
$N_{\rm SN}$	Number of core-collapse supernovae	$30 - 30000$	3000
$\langle N_r \rangle$	Average number of r-process collapsars	$2 - 4$	3
$M_{r,\rm min}$	Minimum r-process yield produced per collapsar (see Eq. 3.1)	$3 \times 10^{-4} - 3 \times 10^{-1}$	3×10^{-2}
α	Power law exponent of M_r distribution (see Eq. 3.1)	$2.2 - 6$	2.8
$y_{\rm Fe,eff}$[1]	Effective supernovae iron yield into the total gas mass, $y_{\rm Fe} f_{\rm retained}/M_{\rm gas}$	$10^{-10} - 10^{-7}$	10^{-9}
f_r	Fraction of supernovae that are collapsars, $\langle N_r \rangle / N_{\rm SN}$	$10^{-4} - 10^{-1}$	10^{-3}
$\langle M_r \rangle$	Average r-process yield produced per collapsar	$7 \times 10^{-4} - 7 \times 10^{-1}$	7×10^{-2}

3.4.1 $\langle N_r \rangle$ and α

We use the model described in Section 3.2 to calculate theoretical cumulative distribution functions (CDF) of stellar [Eu/Fe] abundances. CDFs resulting from different

representative choices of $\langle N_r \rangle$ and α can be seen in Figure 3-3. Each model CDF has an arbitrary offset that shifts the CDF left or right for plotting purposes. Recall that $\langle N_r \rangle$ and α can be constrained using only the shape of the distribution (i.e., the $\mathrm{IQR_{Eu}}$ and f_0). A higher $\langle N_r \rangle$ causes both a lower f_0 since fewer stars will form from un-enriched gas and a narrower distribution due to the central limit theorem. A higher α also narrows the distribution by increasing the rarity of high M_r. When constraining these parameters with the $\mathrm{IQR_{Eu}}$, a higher $\langle N_r \rangle$ thus corresponds to a lower α and vice versa.

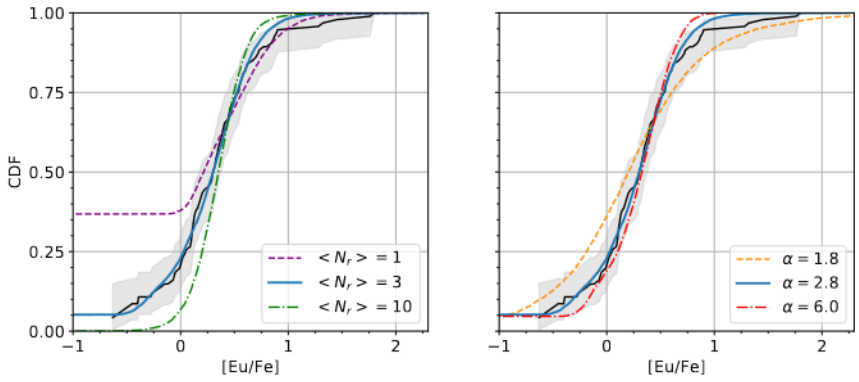

Figure 3-3: Stellar [Eu/Fe] abundance cumulative distribution functions (colored lines) for models with different $\langle N_r \rangle$ and α values. The observed [Eu/Fe] CDF for the RPA sample is shown in black with grey uncertainty. Our fiducial model, $\langle N_r \rangle = 3$ and $\alpha = 2.8$, is shown in solid blue in both plots. When either $\langle N_r \rangle$ or α is not specified, the fiducial value is used. The model CDFs have an arbitrary offset to shift the distribution left or right for plotting purposes, so only the shape (i.e., the IQR and zero-fraction) is relevant.

$\langle N_r \rangle$, the average number of r-process collapsars enriching our stellar population, is constrained by the estimated fraction of stars which formed from gas not enriched by an r-process event, f_0. For $f_0 = 0.04$, $\langle N_r \rangle = 3$ is the best fit value. Figure 3-4a shows how the value of f_0 changes with $\langle N_r \rangle$, independently of α. In this figure, the black boxes outline the parameter values which explain the observed f_0 or $\mathrm{IQR_{Eu}}$. $\langle N_r \rangle = 2$ to 4 can also explain observations. Note that the observed f_0 is an upper limit as the distribution could smoothly continue to lower [Eu/Fe] with a lower f_0. The constraint on $\langle N_r \rangle$ from f_0 is thus a lower bound.

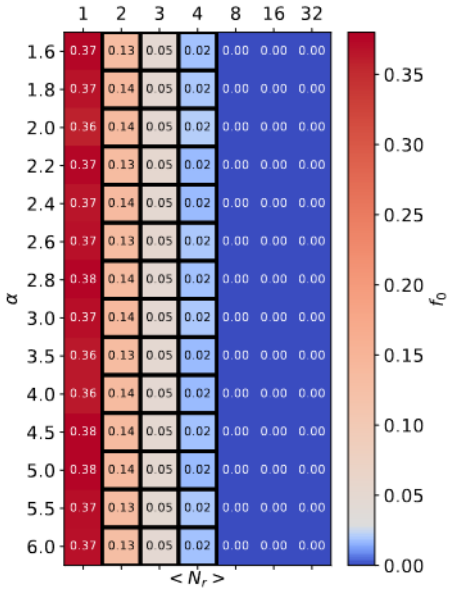

(a) Values of the zero-fraction, f_0, for different models. The heat map colors are normalized to $f_0 = 0.04^{+0.10}_{-0.04}$, the f_0 of the RPA stellar abundance sample (see Table 3.1). Red is higher than observed f_0, blue is lower. $\langle N_r \rangle$ alone affects the f_0 value.

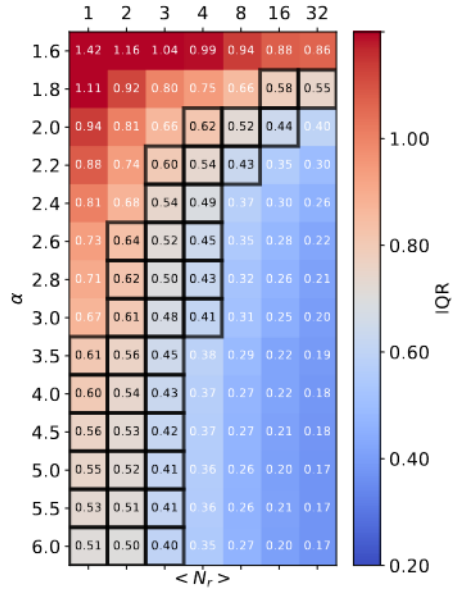

(b) Values of the IQR for different models. The heat map colors are normalized to $\mathrm{IQR}_{\mathrm{Eu}} = 0.50^{+0.15}_{-0.10}$, the IQR of the RPA stellar abundance sample (see Table 3.1). Red is higher than observed IQR, blue is lower. For $\langle N_r \rangle = 1$, we determined the IQR by assuming symmetry and doubling the 50%-75% range (because the distribution is always above 25%).

Figure 3-4: Heat maps showing how the cumulative distribution IQR and zero-fractions of our model vary with $\langle N_r \rangle$ and α. Black boxes outline the parameter combinations that can explain the stellar data within observational uncertainty (using the RPA sample; see Table 3.1). Note: The plotted α values increase by 0.2 until $\alpha = 3.0$, at which point they increase by 0.5 due to increasingly slower variation in $\mathrm{IQR}_{\mathrm{Eu}}$.

To validate our fiducial value of $\langle N_r \rangle = 3$, we also reproduce the evolution in europium scatter with increasing metallicity. This gives an upper bound to the constraint. We examine the RPA stellar abundance sample in several metallicity bins (up to [Fe/H] $= -1.65$; see Figure 3-5). We compare model scatter to the scatter of the RPA distribution as determined by both the Kaplan-Meier estimator (which takes into account europium detections and upper limits) and as determined by only europium detections. The R14 sample is excluded from this plot because it has too few stars in each bin to determine distributions.

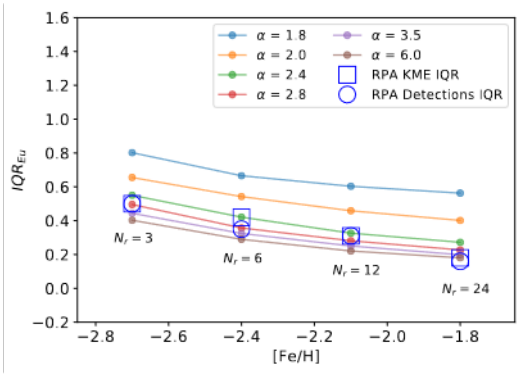

(a) The evolution of the Eu scatter with increasing metallicity can be well explained by our fiducial model choices of $\langle N_r \rangle = 3$ at $\langle [\text{Fe/H}] \rangle = -2.7$ (the mean metallicity of our RPA sample) and $\alpha = 2.8$.

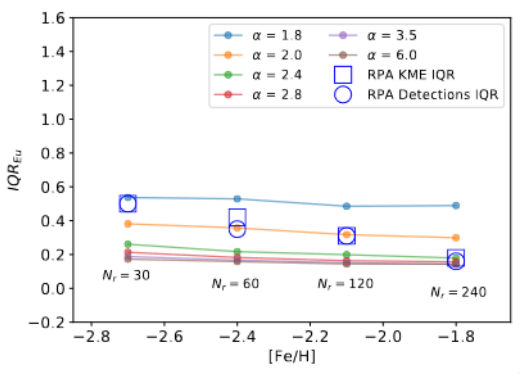

(b) If $\langle N_r \rangle$ is increased to $\langle N_r \rangle = 30$ at $\langle [\text{Fe/H}] \rangle = -2.7$, no single choice of α well explains the evolution of the Eu scatter. Higher $\langle N_r \rangle$ choices result in poorer matches to observations.

Figure 3-5: The decrease in the [Eu/Fe] scatter with higher metallicity seen in the data (hollow circles and squares) is reproduced by our model (colored dots). Each [Fe/H] bin of 0.3 dex corresponds to approximately a factor of 2 increase in supernovae, hence why we double the number of r-process collapsars in each bin. Reproducing the evolution in the scatter at higher metallicity as well as low metallicity increases confidence in our fiducial model choices of $\langle N_r \rangle$ and α.

As metallicity increases, $\langle N_r \rangle$ should increase linearly, but the scatter should decrease with $\sqrt{\langle N_r \rangle}$. Reproducing the IQR_{Eu} in several metallicity bins thus suggests our model uses the correct $\langle N_r \rangle$. When binning on metallicity, our model with $\langle N_r \rangle = 3$ at $\langle [\text{Fe/H}] \rangle = -2.7$ well reproduces the observed decrease in scatter. If we increase $\langle N_r \rangle$ by a factor of 10 or more, our model no longer well reproduces the observed decrease in scatter unless α is allowed to vary with metallicity. Considering all uncertainty from the Kaplan Meier Estimator, the upper bound is $\langle N_r \rangle \approx 50$, but the model favors a much lower $\langle N_r \rangle$. This suggests our fiducial $\langle N_r \rangle = 3$ is roughly correct despite being a lower bound.

To be thorough, we also explore the extreme case where *all* core-collapse supernovae result in r-process collapsars – i.e., all core-collapse supernovae form an accretion disk that is able to synthesize a non-zero amount of r-process material ($\langle N_r \rangle = N_{\text{SN}}$ and $f_r = 1$). We consider the case where $\langle N_r \rangle = 3000$, where 3000 is our fiducial value of N_{SN} (see Section 3.4.2). In this extreme case, the vast majority

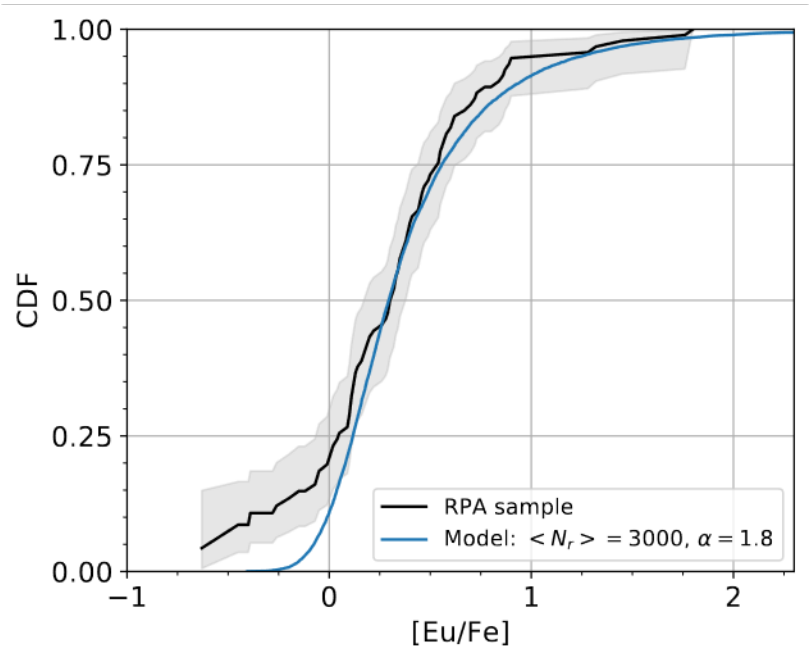

Figure 3-6: Distribution for an extreme model where all core-collapse supernovae produce some r-process material ($f_r = 1$). This extreme model can explain the observed $\mathrm{IQR}_{\mathrm{Eu}}$. It cannot well explain the evolution of scatter with increasing metallicity, however (e.g., Figure 3-5). It also cannot well explain the low [Eu/Fe] tail. For this model, the minimum amount of r-process material per collapsar is extremely small, $M_{r,\mathrm{min}} \approx 10^{-6} M_{\odot}$.

of collapsars would produce extremely small amounts of r-process material. As seen in Figure 3-6, this extreme case can explain the observed $\mathrm{IQR}_{\mathrm{Eu}}$ with a scatter of $\mathrm{IQR}_{\mathrm{Eu}} = 0.45$ for $\alpha = 1.8$. The upper bound set on $\langle N_r \rangle$ by the evolution of scatter with metallicity (Figure 3-5) disfavors this model, however. The situation where all core-collapse supernovae produce r-process is only favored if N_{SN} is below 30, lower than even our most extreme N_{SN} value. This extreme model also does not reproduce the observed distribution at low [Eu/Fe] as well as the fiducial model, though we note that the tails of the observed distribution are less trustworthy than the $\mathrm{IQR}_{\mathrm{Eu}}$. We thus keep $\langle N_r \rangle = 3$ for our results.

α, the exponent of the r-process yield power law distribution, is constrained by the $\mathrm{IQR}_{\mathrm{Eu}}$ value of the distribution, which varies with both α and $\langle N_r \rangle$ as shown in Figure 3-4b. For $\langle N_r \rangle = 3$ and $\mathrm{IQR}_{\mathrm{Eu}} = 0.50^{+0.15}_{-0.10}$, the constrained value is $\alpha = 2.8^{+4.2}_{-0.6}$.

3.4.2 $N_{\rm SN}$ and f_r

The number of supernovae, $N_{\rm SN}$, is linearly related to $y_{\rm Fe,eff}$. To explain the mean metallicity $\langle$[Fe/H]$\rangle = -2.7 \pm 0.1$ (using the method described in Section 3.2.5), on the extreme ends of $y_{\rm Fe,eff}$ values we need anywhere from 30 to 30,000 supernovae; lower $y_{\rm Fe,eff}$ corresponds to higher $N_{\rm SN}$ as more supernovae are needed to explain the mean metallicity. For our fiducial value of $y_{\rm Fe,eff} = 10^{-9}$, $N_{\rm SN} \approx 3000$.

With values for $\langle N_r \rangle$ (from Section 3.4.1) and $N_{\rm SN}$, we can determine the fraction of supernovae that result in r-process material producing collapsars, $f_r = \langle N_r \rangle / N_{\rm SN}$. Considering the extremes of the possible values of $y_{\rm Fe,eff}$, $f_r \approx 0.0001$ to 0.1. For our fiducial values ($\langle N_r \rangle = 3$ and $y_{\rm Fe,eff} = 10^{-9}$), $f_r \approx 0.001$.

To validate our fiducial choice of $y_{\rm Fe,eff}$, we also estimate f_r using observations of ultra-faint dwarf galaxies around the Milky Way. There are now high-resolution spectroscopic abundances for stars in 19 surviving ultra-faint dwarfs. Of these, three of the dwarfs (Grus II, Reticulum II, and Tucana III) exhibit r-process enrichment [Hansen et al., 2020, Ji et al., 2016b, Hansen et al., 2017]. Since these are extremely small systems, we assume each of these three dwarfs experienced one r-process event (as in Ji et al. 2016b, Brauer et al. 2019), and then estimate the total number of supernovae that contributed to all of their stellar populations to estimate f_r. We combined literature values of their absolute magnitudes M_V [Muñoz et al., 2018, Torrealba et al., 2018, Drlica-Wagner et al., 2015, Bechtol et al., 2015, Mutlu-Pakdil et al., 2018] with a Salpeter individual mass function that predicts $0.02 L_0$ supernovae where L_0 is the present-day luminosity in $L_\odot$ [Ji et al., 2016b]. The ultra-faint dwarfs cumulatively experienced about 1800 supernovae. The fraction of supernovae that result in r-process material producing collapsars is thus $f_r \sim 3/1800 = 0.002$. This validates our fiducial model values of $f_r \approx 0.001$ and $y_{\rm Fe,eff} \approx 10^{-9}$. We note again, however, that there is tension between our fiducial estimate of $y_{\rm Fe,eff}$ and several external constraints in very low mass galaxies, as discussed in Section 3.2.4, so we continue to report the full uncertainty in these parameters.

3.4.3 $M_{r,\mathbf{min}}$

The minimum r-process yield produced per collapsar, $M_{r,\mathrm{min}}$ (see Eq. 3.1), depends on α and varies linearly with $y_{\mathrm{Fe,eff}}$. To transform between total r-process yield (nuclei with A $\geq$ 70) and europium yield, we use the solar r-process europium mass fraction $X_{\mathrm{Eu}} \approx 10^{-3}$. To explain the observed mean europium-iron abundance ratio $\langle$[Eu/Fe]$\rangle$, on the extreme ends of $y_{\mathrm{Fe,eff}}$ values, we find that $M_{r,\mathrm{min}} \approx 0.0003 - 0.3 M_{\odot}$; lower $y_{\mathrm{Fe,eff}}$ corresponds to higher $M_{r,\mathrm{min}}$ both because a lower f_{retained} causes less europium to be retained in the galaxy and because higher M_{gas} requires a higher mass of iron and europium to explain the mean [Fe/H] and [Eu/Fe] abundances. For our fiducial values of $y_{\mathrm{Fe,eff}} = 10^{-9}$, $\langle N_r \rangle = 3$, and $\alpha = 2.8$, we find $M_{r,\mathrm{min}} \approx 0.03 M_{\odot}$, or a mean r-process yield per collapsar of $\langle M_r \rangle \approx 0.07 M_{\odot}$.

In the extreme case where all core-collapse supernovae produce a nonzero amount of r-process material (Figure 3-6), the minimum amount of r-process material per collapsar would be extremely small, $M_{r,\mathrm{min}} \approx 10^{-6} M_{\odot}$ for $\langle N_r \rangle \approx 3000$. This situation is disfavored because it does not reproduce the observed decrease of Eu scatter with increasing metallicity unless $y_{\mathrm{Fe,eff}}$ is much higher than our fiducial value.

3.5 Discussion

Using stellar abundance data to constrain parameters in our stochastic collapsar chemical enrichment model produces a self-consistent physical picture, which was not guaranteed a priori. We now discuss this in more detail and place our results in context with other potentially physically relevant values. We also discuss the limitations of this model in Section 3.5.5.

3.5.1 Implications of f_r: The Fraction of CCSN that Produce Collapsars

What fraction of core-collapse supernovae (CCSN) produce collapsars? Recall that our definition of collapsar is motivated by physical picture in which a rapid fallback

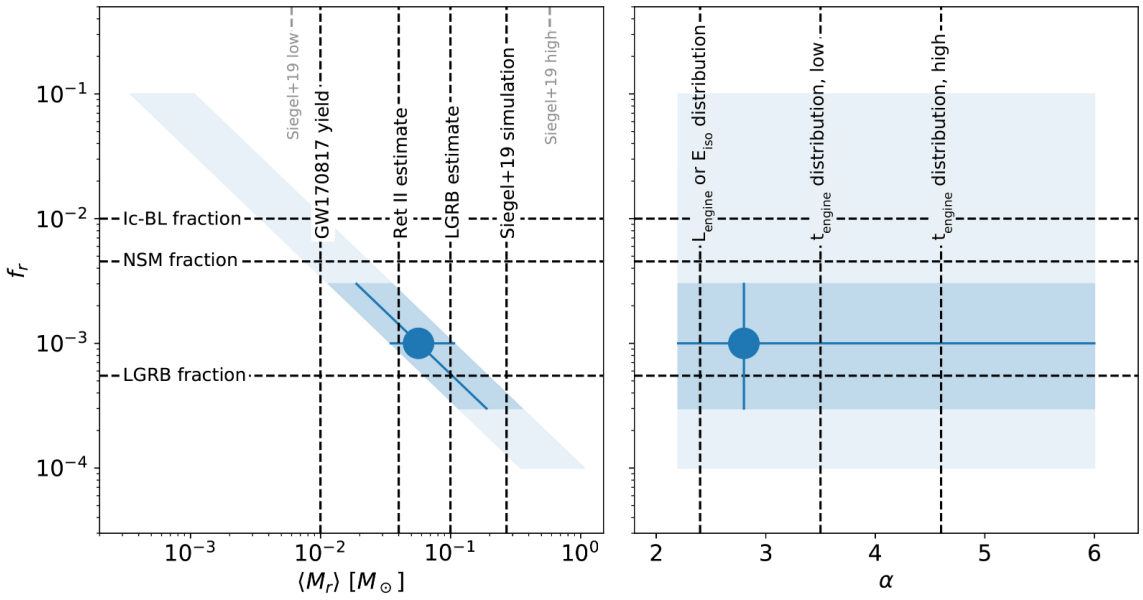

Figure 3-7: Constraints on $\langle M_r \rangle$, f_r, and α from our model (blue) in context of potentially physically relevant values (black dotted lines). For descriptions of the reference values, see Section 3.5. Our fiducial model values are plotted as a blue dot, while the dark blue shaded region represents an order of magnitude uncertainty around our fiducial values and the light blue shaded region represents the full uncertainty.

accretion onto a black hole simultaneously produces heavy r-process material via accretion disk winds and launches a collimated outflow, but does *not* require that a jet successfully break out of the progenitor star. The power law distribution yields adopted in Section 3.2 naturally includes less extreme explosions that produce smaller amounts of r-process material via disk outflows.

To reproduce the observed scatter in [Eu/Fe] abundances at low metallicity with a collapsar-like model, we require that the fraction of CCSN producing r-process material is between 10^{-4} and 10^{-1} with a fiducial value of 10^{-3}. We now compare these values to the observed rates for various classes of transients that have previously been proposed to be powered by collapsars or jet-driven explosions.

We begin with long-duration γ-ray bursts (LGRBs). Current measurements of the local (z=0) rate for LGRBs beamed towards Earth from the *Swift* satellite range from $1.3^{+0.6}_{-0.7}$ Gpc^{-3} yr^{-1} for L>10^{50} ergs [Wanderman and Piran, 2010] to $0.42^{+0.9}_{-0.4}$ Gpc^{-3} yr^{-1} accounting for complex *Swift* trigger criteria [Lien et al., 2014]. Correcting these

for a canonical beaming factor of 50 [Guetta et al., 2005], results in inferred intrinsic rates of $65^{+0.30}_{-0.35}$ Gpc^{-3} yr^{-1} and $21^{+4.5}_{-2}$ Gpc^{-3} yr^{-1}, respectively. Comparing these to the local CCSN rate from the Lick Observatory SN Search (LOSS) of 0.705 ($\pm$0.089) $\times 10^{-4}$ Mpc^{-3} yr^{-1} [Li et al., 2011a] yields $\mathrm{R_{LGRB}/R_{CCSN}}$ values of $(2-9)\times 10^{-4}$. This range of values is only slightly lower than our fiducial value of f_r. LGRBs could thus be linked to r-process production. Our uncertainty on f_r errs toward a higher value for the r-process fraction, though, so f_r could very well be larger than f_{LGRB}. In that case, we would require that massive stars beyond those that launch successful GRBs form accretion disks with physical conditions capable of producing heavy r-process material.

In particular, Type Ic-BL supernovae are a class of hydrogen-poor SN that display high ejecta velocities (hence "broad-lined") and kinetic energies ($\sim 10^{52}$ ergs) for which central engines are commonly evoked. While the nature of the central engine is still debated [Thompson et al., 2004, MacFadyen and Woosley, 1999, Barnes et al., 2018], the fact that all SN observed in association with LGRBs have been Type Ic-BL supernovae has lead to the hypothesis that all events of this class are powered by jets. Differences in the detailed manifestation of these explosions (LGRBs, low-luminosity GRBs, relativistic SN, or "ordinary" Ic-BL SN) would then be driven by a distribution of engine timescales or progenitor radii [e.g. Lazzati et al., 2012, Margutti et al., 2014]. We therefore compare our constraints on f_r to the rates of Type Ic-BL SN to investigate if they are consistent with all Type Ic-BL SN harboring collapsar engines.

Based on the full LOSS sample, Shivvers et al. [2017] find that Type Ic-BL SN account for a fraction of $(1.1 \pm 0.8) \times 10^{-2}$ of CCSN. However, the LOSS sample was a targeted survey, biased towards high metallicity galaxies and it is well established that Type Ic-BL SN show a preference for low metallicity environments [e.g. Modjaz et al., 2020]. It is therefore possible that Type Ic-BL SN represent a higher fraction of all CCSN at low metallicity, which is what our parameter f_r actually constrains. Unfortunately, to date, there has been no untargeted, volume-limited study that examines the fraction of CCSN that are Type Ic-BL at low-metallicity. Graur et al. [2017b] and Arcavi et al. [2010] examine relative rates of different core collapse SN

subtype in "high" and "low" mass galaxies for the LOSS and early PTF samples, respectively. Graur et al. [2017b] find no significant difference in the Type Ic-BL fraction (1-2%), while Arcavi et al. [2010] find that Type Ic-BL may make up a significantly higher fraction of all SN ($\sim 10 - 13\%$) in low luminosity galaxies. We caution, however, that both samples contain only 2-3 Type Ic-BL events and are therefore dominated by low number statistics. More recently, Schulze et al. [2020] investigate the host galaxies of the full sample of 888 SN identified by PTF, including 36 Type Ic-BL. They find that Type Ic-BL production is significantly stifled above a galaxy mass of $\log M/M_\odot = 10$, with Type Ic-BL comprising $\gtrsim 5\%$ of their observed CCSN sample below this threshold compared to $\lesssim 2\%$ above.

R_{Ic-BL}/R_{CCSN} values of 0.01–0.1 fall within the range of f_r found by our model (see Figure 3-7). However, the latter is at the extreme high end, implying that while our model is consistent with all Type Ic-BL SNe producing europium, it favors a scenario in which $\lesssim$10% do. We note that this would not preclude the possibility that all Type Ic-BL SNe harbor jets, but rather require that some lack the accretion disk properties necessary for the production of *heavy* r-process material. This could imply that a subset of Type Ic-BL SNe (a) harbor accreting black holes, but do not reach sufficiently high accretion rates ($> 10^{-3}$ $M_\odot$ s^{-1}) to proceed past ^{56}Ni-rich outflows [Siegel et al., 2019], or (b) harbor magnetar central engines for which neutrino irradiation can limit neucleosynthesis from disk ejecta to the light r-process [e.g. Margalit and Metzger, 2017, Radice et al., 2018].

For comparison, we also calculate a rough effective rate of neutron star mergers per CCSN. The cosmic NSM rate from the second LIGO-Virgo gravitational wave transient catalog is 320^{+490}_{-240} Gpc^{-3} yr^{-1} [The LIGO Scientific Collaboration et al., 2020]. When comparing this to the LOSS rate of galactic CCSN, the estimated NSM fraction is $4.5^{+7.0}_{-3.4} \times 10^{-3}$. This is higher than our fiducial value of f_r, but within model uncertainties. The LIGO rate of NSMs could thus potentially account for the rate of r-process events required by our model to explain metal-poor star abundances, though it is not favored by our fiducial results. We also note that the rate of NSMs in the early universe likely differs from the rate found by LIGO, and that NSMs would

need to be fast-merging to be described by our model.

3.5.2 Implications of $\langle M_r \rangle$: The Amount of r-Process Yield Produced per Collapsar

Our determination of the minimum and average amounts of r-process yield produced per collapsar ($M_{r,\mathrm{min}} \approx 0.03 M_\odot$ and $\langle M_r \rangle \approx 0.07 M_\odot$, respectively) is based entirely on our analysis of RPA stellar abundance data, independent of any previous estimates in literature of the amount of r-process material that might be produced by such events. To place our results in context, we compare them to several reference estimates of r-process yields from single events (see Figure 3-7). Note again that we define r-process yield as the yield of nuclei with mass number A $\geq$ 70.

Siegel et al. [2019] demonstrated that accretion disk outflows in collapsars could produce significant amounts of r-process material. For different presupernova models, they found the amount of europium varied from $6.0 \times 10^{-6}\, M_\odot$ to $5.8 \times 10^{-4}\, M_\odot$, or $M_r = 0.006$ to $0.579\, M_\odot$ (for our definition M_r). Their fiducial model corresponds to $M_r = 0.27 M_\odot$. Their fiducial yield is about four times larger than our fiducial average yield, but our $M_{r,\mathrm{min}}$ and $\langle M_r \rangle$ values fall within their range of yields. In Figure 3-7, the shaded region correspond to the spread of r-process yields found by the Siegel et al. [2019] simulations.

Furthermore, if we assume that the isotropic energy of a γ-ray burst roughly traces the amount of r-process yield, we can compare the energies of LGRBs to that of GW170817 to estimate the M_r from collapsars in which the associated jet successfully breaks out of the progenitor star. This assumption predicates on the ideas that (1) the same physical processes act in both short and long GRBs and (2) the accretion phase during which europium is produced roughly coincides with the phase during which the GRB occurs in the source frame, matching assumptions of Siegel et al. [2019]. Côté et al. [2018b] infer that $\sim 3 - 15 \times 10^{-6} M_\odot$ of europium was ejected from the post-merger accretion disk of GW170817. This translates to $\sim 0.01 M_\odot$ of heavy r-process material for a europium mass fraction of $X_{\mathrm{Eu}} = 10^{-3}$.

The istropic γ-ray energy of GW170817 was $E_{\gamma,iso,GW170817} = 2.1^{+6.4}_{-1.5} \times 10^{52}$ ergs [Hajela et al., 2019], and from a sample of 468 LGRBs, the mean istropic energy of LGRBs is $E_{\gamma,iso,LGRBs} \approx 2.6^{+2.7}_{-0.5} \times 10^{53}$ ergs [Wang et al., 2020]. With these values:

$$M_{r,collapsar} \sim M_{r,GW170817} \frac{E_{\gamma,iso,LGRBs}}{E_{\gamma,iso,GW170817}} \sim 0.1 M_{\odot}$$

(see also Siegel 2020). This aligns with our fiducial value of $\langle M_r \rangle$. In particular, our fiducial results lie near the intersection of the r-process yield expected per LGRB and the fraction of LGRBs per CCSN (see Figure 3-7). This supports the possibility that LGRBs are linked to r-process production.

For the final reference mass, we compare to the amount of r-process yield that was produced in the r-process event that enriched the ultra-faint dwarf galaxy Reticulum II [Ji et al., 2016b]. This galaxy preserves r-process enrichment from a single prolific event in the early universe. To explain the europium abundances of its stars, it likely experienced an event with a europium yield of $10^{-4.3}$ to $10^{-4.6} M_{\odot}$ [Ji et al., 2016b]. With $X_{\rm Eu} = 10^{-3}$, this corresponds to $M_r \sim 0.04 M_{\odot}$. Our $\langle M_r \rangle$ value is only slightly higher than this mass. This yield is also consistent with that expected for neutron star mergers [e.g., the yield estimated from GW170817, Siegel, 2019, Côté et al., 2018b].

3.5.3 Implications of α: Learning About Collapsar Properties from r-Process Abundance Scatter

Unfortunately, the current precision on the shape of the [Eu/Fe] distribution does not provide tight constraints on α, the exponent of our r-process yield power law distribution. For $\langle N_r \rangle = 3$, any $\alpha = 2.2 - 6.0$ can explain the observed scatter. Our fiducial value of $\alpha = 2.8$ best fits the data, but the full range of possible values produces similar distribution widths (see Figure 3-4b).

The α constraints from metal-poor stars can be compared to power law distributions of long γ-ray burst (LGRB) engine duration, engine luminosity, and isotropic energy. Figure 3-7 shows our constraints on α in context with the exponents from these distributions.

Petropoulou et al. [2017] modeled the central engines which power LGRBs, determining power law distributions for both the engine luminosities and engine activity times: $p(L_{engine}) \propto L^{-\alpha_L}$ and $p(t_{engine}) \propto t^{-\alpha_t}$. By assuming that more powerful engines can more quickly break out of the collapsing star to produce γ-ray signals (with a breakout time that scales with jet luminosity as $L^{-\chi}$), they show that the shape of the γ-ray duration distribution can be uniquely determined by the observed GRB luminosity function. In particular, they determine the power law indexes of the L_{engine} and t_{engine} distributions by connecting them with the observed distributions of luminosities and durations of LGRBs. For $\chi = 1/3$, Petropoulou et al. [2017] find $\alpha_L = 2.4$ and $\alpha_t = 3.5$, while for $\chi = 1/2$, they constrain $\alpha_L = 2.4$ and $\alpha_t = 4.6$. In addition, by assuming a single breakout time, Sobacchi et al. [2017] find a power law distribution for t_{engine} consistent with $\alpha_t \sim 4$.

Furthermore, we can determine the isotropic energy distribution of LGRBs since $E \propto L \times t$. Because both L_{engine} and t_{engine} draw from power law distributions, the distribution of their product follows the distribution of the variable with a smaller α, in this case $\alpha_L = 2.4$.

Our α constraint overlaps with all of these values, with the fiducial value falling closer to L_{engine} or E_{iso}. Any of these properties could therefore potentially trace the r-process yield. For a better constraint on α, we need a significantly lower uncertainty on the observed $\mathrm{IQR_{Eu}}$. Figure 3-8 shows how tightly $\mathrm{IQR_{Eu}}$ must be measured for the stellar samples to improve the α constraint. This plot was constructed assuming the $\mathrm{IQR_{Eu}}$ is centered on $\mathrm{IQR_{Eu}} = 0.50$, as found for the RPA sample. To differentiate between the distributions for t_{engine} and L_{engine} or E_{iso}, the $\mathrm{IQR_{Eu}}$ must be measured with uncertainty < 0.05 dex. This abundance precision is better than what current measurements can achieve in metal-poor stars, though it may become achievable in the future as stellar spectroscopy methods improve.

The $\mathrm{IQR_{Eu}}$ is a robust but very inefficient estimator of the distribution shape. Alternatively, we could use the full distribution shape. This requires a reliable selection function, but would likely not demand 0.05 dex precision.

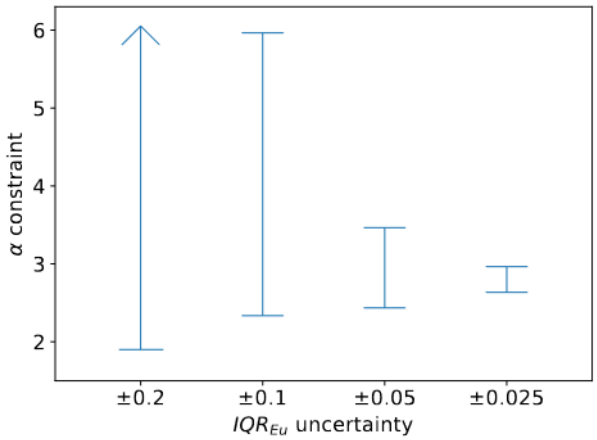

Figure 3-8: To improve our constraint on α, we must improve our measurement of the stellar $\mathrm{IQR_{Eu}}$ for metal-poor stars. Here we show how the α constraint is improved for several different $\mathrm{IQR_{Eu}}$ uncertainties.

3.5.4 Neutron Star Mergers vs. Collapsars

Here we focused on collapsars, demonstrating that a r-process production site with a power law distribution inspired by LGRB jet properties can self-consistently reproduce the abundances and scatter observed in metal-poor stars. These results would also apply to another prompt r-process site ejecting a Solar r-process abundance pattern that scales with a power law, however.

The possibility that collapsars produce r-process material is debated. For example, earlier semi-analytic work on collapsar disk winds by Surman et al. [2006] found that collapsar outflows are too neutron-poor to produce heavy r-process isotopes. A recent study by Miller et al. [2019] that investigated the Siegel et al. [2019] results with more detailed modeling of neutrino transport also found that collapsar outflows are incapable of producing third peak r-process material. Furthermore, Macias and Ramirez-Ruiz [2019] found that any r-process site that also produces large amounts of iron is disfavored by observations of metal-poor stars. Collapsars that do not produce large amounts of iron (e.g., LGRBs without an associated supernovae; Fynbo et al. 2006) would avoid the dilution problems discussed by Macias & Ramirez-Ruiz, but the topic is unsettled.

Neutron star mergers are a demonstrated source of r-process material thanks to GW170817 and, in principle, their europium yields can vary as well with different neutron star binary masses, mass ratios [Korobkin et al., 2012, Bauswein et al., 2013, Hotokezaka et al., 2013, Dietrich et al., 2015, Sekiguchi et al., 2016], and eccentricities [Chaurasia et al., 2018, Papenfort et al., 2018]. Furthermore, the $M_{r,\mathrm{min}}$ and $\langle M_r \rangle$ values in our model are roughly consistent with the r-process yield estimated for GW170817 [Siegel, 2019, Côté et al., 2018b]. Because of this, variable-yield neutron star mergers could also potentially explain the r-process scatter in metal-poor stars via a similar model to that presented in this paper. More work is needed to determine a reasonable distribution of r-process effective yields from neutron star mergers, combining input distributions of binary neutron star properties and yields (e.g., those from the numerical simulations cited above) and kick velocities [e.g., Tarumi et al., 2020, Safarzadeh et al., 2019a, Bonetti et al., 2019].

3.5.5 Limitations of Initial Model

Our initial model is purposefully simple in order to act as a focused exploration of variable-yield collapsars. In particular, the model assumes all abundance scatter is due to variable stellar populations. This assumption allows us to expressly investigate variable yields as a source of scatter, but it does not consider possible effects due to differences in galaxy formation. Real dwarf galaxies have differences in their hierarchical assembly, small amounts of cross-pollution, and experience inhomogeneous mixing [e.g., Venn et al., 2004, Ji et al., 2015b, Griffen et al., 2018]. Abundance scatter is likely affected by these complexities. Inhomogeneous enrichment has been included in some previous models [e.g., Cescutti et al., 2015, Wehmeyer et al., 2015], but it is not a solved problem. In this very metal-poor regime, theoretical work has not yet given a simple way to model the amount of scatter from galaxy formation effects.

This model also assumes that each star probes an independent gas reservoir. For every star in our model, we assume that it originates from a different dwarf galaxy in which a number of SN exploded over some time, the metals fell back down into

the galaxy and fully mixed, and then our model star formed from the mixed gas. This approximates the average star that formed in a given gas reservoir. Real stellar samples likely contain stars that originated together, though. Observational work that studies the accretion origin of stars through, for example, analysis of stellar streams and kinematic clustering will inform the quality of this assumption in the future.

To transcend the limitations of this initial model, future models will consider scatter due to differences in galaxy formation and include a more detailed treatment of chemical enrichment and star formation. We are currently developing high-resolution hydrodynamic simulations of dwarf galaxy evolution that will study these effects and further explore the origins of r-process material.

3.6 Conclusions

We have produced a self-consistent model in which collapsars synthesize all of the r-process material in the early universe. By assuming the r-process material in metal-poor ([Fe/H] < -2.5) stars was formed exclusively in collapsars with stochastic yields, we can reproduce the observed distribution of europium abundances with parameter values that are consistent with other independently determined reference values. This was not guaranteed a priori.

This is not evidence that collapsars dominantly produce r-process material in the early universe, however. Neutron star mergers with variable effective europium yields may also be able to explain the r-process scatter. More work is needed on the effective europium yields of neutron star mergers. In particular, the retention fraction is important for the collapsar model, but it becomes even more important for neutron star mergers with different natal kick velocities and coalescence times.

Abundance scatter of metal-poor stars is an important window into the different mechanisms producing r-process elements. Individual mechanisms can produce scatter without the need for multiple sources. In this paper, we assume a power law distribution of collapsar r-process yields. The range of constrained values for the

exponent α is comparable to those of the distributions for long γ-ray burst isotropic energies, engine luminosities, and engine times (Section 3.5.3). Improved constraints on α could allow us to investigate which, if any, of these collapsar properties trace r-process yield.

Lastly, in our model, the fraction of core-collapse supernovae that result in r-process collapsars, f_r, is comparable to the fraction of core-collapse supernovae that result in long γ-ray bursts. This could indicate a link between LGRBs and r-process. The uncertainty in our model errs to higher f_r, though, and if f_r is higher then we would require a significant number of r-process collapsars that do not produce long γ-ray bursts. Our model also favors a scenario in which $\lesssim 10\%$ of Type Ic-BL supernovae produce europium. This does not preclude all Ic-BL SNe from harboring choked jets, but would imply that some Ic-BL SNe lack the accretion disk properties to synthesize heavy r-process isotopes.

3.7 Appendix: Average Iron Yield from Core-collapse Supernovae

To estimate an average iron yield from core-collapse supernovae (CCSN), we calculate a weighted average between observations of H-rich CCSN and H-poor CCSN. The majority of the iron comes from the Ni-56 $\rightarrow$ Co-56 $\rightarrow$ Fe-56 decay chain, so we adopt mean Ni-56 yields for both Type II SN and Type IIb/Ib/Ic SN as measured from modeling their bolometric light curves, and account for the relative rate between these two broad classes. The mean Ni-56 yield from H-rich CCSN is $0.044 \pm 0.044 M_{\odot}$ [Anderson, 2019]. The mean Ni-56 yield from Type II CCSN is $0.12 \pm 0.12 M_{\odot}$ [Afsariardchi et al., 2020]. For the relative rates of stripped envelope to Type II CCSN, we adopt the results of the Lick Observatory SN Search (LOSS; Li et al. 2011b). While LOSS was a targeted survey, it remains the most complete volume-limited supernova search completed to date. We consider two cases: (1) Based on the entire LOSS sample, Shivvers et al. [2017] find the relative fractions of Type II and stripped envelope

SN of $69.6^{+6.7}_{-6.7}\%$ and $30.4^{+5.0}_{-4.9}\%$, respectively. This implies an average iron yield of $0.067M_{\odot}$. (2) However, the ratio of Type II to stripped envelope SN is metallicity dependent. Graur et al. [2017a] examined the relative rates the LOSS sample as a function of host galaxy mass and metallicity. In their lowest metallicity bin, the ratio of SESN and Type II SN specific rates is $R_{SE}/R_{II} = 0.13^{+0.09}_{-0.08}$, a factor of three lower than the overall LOSS sample above. Adopting this value, and making the (rather large) assumption that the the average nickel yield of each class is not a function of metallicity, we find an average CCSN iron yield of $0.053M_{\odot}$. In both (1) and (2), the average yield is slightly below the order of $y_{\rm Fe} \approx 0.1M_{\odot}$, with the uncertainty of $f_{retained}$ and M_{gas} far outweighing that of $y_{\rm Fe}$.

Chapter 4

Possibilities and Limitations of Kinematically Identifying Stars from Accreted Ultra-Faint Dwarf Galaxies

This chapter is based on work previously published in *The Astrophysical Journal* (Brauer et. al 2022).

4.1 Introduction

Throughout its formation history over billions of years, the Milky Way grew through mergers with many dwarf galaxies. The smallest and oldest of these accreted systems are the ultra-faint dwarf galaxies (UFDs), which were among the first galaxies in the Universe [Frebel, 2010, Simon, 2019]. These systems provide insight into the earliest stages of galaxy formation and are important components of the assembly history of the Milky Way.

Due to low star formation efficiency and quenching from reionization, UFDs preserve information about early chemical enrichment and can display clean signatures of important nucleosynthetic processes such as the rapid neutron-capture process (the r-process, which produces around half of the isotopes of the heaviest chemical elements; see Burbidge et al. [1957], Cameron [1957], Frebel [2018], Cowan et al. [2021]).

For example, the surviving UFD Reticulum II contains highly r-process enhanced stars, implying it was enriched by a prolific early r-process event such as a neutron star merger [Ji et al., 2016a,b, Roederer et al., 2016a]. Tucana III and Grus II also exhibit r-process enhancement [Hansen et al., 2017, 2020]. Satellite galaxies like these are located over 25 kpc away from the Sun [Drlica-Wagner et al., 2015], however, so studying their stars to learn about early chemical enrichment can be difficult.

Because the Milky Way was assembled hierarchically from many neighboring systems including UFDs, bona-fide dwarf galaxy stars can also be found located throughout our galaxy today, including near the Sun. Chemical tagging, i.e. using stellar chemical abundances to identify stars that formed together, is a promising way to identify dispersed UFD stars. Utilizing the Caterpillar simulation suite [Griffen et al., 2016] and a simple model for star formation and parametrized element enrichment, Brauer et al. [2019] suggested that the population of galactic metal-poor r-process enhanced halo stars could have largely originated in UFDs. This idea stems from both observations of surviving UFDs such as Reticulum II, and kinematic studies of r-process stars [Roederer et al., 2018, Gudin et al., 2021] that appear to be chemically and dynamically linked. Further evidence in support of chemically tagging r-process enhanced halo stars remains limited due to small sample size of known stars, but the R-Process Alliance [Hansen et al., 2018, Sakari et al., 2018, Ezzeddine et al., 2020a, Holmbeck et al., 2020a] is continuing to discover more of these stars which should soon provide a rich sample for study. Low-mass galaxies, especially UFDs, also host a higher percentage of metal-poor stars compared to higher-mass galaxies [e.g., Kirby et al., 2013a]. Chemical tagging with r-process elements and/or low-metallicity stars may thus help astronomers identify stars from UFDs.

Alongside chemical tagging, stellar dynamics also retain important information about the disrupted galaxies accreted by the Milky Way. In particular, the orbital actions and energy of a star are quasi-conserved quantities which can, in principle, be used to identify stars that were accreted together (see Section 4.2.3). While these quantities are not truly conserved in the galaxy on long timescales, clustering in $E - L_z - J_r - J_z$ phase space (or a subset of this space) is a common, useful method

to search for accreted structure. Thanks to the *Gaia* mission, detailed 6D phase space information is now available for millions of stars [Gaia Collaboration et al., 2018]. This influx of data has already lead to a better understanding of the major mergers that the Milky Way experienced (e.g., the *Gaia* Sausage, Belokurov et al. 2018, Helmi et al. 2018, Sequoia, Myeong et al. 2019, Kraken, Kruijssen et al. 2019, 2020, Forbes 2020, and more, Naidu et al. 2020, Mardini et al. 2022). However, the low-mass galaxy mergers are far less understood because far fewer stars are contributed to the galaxy from each accreted UFD, rendering the associated dynamic signatures less pronounced and more difficult to isolate.

Currently, several groups are using kinematics to identify groups of stars that may have originated in UFDs. Roederer et al. [2018] explored the possibility of identifying groups of stars that possibly originated together in UFDs by clustering stars with r-process enhancement ("r-process stars") in dynamic phase space. Gudin et al. [2021] expanded on this idea with a much larger data set of 446 stars. Both papers found multiple dynamically linked groups of stars, suggesting that these groups may represent dissolved UFD remnants and that dynamic clustering is indeed a promising method to identify groups of stars from tidally disrupted UFDs. Similarly, Limberg et al. [2021] and Yuan et al. [2020] used clustering algorithms to identify dynamically linked groups among very metal-poor ([Fe/H] < -2) stars, several of which have similar dynamics to r-process enhanced stars.

This area of research is continuously expanding as more groups explore clustering with stellar dynamics – both with and without chemical tagging – as a means to identify possible groups of accreted stars from dwarf galaxies. And as astronomers continue to gather kinematics for millions of stars in our Galaxy, the search for these dwarf galaxy remnants is a difficult but worthwhile endeavor. It is unclear, however, to what degree we can trust the clusters identified by different clustering algorithms, and which clusters are most likely to correspond to real UFD remnants.

In this paper, we explore the possibilities and challenges of kinematically identifying stars from tidally disrupted UFDs in the Milky Way by analyzing a set of 32 cosmological zoom simulations of Milky Way-mass galaxies. Using the *Caterpillar*

simulation suite [Griffen et al., 2016], we trace tagged particles from accreted UFDs to $z = 0$ and test different clustering algorithms in dynamic phase space. Specifically, we explore what fraction of remnant UFDs can be expected to be recovered using basic clustering algorithms, which clustering algorithms work best and most reliably, and which identified dynamically linked groups are most likely to correspond to real UFD remnants. In this work, we focus exclusively on UFDs because prior work has investigated more massive accretion events [e.g., Wu et al., 2022], but UFDs remain poorly understood. While most cosmological simulations do not properly resolve UFDs, the *Caterpillar* simulation suite provides us the unique ability to investigate many different Milky Way-mass galaxies forming in a cosmological context while resolving UFDs.

Section 4.2 describes how we created simulated stellar halos from dark matter cosmological simulations, focusing on the methodology of tagging dark matter particles as tracers of stellar material and measuring the corresponding dynamics at $z = 0$. Section 4.3 describes seven different clustering algorithms and how we test them on different data sets. Section 4.4 discusses our clustering results and their implications for kinematically identifying UFD remnants in real data sets. Section 4.5 discusses the properties of real clusters and how to identify which clusters are most likely to correspond to real accreted UFD remnants. Section 4.6 summarizes the takewaways for clustering observational data sets to best identify stars from accreted UFDs.

4.2 Simulated Stellar Halos

4.2.1 Cosmological Simulations

We simulate stellar halos using 32 dark-matter-only cosmological simulations from the *Caterpillar Project* [Griffen et al., 2016]. Each zoom-in simulation models the formation of a Milky Way-mass dark matter halo down to $z = 0$. The effective resolution is $16,384^3$ particles of mass $3 \times 10^4\ M_\odot$ in and around the galaxies of interest, resolving subhalos down to total mass $\sim 10^6\ M_\odot$. We limit our analysis to

simulated Milky Way-mass halos that experienced no recent major merger; all other aspects of the accretion history are unbiased.

The simulations are fully described in Griffen et al. [2016]. The halos in the zoom-in simulations were selected from a larger, lower resolution parent simulation with cosmological parameters from Planck 2013 ΛCDM cosmology: $\Omega_m = 0.32$, $\Omega_\Lambda = 0.68$, $\Omega_b = 0.05$, $\sigma_8 = 0.83$, $n_s = 0.96$, and H = 100 h km s^{-1} Mpc^{-1} = 67.11 km s^{-1} Mpc^{-1} [Planck Collaboration et al., 2014]. Initial conditions were constructed using `MUSIC` [Hahn and Abel, 2011]. Dark matter subhalos were identified using a modified version of `ROCKSTAR` [Behroozi et al., 2013b, Griffen et al., 2016] and merger trees were constructed by `CONSISTENT-TREES` [Behroozi et al., 2013c]. The halos were assigned a virial mass M_{vir} and radius R_{vir} using the evolution of the virial relation from Bryan and Norman [1998]. For our cosmology, this corresponds to an overdensity of $\Delta_{crit} = 104$ at $z = 0$.

4.2.2 Dark Matter Particles as Tracers of Stellar Material

Since the *Caterpillar* simulations do not directly simulate stars, we tag dark matter (DM) particles as tracers of the stellar material of each accreted galaxy. Stars form tightly bound to their halos and move within the same potential as the dark matter, so a fraction of the most bound DM particles are expected to trace the phase-space distribution of the stars [e.g., Bullock and Johnston, 2005, Cooper et al., 2010]. We refer to the tagged particles as "star particles" and trace their phase-space distribution down to $z = 0$.

There is debate over what fraction of DM particles should be tagged as tracers. The fraction generally ranges from the most bound 1-3% [Cooper et al., 2010, Rashkov et al., 2012, Bailin et al., 2014], to 5% [Le Bret et al., 2017, Cooper et al., 2017, Dooley et al., 2016], to 10% [De Lucia and Helmi, 2008, Morinaga et al., 2019, Tumlinson, 2010, Gómez et al., 2012]. Cooper et al. [2017] finds that a fractions of 1-10% all provide a good approximation to accreted halos of Milky Way analogs, implying that results for accreted galaxies are holistically insensitive to the exact fraction. Our analysis in this paper focuses on ultra-faint dwarf galaxies ($M_{halo} \leq 10^9 M_\odot$), so to

ensure a sufficient number of particles to assess clustering, we tag the 5% most bound particles. At this resolution, each tagged particle in an accreted ultra-faint dwarf galaxy corresponds to $\sim 10 M_{\odot}$ of stellar material. We note that having a single, fixed fraction is a simplifying assumption that breaks down in regions dominated by the baryonic potential and having significant angular momentum, such as the Milky Way disk [Cooper et al., 2017]. However, given that we focus on dwarf galaxies in our analysis which are dark-matter dominated and elliptical, assuming a fixed fraction is not a principal concern.

We tag the 5% most bound DM particles at the snapshot where the accreted halo reaches its peak mass. Alternative methods include tagging the particles at the snapshot before the halo is accreted or "live" tagging where stellar mass is added at each snapshot while the galaxy is star-forming. Our analysis focuses on small galaxies that are generally no longer forming stars at the time of their accretion, so we choose the peak mass as the snapshot at which to tag DM particles. We use a $M_{star} \sim M_{peak}$ relation to estimate the amount of stellar material represented by each tagged particle [Garrison-Kimmel et al., 2017b]. We note for completeness that live tagging would likely produce a more accurate phase space distribution but the significantly increased computational expense is beyond the scope of this work.

While particle tagging is an imperfect method, it has repeatedly been shown to qualitatively capture trends and produce accreted stellar populations with properties (e.g., metallicities, spatial distribution, velocity dispersions) in agreement with observations around the Milky Way [e.g., Cooper et al., 2017, Rashkov et al., 2012]. Given that this study is concerned with the qualitative situations in which kinematic clustering of accreted stars does or does not excel, particle tagging of dark-matter cosmological simulations is an ideal technique as a means to explore such clustering effects in our set of many different Milky Way-mass simulations. Moreover, a simulation with a disk would result in enhanced tidal disruption and phase space diffusion [Errani et al., 2017, Maffione et al., 2018], but because our results highlight the difficulty of identifying UFD remnants via clustering, our point is merely strengthened by our use of N-body simulations without an added disk potential.

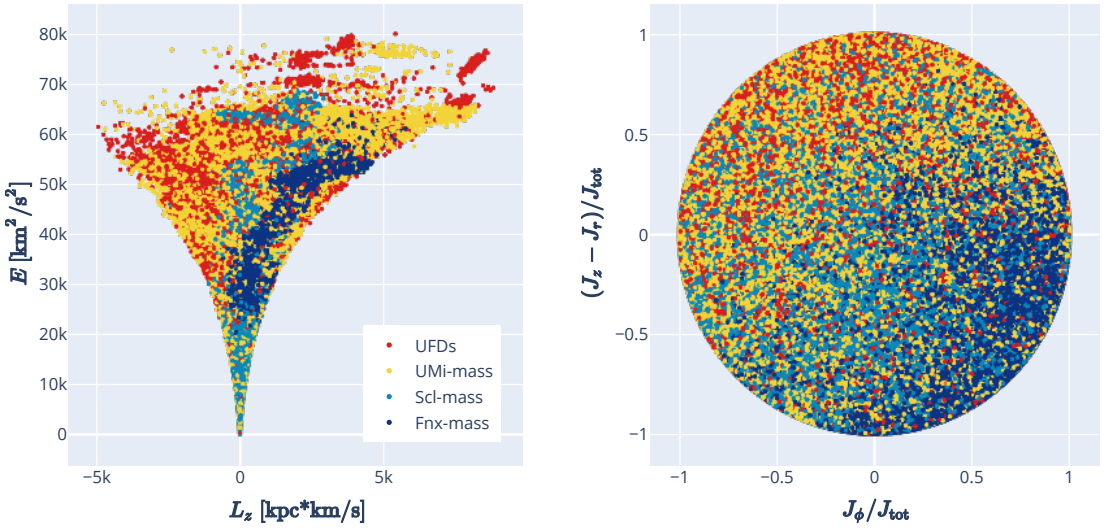

Figure 4-1: Left: $z = 0$ dynamics (energy and z-angular momentum) of all accreted star particles within 50 kpc of the Sun in simulation Cat-14, one of the 32 simulated Milky Way-mass galaxies. The color of each particle corresponds to the mass of the galaxy in which it formed. Star particles from the smallest galaxies, the UFDs, are seen in red. Right: J_r, J_z, and J_θ orbital actions summarized in an action circle for the same star particles.

4.2.3 Stellar Dynamics

We determine the dynamics of each accreted star particle (tagged DM particle) at $z = 0$. In axisymmetric galactic potentials, stellar orbits are described by three integrals of motion called the orbital actions: J_r, J_z, and J_ϕ [see Binney and Tremaine, 2008, §3.5]. Energy is another constant of motion for time-invariant potentials which, while not independent of the orbital actions, is useful during clustering searches. These four quantities are not conserved in realistic, time-varying galactic potentials, and the galactic potentials in the *Caterpillar* simulations, for example, are approximately constant for only the last 5 Gyr or so ($z \lesssim 0.5$) [Griffen et al., 2016]. Despite this, these quantities provide a useful phase space in which to search for dynamically-similar stars that is currently being used by several groups in the search for stars from UFDs. We thus explore the possibilities of using these dynamics. These integrals of motion are defined as [Binney, 2012]:

1. E: the specific orbital energy, the total orbital energy of the star divided by its

mass.

2. J_r: the orbital action that quantifies oscillations of an orbit along the radial direction. J_r is non-negative and increases for more eccentric orbits.

3. J_z: the orbital action that quantifies oscillations about the equatorial plane. J_z is non-negative and increases for orbits that rise more out of the equatorial plane.

4. J_ϕ: the azimuthal orbital action, equal to the angular momentum out of the equatorial plane ($J_\phi = L_z$).

To estimate orbital actions, one first needs an initial estimate of the gravitational potential. For each of our 32 simulations, we use the AGAMA software library [Vasiliev, 2019] to construct an estimated axisymmetric gravitational potential. The potential is built via multipole expansion in spherical harmonics with $l_{max} = 8$, using the locations and masses of all N-body particles at $z = 0$. We validate the estimated potential by comparing it to the value of the potential stored for each particle from the original *Caterpillar* simulation, confirming the same relative potential energy between particles. After constructing the axisymmetric potential, we use the galactocentric positions and velocities of each accreted star particle to compute the associated actions within AGAMA.

As an illustrative example, the $z = 0$ phase space distribution for the accreted star particles in one of our simulations can be seen in Figure 4-1. The particles in these plots are colored based on the peak mass of the galaxy in which each of them formed: UFD ($M_* \leq 10^5 M_\odot$), Ursa Minor-mass ($M_* = 10^5$ to $10^6 M_\odot$), Sculptor-mass ($M_* = 10^6$ to $10^7 M_\odot$), and Fornax-mass ($M_* = 10^7$ to $10^8 M_\odot$). Note that this example galaxy did not accrete more massive dwarfs such as those with masses similar to that of the Large Magellanic Cloud.

In Figure 4-1, the particles from UFDs are only 9% of all the accreted particles within this radial cut, but they are still identifiable in the outskirts of the phase space diagram because virtually all of the particles from more massive dwarfs are overlap

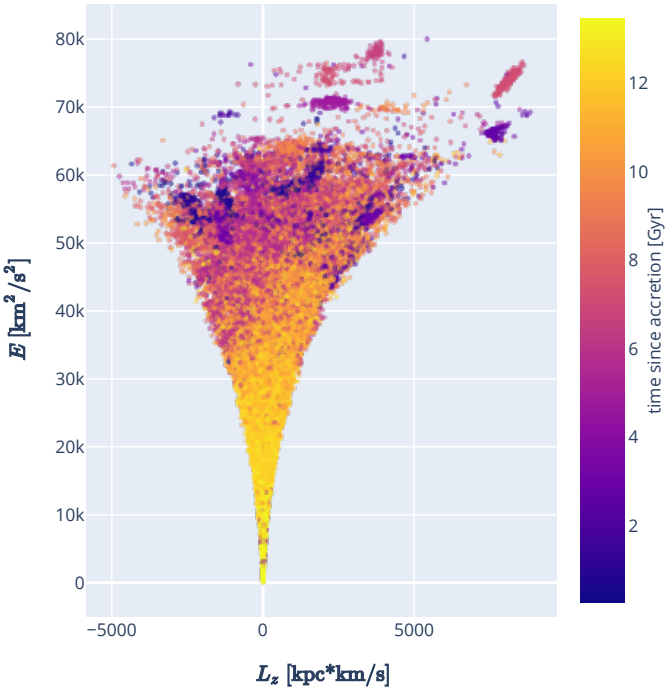

Figure 4-2: $z = 0$ dynamics of star particles that originated from UFDs in one of our simulations (with a 50 kpc radial cut; see Section 4.2.4). The color of each particle corresponds to how long ago it was accreted by the Milky Way-mass host galaxy. Stars that were accreted more recently are, generally, of higher energy and less phase mixed. Over time, the stars mix more in the phase space and are less identifiable by clustering algorithms.

significantly in phase space. This implies we may be able to more easily identify some UFD remnants at, for example, high energy.

Specifically considering the particles from UFDs, in Figure 4-2, we show that any identifiable remnants are from relatively recent accretion events, while the most phase-mixed particles are from accretion events that occurred over 8 Gyr ago. This is to be expected, since more recent accretion events will have maintained a stronger dynamic signature at $z = 0$ compared to stars that have been relaxing in the stellar halo for many gigayears [e.g., Gómez et al., 2010].

4.2.4 The Different Data Sets We Consider

We consider how well clustering works for data sets with three different radial cuts at varying distances from the Sun:

1. All accreted star particles, no radial cut. This is a complete data set which cannot be produced with real observations.

2. All accreted star particles within 50 kpc of the Sun. This is an idealistic data set that extends to roughly where the stellar halo drops off.

3. All accreted star particles within 5 kpc of the Sun. This is a more realistic data set that includes stars for which we can obtain decent parallax measurements from Gaia.

The location of the "Sun" in each simulation is a consistent, randomly chosen location in the equatorial plane 8 kpc from the galactic center.

We also consider data sets with:

1. Only accreted star particles from UFDs. This data set is idealistic. To pursue it observationally, one could focus on limiting to only stars with certain chemical signatures (e.g., low metallicity, r-process enhancement, deficiency in neutron-capture element abundances) and/or removing stars that are known to be associated with larger mergers.

2. All accreted star particles.

After matching each radial cut with UFD-only and all-stars data sets, we have a total of six data sets. Each data set includes stellar dynamics from 32 simulations (though not all simulations are used when performing clustering analysis of the larger radial cuts due to computational limitations). We then quantify how well each clustering algorithm performs in these six situations.

For the data set without a radial cut, Milky Way-mass galaxies accrete on average 187^{+69}_{-65} UFDs. This is $91^{+1}_{-1}\%$ of the total number of accreted systems that Milky Way-mass galaxies will ever accrete. Despite UFDs being the vast majority of

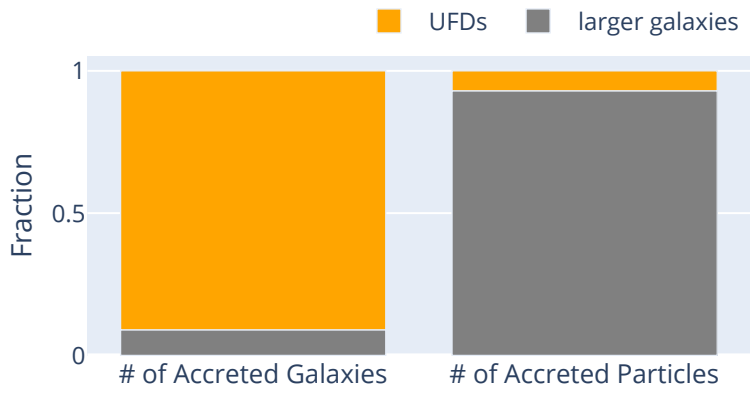

Figure 4-3: Across all 32 simulations, $\sim 91\%$ of the galaxies accreted by Milky Way-mass galaxies are ultra-faint dwarf galaxies. These small galaxies only contribute $\sim 7\%$ of the accreted star particles, however. These fractions are roughly constant with radial cut.

accreted galaxies, though, they only contribute $\sim 7\%$ of the accreted star particles. These fractions are shown in Figure 4-3. These results align with Monachesi et al. [2019], which estimated that the accreted stellar halo had only a handful of significant progenitors. For the data set with a 5 kpc radial cut, the total average number of accreted UFDs seen in the data set drops to 99^{+45}_{-30} but the percentage representation remains the same. We note here that all uncertainty values provided represent 16th – 84th percentile scatter across all the simulations.

4.3 Clustering Methodology

4.3.1 Clustering Algorithms

We apply seven different clustering algorithms on the four-dimensional energy-action space of each simulated Milky Way-like halo. The algorithms studied in this work are HDBSCAN [Campello et al., 2015, McInnes et al., 2017], Gaussian mixture models [GMM; Dempster et al., 1977], agglomerative clustering [Ward Jr, 1963], K-means [Lloyd, 1982, Vassilvitskii and Arthur, 2006], affinity propagation [Frey and Dueck, 2007], mean-shift [Comaniciu and Meer, 2002, Derpanis, 2005], and friends-of-friends [Huchra and Geller, 1982, Press and Davis, 1982, Davis et al., 1985, Gibbons, 2020].

Before running any clustering alogithms on our simulations, we normalize each of the 4D energy-action variables into the range [0, 1]. Here, we briefly comment on each of these algorithms.

HDBSCAN (Hierarchical DBSCAN) is a hierarchical extension of the density-based approach of DBSCAN. It measures the density around each point, constructs a hierarchical cluster tree based on this density information, and returns clusters that are persistent across different density thresholds. As a result, it is sensitive to datasets having true groups at varying densities. It also scales well for massive datasets. Hunt and Reffert [2021] found that, compared to DBSCAN and GMM, it performs best at recovering open clusters in a massive sample of Gaia data. This was also the preferred clustering algorithm of Gudin et al. [2021] and Limberg et al. [2021], two papers that identified dynamically linked groups that may correspond to UFDs.

Agglomerative clustering forms clusters from the bottom up. It starts with each particle as its own cluster. Clusters that are separated by the least linkage distance (in our case, Euclidean distance) are then hierarchically merged until the pre-set number of clusters is reached. Because it has a time complexity of $O(n^3)$ and requires $\Omega(n^2)$ of memory, it is too slow and memory-intensive for large datasets.

K-means is a distance-based algorithm that returns a pre-set number of k clusters, each of equal variance. Starting with k randomly generated initial means, it first assigns each particle to the mean with the least sum-of-squares distance. Particles associated with the same mean form a cluster. The mean (or centroid) of each cluster—and consequently, cluster membership—is then continually updated until convergence.

A Gaussian mixture model can be thought of as a generalization of K-means in that it returns distance-based clusters which may be at different variances. It decomposes the sample into a mixture of a pre-set number of n Gaussian distributions and upon convergence, returns the Gaussian components as separate clusters.

Unlike K-means, agglomerative clustering, and Gaussian mixture models, affinity propagation does not require a pre-set number of clusters before running. Its goal is to find "exemplars" or prototype particles that are representative of a cluster. First,

each particle begins as a potential exemplar. Pairs of particles then pass "messages" to each other about suitability of one particle to be the exemplar of the other. These messages are passed until a stable set of exemplars and, thus, clusters emerge.

Mean-shift is a centroid-based algorithm that treats each particle as a kernel with a pre-set bandwidth. It then performs a gradient ascent on the kernel peaks until convergence. Gómez et al. [2010] used mean-shift on the $E - L - L_z$ space of a mock Gaia catalogue of the solar neighborhood and recovered roughly 50% of all satellite galaxies. We note that this differs from our results because this work focused on a smaller quantity of larger-mass satellites as compared to our UFD-focused analysis.

Friends-of-friends (FoF) is commonly used to identify gravitationally bound halos in cosmological simulations. Particles that are separated by a distance less than a pre-set linking length are linked as "friends," forming a networked cluster of particles. Networks that have no mutual friends are designated as separate clusters. Helmi and Tim de Zeeuw [2000] applied this algorithm on the $E - L - L_z$ space of a mock Gaia catalog to identify simulated Milky Way accretion events.

Other groups have used custom clustering algorithms, e.g. StarGo [Yuan et al., 2018, 2020], Enlink [Sharma and Johnston, 2009, Wu et al., 2022], and other hierarchical clustering techniques [Sofie Lövdal et al., 2022, Ruiz-Lara et al., 2022]. We do not test all of these algorithms, but expect our UFD-focused results to holistically hold for them as well (see Section 4.4.5).

4.3.2 Hyperparameter Choices

All the algorithms included in this paper except affinity propagation require a pre-selected hyperparameter in order to begin clustering. To explore different hyperparameter choices, for each algorithm we:

1. Create a hyperparameter search space consisting of about 20 trial values. For instance, to select the `min_cluster_size` hyperparameter for HDBSCAN, we create a search space composed of integers from 3 to 20 inclusive, and for FoF we explore from 0.001 to 0.2.

2. Run the clustering algorithm with each trial hyperparameter on each simulation in each data set.

3. For every clustering run, count the number of pure and complete clusters. A cluster is "pure" if $\geq \frac{2}{3}$ of the stars in that cluster accreted together from a UFD. A cluster is also "complete" if $\geq \frac{1}{2}$ of the stars from that accreted UFD are found together in that cluster.

4. For every simulation on which a particular hyperparameter is tested, calculate a recovery rate and a realness rate. The recovery rate is defined as:

$$\frac{\text{number of pure and complete clusters}}{\text{number of accreted UFDs in the data set}} \times 100\%$$

   Meanwhile, the realness rate is defined as:

$$\frac{\text{number of pure clusters}}{\text{number of clusters found by the algorithm}} \times 100\%$$

   When calculating these rates, we only consider clusters and remnants with at least 5 particles.

5. For each data set, determine the optimal hyperparameter by assigning a score to each hyperparameter choice. To assign the score, normalize all of the recovery rates and realness rates using a min max scaler, and then add the normalized median recovery and realness rates together. The optimal hyperparameter thus balances the highest UFD recovery rate and the highest realness of its clusters.

We choose an optimal hyperparameter value for each algorithm on each data set. Since we are testing six algorithms that each require hyperparameters on six different data sets, we make a total of 36 optimized hyperparameter selections. A summary of the optimal hyperparameter choices are in the Appendix.

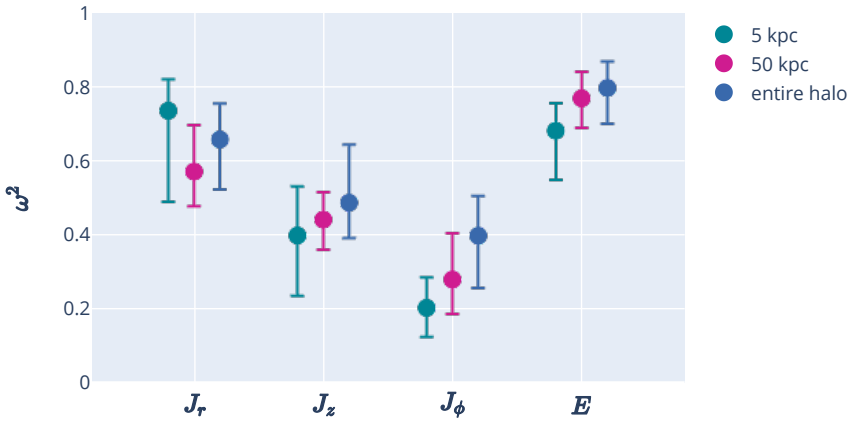

Figure 4-4: Strength of association between actions (J_r, J_z, J_ϕ, E) and the true cluster labels. Higher ω^2 values indicate a stronger association. E has the highest ω^2 values, implying it is the most important variable when seeking to find clustered stars that accreted together. Note that J_ϕ here is equivalent to L_z.

4.3.3 Association of Different Observables with the True Cluster Labels

To help identify which observable variables are most likely to be important during clustering, we perform one-way analysis of variance (ANOVA) tests on the stellar kinematics of each simulation. The ANOVA test assesses the association between a categorical (e.g., the label of each true cluster) and a continuous variable (e.g., each of the kinematic variables) [e.g., McDonald, 2014, Gómez et al., 2014]. If a given kinematic variable is strongly associated with the true cluster labels, it is likely to be important during clustering in situations where we do not know the true labels.

We use the `stats.f_oneway` ANOVA test from the `scipy` python package [Virtanen et al., 2020]. This F-test analyzes whether the means of the continuous variable differs between groups. F = (variation between cluster means) / (variation within the clusters), so high F values for our data signify that a given observable varies more between clusters than within. For these tests, the clusters we are using are the true UFD remnant groups because we take the labels directly from the simulations. To quantify the level of the effect, we also calculate the ω^2 value of each test [e.g., Olejnik and Algina, 2003]. This metric is similar to R^2 in the context of regression analysis while also accounting for the degrees of freedom in the model. ω^2 can vary from -1

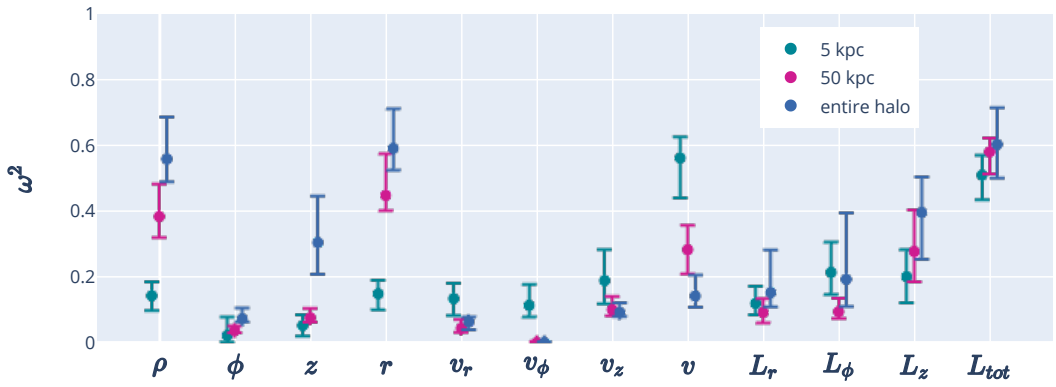

Figure 4-5: Strength of association between different kinematic observables and the true cluster labels. Higher ω^2 values indicate a stronger association. L_{tot} has consistently high ω^2 values, implying it is an important variable when seeking to find clustered stars that accreted together. ρ, ϕ, z and v_r, v_ϕ, v_z are the radius and velocity in cylindrical coordinates, respectively. The importance of r and v is due to their correlation with total energy.

to +1; values far from zero imply a stronger effect.

The ANOVA test results are shown visually in Figures 4-4 and 4-5. Figure 4-4 shows the four axisymmetric actions we use in clustering. All four actions show correlation with the true cluster labels, with energy consistently being the most important observable. Figure 4-5 shows the correlations of other potentially useful observables, demonstrating the high correlation of total angular momentum, L_{tot}. These results support our choice to cluster in E-J_r-J_z-J_ϕ phase space. They also imply that E-L_{tot} phase space can be useful to find UFD remnants in cases where the full axisymmetric actions are unknown. This has been known previously [e.g., Helmi and Tim de Zeeuw, 2000, Gómez et al., 2010].

Figure 4-5 shows that total velocity is likely important at parallax-level cuts (e.g., 5 kpc) and total distance from the galaxy's center is important for data sets with no radial cut. This is simply due to the relationship between velocity, radius, and total energy. All of the test results are summarized in the Appendix in Table 4.2. As an additional check, we also include ANOVA tests for z_{infall}, the redshift at which the particles were accreted by the Milky Way. This variable perfectly aligns with the true cluster labels and thus should have $\omega^2 = 1$, which we find.

4.4 Quantifying the Abilities and Limitations of Clustering Algorithms

We run each clustering algorithms (HDBSCAN, Gaussian Mixture Models, Agglomerative Clustering, Mean-Shift Clustering, K-Means, Friends-of-Friends, and Affinity Propagation; see Section 4.3.1) on each simulation in each of the six data sets (see Section 4.2.4). The hyperparameters of each algorithm are chosen as described in Section 4.3.2. All clustering is done in 4D energy-action space (E, L_z, J_r, and J_z) as supported by the association results presented in Section 4.3.3. Given the seven algorithms, six data sets, up to 32 simulations per data set, and roughly twenty hyperparameter choices per algorithm, we run over 10,000 clustering tests.

The results from these tests are largely a cautionary tale. All of these algorithms have significant limitations when it comes to identifying UFD remnant groups. Hence, in this section, we analyze the possibilities and limitations of the algorithms with a focus on how the results can inform the search for UFD remnants in real data sets since there currently exist no better methods to identify tidally disrupted ultra-faint dwarf galaxies from survey data. In future work, fully modeling the phase-space distribution of all accreted systems simultaneously could offer an alternative method to learn about accreted UFDs as compared to the current method of individually picking out a handful of dynamic clusters that may or may not correspond to UFDs. For now, though, kinematic clustering is one of the few available methods.

The basic problem is that, due to phase mixing and background, most star particles that accreted into the Milky Way-mass galaxies from the small UFD remnants overlap too much with other particles in phase space at $z = 0$ to be reliably identified as coherent remnant groups. This is true for all algorithms across all data sets. The clustering algorithms also frequently return clusters that do not correspond to any true UFD remnant ("false positives"). However, some algorithms work better than others and some identified clusters are more likely to be real than others. We now give more details on algorithm usability.

4.4.1 Example Clustering Results

Figure 4-6 shows example clustering results from each of the seven algorithms. These results use a single Milky Way-mass simulation (simulation Cat-14) from one data set (accreted star particles from UFDs within 50 kpc of the Sun). The left shows the true UFD remnants in phase space; each star particle is colored according to the UFD it was born in (note that each color repeats several times). The star particles in this example originated in 124 different UFDs. The panels on the right show how well each clustering algorithm performs. All clustering algorithms perform poorly in the high density region of phase space and only consistently identify several isolated, high-energy clusters. These high-energy clusters do, in fact, correspond to real UFD remnants. The majority of the rest of the clusters found by these algorithms do not actually correspond to real UFD remnants. This is unsurprising given the high density of overlapping structure in the high density region.

For all of our clustering results, we use the metrics of "realness rate" and "recovery rate" to evaluate the findings. Realness rate is defined as the fraction of clusters which are "pure", defined as clusters for which at least 2/3 of the stars accreted together. Recovery rate is defined as the fraction of UFD remnants which are recovered. A remnant is recovered if (1) its stars are clustered into a pure cluster and (2) that cluster is "complete", defined as clusters for which at least 1/2 of the stars from a remnant are identified together in a single cluster. When determining these rates, we only consider clusters or remnants with at least 5 particles. The purity and completeness thresholds (2/3 and 1/2, respectively) are chosen with a stricter requirement on the "realness" of a cluster as our priority is identifying stars that accreted together. These thresholds can both be varied, though, and are simply chosen as example metrics. The holistic takeaways of this paper remain consistent even if you vary these thresholds.

As an illustrative example, the realness and recovery rates for each algorithm on the Cat-14 simulation are reported in Table 4.1. The example HDBSCAN results are shown in Figure 4-7.

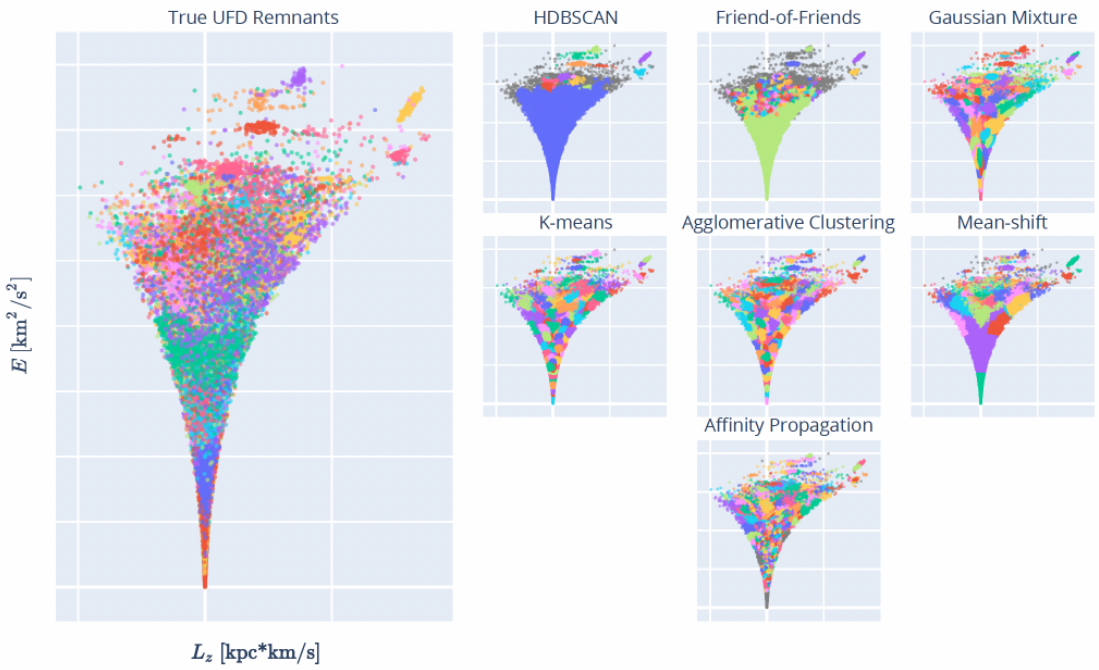

Figure 4-6: Example of clustering results for one simulation (Cat-14) from one data set (accreted star particles from UFDs within 50 kpc of the Sun). Far left: Star particles from true UFD remnants in dynamic phase space. Many of the particles are phase mixed. Right: Results from each of the seven clustering algorithms tested in this paper. Most of the clusters found by these algorithms, especially those at lower energy, do not correspond to true UFD remnants.

Algorithm	Realness Rate	Recovery Rate
HDBSCAN	67% (12 pure clusters / 18 total clusters)	4% (5 pure & complete clusters)
Friend-of-Friends	34% (61 pure clusters / 176 total clusters)	5% (6 pure & complete clusters)
Gaussian Mixture Models	18% (29 pure clusters / 160 total clusters)	5% (6 pure & complete clusters)
K-Means	12% (27 pure clusters / 230 real clusters)	5% (6 pure & complete clusters)
Agglomerative Clustering	13% (32 pure clusters / 248 total clusters)	6% (8 pure & complete clusters)
Mean-Shift	22% (24 pure clusters / 100 total clusters)	3% (4 pure & complete clusters)
Affinity Propagation	5% (52 pure clusters / 989 total clusters)	2% (3 pure & complete clusters)

Table 4.1: For the example simulation shown in Figure 4-6, the realness and recovery rates of different clustering algorithms. The recovery rate is determined by comparing the number of pure & complete clusters to the total number of accreted UFDs in this simulation, 124 UFDs.

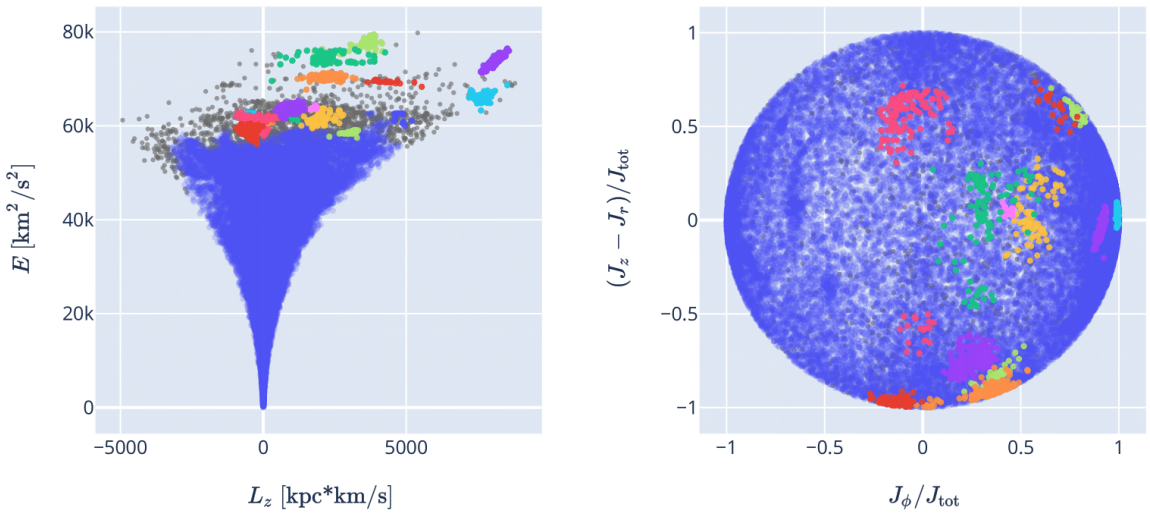

Figure 4-7: Example of the HDBSCAN clustering results for one simulation (Cat-14) from one data set (accreted star particles from UFDs within 50 kpc of the Sun). The clustering is done in 4D energy-action space (E, L_z, J_r, J_z). Grey points are particles not associated with any cluster. For this simulation, HDBSCAN finds eighteen clusters. Twelve of them are real groups of accreted UFD stars, and five of those twelve are fully "recovered" UFD remnants.

4.4.2 Comparing Clustering Algorithms

Throughout this work, we test seven common clustering algorithms (described in Section 4.3.1). For the UFD-only data sets, we test all seven algorithms on every data set. For the all-stars data sets, the larger radial cuts (50 kpc and entire halo) are extremely large, so we only test the more scalable algorithms: HDBSCAN, Friend-of-Friends, Gaussian Mixture Models, and K-Means.

The results for all UFD-only data sets are shown in Figure 4-8. Each line represents the results for a single Milky Way-mass galaxy simulation with the given radial cut. The median result for each algorithm is shown as a circle. The scatter in results across different simulations is significant because Milky Way-mass galaxies with a higher number of recent UFD accretions have higher rates. The results for the all-stars data sets are shown in Figure 4-9.

Even with UFD-only data sets, all algorithms have low UFD remnant recovery rates and cluster realness rates. The local radial cut, 5 kpc, has the worst results; the number of UFD remnants recovered from these simulations is frequently just one.

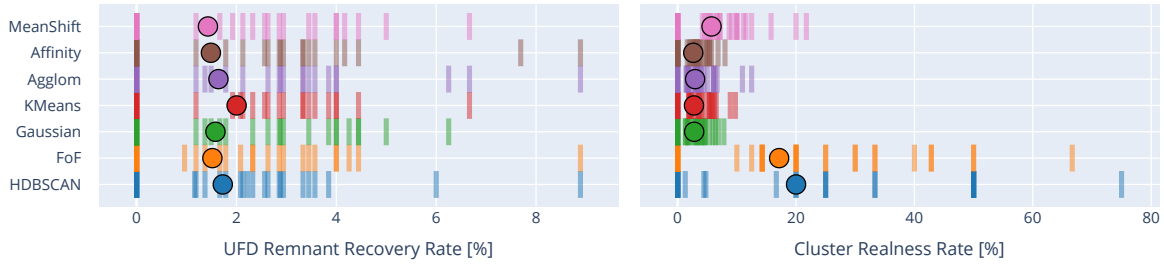

(a) UFD + 5 kpc data sets: All algorithms recover similarly low numbers of UFD remnants. HDBSCAN and FoF have the highest cluster realness rates.

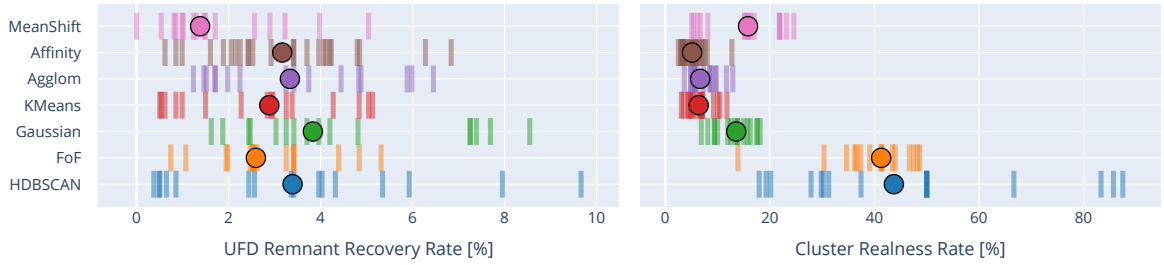

(b) UFD + 50 kpc data sets: Once again, HDBSCAN and FoF have the best balance of UFD remnant recovery and cluster realness rates.

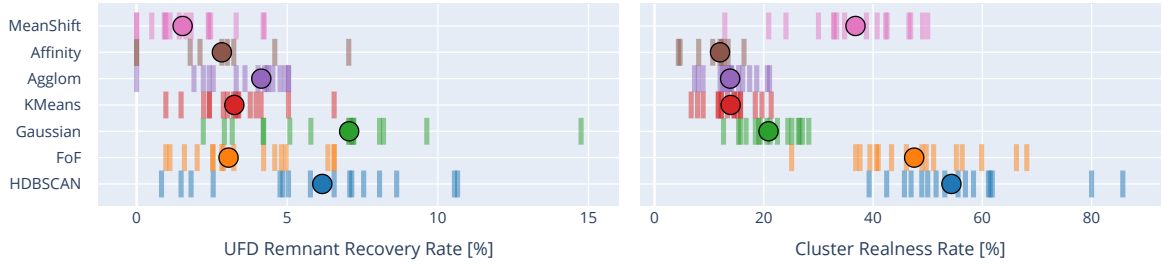

(c) UFD + entire halo data sets: HDBSCAN has the best balance of UFD recovery and cluster realness. FoF has a similar realness rate but recovers far fewer remnants.

Figure 4-8: Results for the UFD-only data sets. Each line represents a single Milky Way-mass galaxy simulation and each circle is the median rate across all simulations. See Section 4.2.4 for descriptions of the different data sets and Section 4.3.2 for definitions of recovery and realness rates. Generally, HDBSCAN and FoF perform better than the other algorithms and are also significantly faster. For results with the all-stars data sets, see Figure 4-9.

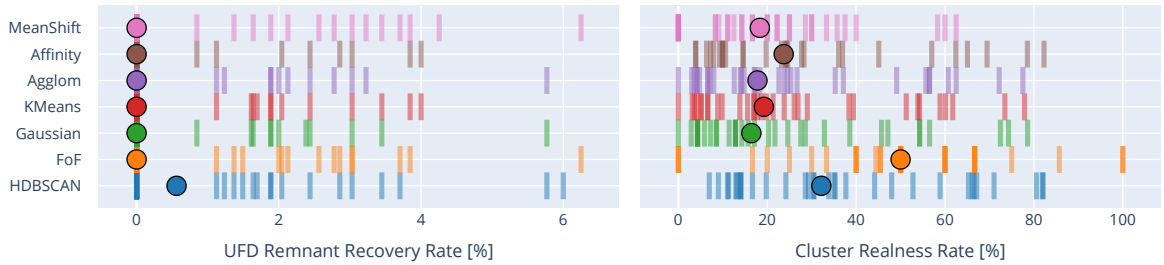

(a) All stars + 5 kpc data sets: Algorithms find real clusters accreted from dwarf galaxies, but almost none of them are UFD remnants.

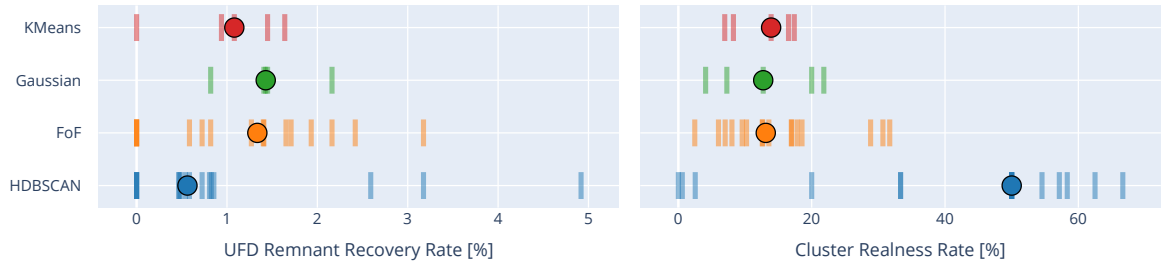

(b) All stars + 50 kpc data sets: Recovery rates are once again low, but realness rates can be high as clusters from larger mass dwarfs are identified. HDBSCAN has highest realness rate, but all recovery rates are low.

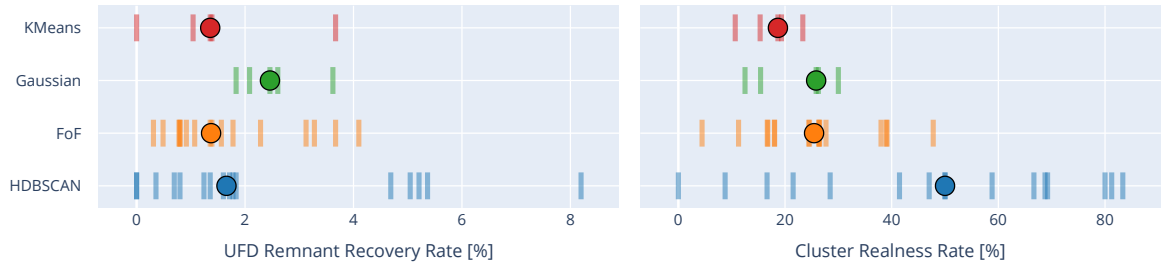

(c) All stars + entire halo data sets: HDBSCAN once again has the best balance of recovery and realness.

Figure 4-9: Results for the all-stars data sets. Each line represents a single Milky Way-mass galaxy simulation and each circle is the median rate across all simulations. On the large data sets, HDBSCAN and FoF are much faster than K-means and Gaussian Mixture Models.

Overall, all algorithms only recover about 2% of UFD remnants within 5 kpc of the Sun. HDBSCAN and FoF have the highest realness rates for the clusters they find, with around 20% of their clusters corresponding to tagged star particles that accreted together.

This clearly implies, in no uncertain terms, that the vast majority of clusters found by these algorithms do not actually represent any truly accreted groups!

In the larger data sets, the clustering algorithms perform better, recovering $\sim 3-6\%$ of UFD remnants and, for HDBSCAN and FoF, having a $\sim 40-60\%$ realness rate. Even with these idealized data sets and specially chosen hyperparameters, though, the rates are still low. We thus discuss how to identify real clusters vs. false positives in Section 4.5.

Generally for the UFD-only data sets, HDBSCAN is the most reliable algorithm choice. FoF also often has a relatively high realness rate. These two algorithms are also the fastest choices for large data sets.

For the all-stars data sets (Figure 4-9), realness rates are higher than the UFD-only data sets because clusters of stars from larger dwarf galaxy remnants are easier to identify than the small clusters of stars from UFD remnants. UFD remnant recovery rates are universally worse in the all-stars data sets, though, because the non-UFD stars act as significant noise during the search for UFD clusters. This is discussed in more detail in Section 4.4.3. Similar to the UFD-only data sets, HDBSCAN is once again generally a reliable choice to balance recovery rates and realness rates in the all-stars data sets. For the largest data sets, computational constraints also become important, and HDBSCAN and FoF scale well computationally.

Overall, HDBSCAN tends to be the most reliable clustering algorithm across different data sets. Currently, it is also a popular clustering algorithm used in astronomy research (see Section 4.3.1). We thus focus on HDBSCAN for most of the rest of our text.

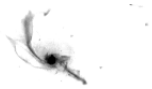

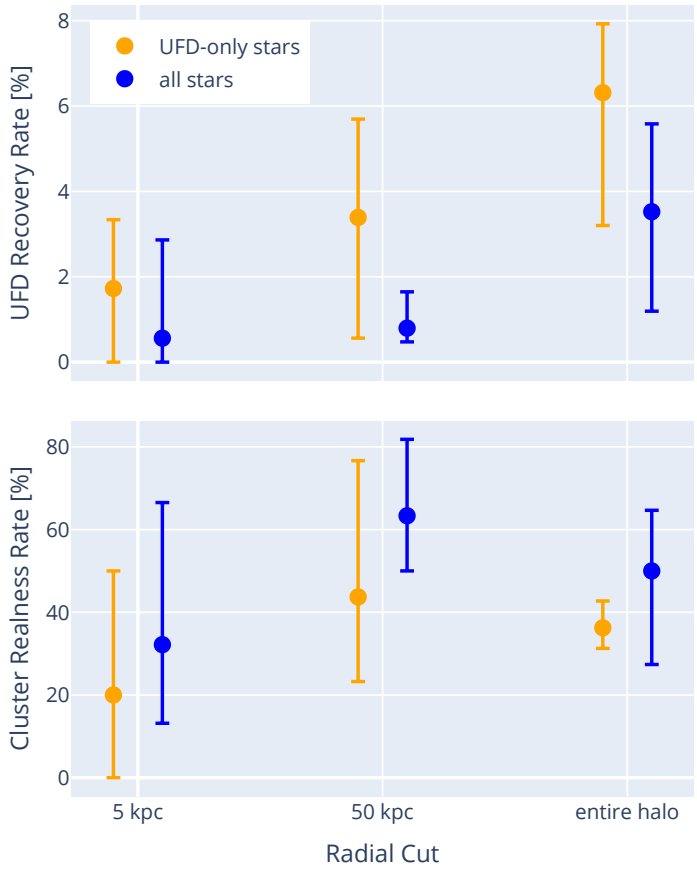

Figure 4-10: Comparing UFD remnant recovery rates and cluster realness rates with HDBSCAN for the data sets with only UFD stars and the data sets with all stars. As expected, the UFD-only data sets result in higher UFD recovery rates. Realness rates for the all-stars data sets include real clusters from larger dwarfs, which are principally easier to identify, so overall realness rates are not improved by using a UFD-only data set. Error bars show 16%-84% scatter across all simulations.

4.4.3 Comparing UFD-Only Data Sets to All-Stars Data Sets

As discussed in Section 4.2.4, we have data sets with (1) only accreted star particles from UFDs and (2) all accreted star particles. The former data set is unrealistic because in real data we cannot know a priori which stars accreted from UFDs. The UFD-only data set can be imperfectly pursued observationally through the use of chemical tagging, however. Stars that formed in UFDs tend to have a lower metallicity distribution function, lower abundances in neutron-capture elements, and may preferentially have strong r-process enrichment [e.g., Kirby et al., 2013a, Brauer et al., 2019, Gudin et al., 2021, Ji et al., 2016a]. Additionally, as we identify kinematic struc-

tures associated with larger-mass accretion events such as Gaia-Enceladus, removing those stars from observational data sets could also help towards creating a UFD-only data set. All these methods are imperfect, but as no more sophisticated and reliable methods exist to date to identify UFD stars e.g., in observed survey data, we must do the best we can with the methods available to us.

In Figure 4-10, we demonstrate the need to find ways to exclude stars from higher-mass accreted dwarfs if we hope to identify UFD remnants. At every radial cut, UFD remnant recovery rates are higher for UFD-only data sets. Realness rates are higher for all-stars data sets, but this is only because structures from higher-mass dwarfs are principally easier to identify than those from UFDs and because pure clusters are generally more common for higher-mass dwarfs since they contribute more stars. This underscores how difficult it is to identify UFD structures even among UFD-only samples. If we hope to identify UFD remnants, though, pursuing data sets with stars from UFDs will be, unsurprisingly, very beneficial.

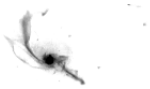

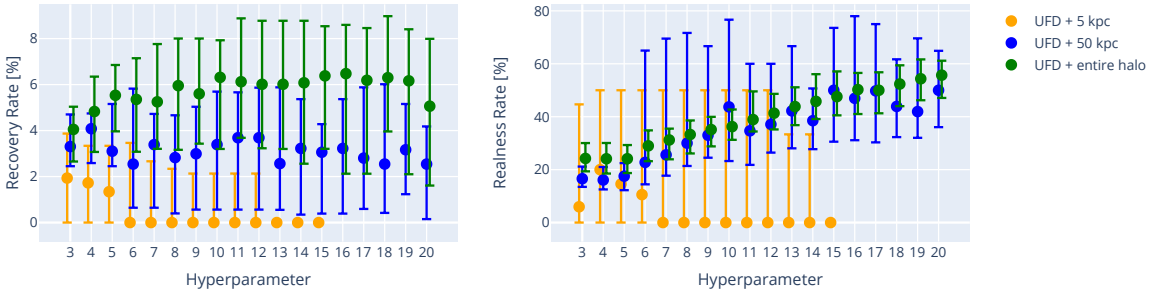

(a) Recovery rates and realness rates for different choices of min_cluster_size for HDBSCAN.

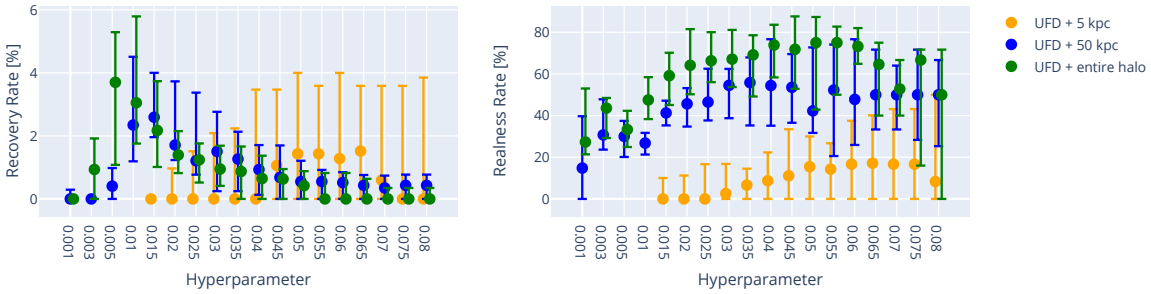

(b) Recovery rates for different choices of linking_length for FoF.

Figure 4-11: For these data sets, the FoF results differ more with varying hyperparameter choices than the HDBSCAN result. The hyperparameter choice is important for all algorithms, however. This causes additional difficulty when using these algorithms to identify UFD remnants. Error bars show 16%-84% scatter across all simulations.

4.4.4 Comparing Hyperparameter Choices

One downfall of most of these clustering algorithms is their dependence on hyperparameters. Each algorithm other than Affinity Propagation requires users to pre-select a value for a hyperparameter, and it is generally not obvious which values are best. In this work, we already know the true labels, and thus have the unique privilege of selecting our hyperparameters to optimize our clustering results (see Section 4.3.2). For observational data sets, however, this is not possible.

The results in all other subsections use optimal hyperparameter values. In this subsection, we vary the hyperparameter choices to illustrate how results differ. Figure 4-11 shows results for different hyperparameter choices of HDBSCAN and FoF. HDBSCAN requires an integer choice for min_cluster_size and thus has a smaller reasonable range of choices. Results can vary significantly with min_cluster_size

choice, but generally results are roughly stable across several integer choices. As expected, the best choice of min_cluster_size tends to increase for data sets with larger radial cuts. For FoF, we tested many possible choices for linking_length and results were more unstable than for HDBSCAN.

Thus, for these data sets, the results from HDBSCAN are more stable with variations in hyperparameter choice. The hyperparameter choice is important for all algorithms, however. This remains a difficulty of automating the search for UFD remnants with these clustering algorithms. Some groups are developing algorithms without a hyperparameter dependence [e.g., Ruiz-Lara et al., 2022] to alleviate these concerns.

Still, for HDBSCAN, the hyperparameter value greatly affects the number of clusters. For too large of min_cluster_size, the algorithm finds no remnants. For example, for the 5 kpc data sets, min_cluster_size > 5 causes, on average, fewer than five total clusters returned by the algorithm, none of which are real UFD remnants. For the larger radial cuts, too small of min_cluster_size leads to too many clusters. For these data sets, min_cluster_size < 9 causes 200 to 2000 clusters while the number of recovered remnants remains constant or decreases. When selecting this hyperparameter, a balance must be struck to avoid the identification of an unreasonably small or large number of clusters in a given sample.

4.4.5 Why Clustering Algorithms Struggle

Due to their small size, the dynamic signatures of tidally-disrupted UFDs are, over 90% of the time, weak and significantly out-numbered by other overlapping accreted structures. The limitations found in this paper are not unique to these clustering algorithms; we expect any clustering algorithm to struggle.

To illustrate this, we estimate signal-to-total ratios (similar to signal-to-noise ratios) for all the tidally-disrupted UFD remnants in our data sets. Normalized histograms of the signal-to-total ratios from different data sets are shown in Figure 4-12. To determine these ratios, for each remnant we draw a 4D sphere in phase space that is exactly large enough to enclose 50% of the particles from that remnant.

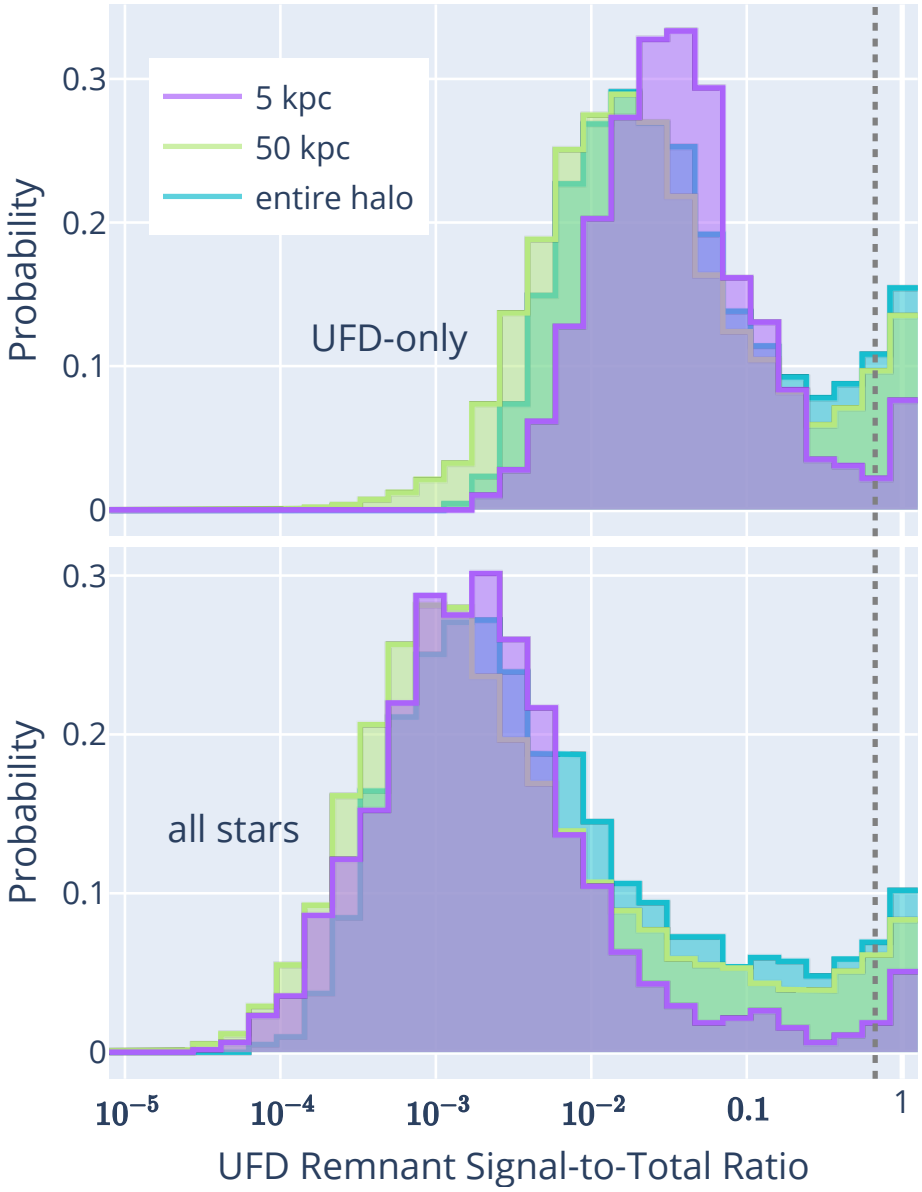

Figure 4-12: Normalized histograms of estimated signal-to-total ratios (similar to signal-to-noise ratios) for all UFD remnants in all data sets. For the vast majority of remnants, the ratio is tiny because the UFD remnant particles significantly overlap with all the other particles. The signal is very weak. For context, the dotted line shows 67%, our purity threshold. Depending on the data set, $92 - 97\%$ of UFD remnants have a signal-to-total ratio below this threshold. The all-stars data sets (bottom plot) have particularly low UFD signals – the median ratio is one UFD remnant particle to 1000 non-remnant particles.

We then compare the number of remnant particles in that volume to the total number of particles in that volume. The maximum value is thus 1 for the case where the tidally-disrupted UFD is isolated from other particles. These ratios are similar to our purity metric, so we plot our purity threshold (67%) as a dotted line on Figure 4-12 for reference. We also note that remnants are generally not spherical in 4D phase space, so this is merely an estimate.

For the vast majority of UFD remnants, the dynamic signature is completely washed out by the other particles in that volume. For UFD-only data sets, the typical remnant has a ratio of one UFD remnant particle to 30 other particles, 1:30. For the all-stars data sets, the typical remnant has a ratio of 1:1000. In the best case scenario, the UFD-only data set with the entire halo, only 8% of remnants have a signal-to-total ratio higher than our purity threshold of 67%.

The remnants with the highest signal-to-total ratios are the remnants that are successfully identified by the clustering algorithms. Most of the other remnants are simply too difficult to find in this dense 4D space, due to a combination of phase-mixing as the stellar dynamics relax over time and/or accreting with dynamics that are already similar to other star particles. We can thus optimize clustering searches to try to find the greatest number of UFD remnants, but most will never be found by these methods. The ones that are kinematically identifiable are those that (1) accreted with outlying dynamics, e.g., higher energy than usual, and (2) recently accreted so that the star particles have not had time to phase-mix.

We also note that an additional difficulty of analyzing only star particles in the inner volume, e.g. our 5 kpc data sets, is that you cannot sample full satellites within this small volume. This issue is described in more detail in Gómez et al. [2010].

4.5 Properties of Real Clusters in Simulations

Even in the best cases, the clustering algorithms find many clusters that do not correspond to real accreted remnant groups. Hence, we compare the properties of real clusters vs. "false positive" clusters to help inform which clusters are more likely

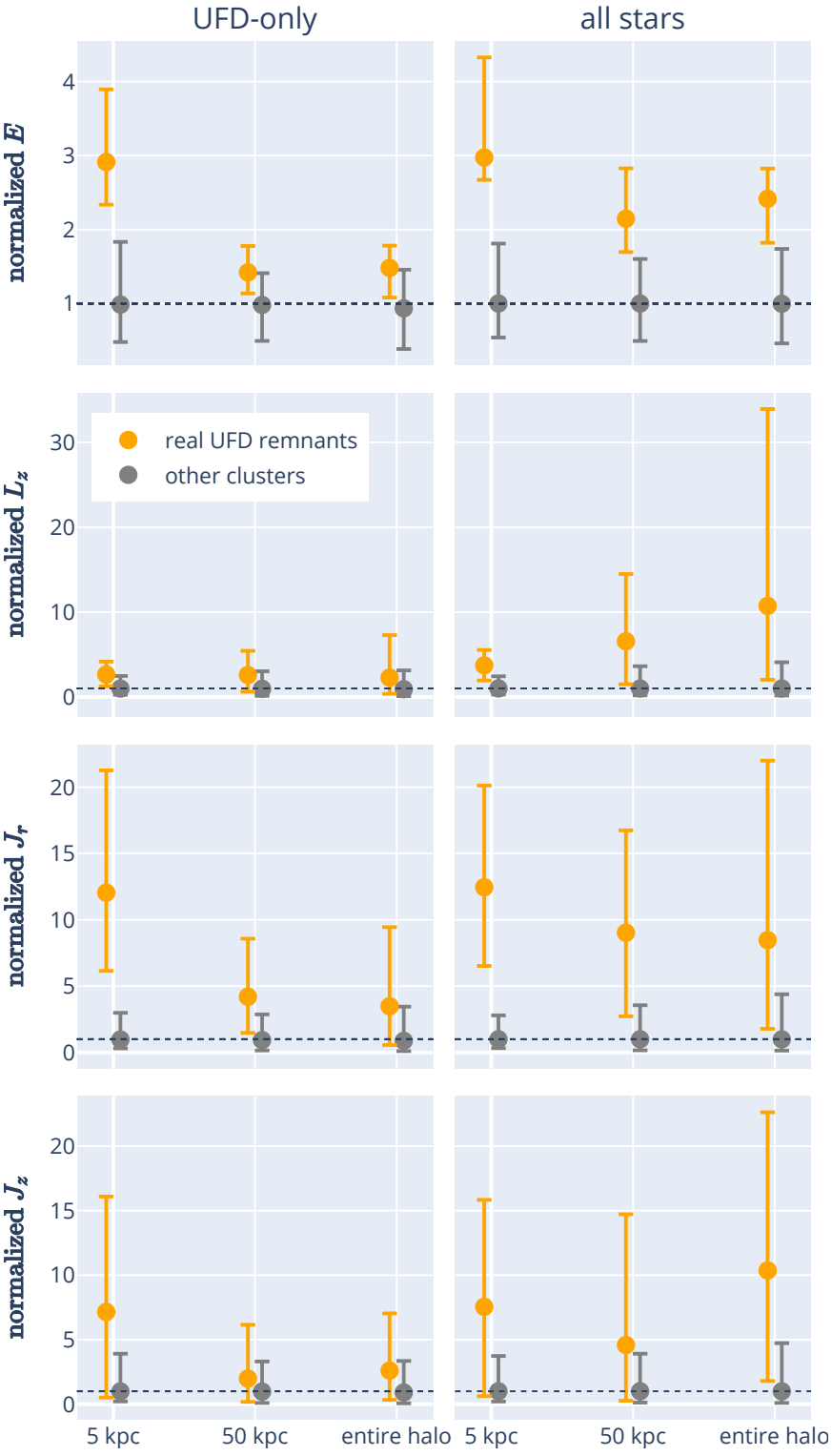

Figure 4-13: Median dynamics for clusters that correspond to real UFD remnants (i.e., pure and complete clusters) compared to other clusters. Clusters with higher actions are more likely to be real. Error bars show 16%-84% scatter across all clusters.

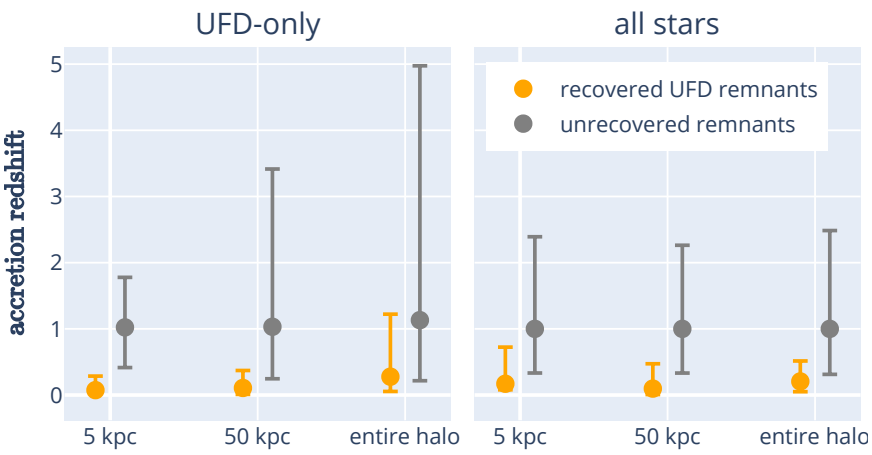

Figure 4-14: Median $z_{accretion}$ (redshift at which a given dwarf galaxy was accreted) for recovered UFD remnants compared to all unrecovered remnants. As expected, the UFD remnants that are recovered by HDBSCAN (and other algorithms) were more recently accreted. Error bars show 16%-84% scatter across all remnants.

to be real in observational data sets.

Figure 4-13 shows the E, L_z, J_r, and J_z of real recovered clusters (i.e., pure and complete clusters – clusters that correspond to an accreted UFD remnant) compared to the dynamics of clusters that do not correspond to UFD remnants. These results use HDBSCAN, but the plots are holistically similar for other algorithms. All dynamics are normalized relative to the median of all clusters in the sample. For each cluster, its energy (or L_z, J_r, J_z) is determined from the median of all star particles in that cluster.

Compared to all clusters, clusters that correspond to real UFD remnants have higher energy and axisymmetric actions. High energy and J_r are most important for distinguishing between real UFD clusters and all other clusters, especially in local (5 kpc) data sets. Of the action variables, L_z is the least important dynamic when determining which clusters are more likely to be real. This aligns with results from the ANOVA tests in Figure 4-4.

Based on these results, clusters with high energy and high J_r are significantly more trustworthy. For example, clusters with median energy higher than twice the median of all clusters in a local sample are pure *and* complete over 90% of the time. This is true for both UFD-only data sets and all-stars data sets.

The UFD remnants recovered in these real clusters are UFDs that, generally, accreted relatively recently. Figure 4-14 shows the median accretion redshift $z_{accretion}$ for UFDs recovered by HDBSCAN compared to all unrecovered remnants. UFDs that were accreted at redshift $z = 1$ and higher are virtually never recovered by any of these clustering algorithms. The dynamic signature of these small dwarfs is completely lost as the stars phase-mix in the dense region of action space, and the remnants are no longer identifiable. This is not surprising because energy and orbital actions are only truly conserved in static potentials, and realistic, time-varying galactic potentials cause the stellar dynamics to relax over time.

As discussed in Section 4.4.5, for a UFD remnant to be reliably identified through kinematic clustering, it needs to both have had outlying dynamics at the time of accretion and also have a recent accretion time, $z_{accretion} \lesssim 0.5$, so that its stars have not had time to significantly phase-mix. Not all recently accreted UFD remnants are identifiable through kinematics (recently accreted UFDs can still end up in the dense regions of phase space; see Figure 4-2), but of the identifiable UFD remnants, virtually all are recently accreted.

4.6 Recommendations for Using Cluster Algorithms

Our study has clearly shown that using clustering algorithms with stellar dynamics to search for accreted UFD remnants is a challenging task, that, unfortunately, does not deliver reliable results a majority of the time.

Dynamically-linked clusters identified by any clustering algorithms should thus not be blindly trusted but amply questioned and investigated, and results presented in a careful manner to avoid the presentation of numerically artificially created results. Case in point is our idealized situations in which we limit our data sets to only accreted UFD star particles and optimize our hyperparameter choices. The resulting UFD recovery rates are around $\sim 6\%$ at best, and the majority of clusters found by all algorithms are not real. Only stars from fairly recently accreted UFDs ($z_{accretion} \lesssim 0.5$) can retain sufficiently strong dynamic signatures to be identified by

these algorithms.

While these findings are unfortunate and must be taken into account in future searches, not all is lost. Clustering with stellar dynamics remains one of the few methods presently available to identify accreted structure in observed Milky Way survey data, and while not all UFDs can be found this way, identifying real remnants is possible.

To ensure that results are as reliable and trustworthy as possible, we recommend that researchers:

- Among these out-of-the-box clustering algorithms, choose HDBSCAN. Across our different data sets, HDBSCAN consistently balances the highest UFD remnant recovery rates and cluster realness rates. It is also more computationally scalable than all algorithms other than Friend-of-Friends.

- UFD dynamic signatures are frequently weak, so incorporate chemical tagging when identifying groups of accreted stars. This can be done, for example, by focusing on low-metallicity stars and/or r-process enhanced stars. Successfully limiting a data set to UFD stars increases your remnant recovery rate by around $3\times$ on average. Chemical abundances can also be used to help validate dynamic clusters.

- Assume most clusters identified by clustering algorithms do not correspond to real UFD remnants. Focus on clusters with higher than average energy and J_r.

- Recognize that only recently accreted UFDs in lower-density areas of phase space are consistently found by these clustering algorithms, so you generally only recover $1-6\%$ of the UFD remnants in a given sample. Samples limited to the region around the Sun have lower recovery rates than samples with larger radial cuts.

- Vary your hyperparameter choices and consider the stability of the clustering results across several hyperparameter values. For HDBSCAN, the best hyperparameter values are the ones which produce fewer than several hundred

clusters (in our samples, requires min_cluster_size $\gtrsim$ 9 for our large radial cuts) and produce more than just a few clusters (in our samples, requires min_cluster_size $\lesssim$ 6 for our 5 kpc radial cut). This will depend on your sample, so test different hyperparameter choices to avoid hyperparameters that result in an unreasonably large or small number of clusters.

This work made extensive use of the python libraries `numpy` [van der Walt et al., 2011], `scipy` [Virtanen et al., 2020], `sqlite3` [Häring, 2006], and `plotly` [Plotly Technologies Inc., 2015].

Table 4.2: Results for the one-way ANOVA tests. Each continuous variable in the table is tested for its level of association to the true cluster labels. The ω^2 values estimate the strength of the association; a high ω^2 value (e.g., near 1) implies that this variable is likely to be important in clustering. Uncertainty values represent 16th – 84th percentile scatter across the 32 simulations.

Variable	Radial Cut	F	ω^2	$p-$value	Variable	Radial Cut	F	ω^2	$p-$value
	5 kpc	2^{+1}_{-1}	$0.14^{+0.04}_{-0.05}$	2e-10^{+6e-8}_{-2e-10}		5 kpc	2^{+1}_{-1}	$0.12^{+0.05}_{-0.04}$	6e-11^{+3e-4}_{-6e-11}
ρ	50 kpc	186^{+93}_{-45}	$0.38^{+0.10}_{-0.06}$	$<$ 1e-300	L_r	50 kpc	28^{+23}_{-7}	$0.09^{+0.04}_{-0.03}$	$<$ 1e-300
	entire halo	460^{+407}_{-97}	$0.56^{+0.13}_{-0.07}$	$<$ 1e-300		entire halo	71^{+75}_{-21}	$0.15^{+0.13}_{-0.04}$	$<$ 1e-300
	5 kpc	1^{+1}_{-1}	$0.02^{+0.06}_{-0.02}$	3e-2^{+4e-1}_{-3e-2}		5 kpc	4^{+1}_{-1}	$0.21^{+0.09}_{-0.07}$	2e-25^{+3e-13}_{-2e-25}
ϕ	50 kpc	13^{+4}_{-3}	$0.04^{+0.01}_{-0.01}$	$<$ 1e-300	L_ϕ	50 kpc	31^{+20}_{-7}	$0.10^{+0.04}_{-0.02}$	$<$ 1e-300
	entire halo	33^{+13}_{-5}	$0.07^{+0.03}_{-0.01}$	$<$ 1e-300		entire halo	98^{+158}_{-45}	$0.19^{+0.20}_{-0.08}$	$<$ 1e-300
	5 kpc	2^{+1}_{-1}	$0.05^{+0.03}_{-0.03}$	7e-4^{+2e-1}_{-7e-4}		5 kpc	3^{+2}_{-1}	$0.20^{+0.08}_{-0.08}$	2e-25^{+2e-8}_{-2e-25}
z	50 kpc	27^{+9}_{-6}	$0.08^{+0.03}_{-0.01}$	$<$ 1e-300	L_z	50 kpc	110^{+101}_{-41}	$0.28^{+0.13}_{-0.09}$	$<$ 1e-300
	entire halo	161^{+147}_{-61}	$0.31^{+0.14}_{-0.10}$	$<$ 1e-300		entire halo	243^{+170}_{-101}	$0.40^{+0.11}_{-0.14}$	$<$ 1e-300
	5 kpc	2^{+2}_{-1}	$0.15^{+0.04}_{-0.05}$	1e-10^{+3e-8}_{-1e-10}		5 kpc	10^{+9}_{-3}	$0.51^{+0.06}_{-0.07}$	2e-93^{+1e-42}_{-2e-93}
r	50 kpc	244^{+137}_{-50}	$0.45^{+0.13}_{-0.05}$	$<$ 1e-300	L_{total}	50 kpc	392^{+111}_{-69}	$0.58^{+0.04}_{-0.07}$	$<$ 1e-300
	entire halo	525^{+466}_{-63}	$0.59^{+0.12}_{-0.07}$	$<$ 1e-300		entire halo	600^{+382}_{-198}	$0.60^{+0.11}_{-0.10}$	$<$ 1e-300
	5 kpc	2^{+1}_{-1}	$0.14^{+0.05}_{-0.05}$	2e-11^{+1e-6}_{-2e-11}		5 kpc	22^{+30}_{-12}	$0.74^{+0.08}_{-0.25}$	3e-$166^{+6e-72}_{-3e-166}$
v_r	50 kpc	15^{+9}_{-4}	$0.05^{+0.03}_{-0.01}$	$<$ 1e-300	J_r	50 kpc	373^{+360}_{-122}	$0.57^{+0.13}_{-0.09}$	$<$ 1e-300
	entire halo	28^{+10}_{-9}	$0.07^{+0.02}_{-0.02}$	$<$ 1e-300		entire halo	760^{+565}_{-298}	$0.66^{+0.10}_{-0.14}$	$<$ 1e-300
	5 kpc	2^{+1}_{-1}	$0.11^{+0.06}_{-0.04}$	2e-13^{+3e-4}_{-2e-13}		5 kpc	7^{+8}_{-3}	$0.40^{+0.13}_{-0.16}$	4e-55^{+1e-26}_{-4e-55}
v_ϕ	50 kpc	1^{+1}_{-1}	$0.00^{+0.00}_{-0.00}$	3e-4^{+10e-1}_{-3e-4}	J_z	50 kpc	229^{+61}_{-68}	$0.44^{+0.07}_{-0.08}$	$<$ 1e-300
	entire halo	2^{+1}_{-1}	$0.00^{+0.00}_{-0.00}$	7e-7^{+9e-1}_{-7e-7}		entire halo	362^{+245}_{-98}	$0.49^{+0.16}_{-0.10}$	$<$ 1e-300
	5 kpc	3^{+2}_{-1}	$0.19^{+0.09}_{-0.07}$	4e-21^{+1e-8}_{-4e-21}		5 kpc	22^{+11}_{-9}	$0.68^{+0.07}_{-0.13}$	6e-$156^{+2e-77}_{-6e-156}$
v_z	50 kpc	35^{+15}_{-7}	$0.10^{+0.04}_{-0.02}$	$<$ 1e-300	E	50 kpc	934^{+755}_{-319}	$0.77^{+0.07}_{-0.08}$	$<$ 1e-300
	entire halo	43^{+14}_{-8}	$0.09^{+0.03}_{-0.01}$	$<$ 1e-300		entire halo	1489^{+1031}_{-567}	$0.80^{+0.07}_{-0.10}$	$<$ 1e-300
	5 kpc	12^{+7}_{-4}	$0.56^{+0.06}_{-0.12}$	2e-98^{+5e-51}_{-2e-98}		5 kpc	$(6^{+11}_{-5}) \times 10^{27}$	$1.00^{+0.00}_{-0.00}$	$<$ 1e-300
v_{total}	50 kpc	117^{+39}_{-37}	$0.28^{+0.07}_{-0.07}$	$<$ 1e-300	z_{infall}	50 kpc	$(5^{+5}_{-4}) \times 10^{27}$	$1.00^{+0.00}_{-0.00}$	$<$ 1e-300
	entire halo	67^{+38}_{-22}	$0.14^{+0.06}_{-0.03}$	$<$ 1e-300		entire halo	$(4^{+3}_{-3}) \times 10^{27}$	$1.00^{+0.00}_{-0.00}$	$<$ 1e-300

Table 4.3: Trial hyperparameter values for all algorithms

Algorithm	Hyperparameter	Hyperparameter Search Space
HDBSCAN	min_cluster_size	3, 4, 5, 6, 7, 8, 9, 10, 11, 12, 13, 14, 15, 16, 17, 18, 19, 20
K-means	n_clusters	60, 70, 80, 90, 100, 110, 120, 130, 140, 150, 160, 170, 180, 190, 200, 210, 220, 230, 240, 250
Gaussian mixture models	n_clusters	
Agglomerative clustering	n_clusters	
Friend-of-friends	linking_length	0.001, 0.003, 0.005, 0.01, 0.015, 0.02, 0.025, 0.03, 0.035, 0.04, 0.045, 0.05, 0.055, 0.06, 0.065, 0.07, 0.075, 0.08, 0.1, 0.125, 0.15, 0.175, 0.2
Mean shift	bandwidth	0.06, 0.07, 0.08, 0.09, 0.1, 0.11, 0.12, 0.13, 0.14, 0.15, 0.16, 0.17, 0.18, 0.19, 0.2
Affinity propagation	-	-

Table 4.4: Optimal hyperparameter values for all datasets

		Chosen Hyperparameters					
		only UFD particles			UFD and non-UFD particles		
Algorithm	**Hyperparameter**	5 kpc	50 kpc	no radial cut	5 kpc	50 kpc	no radial cut
HDBSCAN	min_cluster_size	4	10	15	3	10	19
K-means	n_clusters	60	230	180	200	230	150
Gaussian mixture models	n_clusters	90	160	210	70	220	240
Agglomerative clustering	n_clusters	80	250	250	170	too slow	too slow
Friend-of-friends	linking_length	0.065	0.015	0.01	0.065	0.015	0.01
Mean shift	bandwidth	0.11	0.06	0.06	0.16	too slow	too slow
Affinity propagation	-	-	-	-	-	-	-

Chapter 5

AEOS: Star-by-Star Cosmological Simulation

The work in this chapter was completed by myself, Jennifer Mead, Andrew Emerick, Greg Wise, John Wise, Alexander P. Ji, Mordecai-Mark Mac Low, Benoit Côté, and Anna Frebel.

5.1 Introduction

The first galaxies formed 200-300 million years after the Big Bang, hosting many of the first stars and seeding the creation of every structure in the Universe. The smallest of these early galaxies were quenched by reionization (Brown et al. [2014]), so those that survived until now are composed of ancient stars from 13 billion years ago. Over time, many of these small galaxies merged to form the galaxies we observe today, including the Milky Way. Stars from these ultra-faint dwarf galaxies thus are relics from the era of the first stars and galaxies, preserving clean signatures of early chemical enrichment. They are also vital ingredients in our own formation history.

In the past 15 years, dozens of these ultra-faint dwarf galaxies have been discovered in the Local Group (e.g., Bechtol et al. [2015]). High-resolution spectroscopy has provided chemical abundances of over 15 of these dwarfs, with much more to come in the next decade. Simultaneously, chemical abundances of millions of stars in the

Milky Way stellar halo are being obtained through wide-field spectroscopic programs such as H3, GALAH, and APOGEE, with much more to come from SDSS-5, WEAVE, DESI, and others.

The problem is that observations of stars in dwarf galaxies and our stellar halo are outpacing theoretical models. We have a wealth of data, but we cannot leverage the full detail within it. Observations show scatter around the mean trends of chemical abundances in dwarf stellar populations (e.g., Ji et al. [2020]). Current state-of-the-art chemical evolution models can explain mean trends in the data, but are incapable of modeling the scatter and full distribution because they assume instantaneous formation of clusters of stars with homogeneous mixing of yields (e.g., Côté and Ritter [2018]). New, more detailed models are necessary to fully utilize the data to explore complex galaxy formation processes including source-dependent metal mixing, hierarchical galaxy merging, bursty star formation, and variations across different galaxies. This is especially vital for stars from small, high-redshift galaxies because even JWST cannot directly observe these faint objects (Boylan-Kolchin et al. [2016]), meaning our only path forward is to take full advantage of the dwarf stellar populations around us.

Cosmological simulations of dwarf galaxies with individual stars, detailed chemical yields, and highly-resolved metal mixing are now necessary to interpret chemical abundance data to learn how early galaxies evolved and how they contributed to the formation of the Milky Way. And now is the time to do it because advances in high performance computing and the wealth of stellar abundance data are, for the first time, making such a simulation both feasible and necessary.

The Aeos simulation is the first cosmological simulation with individual star particles, individual stellar feedback with detailed stellar yields, and adaptive grids to capture metal mixing in the interstellar medium from the first stars. This chapter describes the methods and initial results.

5.2 Methods

The Aeos simulation is a hydrodynamic cosmological simulation with individual stars developed using a modified version of Enzo, a community-developed adaptive mesh refinement simulation code [Bryan et al., 2014]. The framework was used in Emerick et al. [2019] to simulate a single isolated dwarf galaxy, and here we expand the models and scope of the simulation. We refer the reader to Emerick et al. [2019] for a detailed description of the methods used in this work and limit our discussion to a summary of the relevant physics and a description of the updated models. This includes the addition of a Pop III star formation and stellar feedback model, which can be considered to be an updated version from what was used in Wise et al. [2012b], and a new set of stellar yields. These are discussed in more detail below.

5.2.1 Radiative Cooling and Chemistry

We use a slightly modified version of the Grackle [Smith et al., 2017] to follow both the nine species non-equilibrium chemistry network (H, H^+, He, He^+, He^{++}, e^-, H^-, H_2, and H_2^+) and the effects of radiative heating and cooling from metals and a UVB. Following Emerick et al. [2019], we include the effects of H_2 formation on dust using a broken-power law dust-to-gas ratio from [Rémy-Ruyer et al., 2014] and a Haardt and Madau [2012] UV metagalactic background accounting for self-shielding in the HI band and propagating its impact self-consistently on other photoionization / photodissociation reaction rates and metal line cooling (see Emerick et al. [2019] for more details). We include a photoelectric heating model from FUV radiation from both individual stars using the same dust to gas ratio scaling mentioned above, and a local attenuation approximation.

New in these simulations is: 1) the additional contribution of the UVB to the FUV band, 2) the use of a constant ϵ efficiency parameter ($\epsilon = 0.05$) instead of one that depends on local gas density in computing the photoelectric heating rate (see Emerick et al. [2019]), 3) the effects both FUV and IR band radiation (new in these simulations, see Section 5.2.3) have on H_2 and H^- reaction rates, and 4) a UVB that

has been extended to high redshift in all bands adopting rates assuming black-body radiation spectrum at 3×10^4 K that turns on at z = 50 and is scaled to be continuous with HM2012 at z = 10. In addition, we use an updated LW background model from both Emerick et al. [2019] and Wise et al. [2012a], adopting the rates from Qin et al. [2020].

5.2.2 Star Formation

Stars in our simulation form stochastically in cold, dense gas that exhibits a converging flow ($\nabla \cdot v < 0$) assuming the local star formation rate is proportional to an efficiency per free-fall time (η), which we take to be $\eta = 2\%$. In this work, we allow star formation below $T_{\rm thresh} = 500$ K and adopt a high density threshold $n_{\rm thresh} = 10^4$ cm^{-3}. We distinguish between Pop III and Pop II star formation based on total gas metallicity. Gas enriched with $Z > 10^{-5}$ is capable of forming Pop II stars, while gas below this threshold forms Pop III stars. For Pop III star formation, we place an additional constraint that the molecular hydrogen fraction ($f_{\rm H_2}$) is above 0.005, as consistent with $f_{\rm H_2}$ in high-resolution simulations of Pop III star formation at our adopted $n_{\rm thresh}$ [Susa et al., 2014]. We describe the behaviors for each channel in more detail below.

Our cosmological simulations are *star-by-star* for both Pop III and Pop II stars. This means that in each star formation event, stellar masses are sampled from an adopted initial mass function (IMF) and assigned to individual, distinct stellar particles.

Pop III Star Formation

The initial mass function (IMF) for Pop III stars is still highly uncertain. We adopt the same IMF as used in Wise et al. [2012b], which behaves as a Salpeter [Salpeter, 1955] IMF with power-law slope $\alpha = 2.3$ above a characteristic mass ($M_{\rm char}$), and has an exponential cut-off below $M_{\rm char}$. Motivated by the work in Wise et al. [2012b] and our own trials with varying parameter choices, we adopt a $M_{\rm char} = 10$ M$_\odot$, with a

minimum and maximum Pop III stellar mass of 1 $M_\odot$ and 100 $M_\odot$ respectively for our fiducial simulation. All Pop III star particles represent individual stars over this mass range. Pop III stars are assigned lifetimes from [Schaerer, 2002].

Pop II Star Formation

Above the C and Fe abundance threshold outlined above, gas is considered to be metal-rich enough to form Pop II stars as sampled from a Kroupa [2001] IMF with a minimum mass of 0.08 $M_\odot$ and maximum of 120 $M_\odot$. Due to computational constraints, we restrict which stars over this mass range are followed individually to those with $M_* > 2$ $M_\odot$. All stars below this threshold in a star formation event are aggregated together into a single particle. These stars are those that do not have significant feedback or metal enrichment on the timescale of these simulations ($\sim$ 1 Gyr), but are key tracers of stellar abundances in present-day low mass dwarf galaxies. As in Paper I, we use the zero-age main sequence properties from the PARSEC [Bressan et al., 2012, Tang et al., 2014] stellar evolution data set to assign stellar radii, effective temperature, surface gravity, lifetimes, and AGB-phase length (when relevant).

5.2.3 Stellar Feedback

We follow the detailed multi-channel stellar feedback from each of our stars, including CCSN and PISN from Pop III stars, CCSN, Type Ia SN, AGB winds, and massive star winds from Pop II stars, and stellar radiation followed in three optically-thin bands (IR, FUV, and Lyman-Werner radiation) and HI, HeI, and HeII ionizing radiation followed with an adaptive ray-tracing radiative transfer method including radiation pressure on HI. These methods are discussed in greater detail below.

Stellar Winds and Supernovae

Stellar winds and supernovae are the two sources of both mass and energy feedback included in these simulations. We consider two distinct types of stellar winds, AGB winds and winds from massive stars, and various types of supernovae (core collapse,

Type Ia, and pair instability). The exact mass, metal abundances, and energy deposited for each of these is discussed in separate sections below. Here we discuss how each is deposited onto the computational grid.

We have sufficiently high resolution (1 pc) in these simulations to reliably resolve the Sedov-Taylor phase of a majority of our supernovae for the typical gas densities in which they explode (see Emerick et al. [2019], and also Smith et al. [2018], Hu [2019]). For this reason, we include only the thermal energy deposition from these events. Each particle deposits mass and energy feedback over a 2 pc radius spherical region centered on each particle. We use a Monte-Carlo volume overlap calculation to approximately compute (to high accuracy) the fractional deposition of mass and energy to grid cells that sit on the boundary of the spherical region.

Similarly, stellar winds are deposited in the same 2 pc radius region. The mass loss rates for both AGB stars and massive star winds are adopted from stellar evolution models (discussed below), but are assumed to have fixed velocities over their lifetime. As discussed in Emerick et al. [2019], the computational expense of fully resolving fast (10^3 km s^{-1}), hot (10^6 K) gas that is continually injected onto the grid is too onerous for long-timescale, galaxy-scale simulations. For that reason, we fix the wind velocity for all massive stars to a maximum value of 100 km s^{-1}, and fully thermalize the kinetic energy before injection. While this model would reduce the dynamical impact of winds on the evolution of our galaxies, we expect that stellar winds are subdominant to both stellar radiation feedback and supernovae, and argue this is a reasonable approximation to make.

Stellar Radiation

In addition to the UV background, we follow the star-by-star radiation in six bands, separated by photon energy $E_{\rm ph}$. Due to computational constraints, we limit the number of radiation sources – while capturing a majority of the photon energy budget of our stars – by restricting radiation to massive stars only ($M_* > 8$ M$_\odot$).

We follow the HI ($E_{\rm ph} > 13.6$ eV), HeI ($E_{\rm ph} > 25.6$ eV), and HeII ($E_{\rm ph} > 54.4$ eV) ionizing photons using the ENZO+MORAY adaptive ray-tracing radiative transfer

model described in detail in Wise and Abel [2011] and Bryan et al. [2014]. Briefly, this method integrates the full equations of radiative transfer propogating photons mapped onto a HEALPix grid, adaptive refining once the separation angle between photon packages becomes large.

In addition, we track the stellar IR (0.76 eV $< E_{\rm ph} <$ 5.6 eV), FUV (5.6 eV $< E_{\rm ph} <$ 11.2 eV), and LW (11.2 eV $< E_{\rm ph} <$ 13.6 eV) radiation using an optically thin approximation. This allows us to follow local variations in the H_2 (LW), H_2^+ (IR, FUV, and LW), and H^- (IR) photo-dissociation rates from each band, in addition to the localized photo-electric heating from stellar FUV radiation. These processes are discussed in more detail in Section 5.2.1.

Pop III Stellar Feedback

We use the table of binned photon counts from Heger and Woosley [2010] with the lifetimes in Schaerer [2002] to compute the constant photon fluxes for our Pop III stars in each radiation bin (IR, FUV, and LW, and HI, HeI, and HeII ionizing radiation) as a function of stellar mass. In practice, this is implemented using a piece-wise polynomial fit to these tables. Stars above 100 $M_\odot$ are assumed to have a constant mass to light ratio (see Fig. 1 of Heger and Woosley [2010]).

Pop III core collapse SNe (10 $M_\odot < M_* <$ 100 $M_\odot$) explode with a fixed energy of 10^{51} erg, while PISNe (when present, 140 $M_\odot < M_* <$ 260 $M_\odot$) energies are determined by the fit produced in Eq. 3 of Wise et al. [2012b]. Over this mass range, PISNe explode with energies ranging from about $\sim 6\times10^{51}$ erg to $\sim 93 \times 10^{51}$ erg. Further details and the yields for each of these events are given in Section 5.2.4.

Pop II Stellar Feedback

Our Pop II stellar feedback model is the same as implemented in Emerick et al. [2019], with the exception of the stellar yields detailed in Section 5.2.4, the addition of IR-band radiation, and an updated Type Ia model. In short, we use the PARSEC [Bressan et al., 2012] grid of stellar evolution tracks to set the lifetime of each star and the start time and length of the AGB phase (if present). This is also used to set the

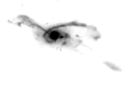

stellar effective temperature, surface gravity, and radius – each of which remain fixed at their zero age main sequence values – which are in turn used to set the radiation properties of each star. Photon fluxes in each radiation band are determined using the OSTAR2002 [Lanz and Hubeny, 2003] grid of O-type stellar models. However, this table does not have complete coverage over all possible stellar properties encounted in these simulations (mainly for stars below about 15 $M_\odot$ and very massive stars with sub-solar metallicity). For the stars off of the grid, we adopt a black-body spectrum with rates scaled to be continuous with the OSTAR2002 grid (see Appendix B of Emerick et al. [2019]). Ionizing photon energies are taken to be the average ionizing photon energy for the corresponding black body spectrum of each star. Stellar wind velocities are fixed to 20 km s^{-1} for AGB stars ($M_* < 8$ $M_\odot$), and 100 km s^{-1} (our wind velocity ceiling, see Section 5.2.3) for massive stars ($M_* > 8$ $M_\odot$). Core collapse supernovae occur for stars between 8 - 25 $M_\odot$ with an energy of 10^{51} erg, and we assume stars more massive than 25 $M_\odot$ direct collapse with no mass or energy feedback.

In Emerick et al. [2019] we used a power-law delay time distribution Type SNIa model assuming a single SNIa channel. We update this model adopting the delay time distribution in Ruiter et al. [2011] (their "standard" model, A1) which gives the total SNIa delay time distribution as the sum of four different channels: 1) double degenerate scenario (DDS), 2) single degenerate scenario (SDS), 3) helium-rich donor scenario (HeRS), and 4) a sub-Chandresekhar mass scenario (sub-M_{ch}). In our model, when stars below 8 $M_\odot$ reach the end of their lives they form white dwarf particles using the initial mass final mass relation of Cummings et al. [2019]. Following Emerick et al. [2019], we assume that stars with initial masses between 3 $M_\odot$ and 8 $M_\odot$ form white dwarfs capable of exploding as SNIa. Given this, the DTD, and our IMF, the fraction of stars capable of forming SNIa progenitors that will explode in a Hubble time is $\eta = 0.1508$ (see Eq. 2 in Emerick et al. [2019]). We pre-tabulate the cumulative probability distribution for both the total DTD and each underlying DTD's. When a WD forms, use a random number draw over the total DTD to set the time (if any) that each SNIa candidate will explode and a separate random number draw to decide

which type. For simplicity, we treat the total energy output for each SNIa the same (10^{51} erg) and differentiate them only by their yields (see Section 5.2.4).

5.2.4 Stellar Yields

We pay careful attention to capturing the detailed chemical evolution driven by nucleosynthesis from distinct yield channels in both Pop III and PopII stars, as detailed below. In total, we track 10 individual metal abundances (in addition to H, He, and the total metallicity): C, N, O, Na, Mg, Ca, Mn, Fe, Sr, and Ba. This well-samples elements from each nucleosynthetic channel, in addition to capturing elements with different mass / metallicity dependence in a given channel. O, Mg, and Ca are produced predominately in CCSN and show a noticeable evolution with supernova progenitor mass, tracing short-timescale (10 Myr) chemical evolution. Fe is produced in both core collapse and Type Ia supernova, and the relative abundances of O, Mg, and Ca to Fe traces the evolution between these two yields sources on timescales of 100 Myr to 1 Gyr. N, Sr, and Ba trace s-process enrichment in low-mass AGB stars on timescales of 100 Myr to 1 Gyr. N and Ba trace the most massive (4-8 $M_{\odot}$) AGB stars, while Sr traces the less massive (< 4 $M_{\odot}$) AGB stars. C has significant production in both low-mass AGB stars and CCSN, but the C to Fe ratio is an important tracer of early Pop III enrichment. All of these elements are readily observed in stellar spectra, with the exception of O, which is the primary tracer of gas-phase abundances.

In addition, we follow tracers tracking the total metal mass in each cell from each yield source in our chemical evolution model: Pop III CCSN, Pop III PISN, AGB winds, massive star ($M > 8$ $M_{\odot}$) winds, Pop II CCSN, and Type Ia SN. Our Type Ia model (discussed in more detail in Section 5.2.4) includes four metal tracers for different Ia progenitor types. We additionally include an r-process yield tracer to post-process r-process abundances. In total – counting the total metallicity field – we follow 20 metal tracer fields.

Pop III Yields

Our Pop III yields are consistent with their feedback properties described above. For the CCSNe from Pop III stars (10 $M_\odot < M_* <$ 100 $M_\odot$), we adopt the yields from Heger and Woosley [2010] and use the PISNe yields from Heger and Woosley [2002]. While the exact fate of Pop III stars in the range ∼70 $M_\odot$-120 $M_\odot$ is uncertain – with some possibly exploding as CCSN, some as PISN, and others undergoing direct collapse with no yield return – it is reasonable to approximate that all of these stars (at least up to 100 $M_\odot$) end their life in a CCSN event [Woosley, 2017].

Much more massive Pop III stars are the likely sources of PISN. In our models that include these events, we follow the Heger and Woosley [2002] model, and assume they occur in stars between 140 $M_\odot$ and 260 $M_\odot$.

Pop II Yields

For AGB winds ($M_* < 8$ $M_\odot$) we adopt the yields of Cristallo et al. [2015], with 8 grid points in $M_* \in [1.3, 6.0]$ $M_\odot$ and 10 in $Z_* \in [1 \times 10^{-4}, 0.02]$. For the winds and CCSNe yields of massive stars, we adopt Limongi and Chieffi [2018], with 9 grid points oevr $M_* \in [13, 120]$ $M_\odot$ and four in $Z \in [3.236 \times 10^{-5}, 0.01345]$. Stellar yields are interpolated linearly between mass and metallicity grid points in each of the tables. For stars with masses outside the mass range sampled by the yield tables, we adopt the abundance ratios of the nearest grid point and scale the yield mass linearly with stellar mass. Yields for stars with metallicities outside the covered range are taken to be the same as the yield of the closest grid point with no extrapolation in Z. This occurs most often at very low metallicities for stars that may have sufficient C and Fe abundance to be considered a Pop II star, but insufficient total metallicity to be beyond the first grid point in the adopted yield set.

The yields models from Limongi and Chieffi [2018] are presented for three different stellar rotations. Rather than accounting for these differences live in our simulations, we adopt a pre-computed mixture model representing a population-averaged yield set using the metallicity-dependent stellar rotation population fractions from Prantzos

et al. [2018]. In order to fully sample the variations in Prantzos et al. [2018] with metallicity, we pre-compute an interpolated mixture model using an additional 3 evenly log-spaced metallicities in between the 4 existing grid points for a total of 13 metallicities.

We adopted this particular set of yield tables based on comparing the results of a one-zone galactic chemical evolution model as applied to a Milky Way mass galaxy. While these yields generally produced reasonable agreement in this model as compared to observations in [X/Fe] vs. [Fe/H] space, Mg is noticeably under-produced in [Mg/Fe] at all [Fe/H], while other α elements tend to agree well. Since one of our primary goals of these simulations is to make detailed observational comparisons, we artificially boost the Mg yield from all massive stars uniformly by a factor of 2.2.

SN Ia Yields

As discussed in 5.2.3, we use a combined delay time distribution from four different sources of Type Ia SNe, each with potentially unique abundance signatures. However, given the uncertainty in yields from each of these sources, we opt instead to make the assumption that there is one yield pattern for each source. This allows us to post-process the abundance patterns from each channel separately. Live in the simulation we assume a single abundance pattern for *all* Type Ia SNe from [Thielemann et al., 1986] and track the contribution of each SN Ia type to the total metallicity as a separate passive scalar tracer field. Given this, and knowing the total number of each SN Ia type that has occurred in the simulation, one can arbitrarily re-scale the abundance patterns for each SN Ia type. Doing so implicitly assumes that the yields for each SN Ia do not affect the dynamical evolution of our galaxies (which it may, for example, by influencing cooling through the Fe abundance), but we do not account for local cooling variations from individual elemental abundances in our simulations anyway.

Dark Matter Halos and Merger Trees

Dark matter subhalos are identified using `ROCKSTAR` [Behroozi et al., 2013b] and mergers trees are constructed by `CONSISTENT-TREES` [Behroozi et al., 2013c]. The halos were assigned a virial mass M_{vir} and radius R_{vir} using the evolution of the virial relation from Bryan and Norman [1998]. To define the "main branch" of a given halo, we trace back the progenitors of the host halo at each simulation time step. At a given time step, the most massive progenitor of the host halo is a member of the "main branch" and all other direct progenitors that merge into main branch halos are the "destroyed subhalos". A subhalo is considered destroyed when it is no longer found by the halo finder.

5.3 Initial Results

The current Aeos simulation is a co-moving 1 Mpc wide volume, simulated from redshift 130 to, presently, 14.5. It has a root-grid resolution of 256^3, a dark matter resolution of 1840 $M_\odot$, and a 1 pc resolution of the gas at the finest scales. Each star greater than 2 $M_\odot$ is represented by a single star particle. The stars and gas have 20 metal tracer fields tracing 10 individual metal abundances and several yield sources (see Section 5.2.4).

5.3.1 Galaxies in the Full Box

At redshift 14.5, the full volume contains 124 star-forming halos of at least $M_{total} > 10^6 M_\odot$ with a total of about $220,000$ star and stellar remnant particles (see Figure 5-1). Pop III star formation begins at $z \sim 28$ and Pop II star formation begins a bit after $z \sim 22$ (see Figure 5-2). Pop II stars, defined as stars with total metals $Z \geq 10^{-5} Z_\odot$, overtake Pop III star formation around $z \sim 17$.

Of the 124 galaxies, the vast majority are tiny, containing stellar masses of a hundred solar masses or fewer. Only one galaxy has a stellar mass greater than $M_* > 10^6 M_\odot$ (see Figure 5-3). 18 of the galaxies have begun forming Pop II stars.

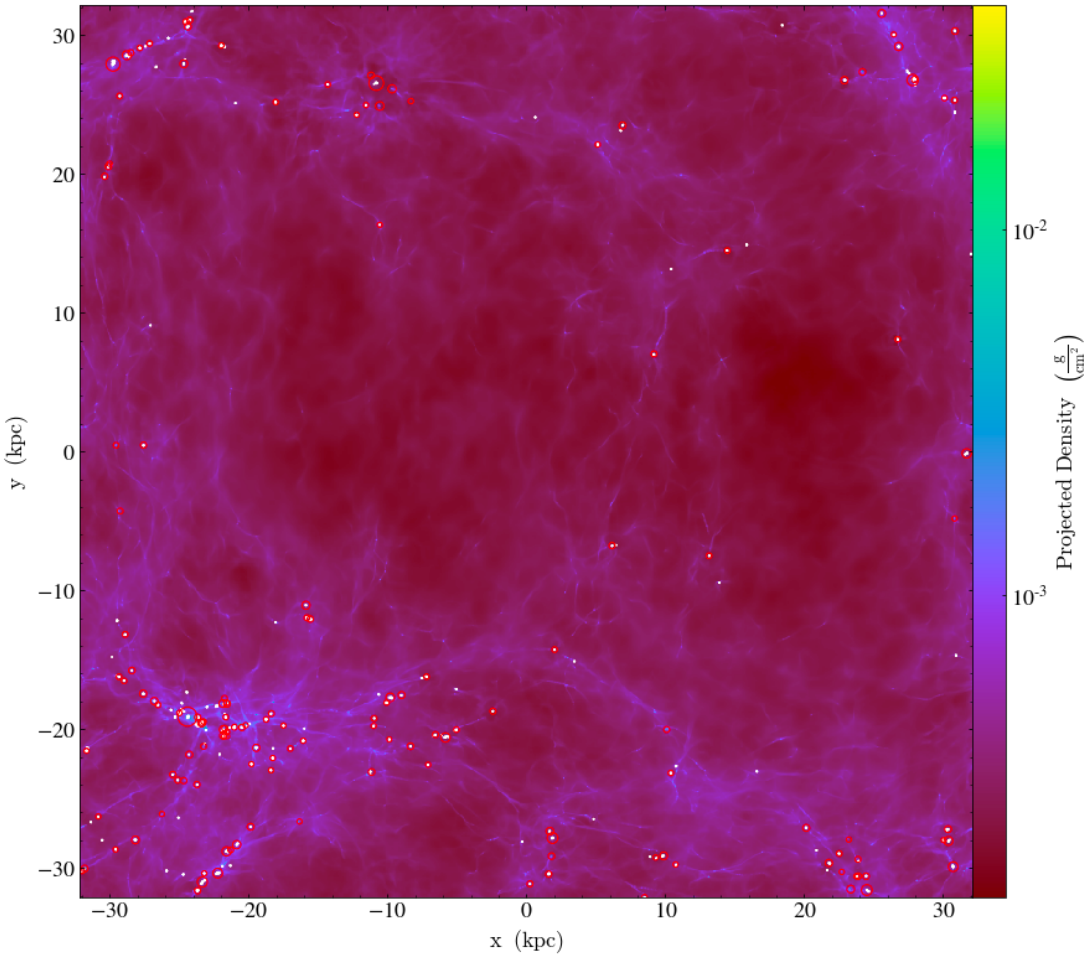

Figure 5-1: Gas projection of the full box simulation at redshift $z = 14.5$. At this redshift, 124 halos contain stars. Each halo is circled in red and the stars are shown as white dots.

For each of these galaxies, the distribution of Pop II vs. Pop III stellar mass is shown in Figure 5-4. Two of these galaxies, Halo 53 and Halo 101, were externally enriched in metals by the larger galaxy they are orbiting. This caused their star formation to begin with Pop II stars.

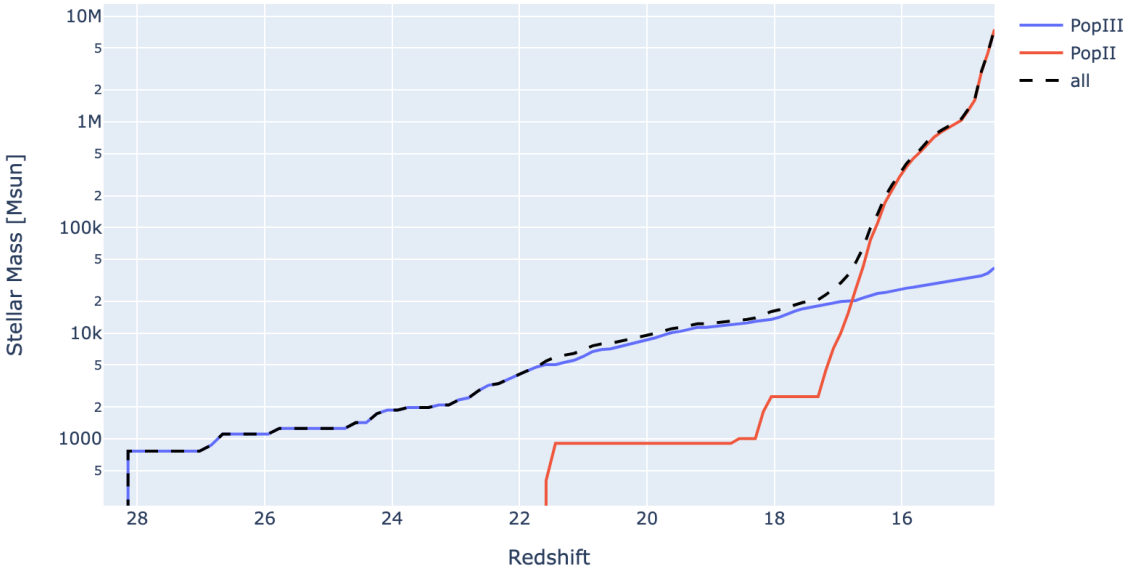

Figure 5-2: Star formation history of the full box simulation at redshift $z = 14.5$.

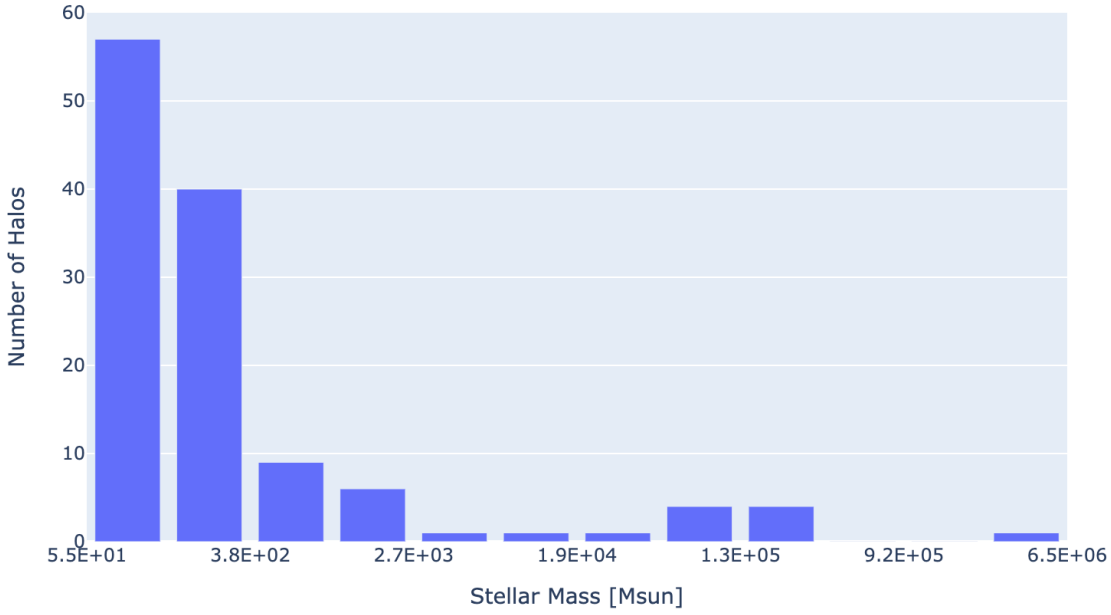

Figure 5-3: Stellar masses of every star-forming halo in the simulation at redshift $z = 14.5$. Only one galaxy has stellar mass $M_* > 10^6 M_\odot$.

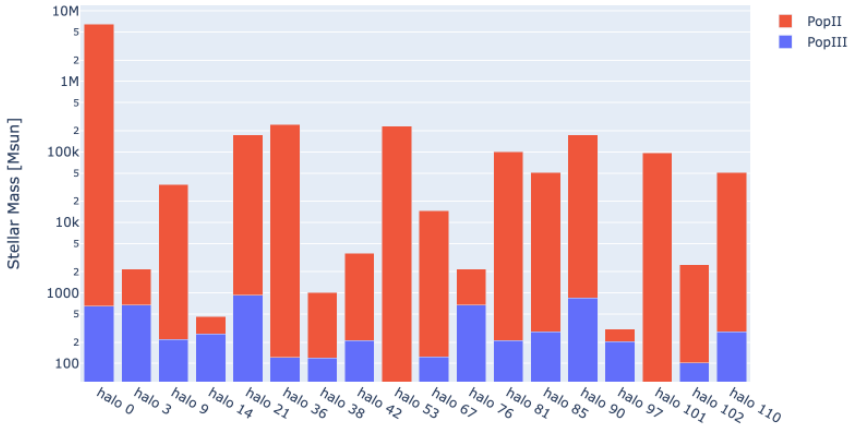

Figure 5-4: For every star-forming halo with Pop II stars, the distribution of Pop II vs. Pop III stellar mass throughout the history of the simulation. Two halos (halo 53 and halo 101) were externally enriched in metals by Halo 0.

5.3.2 Overview of Biggest Galaxy

The majority of the star formation occurs in and around the largest galaxy, henceforth called "Halo 0". This galaxy is the central galaxy in a cluster of several galaxies, including Halo 53 and Halo 101 (the externally enriched satellite galaxies). At $z = 14.5$, Halo 0 has a halo mass of $5.4 \times 10^7 M_\odot$ and a stellar mass of $6.5 \times 10^6 M_\odot$. The median metallicity is [Fe/H] $= -2.1^{+0.1}_{-0.2}$ (with error bars representing 16th to 84th percentile); see Figure 5-5 for the stellar metallicity distribution. See Figure 5-6 for the star formation history and for the halo mass history. Halo 0 started forming stars at redshift $z = 24$ and began Pop II star formation at redshift $z = 17$.

Figure 5-7 top left shows a gas projection of the main galaxy cluster at $z = 14.5$. Top right shows a temperature slice centered on Halo 0. While temperatures around the galaxies can reach higher than $10^6 K$, within the galaxy, temperatures are as low as tens of Kelvin. The bottom two panels show slices of the [Fe/H] and [Mg/Fe] gas abundances as examples of some of the metal fields we trace. The star-forming regions reach metallicities as high as [Fe/H] ~ -2. Many of the metals formed in Halo 0 are lost to outflows (e.g., Figure 5-8), however, hence the external metal enrichment of some of its satellite galaxies.

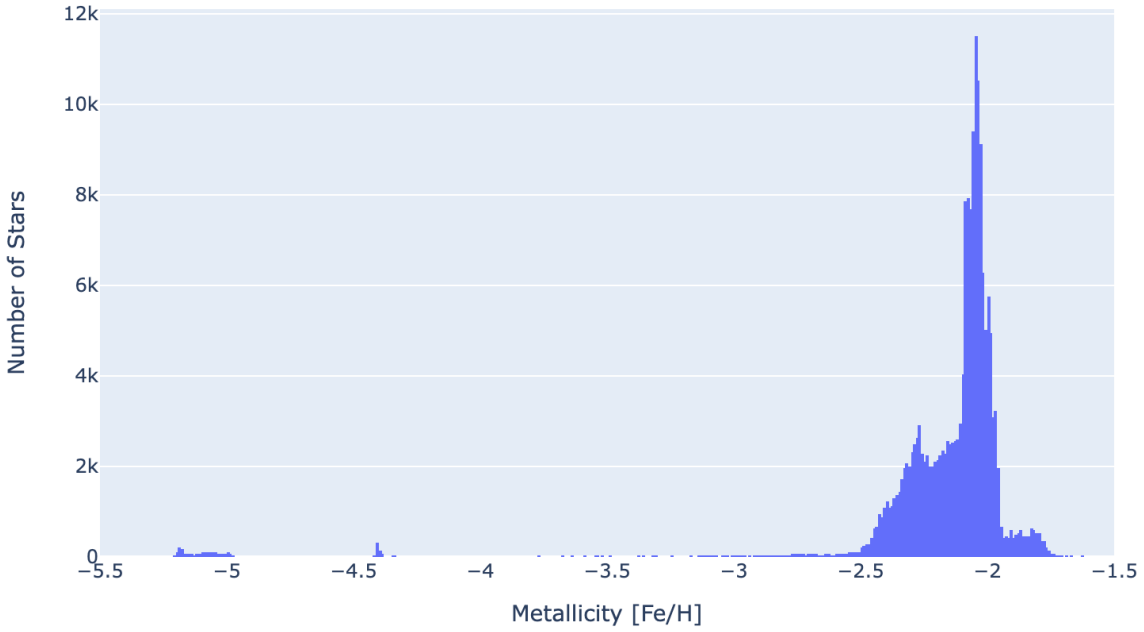

Figure 5-5: Stellar metallicity distribution of the largest galaxy. This plot excludes a single Pop III star which still survives at $z = 14.5$.

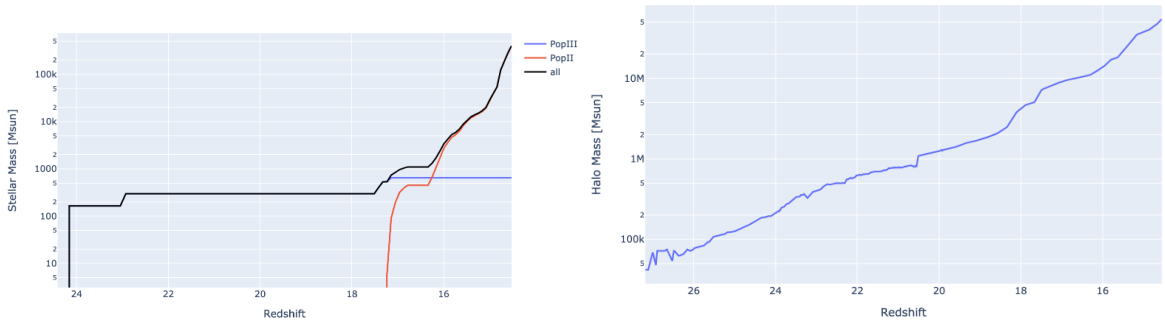

a) Star formation history of Halo 0

b) Halo mass history of Halo 0's main branch

Figure 5-6: Stellar and halo mass histories of the largest galaxy, Halo 0.

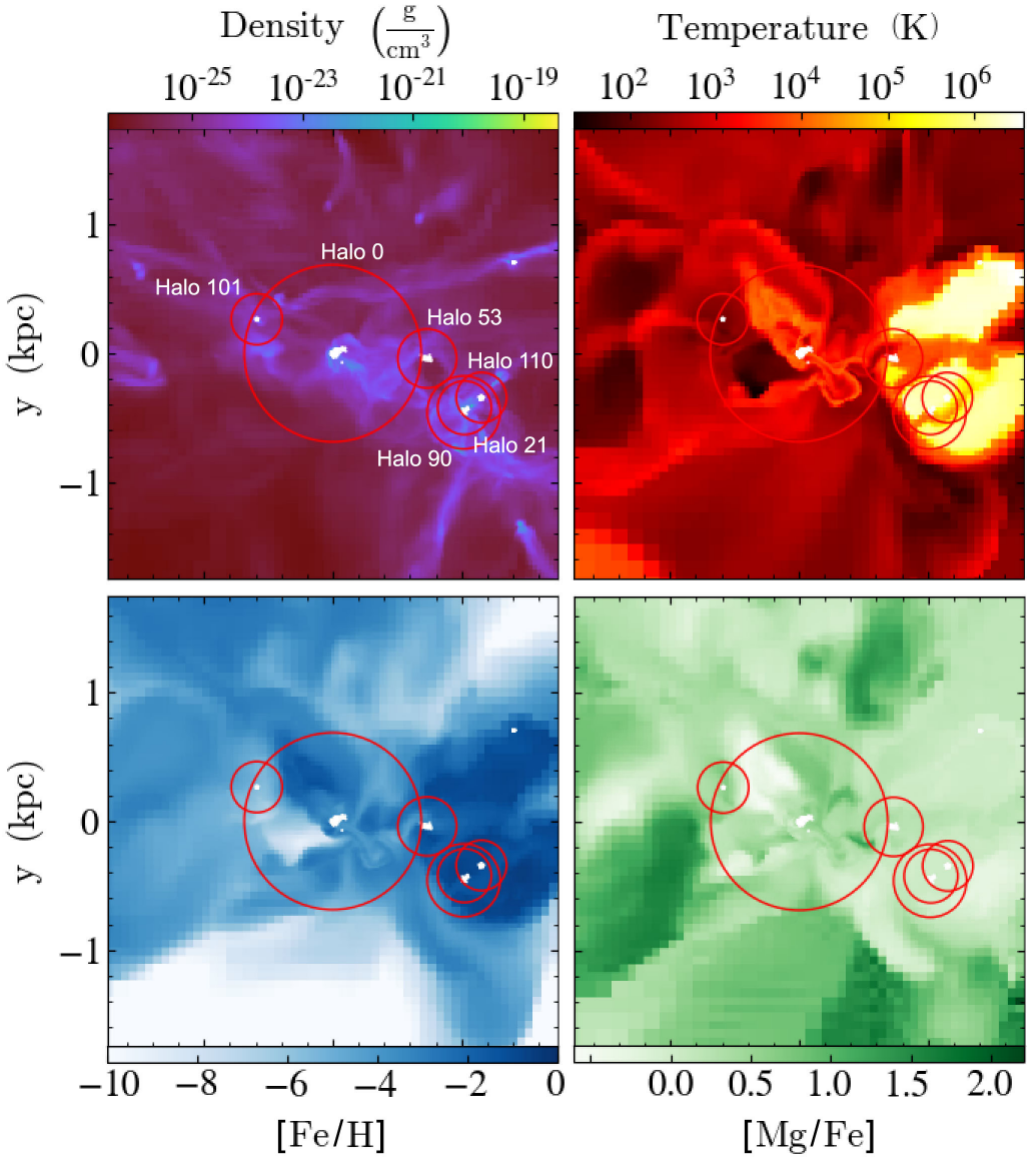

Figure 5-7: Projections and slices of the main galaxy cluster at $z = 14.5$ The largest galaxy, Halo 0, is in the center. The externally enriched galaxies, Halos 53 and 101, are satellites. Top left shows a gas density projection. The top right shows a temperature slice centered on Halo 0. The bottom panels show slices of the [Fe/H] and [Mg/Fe] gas abundances, centered on Halo 0.

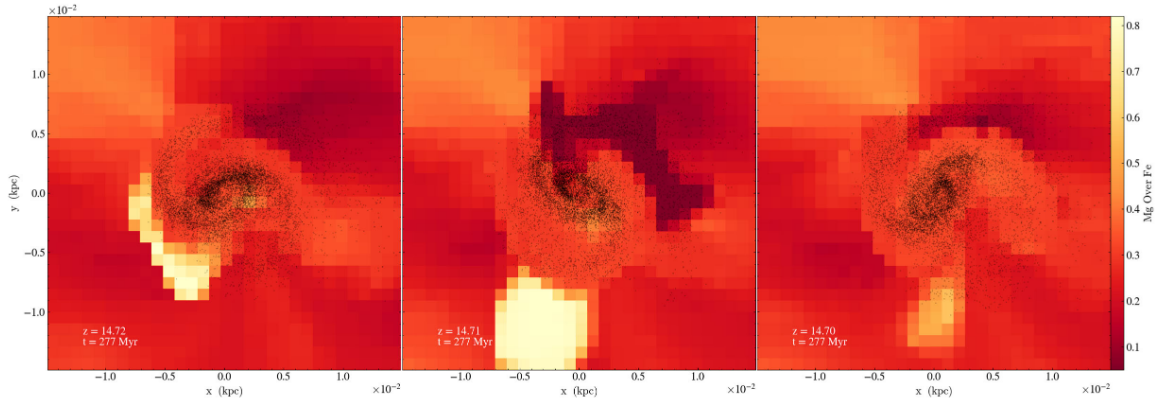

Figure 5-8: Time evolving [Mg/Fe] gas abundances in and directly around Halo 0. Recently formed stars (formed in last 1 Myr) are shown as black dots. The slice is centered on the main galaxy and zoomed in until the 1 pc gas resolution is visible. Magnesium is formed in a supernova and is largely lost from the galaxy through outflows.

5.3.3 Evolution of Chemical Abundances

As discussed in Section 5.2.4, we track 10 individual metal abundances (in addition to H, He, and total metallicity): C, N, O, Na, Mg, Ca, Mn, Fe, Sr, and Ba. This samples from different nucleosynthetic channels and at different mass / metallicity dependence within given channels.

At redshift $z = 14.5$, the main galaxy is primarily forming stars with metallicities between [Fe/H]$= -2.5$ and $= -2$. Many of the metals and some of the gas reservoir are being lost to outflows, resulting in some unexpected evolution in the stellar chemical abundances. For example, several of the more recently formed stars decrease in [Fe/H] and increase in [Mg/Fe] (see Figure 5-9).

There are several clear structures in chemical abundance space. In the [Sr/Fe] stellar abundances (from chemicals formed by AGB stars, see Figure 5-9 and [Ba/Fe] as well), there are three vertical structures at low metallicity. These correspond to three different star-forming clusters within the host galaxy. Also, the horizontal structure from [Fe/H]$= -4$ to $= -2$ forms in the same cluster as the lowest metallicity vertical structure, just a bit later while the metallicity is changing. Structures also exists in the [C/Fe] vs. [Fe/H] stellar abundance space, but with a very low spread

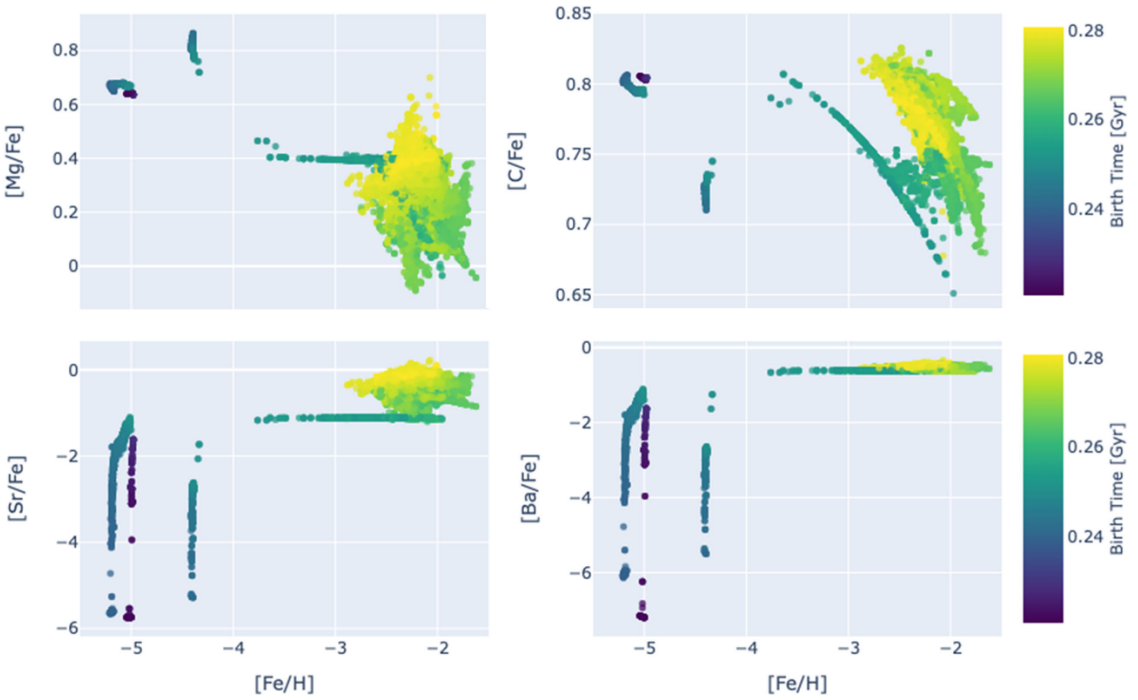

Figure 5-9: Chemical abundances of each star particle in the largest galaxy, colored by their birth time. The top panels show [Mg/Fe] and [C/Fe] vs. [Fe/He], and the bottom panels show [Sr/Fe] and [Ba/Fe] vs. [Fe/H]. The three low [Fe/H] clumps in each panel originate from three different star-forming clusters within the host galaxy.

in [C/Fe]. We expect this is primarily due to the ratio of C and Fe in our Pop III supernovae yield tables.

We note that these plots are somewhat misleading because the vast majority of stars, approximately 100,000 of them, are found in the more recent "blob" located between [Fe/H]$= -2.5$ and $= -2$. See the histogram of stellar metallicities in Figure 5-5.

5.4 Planned Future Work

Using this simulation, I will quantify how metals mix in the interstellar medium of these galaxies, how this affects star formation, and how this varies with different elements and different nucleosynthetic channels to reveal how chemical enrichment proceeds in ultra-faint dwarfs. I will also compare this simulation with individual

star particles to an identical simulation with star cluster particles to determine the effect of different levels of particle resolution on scientific results.

One specific science goal is to determine the origin of chemical abundance scatter in ultra-faint dwarfs. Observations of ultra-faint dwarf galaxy stars reveal scatter in the chemical abundances (e.g., Simon [2019]), but the origin of this scatter is not known. The scatter could be primarily due to differences in galaxy formation history or primarily due to differences in nucleosynthetic yields. Either way, determining the origin of abundance scatter will allow me to use existing data to learn about galaxy formation or chemical enrichment in the early Universe.

For this analysis, I will analyze simulated spreads of abundance patterns in the context of dwarf galaxy observations. This simulation is capable of providing the most realistic ultra-faint dwarf galaxy chemical abundances to-date. This will allow me to answer the important question: what information about early galaxy formation is contained in spreads of stellar abundance patterns observed today? I will explain the stellar abundance scatter we observe and provide new insight into how the dwarf galaxies around us formed.

For each simulated dwarf galaxy stellar population, I will determine the distribution of stellar abundances across the 10 different metals in the simulation. I will compare how the scatter in these distributions differ with variations in galaxy evolution (e.g., merger history, star formation history). I will also quantify the amount of scatter in the distributions that can be explained by differences in the nucleosynthetic yields (e.g., different amounts of barium produced in s- vs. r-process or stochastic differences in yields from single sources). After I quantify the origins of scatter in chemical abundances, I will create physically-motivated analytic models to artificially incorporate scatter in simulations that do not highly-resolve star formation and metal mixing.

Thinking even farther out, additional future analysis will include quantifying the low-mass end of the Milky Way assembly history. The smallest galaxies contributed fewer stars and have far weaker kinematic signatures than larger accreted galaxies (e.g., Chapter 4). To study their remains, we thus must rely mostly on stellar chemi-

cal abundances (e.g., Chapter 2). In particular, the full chemical abundance ratio distributions (CARDs) in the stellar halo should contain information about the Galaxy's assembly history [Cunningham et al., 2022, Lee et al., 2015]. The *Aeos* simulation is ideal to create significantly more realistic chemical abundance ratio distributions for comparison to distributions in the Milky Way stellar halo.

Previous work created templates of CARDs corresponding to different mass galaxies at different redshifts, but used N-body simulations [Lee et al., 2015] or hydrodynamic simulations that do not resolve star formation and metal mixing in small galaxies [Cunningham et al., 2022]. My highly-resolved simulation will provide the opportunity to overcome these previous caveats and create much more realistic simulated chemical abundance distribution templates for small dwarf galaxies. The templates will be produced by directly measuring multi-dimensional chemical abundance ratios of every star particle in different simulated galaxies at different redshifts. These templates will be linearly combined with templates for higher-mass dwarfs to determine which combinations of accreted systems can reproduce observations of the Milky Way stellar halo. Through this, I will estimate the number and properties of dwarf galaxies that merged to form our Milky Way.

Chapter 6

Conclusions

Despite an influx of data on the Milky Way's stellar halo, astronomers still lack ways to reliably identify which stars originated in which dwarf galaxies. This is particularly difficult for the ultra-faint dwarfs (UFDs) because even though they represent $> 90\%$ of all accreted galaxies in the Milky Way, they contributed fewer than 1% of the total number of stars (e.g., Brauer et al. [2022]). These poorly-understood building blocks of the Milky Way are important examples of some of the first galaxies in the Universe, but we are unable to identify their remnants. This thesis determines and explores methods of identifying UFD stars in the Milky Way through chemical abundances and stellar kinematics. I find that stellar chemical abundances are the most promising way to identify UFD stars, especially r-process chemical abundances. Stellar kinematics of stars from accreted UFDs generally have signatures that are too weak to identify. This thesis also investigates collapsars as an alternative source of r-process material and produces a novel cosmological simulation of early galaxy formation with detailed chemical abundances.

6.1 Ultra-Faint Dwarfs and R-Process Enrichment

Because ultra-faint dwarf galaxies contained little gas and formed stars inefficiently, their stars likely have unique chemical abundance signatures. This is supported by observations of highly r-process enhanced surviving UFDs such as Reticulum II (Ji

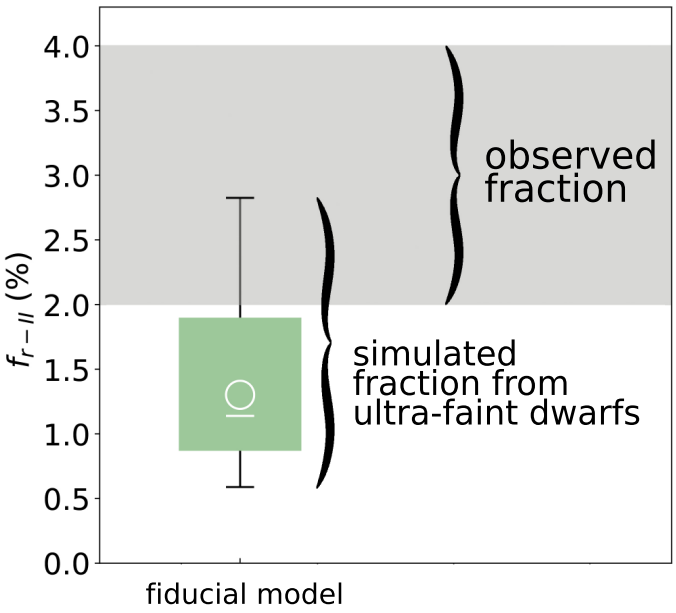

Figure 6-1: Accreted UFD galaxies may have contributed a significant fraction of highly r-process enhanced stars. (Brauer et al. [2019])

et al. [2016a]). In Chapter 2, I explored the possibility of using r-process chemical abundances as a way to identify UFD remnants in the Milky Way stellar halo. Using the *Caterpillar* simulation suite (Griffen et al. [2016]), I modeled the formation of 35 Milky Way stellar halos in which r-process enrichment only occurs in UFDs. I then determined what fraction of metal-poor r-process stars can be accounted for through this single formation pathway.

By only forming highly r-process enhanced stars in UFDs, we accounted for around half of the observed r-process stars in the Milky Way stellar halo. Our simulations produced r-II fractions ($f_{r-II} = \frac{\text{number of metal-poor r-process stars}}{\text{number of metal-poor stars}}$) of $\sim 1.5\%$, compared to the observed Milky Way r-II fraction of $\sim 3\%$ (see Figure 6-1). This implies high r-process enrichment may be strongly linked to small galaxies. R-process enrichment is thus a promising way to identify stars from UFDs to study early galaxy formation and the assembly of the Milky Way.

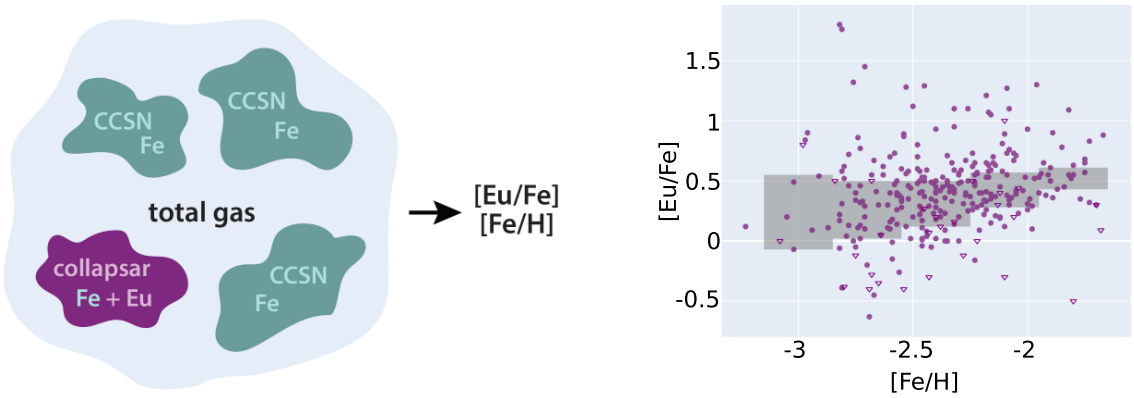

Figure 6-2: Left: A schematic demonstrating my model for europium (Eu) enrichment from collapsars. Right: Observed europium abundances of metal-poor stars and their scatter in different metallicity bins. My model reproduced the observed scatter by assuming enrichment from a single source (collapsars) with stochastic r-process yields. (Brauer et al. [2021])

6.2 r-Process Enrichment in the Early Universe

Neutron star mergers are a confirmed site of the r-process (GW170817; Abbott et al. [2017a]), but it is unclear if they can reproduce observed abundances in metal-poor stars. Concerns around the delay time distribution of neutron star mergers and natal kicks from supernovae imply that neutron star mergers may be incapable of sufficiently enriching early, small galaxies. Collapsars (the supernova- and γ-ray-burst-triggering collapse of rapidly rotating massive stars) are a promising alternative (e.g., Siegel et al. [2019]).

In Chapter 3, I produced a self-consistent analytic model (see Figure 6-2) in which collapsars with stochastic europium yields synthesize all the r-process material in metal-poor ([Fe/H]< -2.5) stars. This model successfully reproduced the observed europium (Eu) scatter across different metallicities. In contrast to other models that produce scatter through different r-process sources, the scatter in this model is produced by a single source (collapsars) with stochastic yields. Fast-merging neutron stars could potentially also fit this model, but these results imply that collapsars could be the dominant source of r-process in the early Universe.

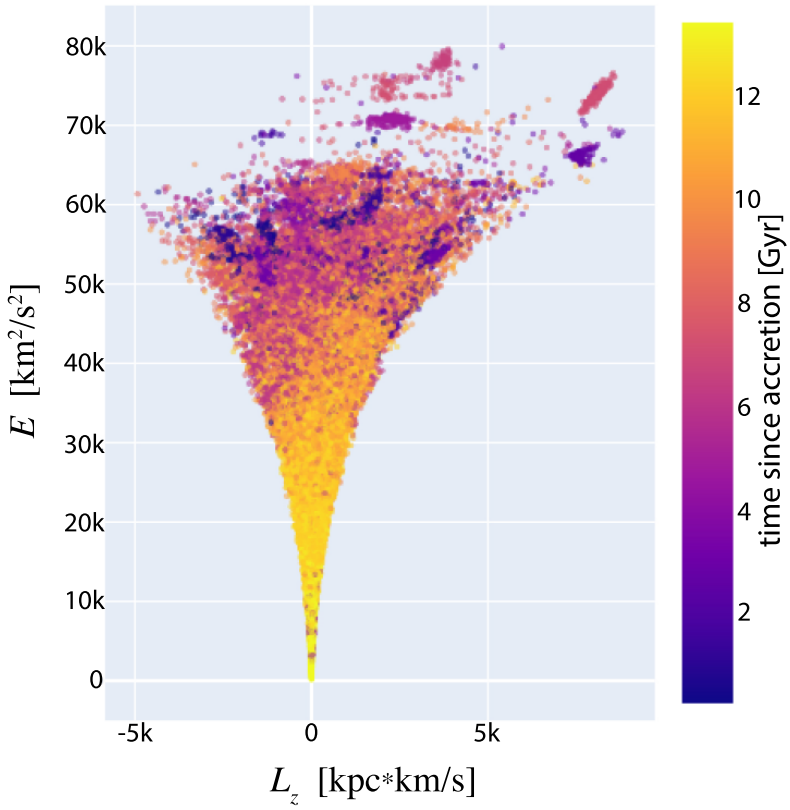

Figure 6-3: Kinematics of simulated stars from accreted ultra-faint dwarfs. The color of each particle corresponds to how long ago it was accreted by the Milky Way-mass host galaxy. Over time, the stars mix more in the phase space and become unidentifiable. (Brauer et al. [2022])

6.3 Ultra-Faint Dwarf Stellar Kinematics

In addition to chemical abundances, stellar kinematics are another way to identify accreted structure in the Milky Way. The orbital actions and energy of a star are quasi-conserved quantities that can, in principle, be used to identify stars that were accreted together. Thanks to Gaia and other large surveys, this method has been extremely successful in recent years in identifying large accreted galaxies (e.g., Belokurov et al. [2018], Helmi et al. [2018], Naidu et al. [2020]). Several groups have also started to use this method to try to identify accreted ultra-faint dwarfs (e.g., Roederer et al. [2018], Gudin et al. [2021]).

In Chapter 4, I explored the possibilities and difficulties of kinematically identify-

ing stars that accreted from UFDs by producing 32 simulated stellar halos of Milky Way-mass galaxies from the *Caterpillar* suite. Each accreted galaxy was tagged and traced to redshift $z = 0$. I then ran clustering algorithms on 4D stellar dynamics to determine how well the remnant galaxies can be recovered. I found that even in highly idealized cases, we only recover $2 - 6\%$ of UFDs remnants. These are UFDs which accreted relatively recently, $z \lesssim 0.5$ (see Figure 6-3). Based on our results, we made recommendations to help guide the search for kinematic groups of tidally-disrupted UFDs. Because the kinematic signatures of these small galaxies are generally unidentifiable, we strongly recommend the use of chemical abundances in future searches for remnants of UFDs.

6.4 Simulating Individual Stars with Detailed Chemical Abundances in Early Galaxies

To study early galaxy formation, we must understand how stellar feedback affects star formation and galaxy evolution in ultra-faint dwarf galaxies. We also must understand how metals mix in the low-metallicity gas of the first galaxies. Current cosmological galaxy simulations do not capture realistic star formation and mixing of the interstellar medium, however. Generally, cosmological simulations represent clusters of stars with a single particle that forms instantaneously and do not resolve metals mixing or detailed metal yields.

To address these problems and produce the most realistic picture of early dwarf galaxy formation to-date, in Chapter 5 I have been extending my previous work to produce, for the first time, a high-resolution cosmological simulation of galaxy formation with individual star particles, individual stellar feedback with detailed stellar yields, and adaptive grids to capture detailed metal mixing in the interstellar medium from the first stars. The simulation is called *Aeos*. Projections and slices of the main galaxy cluster can be seen in Figure 6-4. This is the only simulation that tracks detailed metal yields from individual stars. Currently, we have run a 1 Mpc volume from

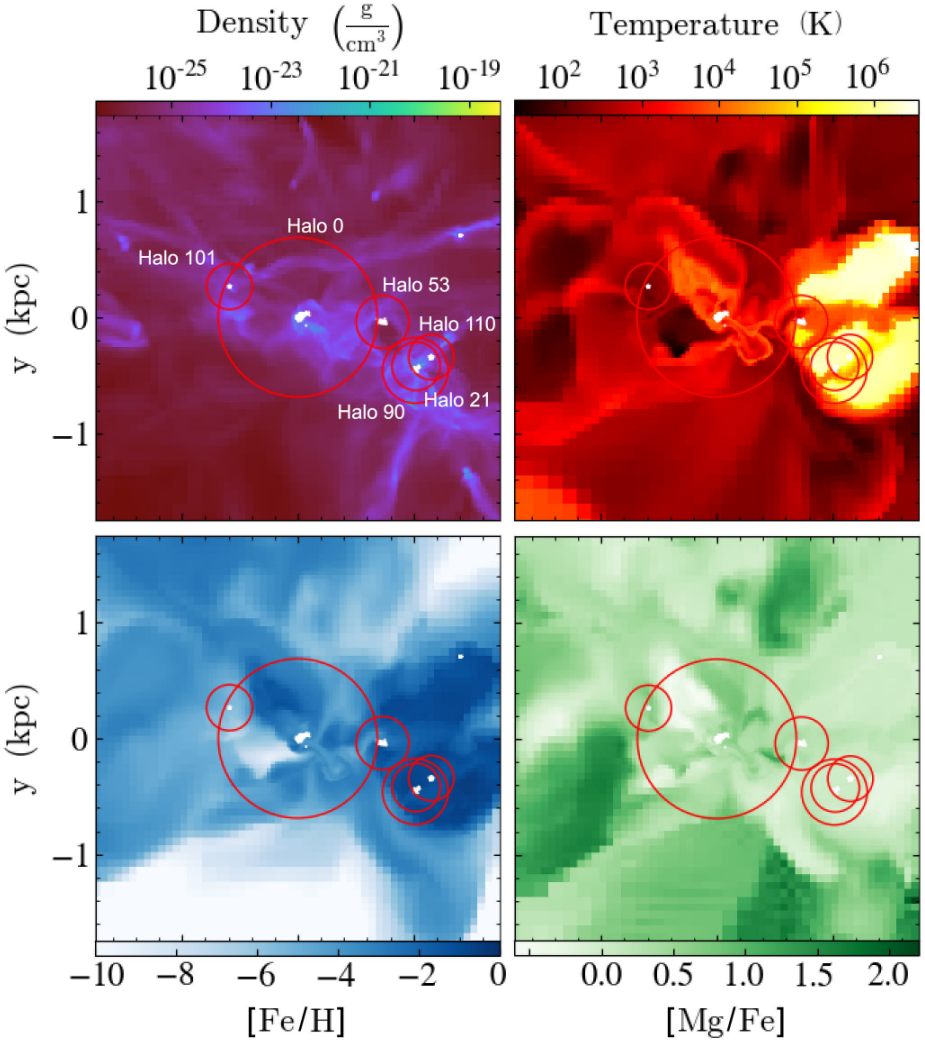

Figure 6-4: Projections and slices of the main galaxy cluster in *Aeos* at $z = 14.5$ The largest galaxy, Halo 0, is in the center and several satellite galaxies are also shown. Stars are shown as white dots. The bottom panels show slices of the [Fe/H] and [Mg/Fe] gas abundances. Fe and Mg are two of the 12 metal abundances tracked in the simulation.

redshift $z = 130$ to $z = 14.5$ and run initial analysis on stellar chemical abundances in the largest galaxy at that time. We identified structures from different progenitor clusters in chemical abundance space and prepared for future work to identify the primary underlying origins of chemical abundance scatter and quantify the low-mass end of the Milky Way assembly history.

Bibliography

B. P. Abbott, R. Abbott, T. D. Abbott, F. Acernese, K. Ackley, C. Adams, T. Adams, P. Addesso, R. X. Adhikari, V. B. Adya, and et al. GW170817: Observation of Gravitational Waves from a Binary Neutron Star Inspiral. *Physical Review Letters*, 119(16):161101, Oct. 2017a. doi: 10.1103/PhysRevLett.119.161101.

B. P. Abbott, R. Abbott, T. D. Abbott, F. Acernese, K. Ackley, C. Adams, T. Adams, P. Addesso, R. X. Adhikari, V. B. Adya, and et al. Multi-messenger Observations of a Binary Neutron Star Merger. *The Astrophysical Journal, Letters*, 848:L12, Oct. 2017b. doi: 10.3847/2041-8213/aa91c9.

A. Abohalima and A. Frebel. JINAbase: A database for chemical abundances of metal-poor stars. *ArXiv e-prints*, Nov. 2017.

N. Afsariardchi, M. R. Drout, D. Khatami, C. D. Matzner, D.-S. Moon, and Y. Q. Ni. The Nickel Mass Distribution of Stripped-Envelope Supernovae: Implications for Additional Power Sources. *arXiv e-prints*, art. arXiv:2009.06683, Sept. 2020.

C. Allende Prieto, A. P. Cooper, A. Dey, B. T. Gänsicke, S. E. Koposov, T. Li, C. Manser, D. L. Nidever, C. Rockosi, M.-Y. Wang, D. S. Aguado, R. Blum, D. Brooks, D. J. Eisenstein, Y. Duan, S. Eftekharzadeh, E. Gaztañaga, R. Kehoe, M. Landriau, C.-H. Lee, M. E. Levi, A. M. Meisner, A. D. Myers, J. Najita, K. Olsen, N. Palanque-Delabrouille, C. Poppett, F. Prada, D. J. Schlegel, M. Schubnell, G. Tarlé, M. Valluri, R. H. Wechsler, and C. Yèche. Preliminary Target Selection for the DESI Milky Way Survey (MWS). *Research Notes of the American Astronomical Society*, 4(10):188, Oct. 2020. doi: 10.3847/2515-5172/abc1dc.

J. P. Anderson. A meta-analysis of core-collapse supernova ^{56}Ni masses. *Astronomy and Astrophysics*, 628:A7, Aug. 2019. doi: 10.1051/0004-6361/201935027.

J. J. Andrews, K. Breivik, C. Pankow, D. J. D'Orazio, and M. Safarzadeh. LISA and the Existence of a Fast-merging Double Neutron Star Formation Channel. *The Astrophysical Journal, Letters*, 892(1):L9, Mar. 2020. doi: 10.3847/2041-8213/ab5b9a.

W. Aoki, S. Honda, T. C. Beers, M. Takada-Hidai, N. Iwamoto, N. Tominaga, H. Umeda, K. Nomoto, J. E. Norris, and S. G. Ryan. Spectroscopic Studies of Extremely Metal-poor Stars with the Subaru High-Dispersion Spectrograph. IV. The α-Element-Enhanced Metal-poor Star BS 16934-002. *The Astrophysical Journal*, 660:747–761, May 2007. doi: 10.1086/512601.

W. Aoki, N. Arimoto, K. Sadakane, E. Tolstoy, G. Battaglia, P. Jablonka, M. Shetrone, B. Letarte, M. Irwin, V. Hill, P. Francois, K. Venn, F. Primas, A. Helmi, A. Kaufer, M. Tafelmeyer, T. Szeifert, and C. Babusiaux. Chemical composition of extremely metal-poor stars in the Sextans dwarf spheroidal galaxy. *Astronomy and Astrophysics*, 502:569–578, Aug. 2009. doi: 10.1051/0004-6361/200911959.

I. Arcavi, A. Gal-Yam, M. M. Kasliwal, R. M. Quimby, E. O. Ofek, S. R. Kulkarni, P. E. Nugent, S. B. Cenko, J. S. Bloom, M. Sullivan, D. A. Howell, D. Poznanski, A. V. Filippenko, N. Law, I. Hook, J. Jönsson, S. Blake, J. Cooke, R. Dekany, G. Rahmer, D. Hale, R. Smith, J. Zolkower, V. Velur, R. Walters, J. Henning, K. Bui, D. McKenna, and J. Jacobsen. Core-collapse Supernovae from the Palomar Transient Factory: Indications for a Different Population in Dwarf Galaxies. *The Astrophysical Journal*, 721(1):777–784, Sept. 2010. doi: 10.1088/0004-637X/721/1/777.

A. Arcones, D. W. Bardayan, T. C. Beers, L. A. Bernstein, J. C. Blackmon, B. Messer, B. A. Brown, E. F. Brown, C. R. Brune, A. E. Champagne, A. Chieffi, A. J. Couture, P. Danielewicz, R. Diehl, M. El-Eid, J. E. Escher, B. D. Fields, C. Fröhlich, F. Herwig, W. R. Hix, C. Iliadis, W. G. Lynch, G. C. McLaughlin, B. S. Meyer, A. Mezzacappa, F. Nunes, B. W. O'Shea, M. Prakash, B. Pritychenko, S. Reddy, E. Rehm, G. Rogachev, R. E. Rutledge, H. Schatz, M. S. Smith, I. H. Stairs, A. W. Steiner, T. E. Strohmayer, F. X. Timmes, D. M. Townsley, M. Wiescher, R. G. T. Zegers, and M. Zingale. White paper on nuclear astrophysics and low energy nuclear physics Part 1: Nuclear astrophysics. *Progress in Particle and Nuclear Physics*, 94: 1–67, May 2017. doi: 10.1016/j.ppnp.2016.12.003.

D. Argast, M. Samland, F.-K. Thielemann, and Y.-Z. Qian. Neutron star mergers versus core-collapse supernovae as dominant r-process sites in the early Galaxy. *Astronomy and Astrophysics*, 416:997–1011, Mar. 2004. doi: 10.1051/0004-6361:20034265.

M. Arnould, S. Goriely, and K. Takahashi. The r-process of stellar nucleosynthesis: Astrophysics and nuclear physics achievements and mysteries. *Physics Reports*, 450:97–213, Sept. 2007. doi: 10.1016/j.physrep.2007.06.002.

M. Asplund, N. Grevesse, A. J. Sauval, and P. Scott. The Chemical Composition of the Sun. *Annual Review of Astronomy and Astrophysics*, 47:481–522, Sept. 2009. doi: 10.1146/annurev.astro.46.060407.145222.

D. Aubert, N. Deparis, P. Ocvirk, P. R. Shapiro, I. T. Iliev, G. Yepes, S. Gottlöber, Y. Hoffman, and R. Teyssier. The Inhomogeneous Reionization Times of Present-day Galaxies. *The Astrophysical Journal*, 856:L22, Apr. 2018. doi: 10.3847/2041-8213/aab14d.

J. Bailin, E. F. Bell, M. Valluri, G. S. Stinson, V. P. Debattista, H. M. P. Couchman, and J. Wadsley. Systematic Problems with Using Dark Matter Simulations

to Model Stellar Halos. *The Astrophysical Journal*, 783(2):95, Mar. 2014. doi: 10.1088/0004-637X/783/2/95.

P. S. Barklem, N. Christlieb, T. C. Beers, V. Hill, M. S. Bessell, J. Holmberg, B. Marsteller, S. Rossi, F. J. Zickgraf, and D. Reimers. The Hamburg/ESO R-process enhanced star survey (HERES). II. Spectroscopic analysis of the survey sample. *Astronomy and Astrophysics*, 439:129–151, Aug. 2005. doi: 10.1051/0004-6361:20052967.

J. Barnes, P. C. Duffell, Y. Liu, M. Modjaz, F. B. Bianco, D. Kasen, and A. I. MacFadyen. A GRB and Broad-lined Type Ic Supernova from a Single Central Engine. *The Astrophysical Journal*, 860(1):38, June 2018. doi: 10.3847/1538-4357/aabf84.

A. Bauswein, S. Goriely, and H.-T. Janka. Systematics of Dynamical Mass Ejection, Nucleosynthesis, and Radioactively Powered Electromagnetic Signals from Neutron-star Mergers. *The Astrophysical Journal*, 773:78, Aug. 2013. doi: 10.1088/0004-637X/773/1/78.

K. Bechtol, A. Drlica-Wagner, E. Balbinot, A. Pieres, J. D. Simon, B. Yanny, B. Santiago, R. H. Wechsler, J. Frieman, A. R. Walker, P. Williams, E. Rozo, E. S. Rykoff, A. Queiroz, E. Luque, A. Benoit-Lévy, D. Tucker, I. Sevilla, R. A. Gruendl, L. N. da Costa, A. Fausti Neto, M. A. G. Maia, T. Abbott, S. Allam, R. Armstrong, A. H. Bauer, G. M. Bernstein, R. A. Bernstein, E. Bertin, D. Brooks, E. Buckley-Geer, D. L. Burke, A. Carnero Rosell, F. J. Castander, R. Covarrubias, C. B. D'Andrea, D. L. DePoy, S. Desai, H. T. Diehl, T. F. Eifler, J. Estrada, A. E. Evrard, E. Fernandez, D. A. Finley, B. Flaugher, E. Gaztanaga, D. Gerdes, L. Girardi, M. Gladders, D. Gruen, G. Gutierrez, J. Hao, K. Honscheid, B. Jain, D. James, S. Kent, R. Kron, K. Kuehn, N. Kuropatkin, O. Lahav, T. S. Li, H. Lin, M. Makler, M. March, J. Marshall, P. Martini, K. W. Merritt, C. Miller, R. Miquel, J. Mohr, E. Neilsen, R. Nichol, B. Nord, R. Ogando, J. Peoples, D. Petravick, A. A. Plazas, A. K. Romer, A. Roodman, M. Sako, E. Sanchez, V. Scarpine, M. Schubnell, R. C. Smith, M. Soares-Santos, F. Sobreira, E. Suchyta, M. E. C. Swanson, G. Tarle, J. Thaler, D. Thomas, W. Wester, J. Zuntz, and The DES Collaboration. Eight New Milky Way Companions Discovered in First-year Dark Energy Survey Data. *The Astrophysical Journal*, 807:50, July 2015. doi: 10.1088/0004-637X/807/1/50.

T. C. Beers and N. Christlieb. The Discovery and Analysis of Very Metal-Poor Stars in the Galaxy. *Annual Review of Astronomy and Astrophysics*, 43:531–580, Sept. 2005. doi: 10.1146/annurev.astro.42.053102.134057.

P. S. Behroozi, R. H. Wechsler, and C. Conroy. The Average Star Formation Histories of Galaxies in Dark Matter Halos from z = 0-8. *The Astrophysical Journal*, 770: 57, June 2013a. doi: 10.1088/0004-637X/770/1/57.

P. S. Behroozi, R. H. Wechsler, and H.-Y. Wu. The ROCKSTAR Phase-space Temporal Halo Finder and the Velocity Offsets of Cluster Cores. *The Astrophysical Journal*, 762:109, Jan. 2013b. doi: 10.1088/0004-637X/762/2/109.

P. S. Behroozi, R. H. Wechsler, H.-Y. Wu, M. T. Busha, A. A. Klypin, and J. R. Primack. Gravitationally Consistent Halo Catalogs and Merger Trees for Precision Cosmology. *The Astrophysical Journal*, 763:18, Jan. 2013c. doi: 10.1088/0004-637X/763/1/18.

K. Belczynski, A. Askar, M. Arca-Sedda, M. Chruslinska, M. Donnari, M. Giersz, M. Benacquista, R. Spurzem, D. Jin, G. Wiktorowicz, and D. Belloni. The origin of the first neutron star - neutron star merger. *Astronomy and Astrophysics*, 615: A91, July 2018. doi: 10.1051/0004-6361/201732428.

E. F. Bell, D. B. Zucker, V. Belokurov, S. Sharma, K. V. Johnston, J. S. Bullock, D. W. Hogg, K. Jahnke, J. T. A. de Jong, T. C. Beers, N. W. Evans, E. K. Grebel, Ž. Ivezić, S. E. Koposov, H.-W. Rix, D. P. Schneider, M. Steinmetz, and A. Zolotov. The Accretion Origin of the Milky Way's Stellar Halo. *The Astrophysical Journal*, 680:295–311, June 2008. doi: 10.1086/588032.

V. Belokurov, D. Erkal, N. W. Evans, S. E. Koposov, and A. J. Deason. Co-formation of the disc and the stellar halo. *Monthly Notices of the Astronomical Society*, 478 (1):611–619, July 2018. doi: 10.1093/mnras/sty982.

P. Beniamini, K. Hotokezaka, and T. Piran. Natal Kicks and Time Delays in Merging Neutron Star Binaries: Implications for r-process Nucleosynthesis in Ultra-faint Dwarfs and in the Milky Way. *The Astrophysical Journal, Letters*, 829:L13, Sept. 2016. doi: 10.3847/2041-8205/829/1/L13.

J. Binney. Actions for axisymmetric potentials. *Monthly Notices of the Astronomical Society*, 426(2):1324–1327, Oct. 2012. doi: 10.1111/j.1365-2966.2012.21757.x.

J. Binney and S. Tremaine. *Galactic Dynamics: Second Edition*. 2008.

A. Bonaca, C. Conroy, A. Wetzel, P. F. Hopkins, and D. Kereš. Gaia Reveals a Metal-rich, in situ Component of the Local Stellar Halo. *The Astrophysical Journal*, 845: 101, Aug. 2017. doi: 10.3847/1538-4357/aa7d0c.

M. Bonetti, A. Perego, M. Dotti, and G. Cescutti. Neutron star binary orbits in their host potential: effect on early r-process enrichment. *Monthly Notices of the Astronomical Society*, 490(1):296–311, Nov. 2019. doi: 10.1093/mnras/stz2554.

M. S. Bovill and M. Ricotti. Where are the Fossils of the First Galaxies? II. True Fossils, Ghost Halos, and the Missing Bright Satellites. *The Astrophysical Journal*, 741:18, Nov. 2011. doi: 10.1088/0004-637X/741/1/18.

M. Boylan-Kolchin, D. R. Weisz, J. S. Bullock, and M. C. Cooper. The Local Group: the ultimate deep field. *Monthly Notices of the Astronomical Society*, 462(1):L51–L55, Oct. 2016. doi: 10.1093/mnrasl/slw121.

J. Bramante and T. Linden. On the R-Process Enrichment of Dwarf Spheroidal Galaxies. *ArXiv e-prints*, Jan. 2016.

K. Brauer, A. P. Ji, A. Frebel, G. A. Dooley, F. A. Gómez, and B. W. O'Shea. The Origin of r-process Enhanced Metal-poor Halo Stars In Now-destroyed Ultra-faint Dwarf Galaxies. *The Astrophysical Journal*, 871(2):247, Feb. 2019. doi: 10.3847/1538-4357/aafafb.

K. Brauer, A. P. Ji, M. R. Drout, and A. Frebel. Collapsar R-process Yields Can Reproduce [Eu/Fe] Abundance Scatter in Metal-poor Stars. *The Astrophysical Journal*, 915(2):81, July 2021. doi: 10.3847/1538-4357/ac00b2.

K. Brauer, H. D. Andales, A. P. Ji, A. Frebel, M. K. Mardini, F. A. Gómez, and B. W. O'Shea. Possibilities and Limitations of Kinematically Identifying Stars from Accreted Ultra-faint Dwarf Galaxies. *The Astrophysical Journal*, 937(1):14, Sept. 2022. doi: 10.3847/1538-4357/ac85b9.

A. Bressan, P. Marigo, L. Girardi, B. Salasnich, C. Dal Cero, S. Rubele, and A. Nanni. PARSEC: stellar tracks and isochrones with the PAdova and TRieste Stellar Evolution Code. *Monthly Notices of the Astronomical Society*, 427:127–145, Nov. 2012. doi: 10.1111/j.1365-2966.2012.21948.x.

O. Bromberg, E. Nakar, and T. Piran. Are Low-luminosity Gamma-Ray Bursts Generated by Relativistic Jets? *The Astrophysical Journal, Letters*, 739(2):L55, Oct. 2011. doi: 10.1088/2041-8205/739/2/L55.

V. Bromm and N. Yoshida. The First Galaxies. *Annual Review of Astronomy and Astrophysics*, 49:373–407, Sept. 2011. doi: 10.1146/annurev-astro-081710-102608.

C. B. Brook, A. Di Cintio, A. Knebe, S. Gottlöber, Y. Hoffman, G. Yepes, and S. Garrison-Kimmel. The Stellar-to-halo Mass Relation for Local Group Galaxies. *The Astrophysical Journal, Letters*, 784:L14, Mar. 2014. doi: 10.1088/2041-8205/784/1/L14.

T. M. Brown, J. Tumlinson, M. Geha, J. D. Simon, L. C. Vargas, D. A. VandenBerg, E. N. Kirby, J. S. Kalirai, R. J. Avila, M. Gennaro, H. C. Ferguson, R. R. Muñoz, P. Guhathakurta, and A. Renzini. The Quenching of the Ultra-faint Dwarf Galaxies in the Reionization Era. *The Astrophysical Journal*, 796:91, Dec. 2014. doi: 10.1088/0004-637X/796/2/91.

G. L. Bryan and M. L. Norman. Statistical Properties of X-Ray Clusters: Analytic and Numerical Comparisons. *The Astrophysical Journal*, 495:80–99, Mar. 1998. doi: 10.1086/305262.

G. L. Bryan, M. L. Norman, B. W. O'Shea, T. Abel, J. H. Wise, M. J. Turk, D. R. Reynolds, D. C. Collins, P. Wang, S. W. Skillman, B. Smith, R. P. Harkness, J. Bordner, J.-h. Kim, M. Kuhlen, H. Xu, N. Goldbaum, C. Hummels, A. G. Kritsuk, E. Tasker, S. Skory, C. M. Simpson, O. Hahn, J. S. Oishi, G. C. So, F. Zhao, R. Cen, Y. Li, and The Enzo Collaboration. ENZO: An Adaptive Mesh Refinement Code for Astrophysics. *The Astrophysical Journal, Supplement*, 211: 19, Apr. 2014. doi: 10.1088/0067-0049/211/2/19.

J. S. Bullock and K. V. Johnston. Tracing Galaxy Formation with Stellar Halos. I. Methods. *The Astrophysical Journal*, 635:931–949, Dec. 2005. doi: 10.1086/497422.

E. M. Burbidge, G. R. Burbidge, W. A. Fowler, and F. Hoyle. Synthesis of the Elements in Stars. *Reviews of Modern Physics*, 29:547–650, 1957. doi: 10.1103/RevModPhys.29.547.

M. Busso, R. Gallino, and G. J. Wasserburg. Nucleosynthesis in Asymptotic Giant Branch Stars: Relevance for Galactic Enrichment and Solar System Formation. *Annual Review of Astronomy and Astrophysics*, 37:239–309, Jan. 1999. doi: 10.1146/annurev.astro.37.1.239.

A. G. W. Cameron. Nuclear Reactions in Stars and Nucleogenesis. *Publications of the Astronomical Society of the Pacific*, 69:201, June 1957. doi: 10.1086/127051.

R. J. Campello, D. Moulavi, A. Zimek, and J. Sander. Hierarchical density estimates for data clustering, visualization, and outlier detection. *ACM Transactions on Knowledge Discovery from Data (TKDD)*, 10(1):1–51, 2015.

D. Carollo, T. C. Beers, M. Chiba, J. E. Norris, K. C. Freeman, Y. S. Lee, Ž. Ivezić, C. M. Rockosi, and B. Yanny. Structure and Kinematics of the Stellar Halos and Thick Disks of the Milky Way Based on Calibration Stars from Sloan Digital Sky Survey DR7. *The Astrophysical Journal*, 712:692–727, Mar. 2010. doi: 10.1088/0004-637X/712/1/692.

G. Cescutti, D. Romano, F. Matteucci, C. Chiappini, and R. Hirschi. The role of neutron star mergers in the chemical evolution of the Galactic halo. *Astronomy and Astrophysics*, 577:A139, May 2015. doi: 10.1051/0004-6361/201525698.

S. V. Chaurasia, T. Dietrich, N. K. Johnson-McDaniel, M. Ujevic, W. Tichy, and B. Brügmann. Gravitational waves and mass ejecta from binary neutron star mergers: Effect of large eccentricities. *Physical Review D: Particles, Fields, Gravitation and Cosmology*, 98(10):104005, Nov. 2018. doi: 10.1103/PhysRevD.98.104005.

G. Chiaki and J. H. Wise. Seeding the second star: enrichment from population III, dust evolution, and cloud collapse. *Monthly Notices of the Astronomical Society*, 482(3):3933–3949, Jan. 2019. doi: 10.1093/mnras/sty2984.

A. Chiti, A. Frebel, A. P. Ji, H. Jerjen, D. Kim, and J. E. Norris. Chemical Abundances of New Member Stars in the Tucana II Dwarf Galaxy. *The Astrophysical Journal*, 857:74, Apr. 2018. doi: 10.3847/1538-4357/aab4fc.

J. G. Cohen and W. Huang. The Chemical Evolution of the Draco Dwarf Spheroidal Galaxy. *The Astrophysical Journal*, 701:1053–1075, Aug. 2009. doi: 10.1088/0004-637X/701/2/1053.

J. G. Cohen and W. Huang. The Chemical Evolution of the Ursa Minor Dwarf Spheroidal Galaxy. *The Astrophysical Journal*, 719:931–949, Aug. 2010. doi: 10.1088/0004-637X/719/1/931.

D. Comaniciu and P. Meer. Mean shift: A robust approach toward feature space analysis. *IEEE Transactions on pattern analysis and machine intelligence*, 24(5): 603–619, 2002.

C. Conroy, A. Bonaca, P. Cargile, B. D. Johnson, N. Caldwell, R. P. Naidu, D. Zaritsky, D. Fabricant, S. Moran, J. Rhee, A. Szentgyorgyi, P. Berlind, M. L. Calkins, S. Kattner, and C. Ly. Mapping the Stellar Halo with the H3 Spectroscopic Survey. *The Astrophysical Journal*, 883(1):107, Sept. 2019. doi: 10.3847/1538-4357/ab38b8.

A. P. Cooper, S. Cole, C. S. Frenk, S. D. M. White, J. Helly, A. J. Benson, G. De Lucia, A. Helmi, A. Jenkins, J. F. Navarro, V. Springel, and J. Wang. Galactic stellar haloes in the CDM model. *Monthly Notices of the Astronomical Society*, 406 (2):744–766, Aug. 2010. doi: 10.1111/j.1365-2966.2010.16740.x.

A. P. Cooper, O. H. Parry, B. Lowing, S. Cole, and C. Frenk. Formation of in situ stellar haloes in Milky Way-mass galaxies. *Monthly Notices of the Astronomical Society*, 454:3185–3199, Dec. 2015. doi: 10.1093/mnras/stv2057.

A. P. Cooper, S. Cole, C. S. Frenk, T. Le Bret, and A. Pontzen. Comparing semi-analytic particle tagging and hydrodynamical simulations of the Milky Way's stellar halo. *Monthly Notices of the Astronomical Society*, 469(2):1691–1712, Aug. 2017. doi: 10.1093/mnras/stx955.

B. Côté and C. Ritter. OMEGA: One-zone Model for the Evolution of GAlaxies. Astrophysics Source Code Library, record ascl:1806.018, June 2018.

B. Côté, C. L. Fryer, K. Belczynski, O. Korobkin, M. Chruślińska, N. Vassh, M. R. Mumpower, J. Lippuner, T. M. Sprouse, R. Surman, and R. Wollaeger. The Origin of r-process Elements in the Milky Way. *The Astrophysical Journal*, 855:99, Mar. 2018a. doi: 10.3847/1538-4357/aaad67.

B. Côté, C. L. Fryer, K. Belczynski, O. Korobkin, M. Chruślińska, N. Vassh, M. R. Mumpower, J. Lippuner, T. M. Sprouse, R. Surman, and R. Wollaeger. The Origin of r-process Elements in the Milky Way. *The Astrophysical Journal*, 855(2):99, Mar. 2018b. doi: 10.3847/1538-4357/aaad67.

D. A. Coulter, R. J. Foley, C. D. Kilpatrick, M. R. Drout, A. L. Piro, B. J. Shappee, M. R. Siebert, J. D. Simon, N. Ulloa, D. Kasen, B. F. Madore, A. Murguia-Berthier, Y. C. Pan, J. X. Prochaska, E. Ramirez-Ruiz, A. Rest, and C. Rojas-Bravo. Swope Supernova Survey 2017a (SSS17a), the optical counterpart to a gravitational wave source. *Science*, 358(6370):1556–1558, Dec. 2017. doi: 10.1126/science.aap9811.

J. J. Cowan, C. Sneden, J. E. Lawler, A. Aprahamian, M. Wiescher, K. Langanke, G. Martínez-Pinedo, and F.-K. Thielemann. Origin of the heaviest elements: The rapid neutron-capture process. *Reviews of Modern Physics*, 93(1):015002, Jan. 2021. doi: 10.1103/RevModPhys.93.015002.

S. Cristallo, O. Straniero, L. Piersanti, and D. Gobrecht. Evolution, Nucleosynthesis, and Yields of AGB Stars at Different Metallicities. III. Intermediate-mass Models, Revised Low-mass Models, and the ph-FRUITY Interface. *The Astrophysical Journal, Supplement*, 219(2):40, Aug. 2015. doi: 10.1088/0067-0049/219/2/40.

X.-Q. Cui, Y.-H. Zhao, Y.-Q. Chu, G.-P. Li, Q. Li, L.-P. Zhang, H.-J. Su, Z.-Q. Yao, Y.-N. Wang, X.-Z. Xing, X.-N. Li, Y.-T. Zhu, G. Wang, B.-Z. Gu, A. L. Luo, X.-Q. Xu, Z.-C. Zhang, G.-R. Liu, H.-T. Zhang, D.-H. Yang, S.-Y. Cao, H.-Y. Chen, J.-J. Chen, K.-X. Chen, Y. Chen, J.-R. Chu, L. Feng, X.-F. Gong, Y.-H. Hou, H.-Z. Hu, N.-S. Hu, Z.-W. Hu, L. Jia, F.-H. Jiang, X. Jiang, Z.-B. Jiang, G. Jin, A.-H. Li, Y. Li, Y.-P. Li, G.-Q. Liu, Z.-G. Liu, W.-Z. Lu, Y.-D. Mao, L. Men, Y.-J. Qi, Z.-X. Qi, H.-M. Shi, Z.-H. Tang, Q.-S. Tao, D.-Q. Wang, D. Wang, G.-M. Wang, H. Wang, J.-N. Wang, J. Wang, J.-L. Wang, J.-P. Wang, L. Wang, S.-Q. Wang, Y. Wang, Y.-F. Wang, L.-Z. Xu, Y. Xu, S.-H. Yang, Y. Yu, H. Yuan, X.-Y. Yuan, C. Zhai, J. Zhang, Y.-X. Zhang, Y. Zhang, M. Zhao, F. Zhou, G.-H. Zhou, J. Zhu, and S.-C. Zou. The Large Sky Area Multi-Object Fiber Spectroscopic Telescope (LAMOST). *Research in Astronomy and Astrophysics*, 12(9):1197–1242, Sept. 2012. doi: 10.1088/1674-4527/12/9/003.

J. D. Cummings, J. S. Kalirai, J. Choi, C. Georgy, P. E. Tremblay, and E. Ramirez-Ruiz. A Novel Approach to Constrain Rotational Mixing and Convective-core Overshoot in Stars Using the Initial-Final Mass Relation. *The Astrophysical Journal, Letters*, 871(1):L18, Jan. 2019. doi: 10.3847/2041-8213/aafc2d.

E. C. Cunningham, R. E. Sanderson, K. V. Johnston, N. Panithanpaisal, M. K. Ness, A. Wetzel, S. R. Loebman, I. Escala, D. Horta, and C.-A. Faucher-Giguère. Reading the CARDs: The Imprint of Accretion History in the Chemical Abundances of the Milky Way's Stellar Halo. *The Astrophysical Journal*, 934(2):172, Aug. 2022. doi: 10.3847/1538-4357/ac78ea.

G. Dalton, S. C. Trager, D. C. Abrams, D. Carter, P. Bonifacio, J. A. L. Aguerri, M. MacIntosh, C. Evans, I. Lewis, R. Navarro, T. Agocs, K. Dee, S. Rousset, I. Tosh, K. Middleton, J. Pragt, D. Terrett, M. Brock, C. Benn, M. Verheijen, D. Cano Infantes, C. Bevil, I. Steele, C. Mottram, S. Bates, F. J. Gribbin, J. Rey, L. F. Rodriguez, J. M. Delgado, I. Guinouard, N. Walton, M. J. Irwin, P. Jagourel, R. Stuik, G. Gerlofsma, R. Roelfsma, I. Skillen, A. Ridings, M. Balcells, J.-B. Daban, C. Gouvret, L. Venema, and P. Girard. WEAVE: the next generation wide-field spectroscopy facility for the William Herschel Telescope. In *Ground-based and Airborne Instrumentation for Astronomy IV*, volume 8446 of *Proceedings for SPIE Astronomical Telescopes*, page 84460P, Sept. 2012. doi: 10.1117/12.925950.

G. Dalton, S. Trager, D. C. Abrams, P. Bonifacio, J. A. López Aguerri, K. Middleton, C. Benn, K. Dee, F. Sayède, I. Lewis, J. Pragt, S. Pico, N. Walton, J. Rey, C. Allende Prieto, J. Peñate, E. Lhome, T. Agócs, J. Alonso, D. Terrett, M. Brock, J. Gilbert, A. Ridings, I. Guinouard, M. Verheijen, I. Tosh, K. Rogers, I. Steele,

R. Stuik, N. Tromp, A. Jasko, J. Kragt, D. Lesman, C. Mottram, S. Bates, F. Gribbin, L. Fernando Rodriguez, J. M. Delgado, C. Martin, D. Cano, R. Navarro, M. Irwin, J. Lewis, E. Gonzalez Solares, N. O'Mahony, A. Bianco, C. Zurita, R. ter Horst, E. Molinari, M. Lodi, J. Guerra, A. Vallenari, and A. Baruffolo. Project overview and update on WEAVE: the next generation wide-field spectroscopy facility for the William Herschel Telescope. In S. K. Ramsay, I. S. McLean, and H. Takami, editors, *Ground-based and Airborne Instrumentation for Astronomy V*, volume 9147 of *Society of Photo-Optical Instrumentation Engineers (SPIE) Conference Series*, page 91470L, July 2014. doi: 10.1117/12.2055132.

C. Davidson-Pilon, J. Kalderstam, N. Jacobson, P. Zivich, B. Kuhn, M. Williamson, sean reed, AbdealiJK, A. Fiore-Gartland, D. Datta, L. Moneda, Gabriel, D. WIlson, A. Parij, A. Moncada-Torres, K. Stark, S. Anton, M. S. Peña, L. Besson, K. Singaravelan, Jona, H. Gadgil, D. Golland, S. Hussey, R. Kumar, M. Begun, J. Noorbakhsh, A. Klintberg, A. F. Rendeiro, and A. Flaxman. Camdavidsonpilon/lifelines: v0.24.8, May 2020. URL `https://doi.org/10.5281/zenodo.3833188`.

M. Davis, G. Efstathiou, C. S. Frenk, and S. D. M. White. The evolution of large-scale structure in a universe dominated by cold dark matter. *The Astrophysical Journal*, 292:371–394, May 1985. doi: 10.1086/163168.

R. S. de Jong, O. Bellido-Tirado, C. Chiappini, É. Depagne, R. Haynes, D. Johl, O. Schnurr, A. Schwope, J. Walcher, F. Dionies, D. Haynes, A. Kelz, F. S. Kitaura, G. Lamer, I. Minchev, V. Müller, S. E. Nuza, J.-C. Olaya, T. Piffl, E. Popow, M. Steinmetz, U. Ural, M. Williams, R. Winkler, L. Wisotzki, W. R. Ansorge, M. Banerji, E. Gonzalez Solares, M. Irwin, R. C. Kennicutt, D. King, R. G. McMahon, S. Koposov, I. R. Parry, D. Sun, N. A. Walton, G. Finger, O. Iwert, M. Krumpe, J.-L. Lizon, M. Vincenzo, J.-P. Amans, P. Bonifacio, M. Cohen, P. Francois, P. Jagourel, S. B. Mignot, F. Royer, P. Sartoretti, R. Bender, F. Grupp, H.-J. Hess, F. Lang-Bardl, B. Muschielok, H. Böhringer, T. Boller, A. Bongiorno, M. Brusa, T. Dwelly, A. Merloni, K. Nandra, M. Salvato, J. H. Pragt, R. Navarro, G. Gerlofsma, R. Roelfsema, G. B. Dalton, K. F. Middleton, I. A. Tosh, C. Boeche, E. Caffau, N. Christlieb, E. K. Grebel, C. Hansen, A. Koch, H.-G. Ludwig, A. Quirrenbach, L. Sbordone, W. Seifert, G. Thimm, T. Trifonov, A. Helmi, S. C. Trager, S. Feltzing, A. Korn, and W. Boland. 4MOST: 4-metre multi-object spectroscopic telescope. In *Ground-based and Airborne Instrumentation for Astronomy IV*, volume 8446 of *Proceedings for SPIE Astronomical Telescopes*, page 84460T, Sept. 2012. doi: 10.1117/12.926239.

R. S. de Jong, O. Agertz, A. A. Berbel, J. Aird, D. A. Alexander, A. Amarsi, F. Anders, R. Andrae, B. Ansarinejad, W. Ansorge, P. Antilogus, H. Anwand-Heerwart, A. Arentsen, A. Arnadottir, M. Asplund, M. Auger, N. Azais, D. Baade, G. Baker, S. Baker, E. Balbinot, I. K. Baldry, M. Banerji, S. Barden, P. Barklem, E. Barthélémy-Mazot, C. Battistini, S. Bauer, C. P. M. Bell, O. Bellido-Tirado, S. Bellstedt, V. Belokurov, T. Bensby, M. Bergemann, J. M. Bestenlehner,

R. Bielby, M. Bilicki, C. Blake, J. Bland-Hawthorn, C. Boeche, W. Boland, T. Boller, S. Bongard, A. Bongiorno, P. Bonifacio, D. Boudon, D. Brooks, M. J. I. Brown, R. Brown, M. Brüggen, J. Brynnel, J. Brzeski, T. Buchert, P. Buschkamp, E. Caffau, P. Caillier, J. Carrick, L. Casagrande, S. Case, A. Casey, I. Cesarini, G. Cescutti, D. Chapuis, C. Chiappini, M. Childress, N. Christlieb, R. Church, M. R. L. Cioni, M. Cluver, M. Colless, T. Collett, J. Comparat, A. Cooper, W. Couch, F. Courbin, S. Croom, D. Croton, E. Daguisé, G. Dalton, L. J. M. Davies, T. Davis, P. de Laverny, A. Deason, F. Dionies, K. Disseau, P. Doel, D. Döscher, S. P. Driver, T. Dwelly, D. Eckert, A. Edge, B. Edvardsson, D. E. Youssoufi, A. Elhaddad, H. Enke, G. Erfanianfar, T. Farrell, T. Fechner, C. Feiz, S. Feltzing, I. Ferreras, D. Feuerstein, D. Feuillet, A. Finoguenov, D. Ford, S. Fotopoulou, M. Fouesneau, C. Frenk, S. Frey, W. Gaessler, S. Geier, N. Gentile Fusillo, O. Gerhard, T. Giannantonio, D. Giannone, B. Gibson, P. Gillingham, C. González-Fernández, E. Gonzalez-Solares, S. Gottloeber, A. Gould, E. K. Grebel, A. Gueguen, G. Guiglion, M. Haehnelt, T. Hahn, C. J. Hansen, H. Hartman, K. Hauptner, K. Hawkins, D. Haynes, R. Haynes, U. Heiter, A. Helmi, C. H. Aguayo, P. Hewett, S. Hinton, D. Hobbs, S. Hoenig, D. Hofman, I. Hook, J. Hopgood, A. Hopkins, A. Hourihane, L. Howes, C. Howlett, T. Huet, M. Irwin, O. Iwert, P. Jablonka, T. Jahn, K. Jahnke, A. Jarno, S. Jin, P. Jofre, D. Johl, D. Jones, H. Jönsson, C. Jordan, I. Karovicova, A. Khalatyan, A. Kelz, R. Kennicutt, D. King, F. Kitaura, J. Klar, U. Klauser, J. P. Kneib, A. Koch, S. Koposov, G. Kordopatis, A. Korn, J. Kosmalski, R. Kotak, M. Kovalev, K. Kreckel, Y. Kripak, M. Krumpe, K. Kuijken, A. Kunder, I. Kushniruk, M. I. Lam, G. Lamer, F. Laurent, J. Lawrence, M. Lehmitz, B. Lemasle, J. Lewis, B. Li, C. Lidman, K. Lind, J. Liske, J. L. Lizon, J. Loveday, H. G. Ludwig, R. M. McDermid, K. Maguire, V. Mainieri, S. Mali, H. Mandel, K. Mandel, L. Mannering, S. Martell, D. Martinez Delgado, G. Matijevic, H. McGregor, R. McMahon, P. McMillan, O. Mena, A. Merloni, M. J. Meyer, C. Michel, G. Micheva, J. E. Migniau, I. Minchev, G. Monari, R. Muller, D. Murphy, D. Muthukrishna, K. Nandra, R. Navarro, M. Ness, V. Nichani, R. Nichol, H. Nicklas, F. Niederhofer, P. Norberg, D. Obreschkow, S. Oliver, M. Owers, N. Pai, S. Pankratow, D. Parkinson, J. Paschke, R. Paterson, A. Pecontal, I. Parry, D. Phillips, A. Pillepich, L. Pinard, J. Pirard, N. Piskunov, V. Plank, D. Plüschke, E. Pons, P. Popesso, C. Power, J. Pragt, A. Pramskiy, D. Pryer, M. Quattri, A. B. d. A. Queiroz, A. Quirrenbach, S. Rahurkar, A. Raichoor, S. Ramstedt, A. Rau, A. Recio-Blanco, R. Reiss, F. Renaud, Y. Revaz, P. Rhode, J. Richard, A. D. Richter, H. W. Rix, A. S. G. Robotham, R. Roelfsema, M. Romaniello, D. Rosario, F. Rothmaier, B. Roukema, G. Ruchti, G. Rupprecht, J. Rybizki, N. Ryde, A. Saar, E. Sadler, M. Sahlén, M. Salvato, B. Sassolas, W. Saunders, A. Saviauk, L. Sbordone, T. Schmidt, O. Schnurr, R. D. Scholz, A. Schwope, W. Seifert, T. Shanks, A. Sheinis, T. Sivov, Á. Skúladóttir, S. Smartt, S. Smedley, G. Smith, R. Smith, J. Sorce, L. Spitler, E. Starkenburg, M. Steinmetz, I. Stilz, J. Storm, M. Sullivan, W. Sutherland, E. Swann, A. Tamone, E. N. Taylor, J. Teillon, E. Tempel, R. ter Horst, W. F. Thi, E. Tolstoy, S. Trager, G. Traven, P. E. Tremblay, L. Tresse, M. Valentini, R. van de Weygaert, M. van den Ancker, J. Veljanoski, S. Venkatesan, L. Wagner, K. Wagner, C. J. Walcher, L. Waller,

N. Walton, L. Wang, R. Winkler, L. Wisotzki, C. C. Worley, G. Worseck, M. Xiang, W. Xu, D. Yong, C. Zhao, J. Zheng, F. Zscheyge, and D. Zucker. 4MOST: Project overview and information for the First Call for Proposals. *The Messenger*, 175:3–11, Mar. 2019. doi: 10.18727/0722-6691/5117.

G. De Lucia and A. Helmi. The Galaxy and its stellar halo: insights on their formation from a hybrid cosmological approach. *Monthly Notices of the Astronomical Society*, 391(1):14–31, Nov. 2008. doi: 10.1111/j.1365-2966.2008.13862.x.

G. M. De Silva, K. C. Freeman, J. Bland-Hawthorn, S. Martell, E. W. de Boer, M. Asplund, S. Keller, S. Sharma, D. B. Zucker, T. Zwitter, B. Anguiano, C. Bacigalupo, D. Bayliss, M. A. Beavis, M. Bergemann, S. Campbell, R. Cannon, D. Carollo, L. Casagrande, A. R. Casey, G. Da Costa, V. D'Orazi, A. Dotter, L. Duong, A. Heger, M. J. Ireland, P. R. Kafle, J. Kos, J. Lattanzio, G. F. Lewis, J. Lin, K. Lind, U. Munari, D. M. Nataf, S. O'Toole, Q. Parker, W. Reid, K. J. Schlesinger, A. Sheinis, J. D. Simpson, D. Stello, Y. S. Ting, G. Traven, F. Watson, R. Wittenmyer, D. Yong, and M. Žerjal. The GALAH survey: scientific motivation. *Monthly Notices of the Astronomical Society*, 449(3):2604–2617, May 2015. doi: 10.1093/mnras/stv327.

A. J. Deason, Y.-Y. Mao, and R. H. Wechsler. The Eating Habits of Milky Way-mass Halos: Destroyed Dwarf Satellites and the Metallicity Distribution of Accreted Stars. *The Astrophysical Journal*, 821:5, Apr. 2016. doi: 10.3847/0004-637X/821/1/5.

A. Dekel and J. Woo. Feedback and the fundamental line of low-luminosity low-surface-brightness/dwarf galaxies. *Monthly Notices of the Astronomical Society*, 344(4):1131–1144, Oct. 2003. doi: 10.1046/j.1365-8711.2003.06923.x.

A. P. Dempster, N. M. Laird, and D. B. Rubin. Maximum likelihood from incomplete data via the em algorithm. *Journal of the Royal Statistical Society: Series B (Methodological)*, 39(1):1–22, 1977.

K. G. Derpanis. Mean shift clustering. *Lecture Notes*, 32, 2005.

T. Dietrich, S. Bernuzzi, M. Ujevic, and B. Brügmann. Numerical relativity simulations of neutron star merger remnants using conservative mesh refinement. *Physical Review D: Particles, Fields, Gravitation and Cosmology*, 91(12):124041, June 2015. doi: 10.1103/PhysRevD.91.124041.

G. A. Dooley, A. H. G. Peter, M. Vogelsberger, J. Zavala, and A. Frebel. Enhanced tidal stripping of satellites in the galactic halo from dark matter self-interactions. *Monthly Notices of the Astronomical Society*, 461(1):710–727, Sept. 2016. doi: 10.1093/mnras/stw1309.

G. A. Dooley, A. H. G. Peter, T. Yang, B. Willman, B. F. Griffen, and A. Frebel. An observer's guide to the (Local Group) dwarf galaxies: predictions for their

own dwarf satellite populations. *Monthly Notices of the Astronomical Society*, 471: 4894–4909, Nov. 2017. doi: 10.1093/mnras/stx1900.

A. Drlica-Wagner, K. Bechtol, E. S. Rykoff, E. Luque, A. Queiroz, Y. Y. Mao, R. H. Wechsler, J. D. Simon, B. Santiago, B. Yanny, E. Balbinot, S. Dodelson, A. Fausti Neto, D. J. James, T. S. Li, M. A. G. Maia, J. L. Marshall, A. Pieres, K. Stringer, A. R. Walker, T. M. C. Abbott, F. B. Abdalla, S. Allam, A. Benoit-Lévy, G. M. Bernstein, E. Bertin, D. Brooks, E. Buckley-Geer, D. L. Burke, A. Carnero Rosell, M. Carrasco Kind, J. Carretero, M. Crocce, L. N. da Costa, S. Desai, H. T. Diehl, J. P. Dietrich, P. Doel, T. F. Eifler, A. E. Evrard, D. A. Finley, B. Flaugher, P. Fosalba, J. Frieman, E. Gaztanaga, D. W. Gerdes, D. Gruen, R. A. Gruendl, G. Gutierrez, K. Honscheid, K. Kuehn, N. Kuropatkin, O. Lahav, P. Martini, R. Miquel, B. Nord, R. Ogando, A. A. Plazas, K. Reil, A. Roodman, M. Sako, E. Sanchez, V. Scarpine, M. Schubnell, I. Sevilla-Noarbe, R. C. Smith, M. Soares-Santos, F. Sobreira, E. Suchyta, M. E. C. Swanson, G. Tarle, D. Tucker, V. Vikram, W. Wester, Y. Zhang, J. Zuntz, and DES Collaboration. Eight Ultra-faint Galaxy Candidates Discovered in Year Two of the Dark Energy Survey. *The Astrophysical Journal*, 813(2):109, Nov. 2015. doi: 10.1088/0004-637X/813/2/109.

M. R. Drout, A. L. Piro, B. J. Shappee, C. D. Kilpatrick, J. D. Simon, C. Contreras, D. A. Coulter, R. J. Foley, M. R. Siebert, N. Morrell, K. Boutsia, F. Di Mille, T. W.-S. Holoien, D. Kasen, J. A. Kollmeier, B. F. Madore, A. J. Monson, A. Murguia-Berthier, Y.-C. Pan, J. X. Prochaska, E. Ramirez-Ruiz, A. Rest, C. Adams, K. Alatalo, E. Bañados, J. Baughman, T. C. Beers, R. A. Bernstein, T. Bitsakis, A. Campillay, T. T. Hansen, C. R. Higgs, A. P. Ji, G. Maravelias, J. L. Marshall, C. Moni Bidin, J. L. Prieto, K. C. Rasmussen, C. Rojas-Bravo, A. L. Strom, N. Ulloa, J. Vargas-González, Z. Wan, and D. D. Whitten. Light Curves of the Neutron Star Merger GW170817/SSS17a: Implications for R-Process Nucleosynthesis. *ArXiv e-prints*, Oct. 2017.

I. Dvorkin, F. Daigne, S. Goriely, E. Vangioni, and J. Silk. The impact of turbulent mixing on the galactic r-process enrichment by binary neutron star mergers across the entire metallicity range. *arXiv e-prints*, art. arXiv:2010.00625, Oct. 2020.

K. El-Badry, J. Bland-Hawthorn, A. Wetzel, E. Quataert, D. R. Weisz, M. Boylan-Kolchin, P. F. Hopkins, C.-A. Faucher-Giguère, D. Kereš, and S. Garrison- Kimmel. Where are the most ancient stars in the Milky Way? *Monthly Notices of the Astronomical Society*, 480:652–668, Oct. 2018. doi: 10.1093/mnras/sty1864.

A. Emerick, G. L. Bryan, and M.-M. Mac Low. Simulating an Isolated Dwarf Galaxy with Multi-Channel Feedback and Chemical Yields from Individual Stars. *ArXiv e-prints*, July 2018.

A. Emerick, G. L. Bryan, and M.-M. Mac Low. Simulating an isolated dwarf galaxy with multichannel feedback and chemical yields from individual stars. *Monthly Notices of the Astronomical Society*, 482:1304–1329, Jan 2019. doi: 10.1093/mnras/sty2689.

R. Errani, J. Peñarrubia, C. F. P. Laporte, and F. A. Gómez. The effect of a disc on the population of cuspy and cored dark matter substructures in Milky Way-like galaxies. *Monthly Notices of the Astronomical Society*, 465(1):L59–L63, Feb. 2017. doi: 10.1093/mnrasl/slw211.

R. Ezzeddine, K. Rasmussen, A. Frebel, A. Chiti, K. Hinojisa, V. M. Placco, A. P. Ji, T. C. Beers, T. T. Hansen, I. U. Roederer, C. M. Sakari, and J. Melendez. The R-Process Alliance: First Magellan/MIKE Release from the Southern Search for R-process-enhanced Stars. *The Astrophysical Journal*, 898(2):150, Aug. 2020a. doi: 10.3847/1538-4357/ab9d1a.

R. Ezzeddine, K. Rasmussen, A. Frebel, A. Chiti, K. Hinojisa, V. M. Placco, I. U. Roederer, A. P. Ji, T. C. Beers, T. T. Hansen, C. M. Sakari, and J. Melendez. The R-process Alliance: First Magellan/MIKE Release from the Southern Search for R-Process-enhanced Stars. *arXiv e-prints*, art. arXiv:2006.07731, June 2020b.

E. D. Feigelson and P. I. Nelson. Statistical methods for astronomical data with upper limits. I. Univariate distributions. *The Astrophysical Journal*, 293:192–206, June 1985. doi: 10.1086/163225.

S. Feltzing, K. Eriksson, J. Kleyna, and M. I. Wilkinson. Evidence of enrichment by individual SN from elemental abundance ratios in the very metal-poor dSph galaxy Boötes I. *Astronomy and Astrophysics*, 508:L1–L4, Dec. 2009. doi: 10.1051/0004-6361/200912833.

W. Fong and E. Berger. The Locations of Short Gamma-Ray Bursts as Evidence for Compact Object Binary Progenitors. *The Astrophysical Journal*, 776(1):18, Oct. 2013. doi: 10.1088/0004-637X/776/1/18.

D. A. Forbes. Reverse engineering the Milky Way. *Monthly Notices of the Astronomical Society*, 493(1):847–854, Mar. 2020. doi: 10.1093/mnras/staa245.

G. Fragione and A. Loeb. Constraining the Milky Way mass with hypervelocity stars. *Nature Astronomy*, 55:32–38, Aug. 2017. doi: 10.1016/j.newast.2017.03.002.

P. François, L. Monaco, P. Bonifacio, C. Moni Bidin, D. Geisler, and L. Sbordone. Abundance ratios of red giants in low-mass ultra-faint dwarf spheroidal galaxies. *Astronomy and Astrophysics*, 588:A7, Apr. 2016. doi: 10.1051/0004-6361/201527181.

A. Frebel. Stellar archaeology: Exploring the Universe with metal-poor stars. *Astronomische Nachrichten*, 331:474–488, May 2010. doi: 10.1002/asna.201011362.

A. Frebel. From Nuclei to the Cosmos: Tracing Heavy-Element Production with the Oldest Stars. *Annual Review of Nuclear and Particle Science*, 68(1):237–269, Oct. 2018. doi: 10.1146/annurev-nucl-101917-021141.

A. Frebel, J. D. Simon, M. Geha, and B. Willman. High-Resolution Spectroscopy of Extremely Metal-Poor Stars in the Least Evolved Galaxies: Ursa Major II and Coma Berenices. *The Astrophysical Journal*, 708:560–583, Jan. 2010. doi: 10.1088/0004-637X/708/1/560.

A. Frebel, J. D. Simon, and E. N. Kirby. Segue 1: An Unevolved Fossil Galaxy from the Early Universe. *The Astrophysical Journal*, 786:74, May 2014. doi: 10.1088/0004-637X/786/1/74.

A. Frebel, J. E. Norris, G. Gilmore, and R. F. G. Wyse. The chemical evolution of the Bootes I ultra-faint dwarf galaxy. *ArXiv e-prints*, May 2016.

K. Freeman and J. Bland-Hawthorn. The New Galaxy: Signatures of Its Formation. *Annual Review of Astronomy and Astrophysics*, 40:487–537, Jan. 2002. doi: 10.1146/annurev.astro.40.060401.093840.

B. J. Frey and D. Dueck. Clustering by passing messages between data points. *science*, 315(5814):972–976, 2007.

J. P. Fulbright, R. M. Rich, and S. Castro. Draco 119: A Remarkable Heavy-Element-deficient Giant. *The Astrophysical Journal*, 612:447–453, Sept. 2004. doi: 10.1086/421712.

J. P. U. Fynbo, D. Watson, C. C. Thöne, J. Sollerman, J. S. Bloom, T. M. Davis, J. Hjorth, P. Jakobsson, U. G. Jørgensen, J. F. Graham, A. S. Fruchter, D. Bersier, L. Kewley, A. Cassan, J. M. Castro Cerón, S. Foley, J. Gorosabel, T. C. Hinse, K. D. Horne, B. L. Jensen, S. Klose, D. Kocevski, J.-B. Marquette, D. Perley, E. Ramirez-Ruiz, M. D. Stritzinger, P. M. Vreeswijk, R. A. M. Wijers, K. G. Woller, D. Xu, and M. Zub. No supernovae associated with two long-duration γ-ray bursts. *Nature*, 444(7122):1047–1049, Dec. 2006. doi: 10.1038/nature05375.

Gaia Collaboration, A. G. A. Brown, A. Vallenari, T. Prusti, J. H. J. de Bruijne, C. Babusiaux, C. A. L. Bailer-Jones, M. Biermann, D. W. Evans, L. Eyer, F. Jansen, C. Jordi, S. A. Klioner, U. Lammers, L. Lindegren, X. Luri, F. Mignard, C. Panem, D. Pourbaix, S. Randich, P. Sartoretti, H. I. Siddiqui, C. Soubiran, F. van Leeuwen, N. A. Walton, F. Arenou, U. Bastian, M. Cropper, R. Drimmel, D. Katz, M. G. Lattanzi, J. Bakker, C. Cacciari, J. Castañeda, L. Chaoul, N. Cheek, F. De Angeli, C. Fabricius, R. Guerra, B. Holl, E. Masana, R. Messineo, N. Mowlavi, K. Nienartowicz, P. Panuzzo, J. Portell, M. Riello, G. M. Seabroke, P. Tanga, F. Thévenin, G. Gracia-Abril, G. Comoretto, M. Garcia-Reinaldos, D. Teyssier, M. Altmann, R. Andrae, M. Audard, I. Bellas-Velidis, K. Benson, J. Berthier, R. Blomme, P. Burgess, G. Busso, B. Carry, A. Cellino, G. Clementini, M. Clotet, O. Creevey, M. Davidson, J. De Ridder, L. Delchambre, A. Dell'Oro, C. Ducourant, J. Fernández-Hernández, M. Fouesneau, Y. Frémat, L. Galluccio, M. García-Torres, J. González-Núñez, J. J. González-Vidal, E. Gosset, L. P. Guy, J. L. Halbwachs, N. C. Hambly, D. L. Harrison, J. Hernández, D. Hestroffer, S. T. Hodgkin, A. Hutton, G. Jasniewicz, A. Jean-Antoine-Piccolo, S. Jordan, A. J. Korn,

A. Krone-Martins, A. C. Lanzafame, T. Lebzelter, W. Löffler, M. Manteiga, P. M. Marrese, J. M. Martín-Fleitas, A. Moitinho, A. Mora, K. Muinonen, J. Osinde, E. Pancino, T. Pauwels, J. M. Petit, A. Recio-Blanco, P. J. Richards, L. Rimoldini, A. C. Robin, L. M. Sarro, C. Siopis, M. Smith, A. Sozzetti, M. Süveges, J. Torra, W. van Reeven, U. Abbas, A. Abreu Aramburu, S. Accart, C. Aerts, G. Altavilla, M. A. Álvarez, R. Alvarez, J. Alves, R. I. Anderson, A. H. Andrei, E. Anglada Varela, E. Antiche, T. Antoja, B. Arcay, T. L. Astraatmadja, N. Bach, S. G. Baker, L. Balaguer-Núñez, P. Balm, C. Barache, C. Barata, D. Barbato, F. Barblan, P. S. Barklem, D. Barrado, M. Barros, M. A. Barstow, S. Bartholomé Muñoz, J. L. Bassilana, U. Becciani, M. Bellazzini, A. Berihuete, S. Bertone, L. Bianchi, O. Bienaymé, S. Blanco-Cuaresma, T. Boch, C. Boeche, A. Bombrun, R. Borrachero, D. Bossini, S. Bouquillon, G. Bourda, A. Bragaglia, L. Bramante, M. A. Breddels, A. Bressan, N. Brouillet, T. Brüsemeister, E. Brugaletta, B. Bucciarelli, A. Burlacu, D. Busonero, A. G. Butkevich, R. Buzzi, E. Caffau, R. Cancelliere, G. Cannizzaro, T. Cantat-Gaudin, R. Carballo, T. Carlucci, J. M. Carrasco, L. Casamiquela, M. Castellani, A. Castro-Ginard, P. Charlot, L. Chemin, A. Chiavassa, G. Cocozza, G. Costigan, S. Cowell, F. Crifo, M. Crosta, C. Crowley, J. Cuypers, C. Dafonte, Y. Damerdji, A. Dapergolas, P. David, M. David, P. de Laverny, F. De Luise, R. De March, D. de Martino, R. de Souza, A. de Torres, J. Debosscher, E. del Pozo, M. Delbo, A. Delgado, H. E. Delgado, P. Di Matteo, S. Diakite, C. Diener, E. Distefano, C. Dolding, P. Drazinos, J. Durán, B. Edvardsson, H. Enke, K. Eriksson, P. Esquej, G. Eynard Bontemps, C. Fabre, M. Fabrizio, S. Faigler, A. J. Falcão, M. Farràs Casas, L. Federici, G. Fedorets, P. Fernique, F. Figueras, F. Filippi, K. Findeisen, A. Fonti, E. Fraile, M. Fraser, B. Frézouls, M. Gai, S. Galleti, D. Garabato, F. García-Sedano, A. Garofalo, N. Garralda, A. Gavel, P. Gavras, J. Gerssen, R. Geyer, P. Giacobbe, G. Gilmore, S. Girona, G. Giuffrida, F. Glass, M. Gomes, M. Granvik, A. Gueguen, A. Guerrier, J. Guiraud, R. Gutiérrez-Sánchez, R. Haigron, D. Hatzidimitriou, M. Hauser, M. Haywood, U. Heiter, A. Helmi, J. Heu, T. Hilger, D. Hobbs, W. Hofmann, G. Holland, H. E. Huckle, A. Hypki, V. Icardi, K. Janßen, G. Jevardat de Fombelle, P. G. Jonker, Á. L. Juhász, F. Julbe, A. Karampelas, A. Kewley, J. Klar, A. Kochoska, R. Kohley, K. Kolenberg, M. Kontizas, E. Kontizas, S. E. Koposov, G. Kordopatis, Z. Kostrzewa-Rutkowska, P. Koubsky, S. Lambert, A. F. Lanza, Y. Lasne, J. B. Lavigne, Y. Le Fustec, C. Le Poncin-Lafitte, Y. Lebreton, S. Leccia, N. Leclerc, I. Lecoeur-Taibi, H. Lenhardt, F. Leroux, S. Liao, E. Licata, H. E. P. Lindstrøm, T. A. Lister, E. Livanou, A. Lobel, M. López, S. Managau, R. G. Mann, G. Mantelet, O. Marchal, J. M. Marchant, M. Marconi, S. Marinoni, G. Marschalkó, D. J. Marshall, M. Martino, G. Marton, N. Mary, D. Massari, G. Matijevič, T. Mazeh, P. J. McMillan, S. Messina, D. Michalik, N. R. Millar, D. Molina, R. Molinaro, L. Molnár, P. Montegriffo, R. Mor, R. Morbidelli, T. Morel, D. Morris, A. F. Mulone, T. Muraveva, I. Musella, G. Nelemans, L. Nicastro, L. Noval, W. O'Mullane, C. Ordénovic, D. Ordóñez-Blanco, P. Osborne, C. Pagani, I. Pagano, F. Pailler, H. Palacin, L. Palaversa, A. Panahi, M. Pawlak, A. M. Piersimoni, F. X. Pineau, E. Plachy, G. Plum, E. Poggio, E. Poujoulet, A. Prša, L. Pulone, E. Racero, S. Ragaini, N. Rambaux, M. Ramos-Lerate, S. Regibo, C. Reylé,

F. Riclet, V. Ripepi, A. Riva, A. Rivard, G. Rixon, T. Roegiers, M. Roelens, M. Romero-Gómez, N. Rowell, F. Royer, L. Ruiz-Dern, G. Sadowski, T. Sagristà Sellés, J. Sahlmann, J. Salgado, E. Salguero, N. Sanna, T. Santana-Ros, M. Sarasso, H. Savietto, M. Schultheis, E. Sciacca, M. Segol, J. C. Segovia, D. Ségransan, I. C. Shih, L. Siltala, A. F. Silva, R. L. Smart, K. W. Smith, E. Solano, F. Solitro, R. Sordo, S. Soria Nieto, J. Souchay, A. Spagna, F. Spoto, U. Stampa, I. A. Steele, H. Steidelmüller, C. A. Stephenson, H. Stoev, F. F. Suess, J. Surdej, L. Szabados, E. Szegedi-Elek, D. Tapiador, F. Taris, G. Tauran, M. B. Taylor, R. Teixeira, D. Terrett, P. Teyssandier, W. Thuillot, A. Titarenko, F. Torra Clotet, C. Turon, A. Ulla, E. Utrilla, S. Uzzi, M. Vaillant, G. Valentini, V. Valette, A. van Elteren, E. Van Hemelryck, M. van Leeuwen, M. Vaschetto, A. Vecchiato, J. Veljanoski, Y. Viala, D. Vicente, S. Vogt, C. von Essen, H. Voss, V. Votruba, S. Voutsinas, G. Walmsley, M. Weiler, O. Wertz, T. Wevers, Ł. Wyrzykowski, A. Yoldas, M. Žerjal, H. Ziaeepour, J. Zorec, S. Zschocke, S. Zucker, C. Zurbach, and T. Zwitter. Gaia Data Release 2. Summary of the contents and survey properties. *Astronomy and Astrophysics*, 616:A1, Aug. 2018. doi: 10.1051/0004-6361/201833051.

S. Garrison-Kimmel, M. Boylan-Kolchin, J. S. Bullock, and K. Lee. ELVIS: Exploring the Local Volume in Simulations. *Monthly Notices of the Astronomical Society*, 438: 2578–2596, Mar. 2014. doi: 10.1093/mnras/stt2377.

S. Garrison-Kimmel, J. S. Bullock, M. Boylan-Kolchin, and E. Bardwell. Organized chaos: scatter in the relation between stellar mass and halo mass in small galaxies. *Monthly Notices of the Astronomical Society*, 464:3108–3120, Jan. 2017a. doi: 10.1093/mnras/stw2564.

S. Garrison-Kimmel, J. S. Bullock, M. Boylan-Kolchin, and E. Bardwell. Organized chaos: scatter in the relation between stellar mass and halo mass in small galaxies. *Monthly Notices of the Astronomical Society*, 464(3):3108–3120, Jan. 2017b. doi: 10.1093/mnras/stw2564.

S. Garrison-Kimmel, A. Wetzel, J. S. Bullock, P. F. Hopkins, M. Boylan-Kolchin, C.-A. Faucher-Giguère, D. Kereš, E. Quataert, R. E. Sanderson, A. S. Graus, and T. Kelley. Not so lumpy after all: modelling the depletion of dark matter subhaloes by Milky Way-like galaxies. *Monthly Notices of the Astronomical Society*, 471:1709–1727, Oct. 2017c. doi: 10.1093/mnras/stx1710.

D. Geisler, V. V. Smith, G. Wallerstein, G. Gonzalez, and C. Charbonnel. "Sculptoring" the Galaxy? The Chemical Compositions of Red Giants in the Sculptor Dwarf Spheroidal Galaxy. *The Astronomical Journal*, 129:1428–1442, Mar. 2005. doi: 10.1086/427540.

S. Gibbons. pyfof. `https://github.com/simongibbons/pyfof`, 2020.

G. Gilmore, J. E. Norris, L. Monaco, D. Yong, R. F. G. Wyse, and D. Geisler. Elemental Abundances and their Implications for the Chemical Enrichment of the Boötes I Ultrafaint Galaxy. *The Astrophysical Journal*, 763:61, Jan. 2013. doi: 10.1088/0004-637X/763/1/61.

N. Y. Gnedin. Effect of Reionization on Structure Formation in the Universe. *The Astrophysical Journal*, 542:535–541, Oct. 2000. doi: 10.1086/317042.

F. A. Gómez, A. Helmi, A. G. A. Brown, and Y.-S. Li. On the identification of merger debris in the Gaia era. *Monthly Notices of the Astronomical Society*, 408 (2):935–946, Oct. 2010. doi: 10.1111/j.1365-2966.2010.17225.x.

F. A. Gómez, C. E. Coleman-Smith, B. W. O'Shea, J. Tumlinson, and R. L. Wolpert. Characterizing the Formation History of Milky Way like Stellar Halos with Model Emulators. *The Astrophysical Journal*, 760(2):112, Dec. 2012. doi: 10.1088/0004-637X/760/2/112.

F. A. Gómez, C. E. Coleman-Smith, B. W. O'Shea, J. Tumlinson, and R. L. Wolpert. Dissecting Galaxy Formation Models with Sensitivity Analysis—a New Approach to Constrain the Milky Way Formation History. *The Astrophysical Journal*, 787 (1):20, May 2014. doi: 10.1088/0004-637X/787/1/20.

F. A. Gómez, R. J. J. Grand, A. Monachesi, S. D. M. White, S. Bustamante, F. Marinacci, R. Pakmor, C. M. Simpson, V. Springel, and C. S. Frenk. Lessons from the Auriga discs: the hunt for the Milky Way's ex situ disc is not yet over. *Monthly Notices of the Astronomical Society*, 472:3722–3733, Dec. 2017. doi: 10.1093/mnras/stx2149.

O. Graur, F. B. Bianco, S. Huang, M. Modjaz, I. Shivvers, A. V. Filippenko, W. Li, and J. J. Eldridge. LOSS Revisited. I. Unraveling Correlations Between Supernova Rates and Galaxy Properties, as Measured in a Reanalysis of the Lick Observatory Supernova Search. *The Astrophysical Journal*, 837(2):120, Mar. 2017a. doi: 10.3847/1538-4357/aa5eb8.

O. Graur, F. B. Bianco, M. Modjaz, I. Shivvers, A. V. Filippenko, W. Li, and N. Smith. LOSS Revisited. II. The Relative Rates of Different Types of Supernovae Vary between Low- and High-mass Galaxies. *The Astrophysical Journal*, 837 (2):121, Mar. 2017b. doi: 10.3847/1538-4357/aa5eb7.

A. S. Graus, J. S. Bullock, T. Kelley, M. Boylan-Kolchin, S. Garrison-Kimmel, and Y. Qi. How low does it go? Too few Galactic satellites with standard reionization quenching. *ArXiv e-prints*, art. arXiv:1808.03654, Aug. 2018.

B. F. Griffen, A. P. Ji, G. A. Dooley, F. A. Gómez, M. Vogelsberger, B. W. O'Shea, and A. Frebel. The Caterpillar Project: A Large Suite of Milky Way Sized Halos. *The Astrophysical Journal*, 818:10, Feb. 2016. doi: 10.3847/0004-637X/818/1/10.

B. F. Griffen, G. A. Dooley, A. P. Ji, B. W. O'Shea, F. A. Gómez, and A. Frebel. Tracing the first stars and galaxies of the Milky Way. *Monthly Notices of the Astronomical Society*, 474:443–459, Feb. 2018. doi: 10.1093/mnras/stx2749.

D. Gudin, D. Shank, T. C. Beers, Z. Yuan, G. Limberg, I. U. Roederer, V. Placco, E. M. Holmbeck, S. Dietz, K. C. Rasmussen, T. T. Hansen, C. M. Sakari, R. Ezzeddine, and A. Frebel. The R-Process Alliance: Chemodynamically Tagged Groups of Halo r-process-enhanced Stars Reveal a Shared Chemical-evolution History. *The Astrophysical Journal*, 908(1):79, Feb. 2021. doi: 10.3847/1538-4357/abd7ed.

D. Guetta, T. Piran, and E. Waxman. The Luminosity and Angular Distributions of Long-Duration Gamma-Ray Bursts. *The Astrophysical Journal*, 619(1):412–419, Jan. 2005. doi: 10.1086/423125.

F. Haardt and P. Madau. Radiative Transfer in a Clumpy Universe. IV. New Synthesis Models of the Cosmic UV/X-Ray Background. *The Astrophysical Journal*, 746:125, Feb. 2012. doi: 10.1088/0004-637X/746/2/125.

O. Hahn and T. Abel. Multi-scale initial conditions for cosmological simulations. *Monthly Notices of the Astronomical Society*, 415:2101–2121, Aug. 2011. doi: 10.1111/j.1365-2966.2011.18820.x.

A. Hajela, R. Margutti, K. D. Alexander, A. Kathirgamaraju, A. Baldeschi, C. Guidorzi, D. Giannios, W. Fong, Y. Wu, A. MacFadyen, A. Paggi, E. Berger, P. K. Blanchard, R. Chornock, D. L. Coppejans, P. S. Cowperthwaite, T. Eftekhari, S. Gomez, G. Hosseinzadeh, T. Laskar, B. D. Metzger, M. Nicholl, K. Paterson, D. Radice, L. Sironi, G. Terreran, V. A. Villar, P. K. G. Williams, X. Xie, and J. Zrake. Two Years of Nonthermal Emission from the Binary Neutron Star Merger GW170817: Rapid Fading of the Jet Afterglow and First Constraints on the Kilonova Fastest Ejecta. *The Astrophysical Journal, Letters*, 886(1):L17, Nov. 2019. doi: 10.3847/2041-8213/ab5226.

T. T. Hansen, J. D. Simon, J. L. Marshall, T. S. Li, D. Carollo, D. L. DePoy, D. Q. Nagasawa, R. A. Bernstein, A. Drlica-Wagner, F. B. Abdalla, S. Allam, J. Annis, K. Bechtol, A. Benoit-Lévy, D. Brooks, E. Buckley-Geer, A. Carnero Rosell, M. Carrasco Kind, J. Carretero, C. E. Cunha, L. N. da Costa, S. Desai, T. F. Eifler, A. Fausti Neto, B. Flaugher, J. Frieman, J. García-Bellido, E. Gaztanaga, D. W. Gerdes, D. Gruen, R. A. Gruendl, J. Gschwend, G. Gutierrez, D. J. James, E. Krause, K. Kuehn, N. Kuropatkin, O. Lahav, R. Miquel, A. A. Plazas, A. K. Romer, E. Sanchez, B. Santiago, V. Scarpine, R. C. Smith, M. Soares-Santos, F. Sobreira, E. Suchyta, M. E. C. Swanson, G. Tarle, A. R. Walker, and DES Collaboration. An r-process Enhanced Star in the Dwarf Galaxy Tucana III. *The Astrophysical Journal*, 838:44, Mar. 2017. doi: 10.3847/1538-4357/aa634a.

T. T. Hansen, E. M. Holmbeck, T. C. Beers, V. M. Placco, I. U. Roederer, A. Frebel, C. M. Sakari, J. D. Simon, and I. B. Thompson. The R-process Alliance: First Release from the Southern Search for R-process-enhanced Stars in the Galactic Halo. *The Astrophysical Journal*, 858:92, May 2018. doi: 10.3847/1538-4357/aabacc.

T. T. Hansen, J. L. Marshall, J. D. Simon, T. S. Li, R. A. Bernstein, A. B. Pace, P. Ferguson, D. Q. Nagasawa, K. Kuehn, D. Carollo, M. Geha, D. James, A. Walker,

H. T. Diehl, M. Aguena, S. Allam, S. Avila, E. Bertin, D. Brooks, E. Buckley-Geer, D. L. Burke, A. C. Rosell, M. C. Kind, J. Carretero, M. Costanzi, L. N. Da Costa, S. Desai, J. De Vicente, P. Doel, K. Eckert, T. F. Eifler, S. Everett, I. Ferrero, J. Frieman, J. García-Bellido, E. Gaztanaga, D. W. Gerdes, D. Gruen, R. A. Gruendl, J. Gschwend, G. Gutierrez, S. R. Hinton, D. L. Hollowood, K. Honscheid, N. Kuropatkin, M. A. G. Maia, M. March, R. Miquel, A. Palmese, F. Paz-Chinchón, A. A. Plazas, E. Sanchez, B. Santiago, V. Scarpine, S. Serrano, M. Smith, M. Soares-Santos, E. Suchyta, M. E. C. Swanson, G. Tarle, T. N. Varga, R. Wilkinson, and DES Collaboration. Chemical Analysis of the Ultrafaint Dwarf Galaxy Grus II. Signature of High-mass Stellar Nucleosynthesis. *The Astrophysical Journal*, 897(2):183, July 2020. doi: 10.3847/1538-4357/ab9643.

B. Harmsen, A. Monachesi, E. F. Bell, R. S. de Jong, J. Bailin, D. J. Radburn-Smith, and B. W. Holwerda. Diverse stellar haloes in nearby Milky Way mass disc galaxies. *Monthly Notices of the Astronomical Society*, 466:1491–1512, Apr. 2017. doi: 10.1093/mnras/stw2992.

K. Hawkins and R. F. G. Wyse. The Fastest Travel Together: Chemical Tagging of the Fastest Stars in Gaia DR2 to the Stellar Halo. *ArXiv e-prints*, June 2018.

C. J. Haynes and C. Kobayashi. Galactic simulations of r-process elemental abundances. *Monthly Notices of the Astronomical Society*, 483(4):5123–5134, Mar. 2019. doi: 10.1093/mnras/sty3389.

A. Heger and S. E. Woosley. The Nucleosynthetic Signature of Population III. *The Astrophysical Journal*, 567(1):532–543, Mar. 2002. doi: 10.1086/338487.

A. Heger and S. E. Woosley. Nucleosynthesis and Evolution of Massive Metal-free Stars. *The Astrophysical Journal*, 724(1):341–373, Nov. 2010. doi: 10.1088/0004-637X/724/1/341.

A. Helmi and P. Tim de Zeeuw. Mapping the substructure in the galactic halo with the next generation of astrometric satellites. *Monthly Notices of the Royal Astronomical Society*, 319(3):657–665, 2000.

A. Helmi, S. D. M. White, P. T. de Zeeuw, and H. Zhao. Debris streams in the solar neighbourhood as relicts from the formation of the Milky Way. *Nature*, 402:53–55, Nov. 1999. doi: 10.1038/46980.

A. Helmi, C. Babusiaux, H. H. Koppelman, D. Massari, J. Veljanoski, and A. G. A. Brown. The merger that led to the formation of the Milky Way's inner stellar halo and thick disk. *Nature*, 563(7729):85–88, Oct. 2018. doi: 10.1038/s41586-018-0625-x.

W. Herschel. On the Construction of the Heavens. *Philosophical Transactions of the Royal Society of London Series I*, 75:213–266, Jan. 1785.

J. Herzog-Arbeitman, M. Lisanti, P. Madau, and L. Necib. Empirical Determination of Dark Matter Velocities Using Metal-Poor Stars. *Physical Review Letters*, 120(4): 041102, Jan. 2018. doi: 10.1103/PhysRevLett.120.041102.

E. M. Holmbeck, T. T. Hansen, T. C. Beers, V. M. Placco, D. D. Whitten, K. C. Rasmussen, I. U. Roederer, R. Ezzeddine, C. M. Sakari, A. Frebel, M. R. Drout, J. D. Simon, I. B. Thompson, J. Bland-Hawthorn, B. K. Gibson, E. K. Grebel, G. Kordopatis, A. Kunder, J. Meléndez, J. F. Navarro, W. A. Reid, G. Seabroke, M. Steinmetz, F. Watson, and R. F. G̈. Wyse. The R-Process Alliance: Fourth Data Release from the Search for R-process-enhanced Stars in the Galactic Halo. *The Astrophysical Journal, Supplement*, 249(2):30, Aug. 2020a. doi: 10.3847/1538-4365/ab9c19.

E. M. Holmbeck, T. T. Hansen, T. C. Beers, V. M. Placco, D. D. Whitten, K. C. Rasmussen, I. U. Roederer, R. Ezzeddine, C. M. Sakari, A. Frebel, M. R. Drout, J. D. Simon, I. B. Thompson, J. Bland-Hawthorn, B. K. Gibson, E. K. Grebel, G. Kordopatis, A. Kunder, J. Meléndez, J. F. Navarro, W. A. Reid, G. Seabroke, M. Steinmetz, F. Watson, and R. F. G̈. Wyse. The R-Process Alliance: Fourth Data Release from the Search for R-process-enhanced Stars in the Galactic Halo. *The Astrophysical Journal, Supplement*, 249(2):30, Aug. 2020b. doi: 10.3847/1538-4365/ab9c19.

K. Hotokezaka, K. Kiuchi, K. Kyutoku, H. Okawa, Y.-i. Sekiguchi, M. Shibata, and K. Taniguchi. Mass ejection from the merger of binary neutron stars. *Physical Review D: Particles, Fields, Gravitation and Cosmology*, 87(2):024001, Jan. 2013. doi: 10.1103/PhysRevD.87.024001.

K. Hotokezaka, T. Piran, and M. Paul. Short-lived ^{244}Pu points to compact binary mergers as sites for heavy r-process nucleosynthesis. *Nature Physics*, 11:1042, Dec. 2015. doi: 10.1038/nphys3574.

C.-Y. Hu. Supernova-driven winds in simulated dwarf galaxies. *Monthly Notices of the Astronomical Society*, 483(3):3363–3381, Mar. 2019. doi: 10.1093/mnras/sty3252.

J. Huchra and M. Geller. Groups of galaxies. i-nearby groups. *The Astrophysical Journal*, 257:423–437, 1982.

E. L. Hunt and S. Reffert. Improving the open cluster census-i. comparison of clustering algorithms applied to gaia dr2 data. *Astronomy & Astrophysics*, 646:A104, 2021.

J. D. Hunter. Matplotlib: A 2d graphics environment. *Computing in Science & Engineering*, 9(3):90–95, 2007. doi: http://dx.doi.org/10.1109/MCSE.2007.55. URL `http://scitation.aip.org/content/aip/journal/cise/9/3/10.1109/MCSE.2007.55`.

G. Häring. SQLite3, 2006. URL `https://docs.python.org/3/library/sqlite3.html`.

M. N. Ishigaki, W. Aoki, N. Arimoto, and S. Okamoto. Chemical compositions of six metal-poor stars in the ultra-faint dwarf spheroidal galaxy Boötes I. *Astronomy and Astrophysics*, 562:A146, Feb. 2014. doi: 10.1051/0004-6361/201322796.

Y. Ishimaru, S. Wanajo, and N. Prantzos. Neutron Star Mergers as the Origin of r-process Elements in the Galactic Halo Based on the Sub-halo Clustering Scenario. *The Astrophysical Journal, Letters*, 804:L35, May 2015. doi: 10.1088/2041-8205/804/2/L35.

Ž. Ivezić, S. M. Kahn, J. A. Tyson, B. Abel, E. Acosta, R. Allsman, D. Alonso, Y. AlSayyad, S. F. Anderson, J. Andrew, J. R. P. Angel, G. Z. Angeli, R. Ansari, P. Antilogus, C. Araujo, R. Armstrong, K. T. Arndt, P. Astier, É. Aubourg, N. Auza, T. S. Axelrod, D. J. Bard, J. D. Barr, A. Barrau, J. G. Bartlett, A. E. Bauer, B. J. Bauman, S. Baumont, E. Bechtol, K. Bechtol, A. C. Becker, J. Becla, C. Beldica, S. Bellavia, F. B. Bianco, R. Biswas, G. Blanc, J. Blazek, R. D. Blandford, J. S. Bloom, J. Bogart, T. W. Bond, M. T. Booth, A. W. Borgland, K. Borne, J. F. Bosch, D. Boutigny, C. A. Brackett, A. Bradshaw, W. N. Brandt, M. E. Brown, J. S. Bullock, P. Burchat, D. L. Burke, G. Cagnoli, D. Calabrese, S. Callahan, A. L. Callen, J. L. Carlin, E. L. Carlson, S. Chandrasekharan, G. Charles-Emerson, S. Chesley, E. C. Cheu, H.-F. Chiang, J. Chiang, C. Chirino, D. Chow, D. R. Ciardi, C. F. Claver, J. Cohen-Tanugi, J. J. Cockrum, R. Coles, A. J. Connolly, K. H. Cook, A. Cooray, K. R. Covey, C. Cribbs, W. Cui, R. Cutri, P. N. Daly, S. F. Daniel, F. Daruich, G. Daubard, G. Daues, W. Dawson, F. Delgado, A. Dellapenna, R. de Peyster, M. de Val-Borro, S. W. Digel, P. Doherty, R. Dubois, G. P. Dubois-Felsmann, J. Durech, F. Economou, T. Eifler, M. Eracleous, B. L. Emmons, A. Fausti Neto, H. Ferguson, E. Figueroa, M. Fisher-Levine, W. Focke, M. D. Foss, J. Frank, M. D. Freemon, E. Gangler, E. Gawiser, J. C. Geary, P. Gee, M. Geha, C. J. B. Gessner, R. R. Gibson, D. K. Gilmore, T. Glanzman, W. Glick, T. Goldina, D. A. Goldstein, I. Goodenow, M. L. Graham, W. J. Gressler, P. Gris, L. P. Guy, A. Guyonnet, G. Haller, R. Harris, P. A. Hascall, J. Haupt, F. Hernandez, S. Herrmann, E. Hileman, J. Hoblitt, J. A. Hodgson, C. Hogan, J. D. Howard, D. Huang, M. E. Huffer, P. Ingraham, W. R. Innes, S. H. Jacoby, B. Jain, F. Jammes, M. J. Jee, T. Jenness, G. Jernigan, D. Jevremović, K. Johns, A. S. Johnson, M. W. G. Johnson, R. L. Jones, C. Juramy-Gilles, M. Jurić, J. S. Kalirai, N. J. Kallivayalil, B. Kalmbach, J. P. Kantor, P. Karst, M. M. Kasliwal, H. Kelly, R. Kessler, V. Kinnison, D. Kirkby, L. Knox, I. V. Kotov, V. L. Krabbendam, K. S. Krughoff, P. Kubánek, J. Kuczewski, S. Kulkarni, J. Ku, N. R. Kurita, C. S. Lage, R. Lambert, T. Lange, J. B. Langton, L. Le Guillou, D. Levine, M. Liang, K.-T. Lim, C. J. Lintott, K. E. Long, M. Lopez, P. J. Lotz, R. H. Lupton, N. B. Lust, L. A. MacArthur, A. Mahabal, R. Mandelbaum, T. W. Markiewicz, D. S. Marsh, P. J. Marshall, S. Marshall, M. May, R. McKercher, M. McQueen, J. Meyers, M. Migliore, M. Miller, D. J. Mills, C. Miraval, J. Moeyens, F. E. Moolekamp, D. G. Monet, M. Moniez, S. Monkewitz, C. Montgomery, C. B. Morrison, F. Mueller, G. P. Muller, F. Muñoz Arancibia, D. R. Neill, S. P. Newbry, J.-Y. Nief, A. Nomerotski, M. Nordby, P. O'Connor, J. Oliver, S. S. Olivier, K. Olsen,

W. O'Mullane, S. Ortiz, S. Osier, R. E. Owen, R. Pain, P. E. Palecek, J. K. Parejko, J. B. Parsons, N. M. Pease, J. M. Peterson, J. R. Peterson, D. L. Petravick, M. E. Libby Petrick, C. E. Petry, F. Pierfederici, S. Pietrowicz, R. Pike, P. A. Pinto, R. Plante, S. Plate, J. P. Plutchak, P. A. Price, M. Prouza, V. Radeka, J. Rajagopal, A. P. Rasmussen, N. Regnault, K. A. Reil, D. J. Reiss, M. A. Reuter, S. T. Ridgway, V. J. Riot, S. Ritz, S. Robinson, W. Roby, A. Roodman, W. Rosing, C. Roucelle, M. R. Rumore, S. Russo, A. Saha, B. Sassolas, T. L. Schalk, P. Schellart, R. H. Schindler, S. Schmidt, D. P. Schneider, M. D. Schneider, W. Schoening, G. Schumacher, M. E. Schwamb, J. Sebag, B. Selvy, G. H. Sembroski, L. G. Seppala, A. Serio, E. Serrano, R. A. Shaw, I. Shipsey, J. Sick, N. Silvestri, C. T. Slater, J. A. Smith, R. C. Smith, S. Sobhani, C. Soldahl, L. Storrie-Lombardi, E. Stover, M. A. Strauss, R. A. Street, C. W. Stubbs, I. S. Sullivan, D. Sweeney, J. D. Swinbank, A. Szalay, P. Takacs, S. A. Tether, J. J. Thaler, J. G. Thayer, S. Thomas, A. J. Thornton, V. Thukral, J. Tice, D. E. Trilling, M. Turri, R. Van Berg, D. Vanden Berk, K. Vetter, F. Virieux, T. Vucina, W. Wahl, L. Walkowicz, B. Walsh, C. W. Walter, D. L. Wang, S.-Y. Wang, M. Warner, O. Wiecha, B. Willman, S. E. Winters, D. Wittman, S. C. Wolff, W. M. Wood-Vasey, X. Wu, B. Xin, P. Yoachim, and H. Zhan. LSST: From Science Drivers to Reference Design and Anticipated Data Products. *The Astrophysical Journal*, 873(2):111, Mar. 2019. doi: 10.3847/1538-4357/ab042c.

P. Jablonka, P. North, L. Mashonkina, V. Hill, Y. Revaz, M. Shetrone, E. Starkenburg, M. Irwin, E. Tolstoy, G. Battaglia, K. Venn, A. Helmi, F. Primas, and P. François. The early days of the Sculptor dwarf spheroidal galaxy. *Astronomy and Astrophysics*, 583:A67, Nov. 2015. doi: 10.1051/0004-6361/201525661.

H. R. Jacobson, S. Keller, A. Frebel, A. R. Casey, M. Asplund, M. S. Bessell, G. S. Da Costa, K. Lind, A. F. Marino, J. E. Norris, J. M. Peña, B. P. Schmidt, P. Tisserand, J. M. Walsh, D. Yong, and Q. Yu. High-Resolution Spectroscopic Study of Extremely Metal-Poor Star Candidates from the SkyMapper Survey. *The Astrophysical Journal*, 807:171, July 2015. doi: 10.1088/0004-637X/807/2/171.

P. Jethwa, D. Erkal, and V. Belokurov. The upper bound on the lowest mass halo. *Monthly Notices of the Astronomical Society*, 473:2060–2083, Jan. 2018. doi: 10.1093/mnras/stx2330.

A. P. Ji and A. Frebel. From Actinides to Zinc: Using the Full Abundance Pattern of the Brightest Star in Reticulum II to Distinguish between Different r-process Sites. *The Astrophysical Journal*, 856:138, Apr. 2018. doi: 10.3847/1538-4357/aab14a.

A. P. Ji, A. Frebel, and V. Bromm. Preserving chemical signatures of primordial star formation in the first low-mass stars. *Monthly Notices of the Astronomical Society*, 454(1):659–674, Nov. 2015a. doi: 10.1093/mnras/stv2052.

A. P. Ji, A. Frebel, and V. Bromm. Preserving chemical signatures of primordial star formation in the first low-mass stars. *Monthly Notices of the Astronomical Society*, 454:659–674, Nov. 2015b. doi: 10.1093/mnras/stv2052.

A. P. Ji, A. Frebel, A. Chiti, and J. D. Simon. R-process enrichment from a single event in an ancient dwarf galaxy. *Nature*, 531(7596):610–613, Mar. 2016a. doi: 10.1038/nature17425.

A. P. Ji, A. Frebel, A. Chiti, and J. D. Simon. R-process enrichment from a single event in an ancient dwarf galaxy. *Nature*, 531:610–613, Mar. 2016b. doi: 10.1038/nature17425.

A. P. Ji, A. Frebel, R. Ezzeddine, and A. R. Casey. Chemical Diversity in the Ultra-faint Dwarf Galaxy Tucana II. *The Astrophysical Journal, Letters*, 832:L3, Nov. 2016c. doi: 10.3847/2041-8205/832/1/L3.

A. P. Ji, A. Frebel, J. D. Simon, and M. Geha. High-resolution Spectroscopy of Extremely Metal-poor Stars in the Least-evolved Galaxies: Bootes II. *The Astrophysical Journal*, 817:41, Jan. 2016d. doi: 10.3847/0004-637X/817/1/41.

A. P. Ji, J. D. Simon, A. Frebel, K. A. Venn, and T. T. Hansen. Chemical Abundances in the Ultra-Faint Dwarf Galaxies Grus I and Triangulum II: Neutron-Capture Elements as a Defining Feature of the Faintest Dwarfs. *ArXiv e-prints*, art. arXiv:1809.02182, Sept. 2018.

A. P. Ji, T. S. Li, J. D. Simon, J. Marshall, A. K. Vivas, A. B. Pace, K. Bechtol, A. Drlica-Wagner, S. E. Koposov, T. T. Hansen, S. Allam, R. A. Gruendl, M. D. Johnson, M. McNanna, N. E. D. Noël, D. L. Tucker, and A. R. Walker. Detailed Abundances in the Ultra-faint Magellanic Satellites Carina II and III. *The Astrophysical Journal*, 889(1):27, Jan. 2020. doi: 10.3847/1538-4357/ab6213.

K. V. Johnston. A Prescription for Building the Milky Way's Halo from Disrupted Satellites. *The Astrophysical Journal*, 495:297–308, Mar. 1998. doi: 10.1086/305273.

K. V. Johnston, L. Hernquist, and M. Bolte. Fossil Signatures of Ancient Accretion Events in the Halo. *The Astrophysical Journal*, 465:278, July 1996. doi: 10.1086/177418.

E. Jones, T. Oliphant, P. Peterson, et al. SciPy: Open source scientific tools for Python, 2001. URL `http://www.scipy.org/`.

J. S. Kalirai, K. M. Gilbert, P. Guhathakurta, S. R. Majewski, J. C. Ostheimer, R. M. Rich, M. C. Cooper, D. B. Reitzel, and R. J. Patterson. The Metal-poor Halo of the Andromeda Spiral Galaxy (M31)1,. *The Astrophysical Journal*, 648:389–404, Sept. 2006. doi: 10.1086/505697.

E. N. Kirby and J. G. Cohen. Detailed Abundances of Two Very Metal-poor Stars in Dwarf Galaxies. *The Astronomical Journal*, 144:168, Dec. 2012. doi: 10.1088/0004-6256/144/6/168.

E. N. Kirby, J. G. Cohen, G. H. Smith, S. R. Majewski, S. T. Sohn, and P. Guhathakurta. Multi-element Abundance Measurements from Medium-resolution Spectra. IV. Alpha Element Distributions in Milky Way Satellite Galaxies. *The Astrophysical Journal*, 727:79, Feb. 2011a. doi: 10.1088/0004-637X/727/2/79.

E. N. Kirby, C. L. Martin, and K. Finlator. Metals Removed by Outflows from Milky Way Dwarf Spheroidal Galaxies. *The Astrophysical Journal, Letters*, 742:L25, Dec. 2011b. doi: 10.1088/2041-8205/742/2/L25.

E. N. Kirby, J. G. Cohen, P. Guhathakurta, L. Cheng, J. S. Bullock, and A. Gallazzi. The Universal Stellar Mass-Stellar Metallicity Relation for Dwarf Galaxies. *The Astrophysical Journal*, 779(2):102, Dec. 2013a. doi: 10.1088/0004-637X/779/2/102.

E. N. Kirby, J. G. Cohen, P. Guhathakurta, L. Cheng, J. S. Bullock, and A. Gallazzi. The Universal Stellar Mass-Stellar Metallicity Relation for Dwarf Galaxies. *The Astrophysical Journal*, 779:102, Dec. 2013b. doi: 10.1088/0004-637X/779/2/102.

E. N. Kirby, J. G. Cohen, J. D. Simon, P. Guhathakurta, A. O. Thygesen, and G. E. Duggan. Triangulum II. Not Especially Dense After All. *The Astrophysical Journal*, 838:83, Apr. 2017. doi: 10.3847/1538-4357/aa6570.

C. Kobayashi, A. I. Karakas, and M. Lugaro. The Origin of Elements from Carbon to Uranium. *arXiv e-prints*, art. arXiv:2008.04660, Aug. 2020.

A. Koch and R. M. Rich. A Chemical Confirmation of the Faint Boötes II Dwarf Spheroidal Galaxy. *The Astrophysical Journal*, 794:89, Oct. 2014. doi: 10.1088/0004-637X/794/1/89.

A. Koch, A. McWilliam, E. K. Grebel, D. B. Zucker, and V. Belokurov. The Highly Unusual Chemical Composition of the Hercules Dwarf Spheroidal Galaxy. *The Astrophysical Journal, Letters*, 688:L13–L16, Nov. 2008. doi: 10.1086/595001.

A. Koch, S. Feltzing, D. Adén, and F. Matteucci. Neutron-capture element deficiency of the Hercules dwarf spheroidal galaxy. *Astronomy and Astrophysics*, 554:A5, June 2013. doi: 10.1051/0004-6361/201220742.

J. A. Kollmeier, G. Zasowski, H.-W. Rix, M. Johns, S. F. Anderson, N. Drory, J. A. Johnson, R. W. Pogge, J. C. Bird, G. A. Blanc, J. R. Brownstein, J. D. Crane, N. M. De Lee, M. A. Klaene, K. Kreckel, N. MacDonald, A. Merloni, M. K. Ness, T. O'Brien, J. R. Sanchez-Gallego, C. C. Sayres, Y. Shen, A. R. Thakar, A. Tkachenko, C. Aerts, M. R. Blanton, D. J. Eisenstein, J. A. Holtzman, D. Maoz, K. Nandra, C. Rockosi, D. H. Weinberg, J. Bovy, A. R. Casey, J. Chaname, N. Clerc, C. Conroy, M. Eracleous, B. T. Gänsicke, S. Hekker, K. Horne, J. Kauffmann, K. B. W. McQuinn, E. W. Pellegrini, E. Schinnerer, E. F. Schlafly, A. D. Schwope, M. Seibert, J. K. Teske, and J. L. van Saders. SDSS-V: Pioneering Panoptic Spectroscopy. *arXiv e-prints*, art. arXiv:1711.03234, Nov. 2017.

O. Korobkin, S. Rosswog, A. Arcones, and C. Winteler. On the astrophysical robustness of the neutron star merger r-process. *Monthly Notices of the Astronomical Society*, 426:1940–1949, Nov. 2012. doi: 10.1111/j.1365-2966.2012.21859.x.

P. Kroupa. On the variation of the initial mass function. *Monthly Notices of the Astronomical Society*, 322(2):231–246, Apr. 2001. doi: 10.1046/j.1365-8711.2001.04022.x.

J. M. D. Kruijssen, J. L. Pfeffer, M. Reina-Campos, R. A. Crain, and N. Bastian. The formation and assembly history of the Milky Way revealed by its globular cluster population. *Monthly Notices of the Astronomical Society*, 486(3):3180–3202, July 2019. doi: 10.1093/mnras/sty1609.

J. M. D. Kruijssen, J. L. Pfeffer, M. Chevance, A. Bonaca, S. Trujillo-Gomez, N. Bastian, M. Reina-Campos, R. A. Crain, and M. E. Hughes. Kraken reveals itself - the merger history of the Milky Way reconstructed with the E-MOSAICS simulations. *Monthly Notices of the Astronomical Society*, 498(2):2472–2491, Oct. 2020. doi: 10.1093/mnras/staa2452.

D. K. Lai, Y. S. Lee, M. Bolte, S. Lucatello, T. C. Beers, J. A. Johnson, T. Sivarani, and C. M. Rockosi. The [Fe/H], [C/Fe], and [α/Fe] Distributions of the Boötes I Dwarf Spheroidal Galaxy. *The Astrophysical Journal*, 738:51, Sept. 2011. doi: 10.1088/0004-637X/738/1/51.

T. Lanz and I. Hubeny. A Grid of Non-LTE Line-blanketed Model Atmospheres of O-Type Stars. *The Astrophysical Journal, Supplement*, 146:417–441, June 2003. doi: 10.1086/374373.

D. Lazzati, B. J. Morsony, C. H. Blackwell, and M. C. Begelman. Unifying the Zoo of Jet-driven Stellar Explosions. *The Astrophysical Journal*, 750(1):68, May 2012. doi: 10.1088/0004-637X/750/1/68.

T. Le Bret, A. Pontzen, A. P. Cooper, C. Frenk, A. Zolotov, A. M. Brooks, F. Governato, and O. H. Parry. Particle tagging and its implications for stellar population dynamics. *Monthly Notices of the Astronomical Society*, 468(3):3212–3222, July 2017. doi: 10.1093/mnras/stx552.

D. M. Lee. *Understanding the Nature of Stellar Chemical Abundance Distributions in Nearby Stellar Systems*. PhD thesis, Columbia University, Jan. 2014.

D. M. Lee, K. V. Johnston, B. Sen, and W. Jessop. Reconstructing the Accretion History of the Galactic Stellar Halo from Chemical Abundance Ratio Distributions. *The Astrophysical Journal*, 802(1):48, Mar. 2015. doi: 10.1088/0004-637X/802/1/48.

N. Leethochawalit, E. N. Kirby, S. M. Moran, R. S. Ellis, and T. Treu. Evolution of the Stellar MassMetallicity Relation. I. Galaxies in the z$\sim$ $0.4 Cluster Cl 0024$. *The Astrophysical Journal*, $856 : 15, Mar. 2018. doi : 10.3847/1538 - 4357/aab26a$.

T. S. Li, J. D. Simon, K. Kuehn, A. B. Pace, D. Erkal, K. Bechtol, B. Yanny, A. Drlica- Wagner, J. L. Marshall, C. Lidman, E. Balbinot, D. Carollo, S. Jenkins, C. E. Martinez-Vazquez, N. Shipp, K. M. Stringer, A. K. Vivas, A. R. Walker, R. H. Wechsler, F. B. Abdalla, S. Allam, J. Annis, S. Avila, E. Bertin, D. Brooks, E. Buckley-Geer, D. L. Burke, A. Carnero Rosell, M. Carrasco Kind, J. Carretero, C. E. Cunha, C. B. D'Andrea, L. N. da Costa, C. Davis, J. De Vicente, P. Doel, T. F. Eifler, A. E. Evrard, B. Flaugher, J. Frieman, J. Garcia-Bellido, E. Gaztanaga, D. W. Gerdes, D. Gruen, R. A. Gruendl, J. Gschwend, G. Gutierrez, W. G. Hartley, D. L. Hollowood, K. Honscheid, D. J. James, E. Krause, M. A. G. Maia, M. March, F. Menanteau, R. Miquel, A. A. Plazas, E. Sanchez, B. Santiago, V. Scarpine, R. Schindler, M. Schubnell, I. Sevilla-Noarbe, M. Smith, R. C. Smith, M. Soares-Santos, F. Sobreira, E. Suchyta, M. E. C. Swanson, G. Tarle, and D. L. Tucker. The First Tidally Disrupted Ultra-Faint Dwarf Galaxy? - Spectroscopic Analysis of the Tucana III Stream. *ArXiv e-prints*, art. arXiv:1804.07761, Apr. 2018.

W. Li, R. Chornock, J. Leaman, A. V. Filippenko, D. Poznanski, X. Wang, M. Ganeshalingam, and F. Mannucci. Nearby supernova rates from the Lick Observatory Supernova Search - III. The rate-size relation, and the rates as a function of galaxy Hubble type and colour. *Monthly Notices of the Astronomical Society*, 412(3): 1473–1507, Apr. 2011a. doi: 10.1111/j.1365-2966.2011.18162.x.

W. Li, J. Leaman, R. Chornock, A. V. Filippenko, D. Poznanski, M. Ganeshalingam, X. Wang, M. Modjaz, S. Jha, R. J. Foley, and N. Smith. Nearby supernova rates from the Lick Observatory Supernova Search - II. The observed luminosity functions and fractions of supernovae in a complete sample. *Monthly Notices of the Astronomical Society*, 412(3):1441–1472, Apr. 2011b. doi: 10.1111/j.1365-2966.2011.18160.x.

A. Lien, T. Sakamoto, N. Gehrels, D. M. Palmer, S. D. Barthelmy, C. Graziani, and J. K. Cannizzo. Probing the Cosmic Gamma-Ray Burst Rate with Trigger Simulations of the Swift Burst Alert Telescope. *The Astrophysical Journal*, 783(1): 24, Mar. 2014. doi: 10.1088/0004-637X/783/1/24.

G. Limberg, S. Rossi, T. C. Beers, H. D. Perottoni, A. Pérez-Villegas, R. M. Santucci, Y. Abuchaim, V. M. Placco, Y. S. Lee, N. Christlieb, et al. Dynamically tagged groups of very metal-poor halo stars from the hk and hamburg/eso surveys. *The Astrophysical Journal*, 907(1):10, 2021.

M. Limongi and A. Chieffi. Presupernova Evolution and Explosive Nucleosynthesis of Rotating Massive Stars in the Metallicity Range -3 $\leq$ [Fe/H] $\leq$ 0. *The Astrophysical Journal, Supplement*, 237(1):13, July 2018. doi: 10.3847/1538-4365/aacb24.

S. Lloyd. Least squares quantization in pcm. *IEEE transactions on information theory*, 28(2):129–137, 1982.

Y. Lu, A. Benson, A. Wetzel, Y.-Y. Mao, S. Tonnesen, A. H. G. Peter, M. Boylan-Kolchin, and R. H. Wechsler. The Importance of Preventive Feedback: Inference from Observations of the Stellar Masses and Metallicities of Milky Way Dwarf

Galaxies. *The Astrophysical Journal*, 846:66, Sept. 2017. doi: 10.3847/1538-4357/aa845e.

X. Ma, P. F. Hopkins, C.-A. Faucher-Giguère, N. Zolman, A. L. Muratov, D. Kereš, and E. Quataert. The origin and evolution of the galaxy mass-metallicity relation. *Monthly Notices of the Astronomical Society*, 456:2140–2156, Feb. 2016. doi: 10.1093/mnras/stv2659.

A. I. MacFadyen and S. E. Woosley. Collapsars: Gamma-Ray Bursts and Explosions in "Failed Supernovae". *The Astrophysical Journal*, 524(1):262–289, Oct. 1999. doi: 10.1086/307790.

P. Macias and E. Ramirez-Ruiz. A Stringent Limit on the Mass Production Rate of r-process Elements in the Milky Way. *The Astrophysical Journal*, 860(2):89, June 2018. doi: 10.3847/1538-4357/aac3e0.

P. Macias and E. Ramirez-Ruiz. Constraining Collapsar r-process Models through Stellar Abundances. *The Astrophysical Journal, Letters*, 877(2):L24, June 2019. doi: 10.3847/2041-8213/ab2049.

N. P. Maffione, F. A. Gómez, P. M. Cincotta, C. M. Giordano, R. J. J. Grand, F. Marinacci, R. Pakmor, C. M. Simpson, V. Springel, and C. S. Frenk. On the relevance of chaos for halo stars in the solar neighbourhood II. *Monthly Notices of the Astronomical Society*, 478(3):4052–4067, Aug. 2018. doi: 10.1093/mnras/sty1297.

M. Magg, T. Nordlander, S. C. O. Glover, C. J. Hansen, M. Ishigaki, A. Heger, R. S. Klessen, C. Kobayashi, and K. Nomoto. A minimum dilution scenario for supernovae and consequences for extremely metal-poor stars. *Monthly Notices of the Astronomical Society*, 498(3):3703–3712, Aug. 2020. doi: 10.1093/mnras/staa2624.

S. R. Majewski, R. P. Schiavon, P. M. Frinchaboy, C. Allende Prieto, R. Barkhouser, D. Bizyaev, B. Blank, S. Brunner, A. Burton, R. Carrera, S. D. Chojnowski, K. Cunha, C. Epstein, G. Fitzgerald, A. E. García Pérez, F. R. Hearty, C. Henderson, J. A. Holtzman, J. A. Johnson, C. R. Lam, J. E. Lawler, P. Maseman, S. Mészáros, M. Nelson, D. C. Nguyen, D. L. Nidever, M. Pinsonneault, M. Shetrone, S. Smee, V. V. Smith, T. Stolberg, M. F. Skrutskie, E. Walker, J. C. Wilson, G. Zasowski, F. Anders, S. Basu, S. Beland, M. R. Blanton, J. Bovy, J. R. Brownstein, J. Carlberg, W. Chaplin, C. Chiappini, D. J. Eisenstein, Y. Elsworth, D. Feuillet, S. W. Fleming, J. Galbraith-Frew, R. A. García, D. A. García-Hernández, B. A. Gillespie, L. Girardi, J. E. Gunn, S. Hasselquist, M. R. Hayden, S. Hekker, I. Ivans, K. Kinemuchi, M. Klaene, S. Mahadevan, S. Mathur, B. Mosser, D. Muna, J. A. Munn, R. C. Nichol, R. W. O'Connell, J. K. Parejko, A. C. Robin, H. Rocha-Pinto, M. Schultheis, A. M. Serenelli, N. Shane, V. Silva Aguirre, J. S. Sobeck, B. Thompson, N. W. Troup, D. H. Weinberg, and O. Zamora. The Apache Point Observatory Galactic Evolution Experiment (APOGEE). *The Astronomical Journal*, 154(3):94, Sept. 2017. doi: 10.3847/1538-3881/aa784d.

M. K. Mardini, A. Frebel, A. Chiti, Y. Meiron, K. V. Brauer, and X. Ou. The Atari Disk, a Metal-Poor Stellar Population in the Disk System of the Milky Way. *arXiv e-prints*, art. arXiv:2206.08459, June 2022.

B. Margalit and B. D. Metzger. Constraining the Maximum Mass of Neutron Stars from Multi-messenger Observations of GW170817. *The Astrophysical Journal, Letters*, 850:L19, Dec. 2017. doi: 10.3847/2041-8213/aa991c.

R. Margutti, D. Milisavljevic, A. M. Soderberg, C. Guidorzi, B. J. Morsony, N. Sanders, S. Chakraborti, A. Ray, A. Kamble, M. Drout, J. Parrent, A. Zauderer, and L. Chomiuk. Relativistic Supernovae have Shorter-lived Central Engines or More Extended Progenitors: The Case of SN 2012ap. *The Astrophysical Journal*, 797(2):107, Dec. 2014. doi: 10.1088/0004-637X/797/2/107.

J. H. McDonald. *Handbook of Biological Statistics, 3rd Edition*, pages 145–156. Sparky House Publishing, 2014.

L. McInnes, J. Healy, and S. Astels. hdbscan: Hierarchical density based clustering. *J. Open Source Softw.*, 2(11):205, 2017.

G. C. McLaughlin and R. Surman. Prospects for obtaining an r process from Gamma Ray Burst Disk Winds. , 758:189–196, July 2005. doi: 10.1016/j.nuclphysa.2005.05.036.

K. B. W. McQuinn, E. D. Skillman, A. Dolphin, J. M. Cannon, J. J. Salzer, K. L. Rhode, E. A. K. Adams, D. Berg, R. Giovanelli, and M. P. Haynes. Leo P: How Many Metals Can a Very Low Mass, Isolated Galaxy Retain? *The Astrophysical Journal, Letters*, 815(2):L17, Dec. 2015. doi: 10.1088/2041-8205/815/2/L17.

D. Milisavljevic, R. Margutti, J. T. Parrent, A. M. Soderberg, R. A. Fesen, P. Mazzali, K. Maeda, N. E. Sanders, S. B. Cenko, J. M. Silverman, A. V. Filippenko, A. Kamble, S. Chakraborti, M. R. Drout, R. P. Kirshner, T. E. Pickering, K. Kawabata, T. Hattori, E. Y. Hsiao, M. D. Stritzinger, G. H. Marion, J. Vinko, and J. C. Wheeler. The Broad-lined Type Ic SN 2012ap and the Nature of Relativistic Supernovae Lacking a Gamma-Ray Burst Detection. *The Astrophysical Journal*, 799 (1):51, Jan. 2015. doi: 10.1088/0004-637X/799/1/51.

J. M. Miller, T. M. Sprouse, C. L. Fryer, B. R. Ryan, J. C. Dolence, M. R. Mumpower, and R. Surman. Full Transport General Relativistic Radiation Magnetohydrodynamics for Nucleosynthesis in Collapsars. *arXiv e-prints*, art. arXiv:1912.03378, Dec. 2019.

M. Modjaz, Y. Q. Liu, F. B. Bianco, and O. Graur. The Spectral SN-GRB Connection: Systematic Spectral Comparisons between Type Ic Supernovae and Broad-lined Type Ic Supernovae with and without Gamma-Ray Bursts. *The Astrophysical Journal*, 832(2):108, Dec. 2016. doi: 10.3847/0004-637X/832/2/108.

M. Modjaz, F. B. Bianco, M. Siwek, S. Huang, D. A. Perley, D. Fierroz, Y.-Q. Liu, I. Arcavi, A. Gal-Yam, A. V. Filippenko, N. Blagorodnova, B. S. Cenko, M. Kasliwal, S. Kulkarni, S. Schulze, K. Taggart, and W. Zheng. Host Galaxies of Type Ic and Broad-lined Type Ic Supernovae from the Palomar Transient Factory: Implications for Jet Production. *The Astrophysical Journal*, 892(2):153, Apr. 2020. doi: 10.3847/1538-4357/ab4185.

A. Monachesi, E. F. Bell, D. J. Radburn-Smith, J. Bailin, R. S. de Jong, B. Holwerda, D. Streich, and G. Silverstein. The GHOSTS survey - II. The diversity of halo colour and metallicity profiles of massive disc galaxies. *Monthly Notices of the Astronomical Society*, 457:1419–1446, Apr. 2016. doi: 10.1093/mnras/stv2987.

A. Monachesi, F. A. Gómez, R. J. J. Grand, C. M. Simpson, G. Kauffmann, S. Bustamante, F. Marinacci, R. Pakmor, V. Springel, C. S. Frenk, S. D. M. White, and P. B. Tissera. The Auriga Stellar Haloes: Connecting stellar population properties with accretion and merging history. *ArXiv e-prints*, art. arXiv:1804.07798, Apr. 2018.

A. Monachesi, F. A. Gómez, R. J. J. Grand, C. M. Simpson, G. Kauffmann, S. Bustamante, F. Marinacci, R. Pakmor, V. Springel, C. S. Frenk, S. D. M. White, and P. B. Tissera. The Auriga stellar haloes: connecting stellar population properties with accretion and merging history. *Monthly Notices of the Astronomical Society*, 485(2):2589–2616, May 2019. doi: 10.1093/mnras/stz538.

Y. Morinaga, T. Ishiyama, T. Kirihara, and K. Kinjo. Statistical properties of substructures around Milky Way-sized haloes and their implications for the formation of stellar streams. *Monthly Notices of the Astronomical Society*, 487(2):2718–2729, Aug. 2019. doi: 10.1093/mnras/stz1373.

P. Mösta, L. F. Roberts, G. Halevi, C. D. Ott, J. Lippuner, R. Haas, and E. Schnetter. r-process Nucleosynthesis from Three-dimensional Magnetorotational Core-collapse Supernovae. *The Astrophysical Journal*, 864(2):171, Sept. 2018. doi: 10.3847/1538-4357/aad6ec.

B. P. Moster, T. Naab, and S. D. M. White. Galactic star formation and accretion histories from matching galaxies to dark matter haloes. *Monthly Notices of the Astronomical Society*, 428:3121–3138, Feb. 2013. doi: 10.1093/mnras/sts261.

R. R. Muñoz, P. Côté, F. A. Santana, M. Geha, J. D. Simon, G. A. Oyarzún, P. B. Stetson, and S. G. Djorgovski. A MegaCam Survey of Outer Halo Satellites. III. Photometric and Structural Parameters. *The Astrophysical Journal*, 860(1):66, June 2018. doi: 10.3847/1538-4357/aac16b.

B. Mutlu-Pakdil, D. J. Sand, J. L. Carlin, K. Spekkens, N. Caldwell, D. Crnojević, A. K. Hughes, B. Willman, and D. Zaritsky. A Deeper Look at the New Milky Way Satellites: Sagittarius II, Reticulum II, Phoenix II, and Tucana III. *The Astrophysical Journal*, 863(1):25, Aug. 2018. doi: 10.3847/1538-4357/aacd0e.

G. C. Myeong, E. Vasiliev, G. Iorio, N. W. Evans, and V. Belokurov. Evidence for two early accretion events that built the Milky Way stellar halo. *Monthly Notices of the Astronomical Society*, 488(1):1235–1247, Sept. 2019. doi: 10.1093/mnras/stz1770.

D. Q. Nagasawa, J. L. Marshall, T. S. Li, T. T. Hansen, J. D. Simon, R. A. Bernstein, E. Balbinot, A. Drlica-Wagner, A. B. Pace, L. E. Strigari, C. M. Pellegrino, D. L. DePoy, N. B. Suntzeff, K. Bechtol, A. R. Walker, T. M. C. Abbott, F. B. Abdalla, S. Allam, J. Annis, A. Benoit-Lévy, E. Bertin, D. Brooks, A. Carnero Rosell, M. Carrasco Kind, J. Carretero, C. E. Cunha, C. B. D'Andrea, L. N. da Costa, C. Davis, S. Desai, P. Doel, T. F. Eifler, B. Flaugher, P. Fosalba, J. Frieman, J. García-Bellido, E. Gaztanaga, D. W. Gerdes, D. Gruen, R. A. Gruendl, J. Gschwend, G. Gutierrez, W. G. Hartley, K. Honscheid, D. J. James, T. Jeltema, E. Krause, K. Kuehn, S. Kuhlmann, N. Kuropatkin, M. March, R. Miquel, B. Nord, A. Roodman, E. Sanchez, B. Santiago, V. Scarpine, R. Schindler, M. Schubnell, I. Sevilla-Noarbe, M. Smith, R. C. Smith, M. Soares-Santos, F. Sobreira, E. Suchyta, G. Tarle, D. Thomas, D. L. Tucker, R. H. Wechsler, R. C. Wolf, and B. Yanny. Chemical Abundance Analysis of Three α-poor, Metal-poor Stars in the Ultrafaint Dwarf Galaxy Horologium I. *The Astrophysical Journal*, 852:99, Jan. 2018. doi: 10.3847/1538-4357/aaa01d.

R. P. Naidu, C. Conroy, A. Bonaca, B. D. Johnson, Y.-S. Ting, N. Caldwell, D. Zaritsky, and P. A. Cargile. Evidence from the H3 Survey That the Stellar Halo Is Entirely Comprised of Substructure. *The Astrophysical Journal*, 901(1):48, Sept. 2020. doi: 10.3847/1538-4357/abaef4.

J. P. Naiman, A. Pillepich, V. Springel, E. Ramirez-Ruiz, P. Torrey, M. Vogelsberger, R. Pakmor, D. Nelson, F. Marinacci, L. Hernquist, R. Weinberger, and S. Genel. First results from the IllustrisTNG simulations: a tale of two elements - chemical evolution of magnesium and europium. *Monthly Notices of the Astronomical Society*, 477:1206–1224, June 2018. doi: 10.1093/mnras/sty618.

O. Newton, M. Cautun, A. Jenkins, C. S. Frenk, and J. C. Helly. The total satellite population of the Milky Way. *Monthly Notices of the Astronomical Society*, 479: 2853–2870, Sept. 2018. doi: 10.1093/mnras/sty1085.

N. Nishimura, T. Takiwaki, and F.-K. Thielemann. The r-process Nucleosynthesis in the Various Jet-like Explosions of Magnetorotational Core-collapse Supernovae. *The Astrophysical Journal*, 810:109, Sept. 2015. doi: 10.1088/0004-637X/810/2/109.

J. E. Norris, D. Yong, G. Gilmore, and R. F. G. Wyse. Boo-1137an Extremely Metal-Poor Star in the Ultra-Faint Dwarf Spheroidal Galaxy Boötes I. *The Astrophysical Journal*, 711:350–360, Mar. 2010. doi: 10.1088/0004-637X/711/1/350.

J. E. Norris, D. Yong, K. A. Venn, G. Gilmore, L. Casagrande, and A. Dotter. The Populations of Carina. II. Chemical Enrichment. *The Astrophysical Journal Supplement Series*, 230:28, June 2017. doi: 10.3847/1538-4365/aa755e.

P. Ocvirk, N. Gillet, P. R. Shapiro, D. Aubert, I. T. Iliev, R. Teyssier, G. Yepes, J.-H. Choi, D. Sullivan, A. Knebe, S. Gottlöber, A. D'Aloisio, H. Park, Y. Hoffman, and T. Stranex. Cosmic Dawn (CoDa): the First Radiation-Hydrodynamics Simulation of Reionization and Galaxy Formation in the Local Universe. *Monthly Notices of the Astronomical Society*, 463:1462–1485, Dec. 2016. doi: 10.1093/mnras/stw2036.

T. Ojima, Y. Ishimaru, S. Wanajo, N. Prantzos, and P. Francois. Stochastic Chemical Evolution of Galactic Sub-halos and the Origin of r-Process Elements. *ArXiv e-prints*, art. arXiv:1808.03390, Aug. 2018.

T. Okamoto, L. Gao, and T. Theuns. Mass loss of galaxies due to an ultraviolet background. *Monthly Notices of the Astronomical Society*, 390:920–928, Nov. 2008. doi: 10.1111/j.1365-2966.2008.13830.x.

S. Olejnik and J. Algina. Generalized eta and omega squared statistics: Measures of effect size for some common research designs. *Psychological methods*, 8(4):434–447, 12 2003. Copyright - © 2003, American Psychological Association; Date completed - 2003-06-23; Date created - 2001-09-17; Date revised - 20031208; 20060710; Number of references - 31; Last updated - 2017-10-02; SubjectsTermNotLitGenreText - Effect Size (Statistical) 2879P1A 405P1A 8696P1A 9196P1A 2869P0A 405P0A 8657P0A 9154P0A; Experimental Design 3252P1A 3267P1A 9196P1A 3240P0A 3255P0A 9154P0A; Statistical Measurement 5338P1A 8701P1A 9196P1A 5315P0A 8662P0A 9154P0A; Statistics 1731P1A 2834P1A 3855P1A 5080P1A 5312P1A 5682P1A 7127P1A 8002P1A 8716P1A 8722P1A 9196P1A 9798P1A 9802P1A 1725P0A 2824P0A 3838P0A 5057P0A 5289P0A 5657P0A 7097P0A 7967P0A 8677P0A 8683P0A 9154P0A 9749P0A 9753P0A; 405P1A 8696P1A 8710P1A 9196P1A 405P0A 8657P0A 8671P0A 9154P0A.

L. J. Papenfort, R. Gold, and L. Rezzolla. Dynamical ejecta and nucleosynthetic yields from eccentric binary neutron-star mergers. *Physical Review D: Particles, Fields, Gravitation and Cosmology*, 98(10):104028, Nov. 2018. doi: 10.1103/PhysRevD.98.104028.

M. Petropoulou, R. Barniol Duran, and D. Giannios. Collapsar γ-ray bursts: how the luminosity function dictates the duration distribution. *Monthly Notices of the Astronomical Society*, 472(3):2722–2727, Dec. 2017. doi: 10.1093/mnras/stx2151.

E. Pian, P. D'Avanzo, S. Benetti, M. Branchesi, E. Brocato, S. Campana, E. Cappellaro, S. Covino, V. D'Elia, J. P. U. Fynbo, F. Getman, G. Ghirland a, G. Ghisellini, A. Grado, G. Greco, J. Hjorth, C. Kouveliotou, A. Levan, L. Limatola, D. Malesani, P. A. Mazzali, A. Melandri, P. Møller, L. Nicastro, E. Palazzi, S. Piranomonte, A. Rossi, O. S. Salafia, J. Selsing, G. Stratta, M. Tanaka, N. R. Tanvir, L. Tomasella, D. Watson, S. Yang, L. Amati, L. A. Antonelli, S. Ascenzi, M. G. Bernardini, M. Boër, F. Bufano, A. Bulgarelli, M. Capaccioli, P. Casella, A. J. Castro-Tirado, E. Chassande-Mottin, R. Ciolfi, C. M. Copperwheat, M. Dadina, G. De Cesare, A. di Paola, Y. Z. Fan, B. Gendre, G. Giuffrida, A. Giunta, L. K.

Hunt, G. L. Israel, Z. P. Jin, M. M. Kasliwal, S. Klose, M. Lisi, F. Longo, E. Maiorano, M. Mapelli, N. Masetti, L. Nava, B. Patricelli, D. Perley, A. Pescalli, T. Piran, A. Possenti, L. Pulone, M. Razzano, R. Salvaterra, P. Schipani, M. Spera, A. Stamerra, L. Stella, G. Tagliaferri, V. Testa, E. Troja, M. Turatto, S. D. Vergani, and D. Vergani. Spectroscopic identification of r-process nucleosynthesis in a double neutron-star merger. *Nature*, 551(7678):67–70, Nov. 2017. doi: 10.1038/nature24298.

Planck Collaboration, P. A. R. Ade, N. Aghanim, C. Armitage-Caplan, M. Arnaud, M. Ashdown, F. Atrio-Barandela, J. Aumont, C. Baccigalupi, A. J. Banday, and et al. Planck 2013 results. XVI. Cosmological parameters. *Astronomy and Astrophysics*, 571:A16, Nov. 2014. doi: 10.1051/0004-6361/201321591.

P. Plotly Technologies Inc. Collaborative data science, 2015. URL `https://plot.ly`.

N. Prantzos, C. Abia, M. Limongi, A. Chieffi, and S. Cristallo. Chemical evolution with rotating massive star yields - I. The solar neighbourhood and the s-process elements. *Monthly Notices of the Astronomical Society*, 476(3):3432–3459, May 2018. doi: 10.1093/mnras/sty316.

W. Press and M. Davis. How to identify and weigh virialized clusters of galaxies in a complete redshift catalog. *The Astrophysical Journal*, 259:449–473, 1982.

Y. Qin, A. Mesinger, J. Park, B. Greig, and J. B. Muñoz. A tale of two sites - I. Inferring the properties of minihalo-hosted galaxies from current observations. *Monthly Notices of the Astronomical Society*, 495(1):123–140, Apr. 2020. doi: 10.1093/mnras/staa1131.

D. Radice, A. Perego, K. Hotokezaka, S. A. Fromm, S. Bernuzzi, and L. F. Roberts. Binary Neutron Star Mergers: Mass Ejection, Electromagnetic Counterparts, and Nucleosynthesis. *The Astrophysical Journal*, 869(2):130, Dec. 2018. doi: 10.3847/1538-4357/aaf054.

E. Ramirez-Ruiz, M. Trenti, M. MacLeod, L. F. Roberts, W. H. Lee, and M. I. Saladino-Rosas. Compact Stellar Binary Assembly in the First Nuclear Star Clusters and r-process Synthesis in the Early Universe. *The Astrophysical Journal, Letters*, 802:L22, Apr. 2015. doi: 10.1088/2041-8205/802/2/L22.

V. Rashkov, P. Madau, M. Kuhlen, and J. Diemand. On the Assembly of the Milky Way Dwarf Satellites and Their Common Mass Scale. *The Astrophysical Journal*, 745(2):142, Feb. 2012. doi: 10.1088/0004-637X/745/2/142.

A. Rémy-Ruyer, S. C. Madden, F. Galliano, M. Galametz, T. T. Takeuchi, R. S. Asano, S. Zhukovska, V. Lebouteiller, D. Cormier, A. Jones, M. Bocchio, M. Baes, G. J. Bendo, M. Boquien, A. Boselli, I. DeLooze, V. Doublier-Pritchard, T. Hughes, O. Ł. Karczewski, and L. Spinoglio. Gas-to-dust mass ratios in local galaxies over a 2 dex metallicity range. *Astronomy and Astrophysics*, 563:A31, Mar. 2014. doi: 10.1051/0004-6361/201322803.

B. Robertson, J. S. Bullock, A. S. Font, K. V. Johnston, and L. Hernquist. Λ Cold Dark Matter, Stellar Feedback, and the Galactic Halo Abundance Pattern. *The Astrophysical Journal*, 632(2):872–881, Oct. 2005. doi: 10.1086/452619.

I. U. Roederer and E. N. Kirby. Detailed abundance analysis of the brightest star in Segue 2, the least massive galaxy. *Monthly Notices of the Astronomical Society*, 440:2665–2675, May 2014. doi: 10.1093/mnras/stu491.

I. U. Roederer, J. J. Cowan, G. W. Preston, S. A. Shectman, C. Sneden, and I. B. Thompson. Nine new metal-poor stars on the subgiant and red horizontal branches with high levels of r-process enhancement. *Monthly Notices of the Astronomical Society*, 445(3):2970–2984, Dec. 2014a. doi: 10.1093/mnras/stu1977.

I. U. Roederer, G. W. Preston, I. B. Thompson, S. A. Shectman, and C. Sneden. Neutron-capture Nucleosynthesis in the First Stars. *The Astrophysical Journal*, 784:158, Apr. 2014b. doi: 10.1088/0004-637X/784/2/158.

I. U. Roederer, G. W. Preston, I. B. Thompson, S. A. Shectman, C. Sneden, G. S. Burley, and D. D. Kelson. A Search for Stars of Very Low Metal Abundance. VI. Detailed Abundances of 313 Metal-poor Stars. *The Astronomical Journal*, 147:136, June 2014c. doi: 10.1088/0004-6256/147/6/136.

I. U. Roederer, M. Mateo, I. Bailey, John I., Y. Song, E. F. Bell, J. D. Crane, S. Loebman, D. L. Nidever, E. W. Olszewski, S. A. Shectman, I. B. Thompson, M. Valluri, and M. G. Walker. Detailed Chemical Abundances in the r-process-rich Ultra-faint Dwarf Galaxy Reticulum 2. *The Astronomical Journal*, 151(3):82, Mar. 2016a. doi: 10.3847/0004-6256/151/3/82.

I. U. Roederer, M. Mateo, J. I. Bailey, III, Y. Song, E. F. Bell, J. D. Crane, S. Loebman, D. L. Nidever, E. W. Olszewski, S. A. Shectman, I. B. Thompson, M. Valluri, and M. G. Walker. Detailed Chemical Abundances in the r-process-rich Ultra-faint Dwarf Galaxy Reticulum 2. *The Astronomical Journal*, 151:82, Mar. 2016b. doi: 10.3847/0004-6256/151/3/82.

I. U. Roederer, K. Hattori, and M. Valluri. Kinematics of Highly r-process-enhanced Field Stars: Evidence for an Accretion Origin and Detection of Several Groups from Disrupted Satellites. *The Astronomical Journal*, 156(4):179, Oct. 2018. doi: 10.3847/1538-3881/aadd9c.

A. J. Ruiter, K. Belczynski, S. A. Sim, W. Hillebrandt, C. L. Fryer, M. Fink, and M. Kromer. Delay times and rates for Type Ia supernovae and thermonuclear explosions from double-detonation sub-Chandrasekhar mass models. *Monthly Notices of the Astronomical Society*, 417(1):408–419, Oct. 2011. doi: 10.1111/j.1365-2966.2011.19276.x.

T. Ruiz-Lara, T. Matsuno, S. Sofie Lövdal, A. Helmi, E. Dodd, and H. H. Koppelman. Substructure in the stellar halo near the Sun. II. Characterisation of independent structures. *arXiv e-prints*, art. arXiv:2201.02405, Jan. 2022.

M. Safarzadeh, E. Ramirez-Ruiz, J. J. Andrews, P. Macias, T. Fragos, and E. Scannapieco. r-process Enrichment of the Ultra-faint Dwarf Galaxies by Fast-merging Double-neutron Stars. *The Astrophysical Journal*, 872(1):105, Feb. 2019a. doi: 10.3847/1538-4357/aafe0e.

M. Safarzadeh, R. Sarmento, and E. Scannapieco. On Neutron Star Mergers as the Source of r-process-enhanced Metal-poor Stars in the Milky Way. *The Astrophysical Journal*, 876(1):28, May 2019b. doi: 10.3847/1538-4357/ab1341.

C. M. Sakari, V. M. Placco, E. M. Farrell, I. U. Roederer, G. Wallerstein, T. C. Beers, R. Ezzeddine, A. Frebel, T. Hansen, E. M. Holmbeck, C. Sneden, J. J. Cowan, K. A. Venn, C. E. Davis, G. Matijevič, R. F. G. Wyse, J. Bland-Hawthorn, C. Chiappini, K. C. Freeman, B. K. Gibson, E. K. Grebel, A. Helmi, G. Kordopatis, A. Kunder, J. Navarro, W. Reid, G. Seabroke, M. Steinmetz, and F. Watson. The R-Process Alliance: First Release from the Northern Search for r-process-enhanced Metal-poor Stars in the Galactic Halo. *The Astrophysical Journal*, 868(2):110, Dec. 2018. doi: 10.3847/1538-4357/aae9df.

E. E. Salpeter. The Luminosity Function and Stellar Evolution. *The Astrophysical Journal*, 121:161, Jan. 1955. doi: 10.1086/145971.

D. Schaerer. On the properties of massive Population III stars and metal-free stellar populations. *Astronomy and Astrophysics*, 382:28–42, Jan 2002. doi: 10.1051/0004-6361:20011619.

J. H. M. M. Schmitt. Statistical analysis of astronomical data containing upper bounds: general methods and examples drawn from X-ray astronomy. *The Astrophysical Journal*, 293:178–191, June 1985. doi: 10.1086/163224.

T. Schörck, N. Christlieb, J. G. Cohen, T. C. Beers, S. Shectman, I. Thompson, A. McWilliam, M. S. Bessell, J. E. Norris, J. Meléndez, S. Ramírez, D. Haynes, P. Cass, M. Hartley, K. Russell, F. Watson, F. J. Zickgraf, B. Behnke, C. Fechner, B. Fuhrmeister, P. S. Barklem, B. Edvardsson, A. Frebel, L. Wisotzki, and D. Reimers. The stellar content of the Hamburg/ESO survey. V. The metallicity distribution function of the Galactic halo. *Astronomy and Astrophysics*, 507: 817–832, Nov. 2009. doi: 10.1051/0004-6361/200810925.

S. Schulze, O. Yaron, J. Sollerman, G. Leloudas, A. Gal, A. H. Wright, R. Lunnan, A. Gal-Yam, E. O. Ofek, D. A. Perley, A. V. Filippenko, M. M. Kasliwal, S. R. Kulkarni, P. E. Nugent, R. M. Quimby, M. Sullivan, N. Linn Strothjohann, I. Arcavi, S. Ben-Ami, F. Bianco, J. S. Bloom, K. De, M. Fraser, C. U. Fremling, A. Horesh, J. Johansson, P. L. Kelly, S. Knezevic, K. Maguire, A. Nyholm, . Semeli Papadogiannakis, T. Petrushevska, A. Rubin, L. Yan, Y. Yang, S. M. Adams, F. Bufano, K. I. Clubb, R. J. Foley, Y. Green, J. Harmanen, A. Y. Q. Ho, I. M. Hook, G. Hosseinzadeh, D. A. Howell, A. K. H. Kong, R. Kotak, T. Matheson, C. McCully, D. Milisavljevic, Y.-C. Pan, D. Poznanski, I. Shivvers, and S. van Velzen. The Palomar Transient Factory Core-Collapse Supernova Host-Galaxy

Sample. I. Host-Galaxy Distribution Functions and Environment-Dependence of CCSNe. *arXiv e-prints*, art. arXiv:2008.05988, Aug. 2020.

Y. Sekiguchi, K. Kiuchi, K. Kyutoku, M. Shibata, and K. Taniguchi. Dynamical mass ejection from the merger of asymmetric binary neutron stars: Radiation-hydrodynamics study in general relativity. *Physical Review D: Particles, Fields, Gravitation and Cosmology*, 93(12):124046, June 2016. doi: 10.1103/PhysRevD.93.124046.

S. Sharma and K. V. Johnston. A Group Finding Algorithm for Multidimensional Data Sets. *The Astrophysical Journal*, 703(1):1061–1077, Sept. 2009. doi: 10.1088/0004-637X/703/1/1061.

S. Shen, R. J. Cooke, E. Ramirez-Ruiz, P. Madau, L. Mayer, and J. Guedes. The History of R-Process Enrichment in the Milky Way. *The Astrophysical Journal*, 807(2):115, July 2015. doi: 10.1088/0004-637X/807/2/115.

M. Shetrone, K. A. Venn, E. Tolstoy, F. Primas, V. Hill, and A. Kaufer. VLT/UVES Abundances in Four Nearby Dwarf Spheroidal Galaxies. I. Nucleosynthesis and Abundance Ratios. *The Astronomical Journal*, 125:684–706, Feb. 2003. doi: 10.1086/345966.

M. D. Shetrone, P. Côté, and W. L. W. Sargent. Abundance Patterns in the Draco, Sextans, and Ursa Minor Dwarf Spheroidal Galaxies. *The Astrophysical Journal*, 548:592–608, Feb. 2001. doi: 10.1086/319022.

I. Shivvers, M. Modjaz, W. Zheng, Y. Liu, A. V. Filippenko, J. M. Silverman, T. Matheson, A. Pastorello, O. Graur, R. J. Foley, R. Chornock, N. Smith, J. Leaman, and S. Benetti. Revisiting the Lick Observatory Supernova Search Volume-limited Sample: Updated Classifications and Revised Stripped-envelope Supernova Fractions. *Publications of the Astronomical Society of the Pacific*, 129(975):054201, May 2017. doi: 10.1088/1538-3873/aa54a6.

D. M. Siegel. GW170817 -the first observed neutron star merger and its kilonova: Implications for the astrophysical site of the r-process. *European Physical Journal A*, 55(11):203, Nov. 2019. doi: 10.1140/epja/i2019-12888-9.

D. M. Siegel. Heavy elements form short and long gamma-ray bursts. *arXiv e-prints*, art. arXiv:2008.06078, Aug. 2020.

D. M. Siegel, J. Barnes, and B. D. Metzger. Collapsars as a major source of r-process elements. *Nature*, 569(7755):241–244, May 2019. doi: 10.1038/s41586-019-1136-0.

R. A. Simcoe, W. L. W. Sargent, and M. Rauch. The Distribution of Metallicity in the Intergalactic Medium at z~2.5: O VI and C IV Absorption in the Spectra of Seven QSOs. *The Astrophysical Journal*, 606(1):92–115, May 2004. doi: 10.1086/382777.

J. D. Simon. The Faintest Dwarf Galaxies. *Annual Review of Astronomy and Astrophysics*, 57:375–415, Aug. 2019. doi: 10.1146/annurev-astro-091918-104453.

J. D. Simon, A. Frebel, A. McWilliam, E. N. Kirby, and I. B. Thompson. High-resolution Spectroscopy of Extremely Metal-poor Stars in the Least Evolved Galaxies: Leo IV. *The Astrophysical Journal*, 716:446–452, June 2010. doi: 10.1088/0004-637X/716/1/446.

J. D. Simon, H. R. Jacobson, A. Frebel, I. B. Thompson, J. J. Adams, and S. A. Shectman. Chemical Signatures of the First Supernovae in the Sculptor Dwarf Spheroidal Galaxy. *The Astrophysical Journal*, 802:93, Apr. 2015. doi: 10.1088/0004-637X/802/2/93.

Á. Skúladóttir, E. Tolstoy, S. Salvadori, V. Hill, M. Pettini, M. D. Shetrone, and E. Starkenburg. The first carbon-enhanced metal-poor star found in the Sculptor dwarf spheroidal. *Astronomy and Astrophysics*, 574:A129, Feb. 2015. doi: 10.1051/0004-6361/201424782.

Á. Skúladóttir, C. J. Hansen, S. Salvadori, and A. Choplin. Neutron-capture elements in dwarf galaxies. I. Chemical clocks and the short timescale of the r-process. *Astronomy and Astrophysics*, 631:A171, Nov. 2019. doi: 10.1051/0004-6361/201936125.

B. D. Smith, G. L. Bryan, S. C. O. Glover, N. J. Goldbaum, M. J. Turk, J. Regan, J. H. Wise, H.-Y. Schive, T. Abel, A. Emerick, B. W. O'Shea, P. Anninos, C. B. Hummels, and S. Khochfar. GRACKLE: a chemistry and cooling library for astrophysics. *Monthly Notices of the Astronomical Society*, 466:2217–2234, Apr. 2017. doi: 10.1093/mnras/stw3291.

M. C. Smith, D. Sijacki, and S. Shen. Supernova feedback in numerical simulations of galaxy formation: separating physics from numerics. *Monthly Notices of the Astronomical Society*, 478:302–331, July 2018. doi: 10.1093/mnras/sty994.

C. Sneden, J. J. Cowan, and R. Gallino. Neutron-Capture Elements in the Early Galaxy. *Annual Review of Astronomy and Astrophysics*, 46:241–288, Sept. 2008. doi: 10.1146/annurev.astro.46.060407.145207.

E. Sobacchi, J. Granot, O. Bromberg, and M. C. Sormani. A common central engine for long gamma-ray bursts and Type Ib/c supernovae. *Monthly Notices of the Astronomical Society*, 472(1):616–627, Nov. 2017. doi: 10.1093/mnras/stx2083.

A. M. Soderberg, S. Chakraborti, G. Pignata, R. A. Chevalier, P. Chandra, A. Ray, M. H. Wieringa, A. Copete, V. Chaplin, V. Connaughton, S. D. Barthelmy, M. F. Bietenholz, N. Chugai, M. D. Stritzinger, M. Hamuy, C. Fransson, O. Fox, E. M. Levesque, J. E. Grindlay, P. Challis, R. J. Foley, R. P. Kirshner, P. A. Milne, and M. A. P. Torres. A relativistic type Ibc supernova without a detected γ-ray burst. *Nature*, 463(7280):513–515, Jan. 2010. doi: 10.1038/nature08714.

S. Sofie Lövdal, T. Ruiz-Lara, H. H. Koppelman, T. Matsuno, E. Dodd, and A. Helmi. Substructure in the stellar halo near the Sun. I. Data-driven clustering in Integrals of Motion space. *arXiv e-prints*, art. arXiv:2201.02404, Jan. 2022.

M. Steinmetz, T. Zwitter, A. Siebert, F. G. Watson, K. C. Freeman, U. Munari, R. Campbell, M. Williams, G. M. Seabroke, R. F. G. Wyse, Q. A. Parker, O. Bienaymé, S. Roeser, B. K. Gibson, G. Gilmore, E. K. Grebel, A. Helmi, J. F. Navarro, D. Burton, C. J. P. Cass, J. A. Dawe, K. Fiegert, M. Hartley, K. S. Russell, W. Saunders, H. Enke, J. Bailin, J. Binney, J. Bland-Hawthorn, C. Boeche, W. Dehnen, D. J. Eisenstein, N. W. Evans, M. Fiorucci, J. P. Fulbright, O. Gerhard, U. Jauregi, A. Kelz, L. Mijović, I. Minchev, G. Parmentier, J. Peñarrubia, A. C. Quillen, M. A. Read, G. Ruchti, R. D. Scholz, A. Siviero, M. C. Smith, R. Sordo, L. Veltz, S. Vidrih, R. von Berlepsch, B. J. Boyle, and E. Schilbach. The Radial Velocity Experiment (RAVE): First Data Release. *The Astronomical Journal*, 132(4): 1645–1668, Oct. 2006. doi: 10.1086/506564.

L. E. Strigari, J. S. Bullock, M. Kaplinghat, J. D. Simon, M. Geha, B. Willman, and M. G. Walker. A common mass scale for satellite galaxies of the Milky Way. *Nature*, 454:1096–1097, Aug. 2008. doi: 10.1038/nature07222.

R. Surman, G. C. McLaughlin, and W. R. Hix. Nucleosynthesis in the Outflow from Gamma-Ray Burst Accretion Disks. *The Astrophysical Journal*, 643(2):1057–1064, June 2006. doi: 10.1086/501116.

H. Susa, K. Hasegawa, and N. Tominaga. The Mass Spectrum of the First Stars. *The Astrophysical Journal*, 792(1):32, Sept. 2014. doi: 10.1088/0004-637X/792/1/32.

M. Tafelmeyer, P. Jablonka, V. Hill, M. Shetrone, E. Tolstoy, M. J. Irwin, G. Battaglia, A. Helmi, E. Starkenburg, K. A. Venn, T. Abel, P. Francois, A. Kaufer, P. North, F. Primas, and T. Szeifert. Extremely metal-poor stars in classical dwarf spheroidal galaxies: Fornax, Sculptor, and Sextans. *Astronomy and Astrophysics*, 524:A58, Dec. 2010. doi: 10.1051/0004-6361/201014733.

J. Tang, A. Bressan, P. Rosenfield, A. Slemer, P. Marigo, L. Girardi, and L. Bianchi. New PARSEC evolutionary tracks of massive stars at low metallicity: testing canonical stellar evolution in nearby star-forming dwarf galaxies. *Monthly Notices of the Astronomical Society*, 445:4287–4305, Dec. 2014. doi: 10.1093/mnras/stu2029.

Y. Tarumi, N. Yoshida, and S. Inoue. R-process enrichment in ultrafaint dwarf galaxies. *Monthly Notices of the Astronomical Society*, 494(1):120–128, Mar. 2020. doi: 10.1093/mnras/staa720.

The LIGO Scientific Collaboration, the Virgo Collaboration, R. Abbott, T. D. Abbott, S. Abraham, F. Acernese, K. Ackley, A. Adams, C. Adams, R. X. Adhikari, V. B. Adya, C. Affeldt, M. Agathos, K. Agatsuma, N. Aggarwal, O. D. Aguiar, L. Aiello, A. Ain, P. Ajith, G. Allen, A. Allocca, P. A. Altin, A. Amato, S. Anand, A. Ananyeva, S. B. Anderson, W. G. Anderson, S. V. Angelova, S. Ansoldi, J. M. Antelis, S. Antier, S. Appert, K. Arai, M. C. Araya, J. S. Areeda, M. Arène, N. Arnaud, S. M. Aronson, K. G. Arun, Y. Asali, S. Ascenzi, G. Ashton, S. M. Aston, P. Astone, F. Aubin, P. Aufmuth, K. AultONeal, C. Austin, V. Avendano, S. Babak, F. Badaracco, M. K. M. Bader, S. Bae, A. M. Baer, S. Bagnasco, J. Baird,

M. Ball, G. Ballardin, S. W. Ballmer, A. Bals, A. Balsamo, G. Baltus, S. Banagiri, D. Bankar, R. S. Bankar, J. C. Barayoga, C. Barbieri, B. C. Barish, D. Barker, P. Barneo, S. Barnum, F. Barone, B. Barr, L. Barsotti, M. Barsuglia, D. Barta, J. Bartlett, I. Bartos, R. Bassiri, A. Basti, M. Bawaj, J. C. Bayley, M. Bazzan, B. R. Becher, B. Bécsy, V. M. Bedakihale, M. Bejger, I. Belahcene, D. Beniwal, M. G. Benjamin, T. F. Bennett, J. D. Bentley, F. Bergamin, B. K. Berger, G. Bergmann, S. Bernuzzi, C. P. L. Berry, D. Bersanetti, A. Bertolini, J. Betzwieser, R. Bhandare, A. V. Bhandari, D. Bhattacharjee, J. Bidler, I. A. Bilenko, G. Billingsley, R. Birney, O. Birnholtz, S. Biscans, M. Bischi, S. Biscoveanu, A. Bisht, M. Bitossi, M. A. Bizouard, J. K. Blackburn, J. Blackman, C. D. Blair, D. G. Blair, R. M. Blair, O. Blanch, F. Bobba, N. Bode, M. Boer, Y. Boetzel, G. Bogaert, M. Boldrini, F. Bondu, E. Bonilla, R. Bonnand, P. Booker, B. A. Boom, R. Bork, V. Boschi, S. Bose, V. Bossilkov, V. Boudart, Y. Bouffanais, A. Bozzi, C. Bradaschia, P. R. Brady, A. Bramley, M. Branchesi, J. E. Brau, M. Breschi, T. Briant, J. H. Briggs, F. Brighenti, A. Brillet, M. Brinkmann, P. Brockill, A. F. Brooks, J. Brooks, D. D. Brown, S. Brunett, G. Bruno, R. Bruntz, A. Buikema, T. Bulik, H. J. Bulten, A. Buonanno, R. Buscicchio, D. Buskulic, R. L. Byer, M. Cabero, L. Cadonati, M. Caesar, G. Cagnoli, C. Cahillane, J. Calderón Bustillo, J. D. Callaghan, T. A. Callister, E. Calloni, J. B. Camp, M. Canepa, K. C. Cannon, H. Cao, J. Cao, G. Carapella, F. Carbognani, M. F. Carney, M. Carpinelli, G. Carullo, T. L. Carver, J. Casanueva Diaz, C. Casentini, S. Caudill, M. Cavaglià, F. Cavalier, R. Cavalieri, G. Cella, P. Cerdá-Durán, E. Cesarini, W. Chaibi, K. Chakravarti, C. L. Chan, C. Chan, K. Chandra, P. Chanial, S. Chao, P. Charlton, E. A. Chase, E. Chassande-Mottin, D. Chatterjee, D. Chattopadhyay, M. Chaturvedi, K. Chatziioannou, A. Chen, H. Y. Chen, X. Chen, Y. Chen, H. P. Cheng, C. K. Cheong, H. Y. Chia, F. Chiadini, R. Chierici, A. Chincarini, A. Chiummo, G. Cho, H. S. Cho, M. Cho, S. Choate, N. Christensen, Q. Chu, S. Chua, K. W. Chung, S. Chung, G. Ciani, P. Ciecielag, M. Cieślar, M. Cifaldi, A. A. Ciobanu, R. Ciolfi, F. Cipriano, A. Cirone, F. Clara, E. N. Clark, J. A. Clark, L. Clarke, P. Clearwater, S. Clesse, F. Cleva, E. Coccia, P. F. Cohadon, D. E. Cohen, M. Colleoni, C. G. Collette, C. Collins, M. Colpi, J. Constancio, M., L. Conti, S. J. Cooper, P. Corban, T. R. Corbitt, I. Cordero-Carrión, S. Corezzi, K. R. Corley, N. Cornish, D. Corre, A. Corsi, S. Cortese, C. A. Costa, R. Cotesta, M. W. Coughlin, S. B. Coughlin, J. P. Coulon, S. T. Countryman, P. Couvares, P. B. Covas, D. M. Coward, M. J. Cowart, D. C. Coyne, R. Coyne, J. D. E. Creighton, T. D. Creighton, M. Croquette, S. G. Crowder, J. R. Cudell, T. J. Cullen, A. Cumming, R. Cummings, L. Cunningham, E. Cuoco, M. Cury{l}o, T. Dal Canton, G. Dálya, A. Dana, L. M. DaneshgaranBajastani, B. D'Angelo, S. L. Danilishin, S. D'Antonio, K. Danzmann, C. Darsow-Fromm, A. Dasgupta, L. E. H. Datrier, V. Dattilo, I. Dave, M. Davier, G. S. Davies, D. Davis, E. J. Daw, R. Dean, D. DeBra, M. Deenadayalan, J. Degallaix, M. De Laurentis, S. Deléglise, V. Del Favero, F. De Lillo, N. De Lillo, W. Del Pozzo, L. M. DeMarchi, F. De Matteis, V. D'Emilio, N. Demos, T. Denker, T. Dent, A. Depasse, R. De Pietri, R. De Rosa, C. De Rossi, R. DeSalvo, O. de Varona, S. Dhurandhar, M. C. Díaz, J. Diaz-Ortiz, M., N. A. Didio, T. Dietrich, L. Di Fiore, C. DiFronzo, C. Di Giorgio, F. Di Giovanni, M. Di Giovanni,

T. Di Girolamo, A. Di Lieto, B. Ding, S. Di Pace, I. Di Palma, F. Di Renzo, A. K. Divakarla, A. Dmitriev, Z. Doctor, L. D'Onofrio, F. Donovan, K. L. Dooley, S. Doravari, I. Dorrington, T. P. Downes, M. Drago, J. C. Driggers, Z. Du, J. G. Ducoin, P. Dupej, O. Durante, D. D'Urso, P. A. Duverne, S. E. Dwyer, P. J. Easter, G. Eddolls, B. Edelman, T. B. Edo, O. Edy, A. Effler, J. Eichholz, S. S. Eikenberry, M. Eisenmann, R. A. Eisenstein, A. Ejlli, L. Errico, R. C. Essick, H. Estellés, D. Estevez, Z. B. Etienne, T. Etzel, M. Evans, T. M. Evans, B. E. Ewing, V. Fafone, H. Fair, S. Fairhurst, X. Fan, A. M. Farah, S. Farinon, B. Farr, W. M. Farr, E. J. Fauchon-Jones, M. Favata, M. Fays, M. Fazio, J. Feicht, M. M. Fejer, F. Feng, E. Fenyvesi, D. L. Ferguson, A. Fernandez-Galiana, I. Ferrante, T. A. Ferreira, F. Fidecaro, P. Figura, I. Fiori, D. Fiorucci, M. Fishbach, R. P. Fisher, J. M. Fishner, R. Fittipaldi, M. Fitz-Axen, V. Fiumara, R. Flaminio, E. Floden, E. Flynn, H. Fong, J. A. Font, P. W. F. Forsyth, J. D. Fournier, S. Frasca, F. Frasconi, Z. Frei, A. Freise, R. Frey, V. Frey, P. Fritschel, V. V. Frolov, G. G. Fronzé, P. Fulda, M. Fyffe, H. A. Gabbard, B. U. Gadre, S. M. Gaebel, J. R. Gair, J. Gais, S. Galaudage, R. Gamba, D. Ganapathy, A. Ganguly, S. G. Gaonkar, B. Garaventa, C. García-Quirós, F. Garufi, B. Gateley, S. Gaudio, V. Gayathri, G. Gemme, A. Gennai, D. George, J. George, L. Gergely, S. Ghonge, A. Ghosh, A. Ghosh, S. Ghosh, B. Giacomazzo, L. Giacoppo, J. A. Giaime, K. D. Giardina, D. R. Gibson, C. Gier, K. Gill, P. Giri, J. Glanzer, A. E. Gleckl, P. Godwin, E. Goetz, R. Goetz, N. Gohlke, B. Goncharov, G. González, A. Gopakumar, S. E. Gossan, M. Gosselin, R. Gouaty, B. Grace, A. Grado, M. Granata, V. Granata, A. Grant, S. Gras, P. Grassia, C. Gray, R. Gray, G. Greco, A. C. Green, R. Green, E. M. Gretarsson, H. L. Griggs, G. Grignani, A. Grimaldi, E. Grimes, S. J. Grimm, H. Grote, S. Grunewald, P. Gruning, J. G. Guerrero, G. M. Guidi, A. R. Guimaraes, G. Guixé, H. K. Gulati, Y. Guo, A. Gupta, A. Gupta, P. Gupta, E. K. Gustafson, R. Gustafson, F. Guzman, L. Haegel, O. Halim, E. D. Hall, E. Z. Hamilton, G. Hammond, M. Haney, M. M. Hanke, J. Hanks, C. Hanna, O. A. Hannuksela, H. Hansen, T. J. Hansen, J. Hanson, T. Harder, T. Hardwick, K. Haris, J. Harms, G. M. Harry, I. W. Harry, D. Hartwig, R. K. Hasskew, C. J. Haster, K. Haughian, F. J. Hayes, J. Healy, A. Heidmann, M. C. Heintze, J. Heinze, J. Heinzel, H. Heitmann, F. Hellman, P. Hello, A. F. Helmling-Cornell, G. Hemming, M. Hendry, I. S. Heng, E. Hennes, J. Hennig, M. H. Hennig, F. Hernandez Vivanco, M. Heurs, S. Hild, P. Hill, A. S. Hines, S. Hochheim, E. Hofgard, D. Hofman, J. N. Hohmann, A. M. Holgado, N. A. Holland, I. J. Hollows, Z. J. Holmes, K. Holt, D. E. Holz, P. Hopkins, C. Horst, J. Hough, E. J. Howell, C. G. Hoy, D. Hoyland, Y. Huang, M. T. Hübner, A. D. Huddart, E. A. Huerta, B. Hughey, V. Hui, S. Husa, S. H. Huttner, B. M. Hutzler, R. Huxford, T. Huynh-Dinh, B. Idzkowski, A. Iess, S. Imperato, H. Inchauspe, C. Ingram, G. Intini, M. Isi, B. R. Iyer, V. JaberianHamedan, T. Jacqmin, S. J. Jadhav, S. P. Jadhav, A. L. James, K. Jani, K. Janssens, N. N. Janthalur, P. Jaranowski, D. Jariwala, R. Jaume, A. C. Jenkins, M. Jeunon, J. Jiang, G. R. Johns, A. W. Jones, D. I. Jones, J. D. Jones, P. Jones, R. Jones, R. J. G. Jonker, L. Ju, J. Junker, C. V. Kalaghatgi, V. Kalogera, B. Kamai, S. Kandhasamy, G. Kang, J. B. Kanner, S. J. Kapadia, D. P. Kapasi, C. Karathanasis, S. Karki, R. Kashyap, M. Kasprzack, W. Kastaun, S. Katsanevas, E. Katsavouni-

dis, W. Katzman, K. Kawabe, F. Kéfélian, D. Keitel, J. S. Key, S. Khadka, F. Y. Khalili, I. Khan, S. Khan, E. A. Khazanov, N. Khetan, M. Khursheed, N. Kijbunchoo, C. Kim, G. J. Kim, J. C. Kim, K. Kim, W. S. Kim, Y. M. Kim, C. Kimball, P. J. King, M. Kinley-Hanlon, R. Kirchhoff, J. S. Kissel, L. Kleybolte, S. Klimenko, T. D. Knowles, E. Knyazev, P. Koch, S. M. Koehlenbeck, G. Koekoek, S. Koley, M. Kolstein, K. Komori, V. Kondrashov, A. Kontos, N. Koper, M. Korobko, W. Z. Korth, M. Kovalam, D. B. Kozak, C. Krämer, V. Kringel, N. V. Krishnendu, A. Królak, G. Kuehn, A. Kumar, P. Kumar, R. Kumar, R. Kumar, K. Kuns, S. Kwang, B. D. Lackey, D. Laghi, E. Lalande, T. L. Lam, A. Lamberts, M. Landry, B. B. Lane, R. N. Lang, J. Lange, B. Lantz, R. K. Lanza, I. La Rosa, A. Lartaux-Vollard, P. D. Lasky, M. Laxen, A. Lazzarini, C. Lazzaro, P. Leaci, S. Leavey, Y. K. Lecoeuche, H. M. Lee, H. W. Lee, J. Lee, K. Lee, J. Lehmann, E. Leon, N. Leroy, N. Letendre, Y. Levin, A. Li, J. Li, K. J. L. Li, T. G. F. Li, X. Li, F. Linde, S. D. Linker, J. N. Linley, T. B. Littenberg, J. Liu, X. Liu, M. Llorens-Monteagudo, R. K. L. Lo, A. Lockwood, L. T. London, A. Longo, M. Lorenzini, V. Loriette, M. Lormand, G. Losurdo, J. D. Lough, C. O. Lousto, G. Lovelace, H. Lück, D. Lumaca, A. P. Lundgren, Y. Ma, R. Macas, M. MacInnis, D. M. Macleod, I. A. O. MacMillan, A. Macquet, I. Magaña Hernandez, F. Magaña-Sandoval, C. Magazzù, R. M. Magee, E. Majorana, I. Maksimovic, S. Maliakal, A. Malik, N. Man, V. Mandic, V. Mangano, G. L. Mansell, M. Manske, M. Mantovani, M. Mapelli, F. Marchesoni, F. Marion, S. Márka, Z. Márka, C. Markakis, A. S. Markosyan, A. Markowitz, E. Maros, A. Marquina, S. Marsat, F. Martelli, I. W. Martin, R. M. Martin, M. Martinez, V. Martinez, D. V. Martynov, H. Masalehdan, K. Mason, E. Massera, A. Masserot, T. J. Massinger, M. Masso-Reid, S. Mastrogiovanni, A. Matas, M. Mateu-Lucena, F. Matichard, M. Matiushechkina, N. Mavalvala, E. Maynard, J. J. McCann, R. McCarthy, D. E. McClelland, S. McCormick, L. McCuller, S. C. McGuire, C. McIsaac, J. McIver, D. J. McManus, T. McRae, S. T. McWilliams, D. Meacher, G. D. Meadors, M. Mehmet, A. K. Mehta, A. Melatos, D. A. Melchor, G. Mendell, A. Menendez-Vazquez, R. A. Mercer, L. Mereni, K. Merfeld, E. L. Merilh, J. D. Merritt, M. Merzougui, S. Meshkov, C. Messenger, C. Messick, R. Metzdorff, P. M. Meyers, F. Meylahn, A. Mhaske, A. Miani, H. Miao, I. Michaloliakos, C. Michel, H. Middleton, L. Milano, A. L. Miller, S. Miller, M. Millhouse, J. C. Mills, E. Milotti, M. C. Milovich-Goff, O. Minazzoli, Y. Minenkov, L. M. Mir, A. Mishkin, C. Mishra, T. Mistry, S. Mitra, V. P. Mitrofanov, G. Mitselmakher, R. Mittleman, G. Mo, K. Mogushi, S. R. P. Mohapatra, S. R. Mohite, I. Molina, M. Molina-Ruiz, M. Mondin, M. Montani, C. J. Moore, D. Moraru, F. Morawski, G. Moreno, S. Morisaki, B. Mours, C. M. Mow-Lowry, S. Mozzon, F. Muciaccia, A. Mukherjee, D. Mukherjee, S. Mukherjee, S. Mukherjee, N. Mukund, A. Mullavey, J. Munch, E. A. Muñiz, P. G. Murray, S. L. Nadji, A. Nagar, I. Nardecchia, L. Naticchioni, R. K. Nayak, B. F. Neil, J. Neilson, G. Nelemans, T. J. N. Nelson, M. Nery, A. Neunzert, K. Y. Ng, S. Ng, C. Nguyen, P. Nguyen, T. Nguyen, S. A. Nichols, S. Nissanke, F. Nocera, M. Noh, C. North, D. Nothard, L. K. Nuttall, J. Oberling, B. D. O'Brien, J. O'Dell, G. Oganesyan, G. H. Ogin, J. J. Oh, S. H. Oh, F. Ohme, H. Ohta, M. A. Okada, C. Olivetto, P. Oppermann, R. J. Oram, B. O'Reilly, R. G. Ormiston, N. Ormsby, L. F. Ortega,

R. O'Shaughnessy, S. Ossokine, C. Osthelder, D. J. Ottaway, H. Overmier, B. J. Owen, A. E. Pace, G. Pagano, M. A. Page, G. Pagliaroli, A. Pai, S. A. Pai, J. R. Palamos, O. Palashov, C. Palomba, H. Pan, P. K. Panda, T. H. Pang, C. Pankow, F. Pannarale, B. C. Pant, F. Paoletti, A. Paoli, A. Paolone, W. Parker, D. Pascucci, A. Pasqualetti, R. Passaquieti, D. Passuello, M. Patel, B. Patricelli, E. Payne, T. C. Pechsiri, M. Pedraza, M. Pegoraro, A. Pele, S. Penn, A. Perego, C. J. Perez, C. Périgois, A. Perreca, S. Perriès, J. Petermann, D. Petterson, H. P. Pfeiffer, K. A. Pham, K. S. Phukon, O. J. Piccinni, M. Pichot, M. Piendibene, F. Piergiovanni, L. Pierini, V. Pierro, G. Pillant, F. Pilo, L. Pinard, I. M. Pinto, K. Piotrzkowski, M. Pirello, M. Pitkin, E. Placidi, W. Plastino, C. Pluchar, R. Poggiani, E. Polini, D. Y. T. Pong, S. Ponrathnam, P. Popolizio, E. K. Porter, A. Poverman, J. Powell, M. Pracchia, A. K. Prajapati, K. Prasai, R. Prasanna, G. Pratten, T. Prestegard, M. Principe, G. A. Prodi, L. Prokhorov, P. Prosposito, A. Puecher, M. Punturo, F. Puosi, P. Puppo, M. Pürrer, H. Qi, V. Quetschke, P. J. Quinonez, R. Quitzow-James, F. J. Raab, G. Raaijmakers, H. Radkins, N. Radulesco, P. Raffai, H. Rafferty, S. X. Rail, S. Raja, C. Rajan, B. Rajbhandari, M. Rakhmanov, K. E. Ramirez, T. D. Ramirez, A. Ramos-Buades, J. Rana, K. Rao, P. Rapagnani, U. D. Rapol, B. Ratto, V. Raymond, M. Razzano, J. Read, T. Regimbau, L. Rei, S. Reid, D. H. Reitze, P. Rettegno, F. Ricci, C. J. Richardson, J. W. Richardson, L. Richardson, P. M. Ricker, G. Riemenschneider, K. Riles, M. Rizzo, N. A. Robertson, F. Robinet, A. Rocchi, J. A. Rocha, S. Rodriguez, R. D. Rodriguez-Soto, L. Rolland, J. G. Rollins, V. J. Roma, M. Romanelli, R. Romano, C. L. Romel, A. Romero, I. M. Romero-Shaw, J. H. Romie, S. Ronchini, C. A. Rose, D. Rose, K. Rose, M. J. B. Rosell, D. Rosińska, S. G. Rosofsky, M. P. Ross, S. Rowan, S. J. Rowlinson, S. Roy, S. Roy, P. Ruggi, K. Ryan, S. Sachdev, T. Sadecki, J. Sadiq, M. Sakellariadou, O. S. Salafia, L. Salconi, M. Saleem, A. Samajdar, E. J. Sanchez, J. H. Sanchez, L. E. Sanchez, N. Sanchis-Gual, J. R. Sanders, K. A. Santiago, E. Santos, T. R. Saravanan, N. Sarin, B. Sassolas, B. S. Sathyaprakash, O. Sauter, R. L. Savage, V. Savant, D. Sawant, S. Sayah, D. Schaetzl, P. Schale, M. Scheel, J. Scheuer, A. Schindler-Tyka, P. Schmidt, R. Schnabel, R. M. S. Schofield, A. Schönbeck, E. Schreiber, B. W. Schulte, B. F. Schutz, O. Schwarm, E. Schwartz, J. Scott, S. M. Scott, M. Seglar-Arroyo, E. Seidel, D. Sellers, A. S. Sengupta, N. Sennett, D. Sentenac, V. Sequino, A. Sergeev, Y. Setyawati, T. Shaffer, M. S. Shahriar, S. Sharifi, A. Sharma, P. Sharma, P. Shawhan, H. Shen, M. Shikauchi, R. Shink, D. H. Shoemaker, D. M. Shoemaker, K. Shukla, S. ShyamSundar, M. Sieniawska, D. Sigg, L. P. Singer, D. Singh, N. Singh, A. Singha, A. Singhal, A. M. Sintes, V. Sipala, V. Skliris, B. J. J. Slagmolen, T. J. Slaven-Blair, J. Smetana, J. R. Smith, R. J. E. Smith, S. N. Somala, E. J. Son, S. Soni, B. Sorazu, V. Sordini, F. Sorrentino, N. Sorrentino, R. Soulard, T. Souradeep, E. Sowell, A. P. Spencer, M. Spera, A. K. Srivastava, V. Srivastava, K. Staats, C. Stachie, D. A. Steer, M. Steinke, J. Steinlechner, S. Steinlechner, D. Steinmeyer, S. P. Stevenson, G. Stolle-McAllister, D. J. Stops, M. Stover, K. A. Strain, G. Stratta, A. Strunk, R. Sturani, A. L. Stuver, J. Südbeck, S. Sudhagar, V. Sudhir, H. G. Suh, T. Z. Summerscales, H. Sun, L. Sun, S. Sunil, A. Sur, J. Suresh, P. J. Sutton, B. L. Swinkels, M. J. Szczepańczyk, M. Tacca, S. C. Tait, C. Talbot, A. J. Tanasijczuk, D. B. Tan-

ner, D. Tao, A. Tapia, E. N. Tapia San Martin, J. D. Tasson, R. Taylor, R. Tenorio, L. Terkowski, M. P. Thirugnanasambandam, L. Thomas, M. Thomas, P. Thomas, J. E. Thompson, S. R. Thondapu, K. A. Thorne, E. Thrane, S. Tiwari, S. Tiwari, V. Tiwari, K. Toland, A. E. Tolley, M. Tonelli, Z. Tornasi, A. Torres-Forné, C. I. Torrie, I. T. e. Melo, D. Töyrä, A. T. Tran, A. Trapananti, F. Travasso, G. Traylor, M. C. Tringali, A. Tripathee, A. Trovato, R. J. Trudeau, D. S. Tsai, K. W. Tsang, M. Tse, R. Tso, L. Tsukada, D. Tsuna, T. Tsutsui, M. Turconi, A. S. Ubhi, R. P. Udall, K. Ueno, D. Ugolini, C. S. Unnikrishnan, A. L. Urban, S. A. Usman, A. C. Utina, H. Vahlbruch, G. Vajente, A. Vajpeyi, G. Valdes, M. Valentini, V. Valsan, N. van Bakel, M. van Beuzekom, J. F. J. van den Brand, C. Van Den Broeck, D. C. Vander-Hyde, L. van der Schaaf, J. V. van Heijningen, M. Vardaro, A. F. Vargas, V. Varma, S. Vass, M. Vasúth, A. Vecchio, G. Vedovato, J. Veitch, P. J. Veitch, K. Venkateswara, J. Venneberg, G. Venugopalan, D. Verkindt, Y. Verma, D. Veske, F. Vetrano, A. Viceré, A. D. Viets, V. Villa-Ortega, J. Y. Vinet, S. Vitale, T. Vo, H. Vocca, C. Vorvick, S. P. Vyatchanin, A. R. Wade, L. E. Wade, M. Wade, R. C. Walet, M. Walker, G. S. Wallace, L. Wallace, S. Walsh, J. Z. Wang, S. Wang, W. H. Wang, Y. F. Wang, R. L. Ward, J. Warner, M. Was, N. Y. Washington, J. Watchi, B. Weaver, L. Wei, M. Weinert, A. J. Weinstein, R. Weiss, F. Wellmann, L. Wen, P. Weßels, J. W. Westhouse, K. Wette, J. T. Whelan, D. D. White, L. V. White, B. F. Whiting, C. Whittle, D. M. Wilken, D. Williams, M. J. Williams, A. R. Williamson, J. L. Willis, B. Willke, D. J. Wilson, M. H. Wimmer, W. Winkler, C. C. Wipf, G. Woan, J. Woehler, J. K. Wofford, I. C. F. Wong, J. Wrangel, J. L. Wright, D. S. Wu, D. M. Wysocki, L. Xiao, H. Yamamoto, L. Yang, Y. Yang, Z. Yang, M. J. Yap, D. W. Yeeles, A. Yoon, H. Yu, H. Yu, S. H. R. Yuen, A. Zadrożny, M. Zanolin, T. Zelenova, J. P. Zendri, M. Zevin, J. Zhang, L. Zhang, R. Zhang, T. Zhang, C. Zhao, G. Zhao, M. Zhou, Z. Zhou, X. J. Zhu, A. B. Zimmerman, M. E. Zucker, and J. Zweizig. Population Properties of Compact Objects from the Second LIGO-Virgo Gravitational-Wave Transient Catalog. *arXiv e-prints*, art. arXiv:2010.14533, Oct. 2020.

F.-K. Thielemann, K. Nomoto, and K. Yokoi. Explosive nucleosynthesis in carbon deflagration models of Type I supernovae. *Astronomy and Astrophysics*, 158:17–33, Apr. 1986.

F. K. Thielemann, M. Eichler, I. V. Panov, and B. Wehmeyer. Neutron Star Mergers and Nucleosynthesis of Heavy Elements. *Annual Review of Nuclear and Particle Science*, 67:253–274, Oct. 2017. doi: 10.1146/annurev-nucl-101916-123246.

T. A. Thompson, P. Chang, and E. Quataert. Magnetar Spin-Down, Hyperenergetic Supernovae, and Gamma-Ray Bursts. *The Astrophysical Journal*, 611(1):380–393, Aug. 2004. doi: 10.1086/421969.

G. Torrealba, V. Belokurov, S. E. Koposov, K. Bechtol, A. Drlica-Wagner, K. A. G. Olsen, A. K. Vivas, B. Yanny, P. Jethwa, A. R. Walker, T. S. Li, S. Allam, B. C. Conn, C. Gallart, R. A. Gruendl, D. J. James, M. D. Johnson, K. Kuehn, N. Kuropatkin, N. F. Martin, D. Martinez-Delgado, D. L. Nidever, N. E. D. Noël,

J. D. Simon, G. S. Stringfellow, and D. L. Tucker. Discovery of two neighbouring satellites in the Carina constellation with MagLiteS. *Monthly Notices of the Astronomical Society*, 475(4):5085–5097, Apr. 2018. doi: 10.1093/mnras/sty170.

T. Tsujimoto and T. Shigeyama. Enrichment history of r-process elements shaped by a merger of neutron star pairs. *Astronomy and Astrophysics*, 565:L5, May 2014. doi: 10.1051/0004-6361/201423751.

T. Tsujimoto, M. N. Ishigaki, T. Shigeyama, and W. Aoki. Chemical feature of Eu abundance in the Draco dwarf spheroidal galaxy. *Publications of the Astronomical Society of Japan*, 67:L3, June 2015. doi: 10.1093/pasj/psv035.

T. Tsujimoto, T. Matsuno, W. Aoki, M. N. Ishigaki, and T. Shigeyama. Enrichment in r-process Elements from Multiple Distinct Events in the Early Draco Dwarf Spheroidal Galaxy. *The Astrophysical Journal*, 850:L12, Nov. 2017. doi: 10.3847/2041-8213/aa9886.

J. Tumlinson. Chemical Evolution in Hierarchical Models of Cosmic Structure. II. The Formation of the Milky Way Stellar Halo and the Distribution of the Oldest Stars. *The Astrophysical Journal*, 708(2):1398–1418, Jan. 2010. doi: 10.1088/0004-637X/708/2/1398.

U. Ural, G. Cescutti, A. Koch, J. Kleyna, S. Feltzing, and M. I. Wilkinson. An inefficient dwarf: chemical abundances and the evolution of the Ursa Minor dwarf spheroidal galaxy. *Monthly Notices of the Astronomical Society*, 449:761–770, May 2015. doi: 10.1093/mnras/stv294.

F. van de Voort, E. Quataert, P. F. Hopkins, D. Kereš, and C.-A. Faucher-Giguère. Galactic r-process enrichment by neutron star mergers in cosmological simulations of a Milky Way-mass galaxy. *Monthly Notices of the Astronomical Society*, 447: 140–148, Feb. 2015. doi: 10.1093/mnras/stu2404.

S. van der Walt, S. C. Colbert, and G. Varoquaux. The numpy array: A structure for efficient numerical computation. *Computing in Science & Engineering*, 13(2):22–30, 2011. doi: http://dx.doi.org/10.1109/MCSE.2011.37. URL `http://scitation.aip.org/content/aip/journal/cise/13/2/10.1109/MCSE.2011.37`.

E. Vasiliev. AGAMA: action-based galaxy modelling architecture. *Monthly Notices of the Astronomical Society*, 482(2):1525–1544, Jan. 2019. doi: 10.1093/mnras/sty2672.

S. Vassilvitskii and D. Arthur. k-means++: The advantages of careful seeding. In *Proceedings of the eighteenth annual ACM-SIAM symposium on Discrete algorithms*, pages 1027–1035, 2006.

K. A. Venn, M. Irwin, M. D. Shetrone, C. A. Tout, V. Hill, and E. Tolstoy. Stellar Chemical Signatures and Hierarchical Galaxy Formation. *The Astronomical Journal*, 128:1177–1195, Sept. 2004. doi: 10.1086/422734.

K. A. Venn, M. D. Shetrone, M. J. Irwin, V. Hill, P. Jablonka, E. Tolstoy, B. Lemasle, M. Divell, E. Starkenburg, B. Letarte, C. Baldner, G. Battaglia, A. Helmi, A. Kaufer, and F. Primas. Nucleosynthesis and the Inhomogeneous Chemical Evolution of the Carina Dwarf Galaxy. *The Astrophysical Journal*, 751:102, June 2012. doi: 10.1088/0004-637X/751/2/102.

K. A. Venn, E. Starkenburg, L. Malo, N. Martin, and B. P. M. Laevens. Gemini/GRACES spectroscopy of stars in Tri II. *Monthly Notices of the Astronomical Society*, 466:3741–3752, Apr. 2017. doi: 10.1093/mnras/stw3198.

P. Virtanen, R. Gommers, T. E. Oliphant, M. Haberland, T. Reddy, D. Cournapeau, E. Burovski, P. Peterson, W. Weckesser, J. Bright, S. J. van der Walt, M. Brett, J. Wilson, K. J. Millman, N. Mayorov, A. R. J. Nelson, E. Jones, R. Kern, E. Larson, C. J. Carey, İ. Polat, Y. Feng, E. W. Moore, J. VanderPlas, D. Laxalde, J. Perktold, R. Cimrman, I. Henriksen, E. A. Quintero, C. R. Harris, A. M. Archibald, A. H. Ribeiro, F. Pedregosa, P. van Mulbregt, and SciPy 1.0 Contributors. SciPy 1.0: Fundamental Algorithms for Scientific Computing in Python. *Nature Methods*, 17:261–272, 2020. doi: 10.1038/s41592-019-0686-2.

D. Wanderman and T. Piran. The luminosity function and the rate of Swift's gamma-ray bursts. *Monthly Notices of the Astronomical Society*, 406(3):1944–1958, Aug. 2010. doi: 10.1111/j.1365-2966.2010.16787.x.

F. Wang, Y.-C. Zou, F. Liu, B. Liao, Y. Liu, Y. Chai, and L. Xia. A Comprehensive Statistical Study of Gamma-Ray Bursts. *The Astrophysical Journal*, 893(1):77, Apr. 2020. doi: 10.3847/1538-4357/ab0a86.

J. H. Ward Jr. Hierarchical grouping to optimize an objective function. *Journal of the American Statistical Association*, 58(301):236–244, 1963.

M. Wardle and G. R. Knapp. The statistical distribution of the neutral-hydrogen content of SO galaxies. *The Astronomical Journal*, 91:23–48, Jan. 1986. doi: 10.1086/113976.

B. Wehmeyer, M. Pignatari, and F.-K. Thielemann. Galactic evolution of rapid neutron capture process abundances: the inhomogeneous approach. *Monthly Notices of the Astronomical Society*, 452:1970–1981, Sept. 2015. doi: 10.1093/mnras/stv1352.

S. D. M. White and M. J. Rees. Core condensation in heavy halos: a two-stage theory for galaxy formation and clustering. *Monthly Notices of the Astronomical Society*, 183:341–358, May 1978. doi: 10.1093/mnras/183.3.341.

B. F. Williams, J. J. Dalcanton, E. F. Bell, K. M. Gilbert, P. Guhathakurta, C. Dorman, T. R. Lauer, A. C. Seth, J. S. Kalirai, P. Rosenfield, and L. Girardi. Tracing the Metal-poor M31 Stellar Halo with Blue Horizontal Branch Stars. *The Astrophysical Journal*, 802:49, Mar. 2015. doi: 10.1088/0004-637X/802/1/49.

J. H. Wise and T. Abel. ENZO+MORAY: radiation hydrodynamics adaptive mesh refinement simulations with adaptive ray tracing. *Monthly Notices of the Astronomical Society*, 414:3458–3491, July 2011. doi: 10.1111/j.1365-2966.2011.18646.x.

J. H. Wise, T. Abel, M. J. Turk, M. L. Norman, and B. D. Smith. The birth of a galaxy - II. The role of radiation pressure. *Monthly Notices of the Astronomical Society*, 427:311–326, Nov. 2012a. doi: 10.1111/j.1365-2966.2012.21809.x.

J. H. Wise, M. J. Turk, M. L. Norman, and T. Abel. The Birth of a Galaxy: Primordial Metal Enrichment and Stellar Populations. *The Astrophysical Journal*, 745:50, Jan. 2012b. doi: 10.1088/0004-637X/745/1/50.

T.-W. Wong, B. Willems, and V. Kalogera. Constraints on Natal Kicks in Galactic Double Neutron Star Systems. *The Astrophysical Journal*, 721(2):1689–1701, Oct. 2010. doi: 10.1088/0004-637X/721/2/1689.

S. E. Woosley. Pulsational Pair-instability Supernovae. *The Astrophysical Journal*, 836(2):244, Feb. 2017. doi: 10.3847/1538-4357/836/2/244.

Y. Wu, M. Valluri, N. Panithanpaisal, R. E. Sanderson, K. Freese, A. Wetzel, and S. Sharma. Using action space clustering to constrain the recent accretion history of Milky Way-like galaxies. *Monthly Notices of the Astronomical Society*, 509(4): 5882–5901, Feb. 2022. doi: 10.1093/mnras/stab3306.

B. Yanny, C. Rockosi, H. J. Newberg, G. R. Knapp, J. K. Adelman-McCarthy, B. Alcorn, S. Allam, C. Allende Prieto, D. An, K. S. J. Anderson, S. Anderson, C. A. L. Bailer-Jones, S. Bastian, T. C. Beers, E. Bell, V. Belokurov, D. Bizyaev, N. Blythe, J. J. Bochanski, W. N. Boroski, J. Brinchmann, J. Brinkmann, H. Brewington, L. Carey, K. M. Cudworth, M. Evans, N. W. Evans, E. Gates, B. T. Gänsicke, B. Gillespie, G. Gilmore, A. Nebot Gomez-Moran, E. K. Grebel, J. Greenwell, J. E. Gunn, C. Jordan, W. Jordan, P. Harding, H. Harris, J. S. Hendry, D. Holder, I. I. Ivans, Ž. Ivezič, S. Jester, J. A. Johnson, S. M. Kent, S. Kleinman, A. Kniazev, J. Krzesinski, R. Kron, N. Kuropatkin, S. Lebedeva, Y. S. Lee, R. French Leger, S. Lépine, S. Levine, H. Lin, D. C. Long, C. Loomis, R. Lupton, O. Malanushenko, V. Malanushenko, B. Margon, D. Martinez-Delgado, P. McGehee, D. Monet, H. L. Morrison, J. A. Munn, J. Neilsen, Eric H., A. Nitta, J. E. Norris, D. Oravetz, R. Owen, N. Padmanabhan, K. Pan, R. S. Peterson, J. R. Pier, J. Platson, P. Re Fiorentin, G. T. Richards, H.-W. Rix, D. J. Schlegel, D. P. Schneider, M. R. Schreiber, A. Schwope, V. Sibley, A. Simmons, S. A. Snedden, J. Allyn Smith, L. Stark, F. Stauffer, M. Steinmetz, C. Stoughton, M. SubbaRao, A. Szalay, P. Szkody, A. R. Thakar, T. Sivarani, D. Tucker, A. Uomoto, D. Vanden Berk, S. Vidrih, Y. Wadadekar, S. Watters, R. Wilhelm, R. F. G. Wyse, J. Yarger, and D. Zucker. SEGUE: A Spectroscopic Survey of 240,000 Stars with g = 14-20. *The Astronomical Journal*, 137(5):4377–4399, May 2009. doi: 10.1088/0004-6256/137/5/4377.

Z. Yuan, J. Chang, P. Banerjee, J. Han, X. Kang, and M. C. Smith. StarGO: A New Method to Identify the Galactic Origins of Halo Stars. *The Astrophysical Journal*, 863(1):26, Aug. 2018. doi: 10.3847/1538-4357/aacd0d.

Z. Yuan, G. C. Myeong, T. C. Beers, N. W. Evans, Y. S. Lee, P. Banerjee, D. Gudin, K. Hattori, H. Li, T. Matsuno, V. M. Placco, M. C. Smith, D. D. Whitten, and G. Zhao. Dynamical Relics of the Ancient Galactic Halo. *The Astrophysical Journal*, 891(1):39, Mar. 2020. doi: 10.3847/1538-4357/ab6ef7.

M. Zevin, K. Kremer, D. M. Siegel, S. Coughlin, B. T. H. Tsang, C. P. L. Berry, and V. Kalogera. Can Neutron-star Mergers Explain the r-process Enrichment in Globular Clusters? *The Astrophysical Journal*, 886(1):4, Nov. 2019. doi: 10.3847/1538-4357/ab498b.